Hybrid Materials Based on Molecular Self-Assembled Monolayers for the Fabrication of Switches and Sensors

Ángel Campos Lendínez

Universitat Autònoma de Barcelona

Hybrid Materials Based on Molecular Self-Assembled Monolayers for the Fabrication of Switches and Sensors

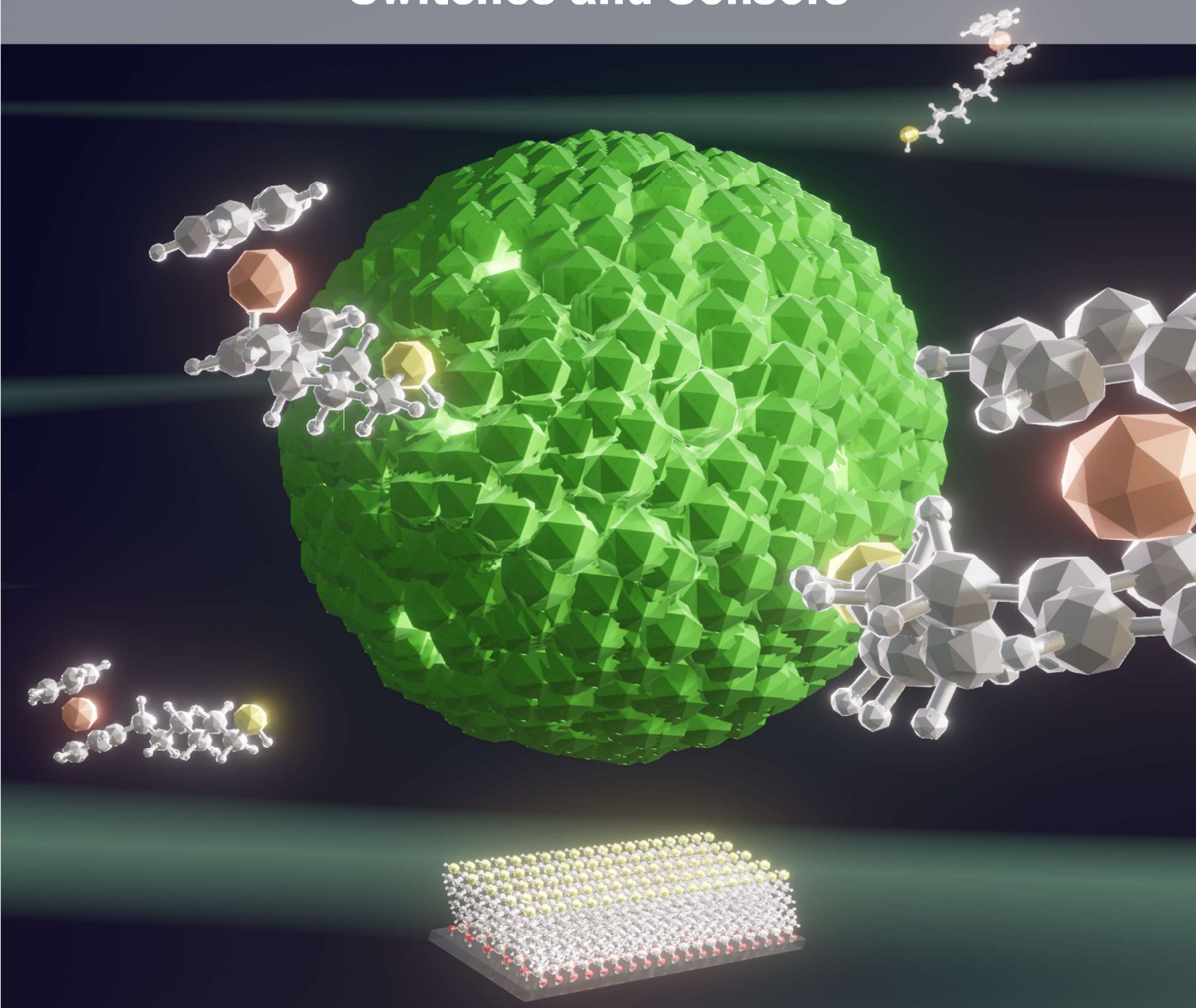

Ángel Campos Lendínez

Doctoral Thesis
July 2023

Hybrid Materials Based on Molecular Self-Assembled Monolayers for the Fabrication of Switches and Sensors

Ángel Campos Lendínez

Doctoral Thesis

Physics and Chemistry Department

Universidad Autónoma de Barcelona

PhD Programme in Materials Science

Supervisor/Director: Prof. Marta Mas Torrent and Dr. Núria Crivillers i Clusella

Molecular Nanoscience and Organic Materials (NANOMOL)

Institut de Ciència de Materials de Barcelona (ICMAB-CSIC)

July, 2023

Memoria presentada para aspirar al Grado de Doctor por:

Ángel Campos Lendínez

Visto y aprobado:

Porf. Marta Mas Torrent

Dr. Núria Crivillers i Clusella

Bellaterra, 14 de Julio de 2023

MARTA MAS TORRENT and **NÚRIA CRIVILLER I CLUSELLA**, Research Scientists of the Spanish Council of Research (CSIC) at the Materials Science Institute of Barcelona (ICMAB)

CERTIFIES

Under their supervision, **Ángel Campos Lendínez** has performed the research entitled "**Hybrid Materials Based on Molecular Self-Assembled Monolayers for the Fabrication of Switches and Sensors**". This work has been carried out under the framework of the Materials Science PhD Programme of the Physics and Chemistry Department of the Autonomous University of Barcelona.

And in witness whereof this is signed by

Director:

Prof. Marta Mas Torrent Dr. Núria Crivillers i Clusella

Bellaterra, July 14th, 2023

Acknowledgements

Me resulta extremadamente difícil pensar en todas las personas que de alguna manera u otra me han ayudado a terminar esta Tesis. Ha sido un camino lleno de alti bajos, de ansiedades, momentos brillantes, de miedos, felicidad, de caídas y subidas…. ¡Pero sobre todo de experiencias!. Pensaba que llegado este momento tendría claro como hacerlo, pero echando una vista atrás durante estos largos cinco años, hay demasiados sentimientos.

Esta Tesis va especialmente dedicada a mis Padres. Ellos han sido los que incondicionalmente me han apoyado en cada momento y los que más han sufrido mis fracasos y celebrado mis éxitos. Siempre me han escuchado, me han calmado o me han animado a seguir adelante. No sabría cómo describir con palabras todo lo que han hecho por mí. Aún estando lejos, los sentía cerca.

Gracias a Marta y Nuria, mis directoras de Tesis. Ellas también han sufrido mis peores situaciones, y aún así, siempre me han animado a seguir adelante. Si no hubieran sido tan comprensivas con las dificultades que se atraviesa en un camino así, probablemente no estaría escrbiendo estas palabras. Su trabajo y guía han hecho de mí un mejor investigador y no puedo estarles más agradecido. Sobre todo en este último periodo dónde han sacrificado tiempo para terminar todo el trabajo de cinco años. ¡Gracias por todo!

Recuerdo que cuando empecé mis estudios de Química en la Universidad hace ya trece años, se empezó a sembrar un sentimiento de curiosidad por descubrir cómo funcionaba el mundo que me rodeaba. Este sentimiento fue sutilmente incorporándose por un persona que endulzó mi vida en un momento amargo. Lara, gracias por tanto que

hiciste en mí únicamente utilizando un café y un sonrisa. No sé qué habría sido de mí sin que estuvieras en mi vida.

A los años, cuando finalemte llegué a Barcelona paraa empezar esta Tesis, fue un golpe de miedo y emoción por esta etapa. La incertidumbre de empezar una nueva vida fue abrumadora, pero no esperaba encontrarme con las personas que conocí. A todos mi compañeros de NANOMOL, del ICMAB y todas las personas que han formado parte de mi vida en esta aventura diaria fuera de las instituciones. Amigos que me han hecho sacar lo mejor de este periodo. Aprovechar cada minuto y hacer que quiera seguir aquí de una manera tan indeterminada que no me plantearía mudarme a ningún otro lugar. Si tuviera que hacer una dedicatoria a cada persona que he conocido y me ha hecho ser mejor, probablemente estos agradecimientos extenderían una Tesis. Por ello, mi agradecimiento es eterno a todas las personas que estuvieron, que están y que estarán. A todos los amigos que siguen estando día a día, que me han hecho formar parte de su entorno más íntimo, que han contado conmigo, que me han mantenido cerca a pesar de mis despistes y que hacen que mi vida sea mejor. No puedo estarles más agradecido por ser cómo son y por cómo están. ¡Gracias por tanto!

No puedo dejar de paso a otra persona que ha hecho de mí un cambio a todos los niveles en los últimos años. Stefania llegó a mi vida como un terremoto, haciendo temblar todos los cimientos que había creado para construir algo más firme y alto. Iniciamos este viaje juntos en Barcelona y me ha alzado como pocas personas imaginaría que harían. No tengo palabras para definir los cambios a todos los niveles que ha creado.

A Jose, por guiarme, escucharme y aunque no exento de discusiones, hacía que echara en falta su presencia cuando no estaba. Haces que mi vida sea más florida y me calmas con cada abrazo que me das.

A mi familia, mis hermanos y mis amigos en Jaén. Sois los contrafuertes de mi vida, no se perciben todos los días pero sin vosotros no podría mantenerme firme. Especialmente a mi hermano Sergio, por llamarme cada semana, preocuparse y por ser alguien con quien he podido hablar de sin ningún miedo de cualquier tema.

Finalmente, quería agradecer la imaginación, perseverancia y motivación de Jamila por hacer la portada de esta Tesis. Sin tu trabajo no habría sido igual.

No pensaba extenderme tanto en estos agradecimientos, y es gracias a todas las personas que han moldeado mi camino para llegar hasta aquí. Mi cariño es eterno y sin vosotros esto no habría sido igual. ¡GRACIAS POR TODO!

Summary

Molecular electronics aims to employ individual or an ensemble of functional molecules as active components in devices. To progress in this field there is a clear need of immobilizing the target molecules on surfaces. This Thesis is focused on the preparation of functional molecular self-assembled monolayers (SAMs) for the development of smart switchable surfaces and electrochemical sensors.

Electrochemically switchable SAMs based on redox active molecules have been developed. First, two methodologies have been demonstrated to prepare SAMs on gold based on an urazole organic radical. Urazole radicals show limited stability in solution since they tend to dimerize and are not possible to be isolated in solid state. By generating in situ the radical or by employing a SAM of a radical precursor, the radical SAMs were successfully achieved exhibiting magnetic and redox activity. Secondly, SAMs of semiconductor quantum dots (QDs) functionalized with ferrocene (Fc) have been prepared. The emission intensity (optical output) of the QDs was tuned by changing the redox state of the grafted Fc (electrical input). Highly stable and reversible binary and ternary switches were realised.

Furthermore, SAMs have been employed to develop highly sensitive sensors based on the supramolecular interactions between the modified surface and the analyte. Based on this, an impedimetric sensor platform to selectively detect Polycyclic Aromatic Hydrocarbons (PAHs) pollutants in water has been prepared. It has been shown that surface-anchored PAHs can selectively interact with a specific PAH target thanks to the unique π–stacking interactions between identical small aromatic molecules. Finally, a pH sensor based on an electrolyte-gated organic field-effect transistor (EGOFET) able to

operate in a wide pH range (i.e., from 1 to 10) with high sensitivity was fabricated. In this device a magnetic carbon electrode able to trap functionalised magnetic nanoparticles in its surface was used as gate contact. The pH dependent host-guest complex formation between grafted β-cyclodextrins and imidazole was exploited as indirect indication of the solution pH.

List of Abbreviations and Symbols

Abbreviations

11-MUA	11-Mercaptoundecanoic Acid
4-MPD	4-Mercaptophenyldiazonium Tetrafluoroborate
AFM	Atomic Force Microscopy
AQ	Anthraquinone
AuNP	Gold Nanoparticle
BE	Binding Energy
CA	Contact Angle
C-AFM	Conducting Atomic Force Microscopy
CD	Cyclodextrin
CE	Counter Electrode
CGE	Carbon Paste Gate Electrode
CPE	Carbon Composite Electrode
CV	Cyclic Voltammetry
D	Drain Electrode
diF-TES-ADT	2,8-Difluoro-5,11-Bis(Triethylsilylethynyl)Anthradithiophene
DPV	Different Pulse Voltammetry
DPW	Differential Pulse Voltammetry
DSP	Dithiobis/ Succinimidyl Propionate
EDL	Electric Double Layer
EGOFET	Electrolyte-Gated Organic Field Effect Transistor
EIS	Electrochemical Impedance Spectroscopy
EPA	Environmental Protection Agency
EPR	Electron Paramagnetic Resonance

ET	Electron Transfer
Fc	Ferrocene
Fc^+	Ferrocenium
FcSH	6-(Ferrocenyl)Hexanethiol
FWHM	Full Width at Half the Maximum Peak Height
GC-MS	Gas-Chromatography Coupled with Mass Spectrometry
HOMO	Highest Occupied Molecular Orbital
HPLC	Liquid Chromatography
IARC	Agency for Research on Cancer
IRRAS	Infrared Reflection Absorption Spectroscopy
ITO	Indium Tin Oxide
LED	Light-Emitting Diode
LOD	Limits of Detection
LUMO	Lowest Unoccupied Molecular Orbital
MCH	6-Mercapto-1-Hexanol
MNP	Magnetic Nanoparticle
MOF	Metal-Organic Framework
NEXAFS	Near Edge X-Ray Absorption Fine Structure
NP	Nanoparticle
Octopus-PC	Octopus-Type Crown-Bisphthalocyaninate
OSC	Organic Semiconducting
PAH	Polycyclic Aromatic Hydrocarbon
PCB	Polychlorinated Biphenyl
POC	Point-of-Care
PS	Polystyrene
PTM	Perchlorotriphenylmethyl Radical
QD	Quantum Dot
RE	Reference Electrode
RTIL	Room Temperature Ionic Liquid

S	Source Electrode
SAM	Self-Assembled Monolayer
SPM	Scanning Probe Microscopy
STM	Scanning Tunnelling Microscopy
SWV	Square Wave Voltammetry
ToF-SIMS	Time-of-Flight Secondary Ion Mass Spectrometry
TOP	Trioctylphosphine
TOPO	Trioctylphosphine Oxide
TTF	Tetrathiafulvalene
TTF	Tetrathiafulvalene
UV-Vis	Ultraviolet-Visible
WE	Working Electrode
XPS	X-ray Photoelectron Spectroscopy
β-CD	β-Cyclodextrin

Symbols

A_{peak}	Integrated Area under the Peak
A_{SUR}	Electrode Surface Area
c	Adsorbate Concentration
C	Capacitor
C_{DL}	Double-Layer Capacitance
C_{imag}	Imaginary Capacitance
C_{real}	Real Capacitance
E(t)	Alternating Voltage
$E_{1/2}$	Formal Redox Potential
E_{PA}	Oxidation/Anodic Process
E_{PC}	Reduction/Cathodic Process
F	Faraday Constant
H_{AB}	Donor-Acceptor Electronic Coupling
I	Inductance
I(t)	Alternating Current
I_{ch}	Capacitive Current
I^{o}	Current Oscillation
I_{PA}	Anodic Current
I_{PA}	Cathodic Current
k	Rate Constant
m	Slope
n	Transferred Electrons
R	Resistor
R_{ct}	Charge Transfer Resistance
R_{CT}	Electron Transfer Resistance

$R_{CT'}$	Normalized Electron Transfer Resistance
R_f	Final Electron Transfer Resistance
R_i	Initial Electron Transfer Resistance
R_Ω	Solution Resistance
T	Temperature
t	Time
V_{th}	Threshold Voltage
Z	Impedance
Z_{imag}	Imaginary Impedance
Z_{real}	Real Impedance
Z_W	Warbuck Impedance
α	Angle
Γ	Surface Coverage
ΔG	Gibbs Free Energy
θ	Monolayer Coverage
Θ	Phase Angle
λ	Reorganization Energy
λ_{em}	Emission Wavelength
λ_{ex}	Excitation Wavelength
ν	Scan Rate
ω	Frequency
Ω	Resistance

Table of Contents

CHAPTER 1:
General Introduction

The progressive development of society is inextricably linked with the development, improvement, and progress of technology. Nowadays, "making things smaller" is one of the most relevant technological requirements. This was envisioned by the Nobel Prize laureate Richard Feynman, who introduced the concept of nanotechnology in 1959, describing it as the upcoming *Fourth Industrial Revolution* (*Nanotechnology Revolution*).[1,2] Indeed, nanotechnology has emerged over the years as a revolutionary and breakthrough "miniaturization" approach and, as Feynman said, "it is a field, in which little has been done, but in which an enormous amount can be done in principle [...] because there is plenty of room at the bottom" .[3]

Nanomaterials are those in which at least one of their dimensions is in the nanometre range, typically below 100 nm. These nanostructures have unique properties, often diverse from their macroscopic counterparts, opening a new avenue of novel applications that were not possible before.[4] Their preparation is usually achieved

following a *Top-down* or a *Bottom-up* approach (Figure 1.1).[5] *Top-down* consists in constructing nano-objects, usually using conventional lithographic techniques, from larger entities without atomic-level control. This methodology has some limitations, being one of the most important the high cost of material manufacturing below 50 nm.[6] On the contrary, the *Bottom-up* methodology is based on assembling atoms or molecules to form larger nanometric structures. Molecules have served as building blocks to prepare ultra-miniaturized devices, even at single molecule level in molecular junctions.[7–9] The *Bottom-up* approach is generally based on molecular self-assembly processes, supramolecular chemistry and surface modification. To this end, one widely employed methodology to robustly modify surfaces with molecules organizations is by preparing chemically-bonded molecular Self-Assembled Monolayers (SAMs).[10]

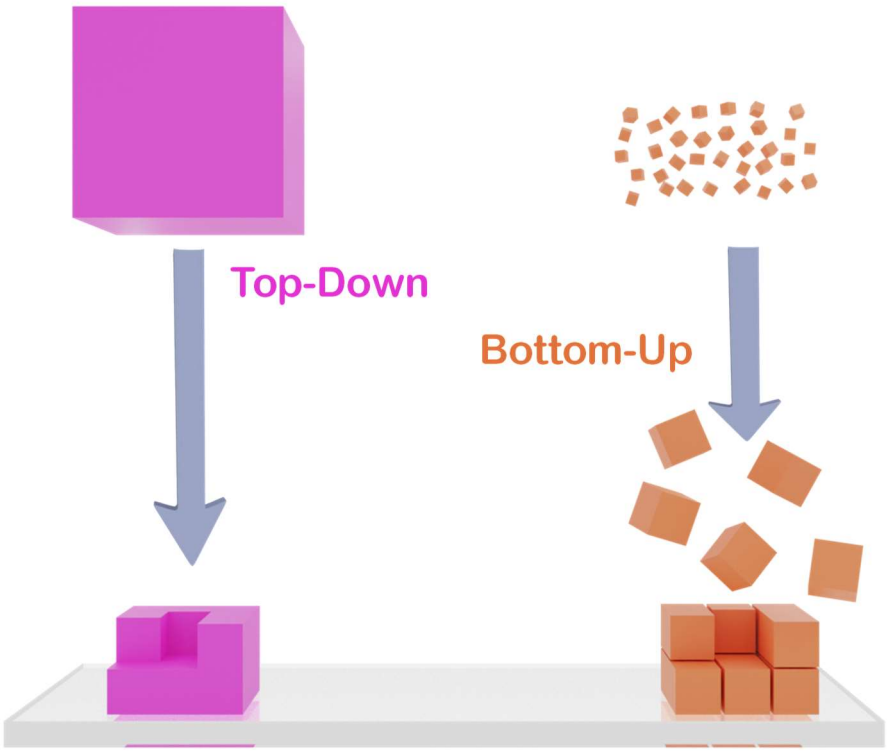

Figure 1.1: *Top-Down* and *Bottom-Up* approaches for nanostructures preparation.

1.1. Self-Assembled Monolayers (SAMs)

Chemically-bonded SAMs are molecular monolayers self-organized from the solution or gas phase onto a specific substrate forming a chemical bond (Figure 1.2). They are unique and highly versatile platforms to manipulate chemical and physical interfacial properties.

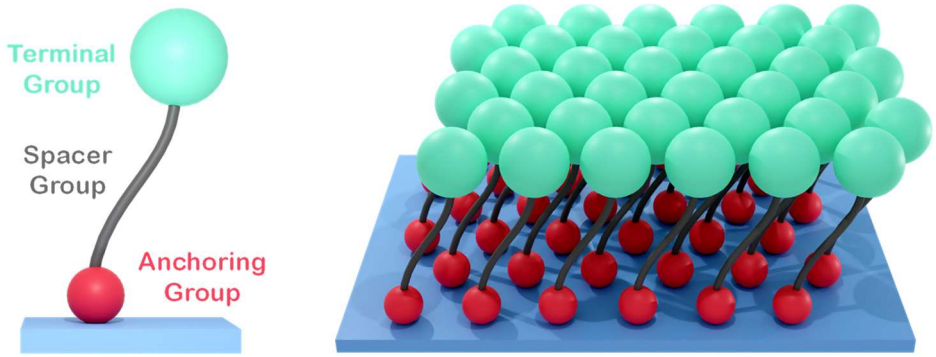

Figure 1.2: Left. Illustration of a single molecule attached on a surface displaying the anchoring, spacer and terminal group. Right. Scheme of a SAM on a substrate.

The molecules employed for the preparation of SAMs are mainly composed of three different groups (Figure 1.2):[11]

i) *Anchoring group*: It is responsible for the interaction between the molecule and the surface. The nature of this group plays an essential role in forming a well-ordered and dense SAM and in its stability. The most studied SAMs are derived from the adsorption of thiol derivatives on gold substrates[12] and silanes on oxides.[13] Nevertheless, other anchoring groups like carboxyl,[14] organophosphorus[15,16] aryl-diazonium[17] and terminal alkynes,[18] have also been employed to functionalize surfaces.

ii) *Spacer group:* It bridges the anchoring and terminal groups and determines the distance between the substrate and the terminal group. In addition, the

intermolecular interactions between neighbouring spacers (van der Waals, hydrogen bonds) help to stabilize the monolayer and improve the SAM packing.

iii) *Terminal group:* It is the functional group of the SAM, also known as the "head" group and determines its functionality. This terminal group can also be used as a template for the chemical coupling with other species.

Thanks to their characteristics, which can be tailored depending on the chemical nature of their components, SAMs have been applied for several purposes such as for (bio)molecular recognition, sensing, energy, catalysis, corrosion prevention, wettability modification, and other areas where tailoring the physicochemical properties of an interface is required (Figure 1.3).[19–26]

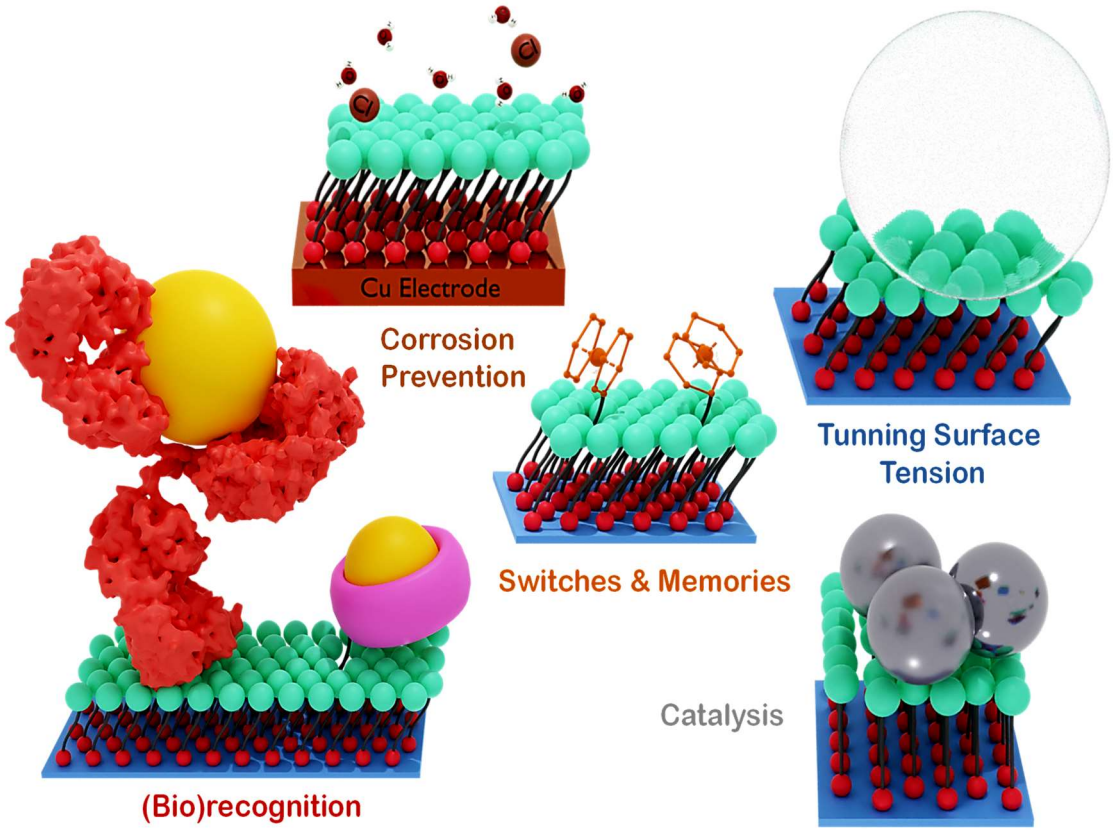

Figure 1.3: Different applications in which SAMs are employed.

Generally, the adsorption kinetics of SAMs is described by the Langmuir kinetics model, which assumes that the growth rate is proportional to the number of available sites on the surface, as follows:[27]

$$\frac{d\theta}{dt} = kC(1-\theta) \quad (1)$$

where k is a rate constant, C is the adsorbate concentration and θ the normalized monolayer coverage, obtained from Eq. 2. In this latter equation, Q is the desorption charge at a given time, and Q_{max} is the maximum reductive charge:

$$\theta = \frac{Q}{Q_{max}} \quad (2)$$

By integrating Eq. 1, the following expression is reached:

$$ln(1-\theta) = -kCt \quad (3)$$

This is the simplest model usually used to describe SAM growth kinetics on the surface.[28] However, this model is only strictly valid if the adsorbed molecules do not interact with each other (i.e. there is no island-type distribution).[29] Furthermore, it should be considered that the type of adsorbate-substrate interaction, preparation method and intermolecular interactions will strongly influence the SAM kinetics formation and organization.

1.1.1 Preparation Methods and Parameters Influencing the SAM Formation

SAMs can be prepared from the liquid or vapour phase. Both methods have been demonstrated to lead to high-ordered SAMs and are extensively used.[30] Considering the

solution-based methods, the most common is the immersion approach since it is simple and versatile.[31] However, other approaches, such as the Langmuir-Blodgett deposition[32,33] or spin coating, have also been used when faster processes are required.[34,35]

The immersion approach involves immersing the substrate in a solution containing the adsorbate (typically for a few hours), where the molecules can spontaneously self-assemble on the surface, forming a monolayer (Figure 1.4). Subsequently, the substrate is removed and rinsed to eliminate physisorbed material. It should be considered that the solvent should not interact chemically with the substrate to avoid undesirable reactions and also that several experimental factors might influence the monolayer formation.

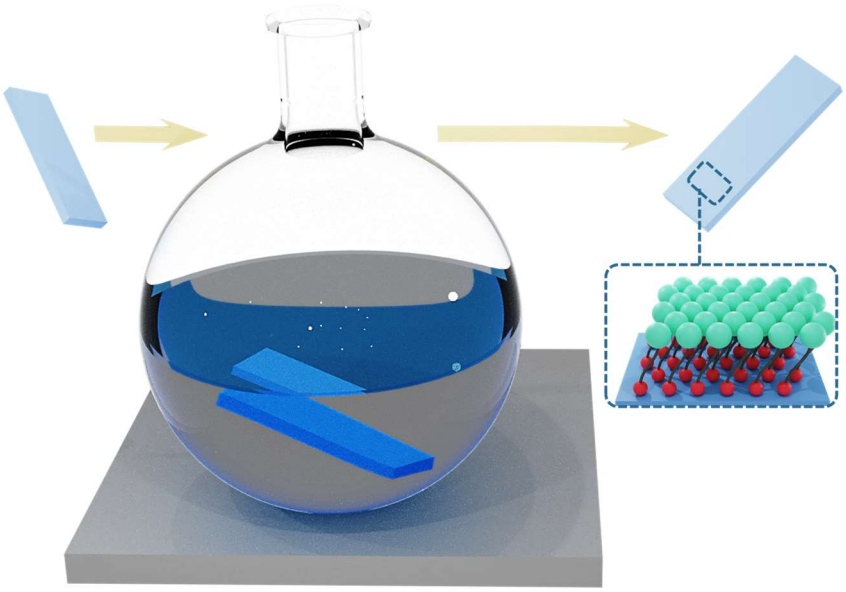

Figure 1.4: Illustration of the SAM formation by the immersion approach.

The main parameters that affect the SAM formation are:

- **Substrate:** The surface roughness directly impacts the SAM packing and the formation of defects.[36,37] Further, activating or pre-treating the substrates is required depending on the substrate-anchoring group reactivity.[38] For instance, oxide substrates are typically activated with an oxidant solution, piranha etching[39,

or plasma,[40,41] to promote the formation of hydroxyl groups at the surface, which can react with silane (-Si-$(OR)_3$) derivatives. In the case of gold substrates, surface pre-treatment methodologies include acid exposition[42] or mechanical (polishing) processes.[43]

- **Solvent:** The molecule solvation and solvent-substrate interaction affect the self-assembly kinetics and thermodynamics. For example, in general terms, higher molecular solvation fosters a large surface coverage and hinders intermolecular interaction.[44] In the case of alkanethiols, the rate of SAM formation is higher in non-polar solvents (e.g. hexane). However, ethanol promotes the formation of a highly well-ordered monolayer. Additionally, thiolated SAMs have a nucleophilic nature, so a solvent that does not react with the molecules must be chosen.[44,45]
- **Water:** When working with silanes, the excess or deficiency of water can be detrimental to the molecular assembly formation; water excess could result in silane polymerization in solution, while the absence results in incomplete monolayer formation since the initial required hydrolysis step does not take place (see below).[45]
- **Temperature:** High temperatures can lead to either layer desorption[46] or amorphous material on the surface.[47] Conversely, if the temperature is too low, the necessary adsorbate-substrate activation energy for the covalent bonding formation might not be reached efficiently, resulting in an incompletely packed monolayer. Hence, a compromise temperature has to be found.
- **Concentration and immersion time:** Both parameters are related to each other.[27] Generally, using a low adsorbate concentrated solution requires longer immersion time to achieve well-packed SAMs. Additionally, long immersion times are usually used to improve the self-molecular reorganization within the monolayer.

In summary, the parameters mentioned above must be considered to minimize the formation of defects in the SAMs. In Figure 1.5, an illustration of some of the most common defects that can be found in SAMs is shown.[48]

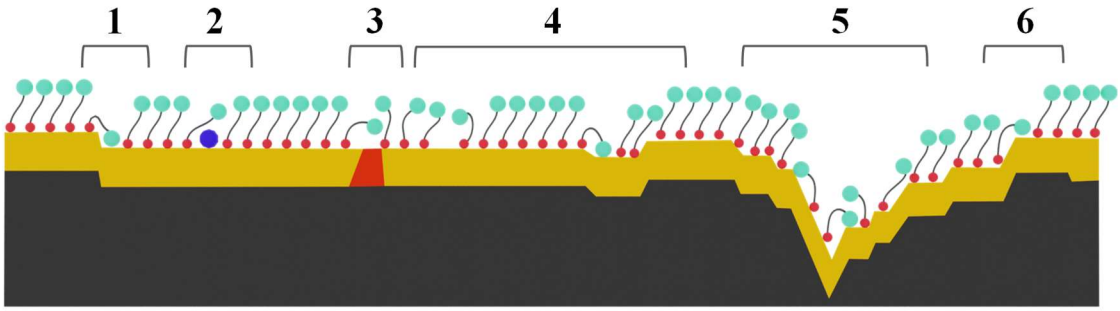

Figure 1.5: Different types of SAM defects: *1)* step edges, *2)* airborne impurities, *3)* SAM crystal edges, *4)* gauche, *5)* gold grain boundaries and *6)* step edges. Image adapted from ref.[48]

1.1.2 Thiol-based SAMs

Thiol-based SAMs have been extensively studied since Nuzzo and Allara's discovery at the beginning of the 1980s.[49] Numerous studies and thousands of publications have been published regarding fundamental and applied studies of SAMs, both on gold surfaces and nanoparticles. Thiol-based SAMs on metals gained much interest because of their simplicity in preparation and high stability mediated by the strength of the S-Au bond. These monolayers typically display high molecular order and are often stable in environmental conditions.

Experimental evidence and theoretical models challenge the conventional view of a static, unreconstructed Au(111) surface with the molecules adsorbed at specified places generating thiolate linkages. Many fundamental aspects of these SAMs remain debatable

more than 25 years after their discovery. Nevertheless, most of the authors agree that the SAM formation (interaction of thiols with gold) follows two stages:[50–53]

- The first step is rapid and takes only a few minutes and involves forming a thin monolayer on the substrate, which is first physisorbed and then chemisorbed.[29] It is not clearly known how the deprotonation process occurs after forming the covalent S-Au bond. The most accepted hypothesis is that the acidic hydrogen from the thiol reacts to generate H_2 (Figure 1.6).[54]
- The second stage is a longer process (between 10 and 20 hours) in which the SAM molecules are rearranged on the surface to achieve highly-ordered structures.

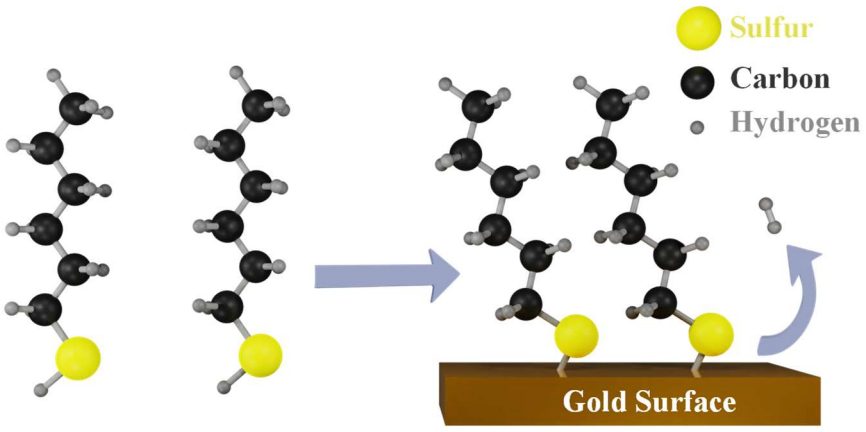

Figure 1.6: Scheme of the thiol-Au reaction to form a SAM. H are indicated as grey spheres.

Regarding the kinetics, the two processes are described as follows:

$$\mathrm{Ads} + \mathrm{Au} \underset{kd}{\overset{ka}{\rightleftharpoons}} \mathrm{Ads_I} - \mathrm{Au}$$

$$\mathrm{Ads_I} - \mathrm{Au} \xrightarrow{kt} \mathrm{Ads_R} - \mathrm{Au}$$

where Ads is the adsorbate, Ads_I-Au is the initially adsorbed molecules on the gold surface, Ads_R-Au is the rearranged species, *ka* and *kd* the association and dissociation rates, respectively, and *kt* is the rate constant for the molecular rearrangement in the second stage.

1.1.3 Silane-based SAMs

Another type of extensively used SAM is based on silane derivatives for functionalizing oxide substrates. Three stages govern the assembly formation of these SAMs: growth (nucleation), aggregation and coalescence.[55,56] To improve the functionalization degree, the substrates are first treated to increase the presence of -OH groups, which are active sites for the monolayer formation. Mono-, bi- or tri-dentate covalent bindings can be formed between the molecule and the surface. Additionally, silane groups polymerize, promoting Si-O-Si bonds between neighbouring molecules (Figure 1.7).[57]

First, the silane is hydrolyzed. This process occurs at a different rate depending on the silane derivative,[58] being slower if the leaving group is larger and ramified,[59] e.g., the hydrolysis rate decreases in the case of alkoxysilanes in the order methoxy > ethoxy > propoxy > butoxy silanes. Chlorosilanes are highly reactive and are often avoided since they polymerize too fast, forming a multilayer film.

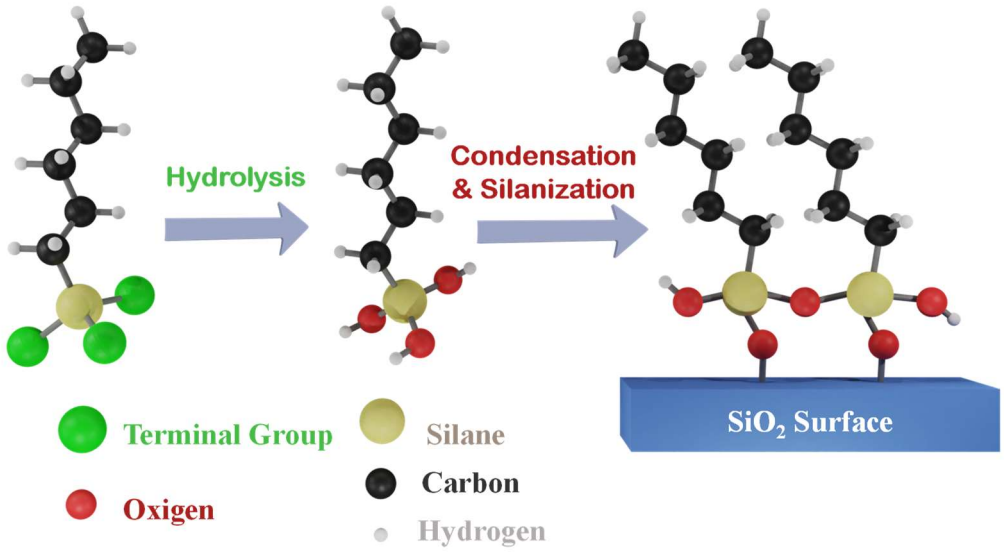

Figure 1.7: Scheme of the formation of a SAM of a silane –(Si-$(OR)_3$) on a silicon oxide surface.

Generally, this monolayer growth kinetics follows the Langmuir model, except in the early stages.[60,61] The kinetic of the SAM formation is determined by the ambient humidity, temperature, number and type of hydrolyzable groups, and inter-molecular interactions between adsorbates, substrate-adsorbate and adsorbate-solvent.[62]

1.2. Surface Characterization Techniques

This section briefly describes the most common techniques and the methods employed in this Thesis to characterize SAMs.

1.2.1 Contact Angle

The measurement of the Contact Angle (CA) or wetting angle is a simple and widespread tool employed to determine the hydrophobicity character of surfaces or, in other words, the wettability of a solid by a liquid. It consists of dropping a small volume

of a liquid (typically water) on a functionalized surface, and the angle between the drop and the surface is measured (see Figure 1.8).[63,64]

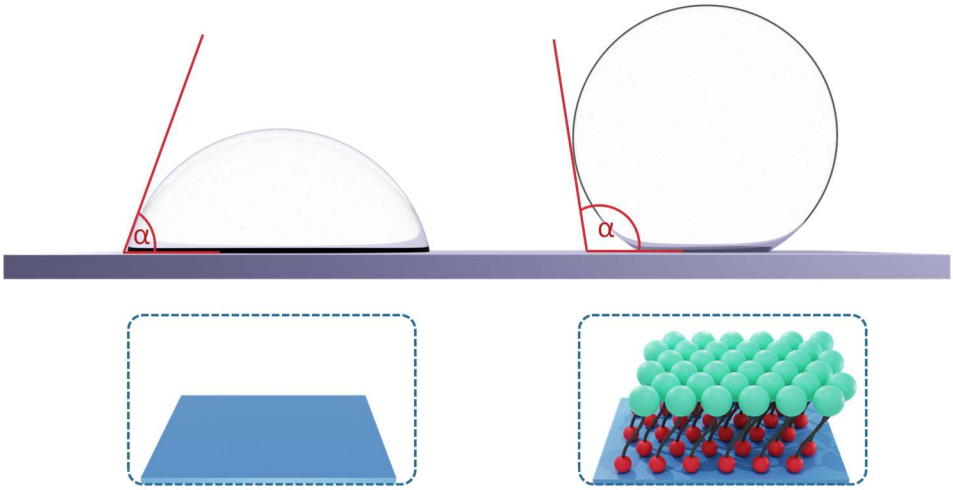

Figure 1.8: Illustration of the CA (α) formed between a water droplet and the surface, with two different wettability characteristics, without (left) and with (right) the presence of a SAM terminated with a hydrophobic group on the surface.

1.2.2 Scanning Probe Microscopies (SPM)

Two Scanning Probe Microscopies are commonly used for studying the self-assembly of molecules at the surface: Scanning Tunnelling Microscopy (STM) and Atomic Force Microscopy (AFM).

Scanning Tunnelling Microscopy (STM) uses a highly sharp conducting tip to image conducting surfaces at atomic scales. This tip can distinguish features smaller than 0.1 nm with 0.01 nm depth resolution. Most STMs operate at ultra-high vacuum, at room or shallow temperatures, although ambient STMs, even working at the liquid/air interface, are also used to characterize SAMs. This microscope is based on quantum tunnelling. The tip approaches extremely close to the surface, slightly above the sample, where repulsive and attractive interactions coexist. The tip position is controlled by piezoelectric scanner tubes and altered by a control voltage. Then, a bias voltage between the tip and the surface

is applied, and the electrons tunnel through the vacuum, separating the tip and the surface. The tip moves across the surface (in the x-y matrix), displaying an image. There are two main working modes: *constant height* and *current modes*. In the former, the tip height is maintained, and the tunnelling is measured, while in the latter, the tip height is altered to maintain constant the current.[65] STM provides easy access to topographic information on molecular nanostructures in real space and their characteristic electronic structures on surfaces. The nanostructure growth (i.e. following on-surface reactions, molecular rearrangement, etc.) is also very relevant in the field. [66–68]

Atomic Force Microscopy (AFM) also involves scanning a surface with a tip. In this case, the forces between the probe and the surface are measured as a function of their mutual separation. AFM is performed using a sharp tip about 10–20 nm in diameter attached to a cantilever. The tip scans the sample surface, allowing the so-called near-physical interactions. These vibrating interactions are recorded, and three-dimensional images are obtained. The cantilever deflection measures the force generated, and a laser reflection monitors the tip vibration into a photodiode.[69,70] AFM is operated in two basic modes, contact and tapping. In the contact mode, the AFM tip is continuously in contact with the surface, while in the tapping mode, the AFM cantilever is vibrated above the sample surface so that the tip is in contact with the surface only intermittently. The tapping mode is the most commonly used for imaging, while the contact mode is usually used for more specific measurements, such as force or conducting measurements.[71] AFM is suitable for most non-conductive SAMs, including those formed by multilayers or containing large molecules, such as proteins.[72,73] A conductive substrate is not needed for the AFM, but this technique offers the possibility of measuring conducting-AFM (C-AFM).

1.2.3 Spectroscopic Techniques

X-ray Photoelectron Spectroscopy (XPS) is a surface-sensitive analytical method that bombards a surface with X-rays and measures the kinetic energy of the emitted electrons. Information about the electronic structure and the sample's elemental composition can be obtained. The power of this technique is its surface sensitivity and capacity to extract chemical state information from the elements composing the sample.[74] It is susceptible to the chemical environment of the elements, such as the chemical bonds and charge transfer from/to the surface.[75] The data is represented in a spectrum as a function of the binding energy (BE). Photoelectron peaks with a specific BE are the fingerprint of an element, environment and orbital from which they were ejected. XPS can be quantitative, but it has to be taken into account that a photoelectron must go through the sample to escape, and the number of photoemitted electrons can be decreased by inelastic collisions, recombination, excitation of the sample, recapture, or trapping in different excited states within the material.[76] Furthermore, since XPS is a surface-sensitive technique, it is susceptible to contamination, sometimes hindering its use in a quantification manner.[77]

Near Edge X-Ray Absorption Fine Structure (NEXAFS) is a spectroscopy technique based on the absorption of X-ray photons by a core level with a consequent photoelectron emission, resulting in a core hole filled by either the Auger process or by electron capturing from another shell. A fluorescent photon emission follows this process. This technique is usually employed to identify the local bonding environment and is often used as a spectral "fingerprint".[78] Furthermore, NEXAFS can be used to determine the SAM orientation on the surface plane and the elementary composition.[79–81] Figure 1.9 shows the main differences between XPS and NEXAFS.

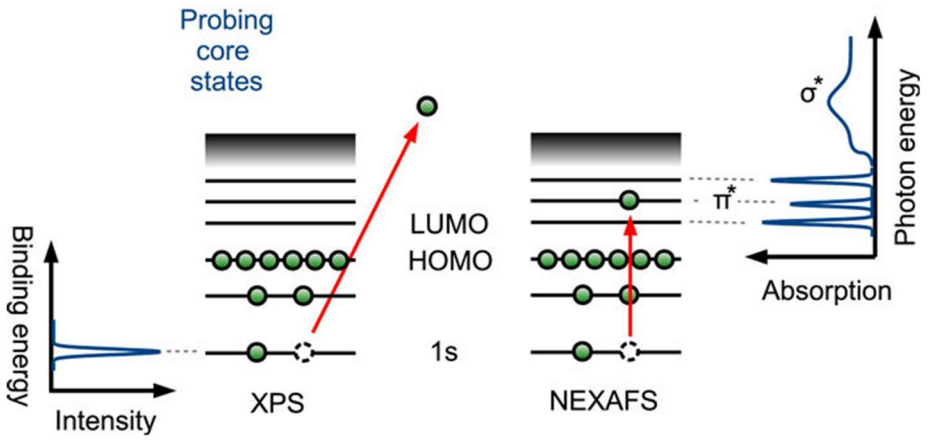

Figure 1.9: Scheme of the principle of the mechanism in XPS and NEXAFS spectroscopy. X-ray radiation leads to the emission of core electrons (XPS, left) or excitation into unoccupied molecular π∗ and σ∗ states (NEXAFS, right). Adapted from ref.[82]

Time-of-Flight Secondary Ion Mass Spectrometry (ToF-SIMS) is a surface analytical technique which uses a pulsed ion beam to remove molecules from the surface and, thus, to do an elemental or molecular composition and mapping of the surface.[83] Primary particles are produced near the impact site and dissociated into ions. Additionally, secondary particles are emitted further from the impact site corresponding to molecular species on the surface. These molecular compounds (usually fragmented) are accelerated into a flight path to a detector, and a mass plot is displayed.

Infrared Reflection Absorption Spectroscopy (IRRAS) is a spectral technique commonly used to study ultrathin organic films deposited on reflective surfaces, such as metals. It provides information on the type of molecular groups forming the thin film and their orientation relative to the metal surface. IRRAS measures the sample's reflectance accompanied by the absorption and usually needs to be performed at grazing incidence to improve the sensitivity. Vibrational modes from the molecule with a dipole change component perpendicular to the surface are detected.[84–86]

Ultraviolet-visible (UV-Vis) spectroscopy is considered the most widely used technique in spectroscopy for a broad range of compound analyses by measuring the interaction of electromagnetic radiation with molecules at a particular wavelength. It measures the discrete wavelengths of UV or visible light absorbed by or transmitted through a sample.[87] For SAMs, their characterization is done in transmission mode using transparent surfaces such as glass, quartz, or oxides (like Indium Tin Oxide (ITO)).[88,89]

Fluorescence spectroscopy can be employed for SAMs containing fluorophores attached to the surface to characterize their emission properties. To observe fluorescence emission in a sample, an electron must overcome the gap energy barrier followed by a non-radiative relaxation to the fundamental state, resulting in photon emission. The samples are typically measured at the excitation wavelength, at which the emission wavelength is maximum.[90–92]

Electron paramagnetic resonance spectroscopy (EPR) characterizes the paramagnetic character of a SAM composed of metal complexes or organic radicals.[89,93] In an EPR experiment, the frequency is maintained constant and the magnetic field is swept. For paramagnetic species, such as organic radicals, EPR measures microwave radiation absorption by the unpaired electron spin.[94]

As above-explained, different techniques can be used to characterize the SAM formation on surface. Additionally, electrochemical techniques have also been extensively employed for this purpose. Since, in this Thesis, electrochemical tools have been a main focus of our work, they are explained in more detail in the next section.

1.3. Electrochemical Techniques

Electrochemical techniques are highly powerful in characterizing SAMs of electroactive and non-electroactive species.

The electrochemical characterization of grafted molecules can be done by directly investigating the redox response of the anchored molecules (if they are electroactive) or by using a redox probe in the solution (like $[Fe(CN)_6]^{3-/4}$) and studying the electron transfer rate (ET) through the monolayer following Marcus theory. The Marcus theory describes that the rate of ET between a donor and an acceptor is dependent on the reorganization energy (λ), temperature (T), Gibbs free energy (ΔG) and the donor-acceptor electronic coupling (H_{AB}). These variables are related to the molecular chain structure and length, the nature of the redox functional group, the environment, etc.[95,96] These measurements can also give information on the surface coverage or the degree of passivation of the electrode.

In general, the electrochemical characterization of a substrate modified with a SAM is carried out in a three-electrode configuration cell containing a working electrode (WE, functionalized with the SAM and where the redox event occurs), a counter electrode (CE) towards which the current flows and, a reference electrode (RE). Gold, conducting oxides (e.g., ITO) and carbon-based electrodes (e.g., glassy carbon) can be used as WE. Typically, the CE is a platinum wire, and the RE must have a well-known and stable electrode potential, and it is usually formed by a metallic surface and a counter ion (e.g., Ag/AgCl). In the absence of the counter ion, RE is known as a *pseudo*-reference owing to the lack of thermodynamic equilibrium and needs to be calibrated with an internal redox reference.[97] The electrochemical cell is filled in with a supporting electrolyte solution responsible for the charge transfer in the medium. The use of different solvents

and salts can influence the electrochemical response.[98] The main electrochemical methods used in this Thesis for the SAMs characterization are Cyclic Voltammetry (CV) and Electrochemical Impedance Spectroscopy (EIS).[99]

1.3.1 Cyclic Voltammetry (CV)

CV is the most commonly used electrochemical tool and does not require expensive or sophisticated instrumentation, becoming a very accessible technique.[100] It consists of sweeping the voltage applied to the WE while measuring the current to determine the redox processes associated with the adsorbed species at the electrode or in the solution. The voltammogram plots display these electron transfer processes under a hysteresis curve (see Figure 1.10). Each faradaic or redox event shows the oxidation/anodic (E_{PA}) and reduction/cathodic (E_{PC}) peaks, at specific potentials, with their respective anodic (I_{PA}) and cathodic (I_{PC}) current represented by the height under the hysteresis curve of each event. The formal redox potential ($E_{1/2}$) is found in the mid-way of both anodic-cathodic potentials as follows:[99]

$$E_{1/2} = \frac{E_{PC}+E_{PA}}{2} \quad (4)$$

In solution, the potential difference between the oxidation and reduction peaks ($\Delta E_P = E_{PC}$-E_{PA}) differs from zero, but for species immobilized on the electrode surface, since there is no diffusion, they should show an ideal Nernstian electron transfer with similar peaks potentials ($\Delta E_P \sim 0$ V).

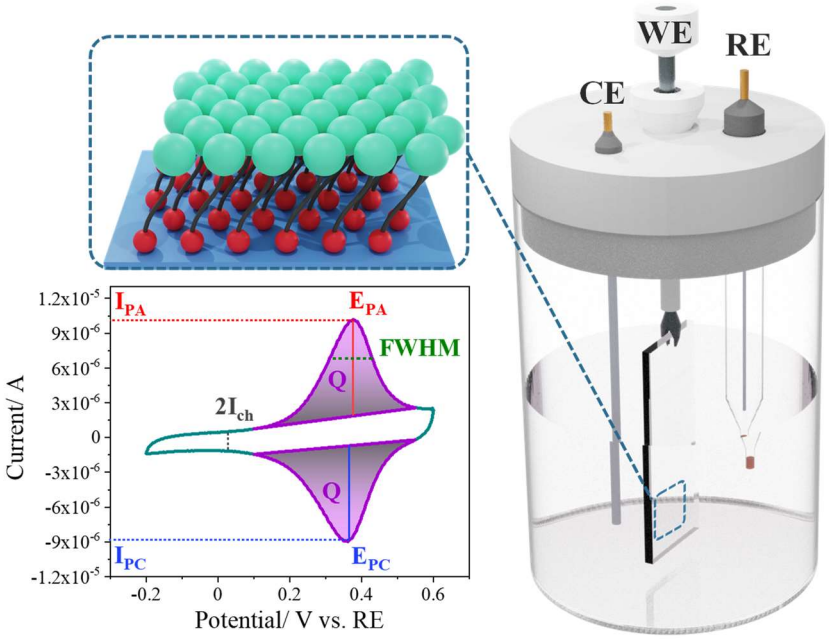

Figure 1.10: Left: Typical ideal cyclic voltammogram (bottom) of an electroactive SAM grafted on the electrode surface, (top) indicating the most relevant parameters that can be extracted. Right: Scheme of an electrochemical cell adapted to characterize a modified electrode.

Additionally, in electroactive SAMs, the surface coverage can be estimated by integrating the anodic or cathodic peak area (faradaic current), avoiding the capacitive (background) area (in purple in Figure 1.10) using the following equation:[99]

$$\Gamma = \frac{A_{peak}}{n \cdot F \cdot \nu} \qquad (5)$$

where Γ is the surface coverage (in mol·cm^{-2}), n is the transferred electrons, A_{peak} is the integrated area under the anodic or cathodic peak (in A·V·cm^{-2}), F is the Faraday constant (96.485 A·s·mol^{-1}) and ν the scan rate. Besides, it should be noted that the peak current should linearly increase with the scan rate when molecules are confined on the surface, and the diffusion is negligible.[101]

Broad peaks correspond to slow electron transfer and possibly higher molecular lateral interactions between the confined species forming the SAM, thus giving some information on the layer homogeneity. This last parameter can be extrapolated from the full width at half the maximum peak height (FWHM).[99,102] The FWHM of an ideal situation is given by Eq. 6:

$$FWHM = 3.53\frac{RT}{nF} = \frac{90.6}{n} \quad (6)$$

Further, the background (capacitive current, $I_{ch,}$ indicated in Figure 1.10) can also provide evidence of the SAM formation. At the voltage range where any redox process occurs, the capacitive current (I_{ch}) is correlated with the electrical double-layer capacitance (C_{DL}), often normalized by the electrode surface area (A_{SUR}).[99]

$$\frac{I_{ch}}{A_{SUR}} = \frac{C_{DL}}{A_{SUR}} \cdot \nu \quad (7)$$

As mentioned, a redox marker in solution is commonly employed in the case of a non-electroactive SAM. The efficiency of the electron transfer process from the solution to the electrode through the SAM gives information on the SAM surface coverage and its molecular/electronic structure.[103.104]

1.3.2 Electrochemical Impedance Spectroscopy (EIS)

Electrochemical Impedance Spectroscopy (EIS) is a powerful technique for analyzing interfacial properties and events occurring at the electrode surface. This method is being used in many fields, such as corrosion, batteries, bioelectrochemistry and solid-state electrochemistry.[105]

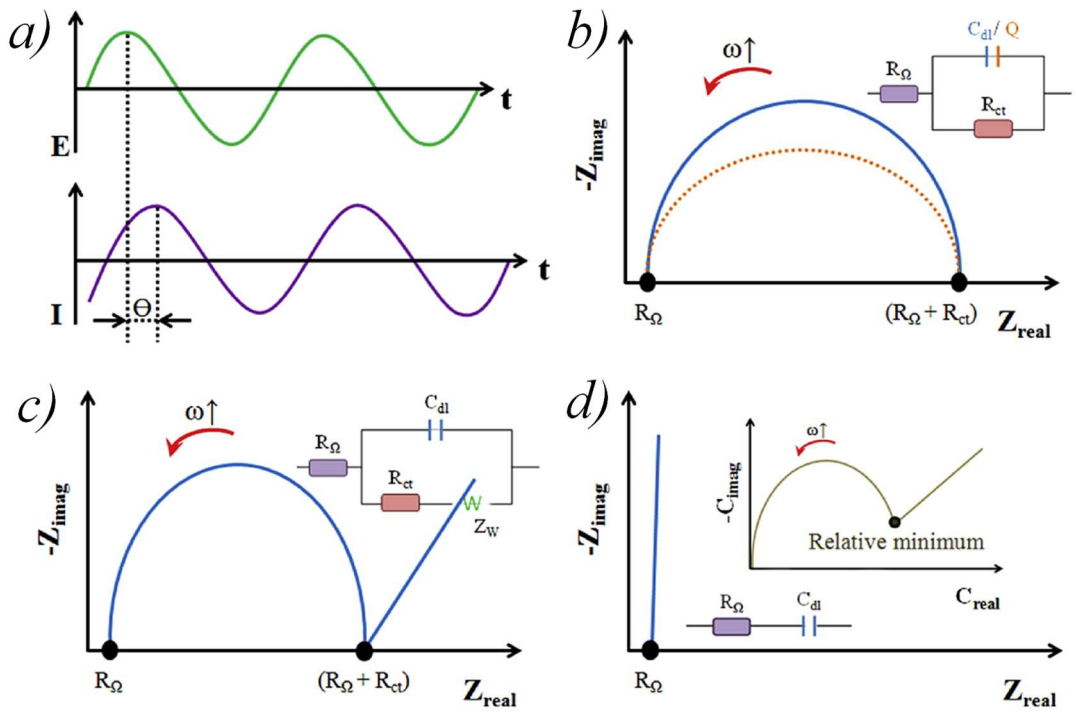

Figure 1.11: *a)* Sinusoidal excitation signal on the system and the sinusoidal current recorded, shifted in phase. Nyquist plots for a Faradaic system: *b)* kinetic-controlled process and *c)* mixed diffusion- and kinetic-controlled (inset: equivalent Randles circuit). D*)* Nyquist plot for a non-Faradaic system (inset: capacitance plot). Extracted from ref.[106]

Impedance (Z) is the ability of a circuit to resist an alternating current (AC) flow, measured in the same units as resistance (Ω). Therefore, in a typical measurement, an AC voltage, E(t), is applied on a range of frequencies (ω), measuring the resulting sinusoidal current. This resulting AC current, I(t), is shifted in phase angle (θ), changing the period of the sinusoidal waves. The phase shift between the AC voltage and the measured current (or vice versa) directly depends on the electrochemical system and its relative capacitive and resistive features (Figure 1.11a).[107]

$$E(t) = E^o \sin(\omega t) \qquad (8)$$

$$I(t) = I^o \sin(\omega t - \theta) \qquad (9)$$

where *t* is the time, and I^o represents the magnitude of the current oscillation. The total impedance (Z) is analogously calculated using Ohm's Law as follows:[108]

$$Z = \frac{E(t)}{I(t)} \quad (10)$$

Following Euler's formula (Eq. 11), considering Eq. 10, and knowing that the impedance has a phase shift θ, and an amplitude $Z^o=E^o/I^o$, Z can be expressed as Eq. 12:

$$e^{j\theta} = cos(\theta) + j\ sin(\theta) \quad (11)$$

$$Z = Z^o[cos(\theta) + j\ sin(\theta)] = Z_{real} + Z_{imag} \quad (12)$$

where Z_{real} corresponds to the real component of the resistance and Z_{imag} to the imaginary component. Therefore, impedance is the sum of the circuit's resistance and capacitance.[106]

Real component: $Z_{real} = |Z|(cos\,\theta)$ (13)

Imaginary component: $Z_{imag} = |Z|(j\ sin\,\theta)$ (14)

EIS measurements are typically plotted using the Nyquist diagram (also called Cole-Cole),[109,110] where Z_{real} (x-axis) is represented *versus* Z_{imag} (y-axis). Bode plots can also be used in which |Z| and θ are plotted against log ω.

EIS plots are usually analyzed by fitting the curves to an equivalent circuit, typically containing a resistor I, a capacitor I, and an inductance (L) component. In the case of SAMs, the most important parameters that can be extracted from the equivalent circuit are:[106,111]

i. Solution resistance (R_Ω): dependent on the type of electrolyte (i.e., type of ions), concentration and electrode area.

ii. Charge transfer resistance (R_{ct}): inversely proportional to the electron transfer rate.

iii. Double-layer capacitance (C_{DL}): related to the background and charging current.

iv. Warbuck impedance (Z_W): this constant phase element results from mass-transfer limitations and can be used to determine the effective diffusion coefficient.

Other constant phase elements can also be included in the model. Thus, the impedance spectra allow a broad overview of the different processes at the electrochemical interface (i.e., capacitive, resistive, diffusion effects), and each one dominates more at a specific range of frequencies.

By EIS, Faradaic and non-Faradic processes can be studied. For Faradaic processes, the electrochemical reaction mechanism can show two limiting factors. The process is kinetically-controlled when the diffusion is fast and the electron transfer rate is the limiting factor. The Nyquist plot appears as a semicircle (Figure 1.11b). However, often in the Nyquist plots, in addition to the semicircle, a linear region is observed where the process is diffusion-controlled (Figure 1.11c). In this regime, the electron transfer is fast, and the mass diffusion of the electroactive species from the bulk to the electrode limits the process.

A kinetically-controlled process is often modelled by the Randles circuit (see inset in Figure 1.11c), which is the simplest model. With this model, from the semicircle of the Nyquist plot, R_Ω can be extracted as the interception of the semicircle with the x-axis at high frequency, while the semicircle diameter corresponds to R_{ct}. Nevertheless, the non-ideal behaviour of C_{DL} can modify the semicircle, and other elements can be introduced

to the equivalent circuit to improve the fitting, such as a CPE.[112,113] Mass-transport control is represented in a Randles equivalent circuit by introducing the Warburg impedance element (Z_W) in series with the charge transfer resistance. The Warburg impedance is visible in the Nyquist plot as a straight line with a 45° angle to the abscissa, and it is predominant at lower frequencies.[114]

In a non-faradaic process, the charge transfer resistance and diffusion contributions can be omitted, becoming a simpler electrical circuit, as shown in Figure 1.11d (inset). Then, the imaginary part of the impedance is inversely proportional to the electrical double layer (C_{DL}) of the electrochemical system and can be the sum of the real (C_{real}) and imaginary (C_{imag}) capacitance components and calculated as follows:[106]

$$C_{DL} = \frac{1}{j \cdot w \cdot Z} \quad (154)$$

$$C_{DL} = -\frac{Z_{imag}}{\omega |Z|^2} - j\frac{Z_{real}}{\omega |Z|^2} = C_{real} + jC_{imag} \quad (165)$$

1.4. SAMs for the Development of Molecular Switches and Sensors

Following the current society's demand, electronic devices (mostly silicon-based), have progressed quickly towards smaller and higher storage capacity components. Nevertheless, the limitation of silicon technology miniaturization has prompted the search for new materials and alternative technologies.[115]

Molecular electronics aims to use molecules as active components in electronic devices (for sensing, switching, current rectification etc.).[116–118] Over the past decades,

molecular electronics have experienced remarkable growth thanks to the increased efforts from researchers from different fields (chemistry, physics and engineering). Currently, robust single-molecule devices and large molecular junctions (using an ensemble of molecules) can be realized owing to the advancement of materials synthesis, surface chemistry and surface characterization techniques, and new theoretical tools to rationalize and predict the results.[119,120]

In this regard, as mentioned at the beginning of the introduction of this Chapter, molecular SAMs are very attractive and chemically versatile platforms for several applications in this field.[121,122] SAMs can be exploited as *i)* the active response layer or *ii)* to tune specific device properties. In the first case, depending on the nature of the molecular species forming the SAM, the modified surfaces can act as switches (presenting at least two commutable states),[89,123,124] as sensors (having a recognition unit to certain analytes)[125,126] or as molecular wires (where charge transport occurs through the molecule), among others. In the second case, SAMs have been used to modify the work function of electrodes (improving, for example, charge injection in field-effect transistors), or to change the wettability of the surface (tuning the properties of a material deposited on it), etc.[127,128] In both situations, the use of SAMs implies several advantages such as: *i)* easy surface functionalization without altering the substrate composition, *ii)* large functionalized surface area, *iii)* easy miniaturization and *iv)* low-cost.

In particular, in this Thesis, we have used SAMs to develop electrochemical switches and sensors.

1.4.1 Electrochemically Triggered SAMs for Molecular Switches

One particular family of molecules employed for developing novel molecular-based devices are molecular switches. When an external stimulus is applied, these systems can be reversibly interconverted between at least two stable states. Preparing SAMs based on switchable molecules is an appealing strategy towards practical applications. Several external stimuli may activate these molecular switches on surfaces, such as light,[129,130] an electric/magnetic field,[131,132] temperature,[133] a voltage[134] or the presence of specific chemicals.[135,136] As a result, the molecular properties can be modulated, such as the dipole orientation, molecular conformation, charge or spin states and can even promote the formation of new chemical bonds.[137] It should be highlighted that it is key to ensure that the molecular switching ability is not inhibited upon surface grafting and, further, that the system reveals low or negligible switching fatigue during the application of switching cycles.

Electrochemical or redox switches are based on using an electrical input to change the redox state of the molecules. For this purpose, electroactive molecules are employed. Figure 1.12 shows an example of a ferrocene SAM on gold, where applying a voltage to the surface leads to ferrocene (Fc) oxidation to ferrocenium (Fc^+) and vice versa. Importantly, the SAM must not be desorbed from the surface while applying the voltage to achieve robust electrochemical switchable SAMs. For this reason, redox species that can be triggered at low voltage values are more appealing. Since these systems exhibit at least two ("0" and "1" states) or more accessible states, they are suitable for the fabrication of molecular memories.

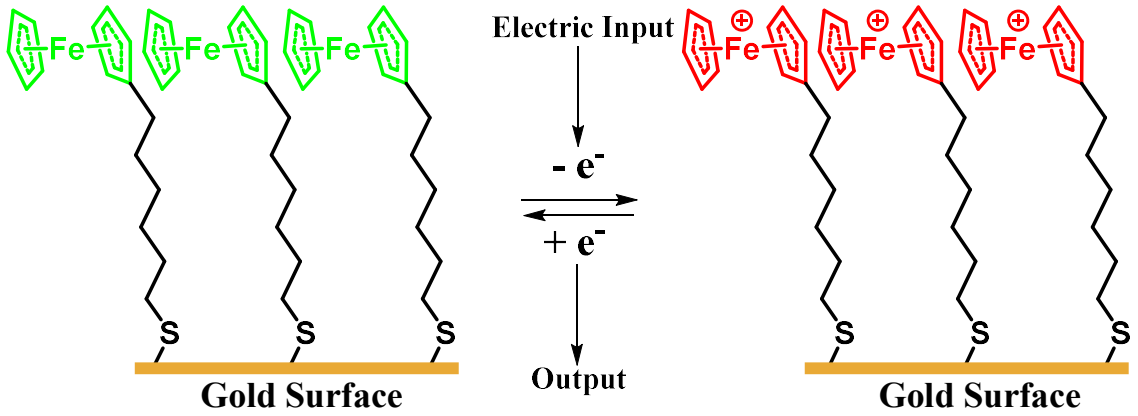

Figure 1.12: Illustration of an alkanethiol SAM on gold surface containing ferrocene as terminal group. A voltage is used to tune the redox state of ferrocene.

The output (i.e., the state reading) of these switches can be diverse depending on the nature of the molecule. For instance, interfacial layer capacitance can be measured if charges are created at the surface, [138] but also, their optical and/or magnetic properties can be used as readouts if these properties differ depending on the molecular redox state. Figure 1.13a depicts a SAM based on a tetrathiafulvalene (TTF) prepared on a transparent indium tin oxide (ITO) surface previously reported by our research group.[139] TTFs show three distinct redox states: neutral (state 0), radical-cation (state 1) and dication (state 2). Absorption and electron paramagnetic resonance (EPR) spectroscopy were used to read this ternary switch. The radical-cation state was the only EPR active (S1a in Figure 1.13b), whereas the absorption of the SAM at 420 nm showed three different distinguishable values depending on the redox state (Figure 1.13c).

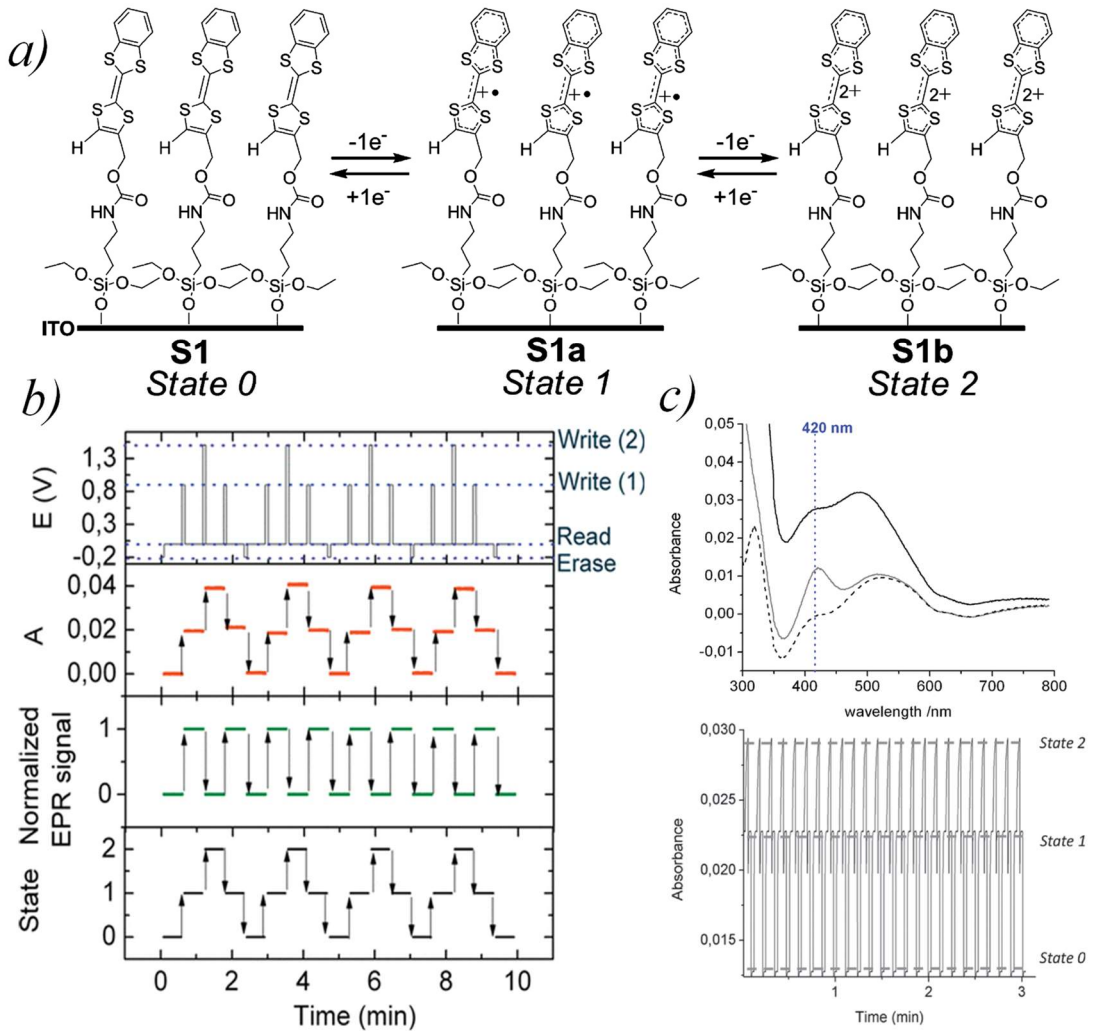

Figure 1.13: a) Scheme of a multistable redox switch based on a tetrathiafulvalene (TTF) SAM displaying three redox states. b) Output response of the switch followed optically (Absorbance (A) at 420 nm) or magnetically (Normalized EPR signal). c) Absorbance spectra recorded for the different states and Absorbance at 420 nm upon the application of different reduction/oxidation cycles. Adapted from ref.[139]

The realization of switches showing multiple accessible states can be achieved by using electroactive molecules displaying different redox states, as previously mentioned, or by preparing mixed SAMs. For example, in the work reported by Casado-Montenegro *et al.*,[140] a SAM containing ferrocene as an electron-donor and anthraquinone as an acceptor was prepared, reaching multiple stable redox states in a narrow voltage window.

Another approach to enhance the number of accessible states is the introduction of multilayers. An interesting system to illustrate this concept is the one developed by Shokurov *et al.*,[141] who synthesized an octopus-type crown-bisphthalocyaninate (octopus-Pc) with eight thioacetate-terminated "tentacles" (Figure 1.14). This macromolecule was strongly attached on a gold surface and displayed three stable redox states. Furthermore, adding an extra molecular layer by supramolecular interactions permitted to reach a four-state system (R, N, O and O' in Figures 1.14 b and c). The different states were identified in the CV (indicated with dashed lines in Figure 1.14c).

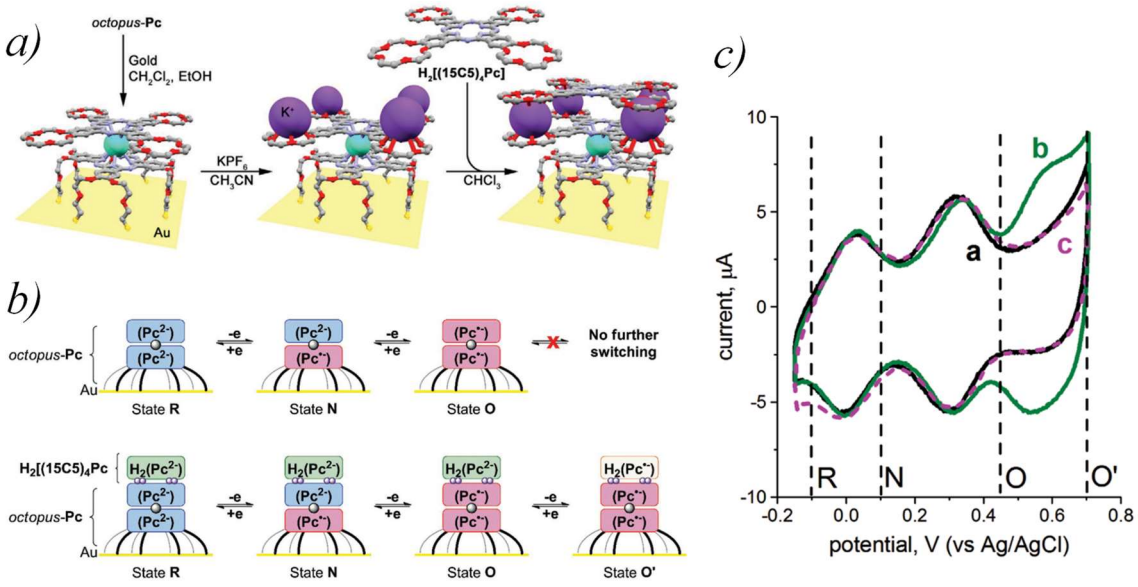

Figure 1.14: *a)* Scheme of the octopus-Pc SAM on gold and the formation of a multilayer assembly driven by supramolecular interactions, *b)* redox states reached for both systems and *c)* CV showing the four redox states of the multilayer SAM. Adapted from ref.[141]

The modification of the surface wettability with the application of a voltage has been shown to be attractive for various applications, such as for water actuation.[142] Maglione *et al.* reported the fabrication of an ITO conductive substrate coated with a SAM containing terminal anthraquinone groups (AQ) (Figure 1.15).[142] When the redox state of AQ was switched between the oxidized and reduced state, the surface wettability

could be altered by as much as 26° (Figures 1.15 c and d). Mixing and dispensing water droplets at the sub-nanoliter scale was achieved by fabricating an array of planar electrodes integrated into a microfluidic device (Figures 1.15e and d). Additionally, the surface electrowetting phenomenon was utilized to facilitate the transportation of cells across different microfluidic compartments in a culture medium. Thus, this example illustrates the potential of electrochemically switchable SAMs to be implemented in relevant technological applications.

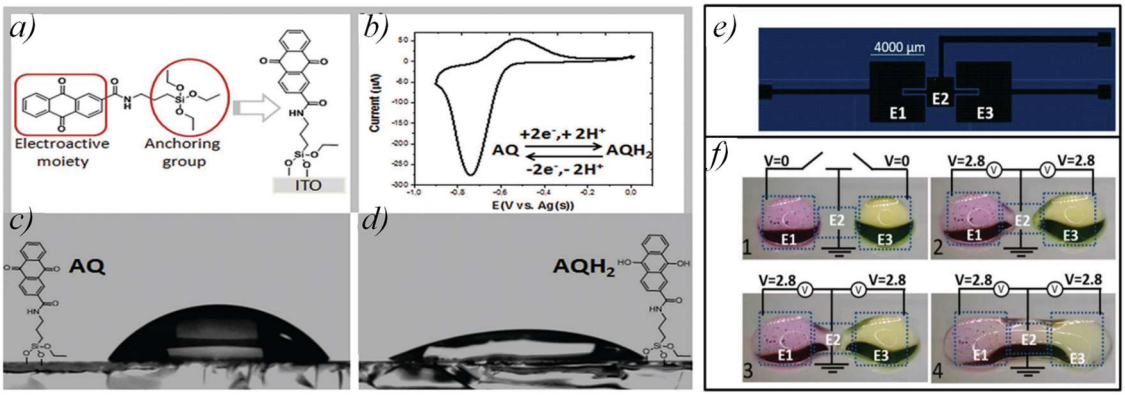

Figure 1.15: *a)* Molecular structure of AQ-Silane and the schematic representation of the AQ-Silane SAM on ITO. *b)* CV of AQ-Silane SAM in a phosphate buffer solution (pH: 6.9). Optical images showcasing water droplets (5 µL) *c)* before and *d)* after the electrochemical SAM reduction. f) CAD drawing of the three-electrode array and f) snapshots of droplet merging by applying a voltage. Adapted from ref.[142]

1.4.2 SAMs for Electrochemical Sensors: Chemical Input and Electrochemical Output

SAMs have been widely employed for the fabrication of electrochemical sensors. For this purpose, the SAMs should interact with the analyte of interest and provide an electrochemical response.[143]

The SAM is typically designed to have specific functional groups that selectively interact with the target analyte through supramolecular interactions: van der Waals forces, π-π stacking, hydrogen bonding, metal-ligand coordination, electrostatic interactions, and host-guest. In particular, SAMs have been extensively used in biosensing by exploiting the highly selective antigen-antibody interactions.[144,145]

Thanks to receptor-analyte interactions, the detection and quantification of the analyte concentration in a sample solution can be realized. For the electrochemical readout, the sensing process typically implies a change of the current intensity and/or a shift of the potential due to the interface modification or a change of the double-layer capacitance or charge transfer resistance. Generally, electrochemical sensors based on SAMs offer easy preparation and robustness, versatility for a wide range of different analytes, low-cost, fast measurements and low limits of detection (LOD).[146] For all these reasons, they are appealing for the development of low-cost point-of-care tests or in-field analysis.

Cyclic voltammetry and EIS are the most common electrochemical techniques employed for analyte determination. Differential pulse voltammetry (DPV) or square wave voltammetry (SWV) can also be used.[147]

When the species at the electrode surface are non-electroactive, the small changes taking place at the electrode interface can be followed by EIS[148] using a redox probe in the electrolyte solution. In Figure 1.16a, this is exemplified in a SAM bearing a crown-ether ring able to form a host-guest complex with Na^+.[149] The charge transfer resistance (measured by EIS) increases with the formation of the complex, as evidenced by the increase of the semicircle diameter in the Nyquist plot. Accordingly, CV could also follow

this process, where a decrease in the current intensity and an increase in the ΔE_P would be expected.

Alternatively, if the monolayer is able to detect an analyte but it is also redox-active, the use of a redox probe in the electrolyte is not required, and the electrochemical properties of the SAM can be used as readout. This is the case of the TTF-based SAM functionalized with a crown-ether ring shown in Figure 1.16b.[149] Here, changes in the TTF redox peak (intensity and voltage) occurring upon the interaction with metal cations can be directly used to determine the analyte concentration.

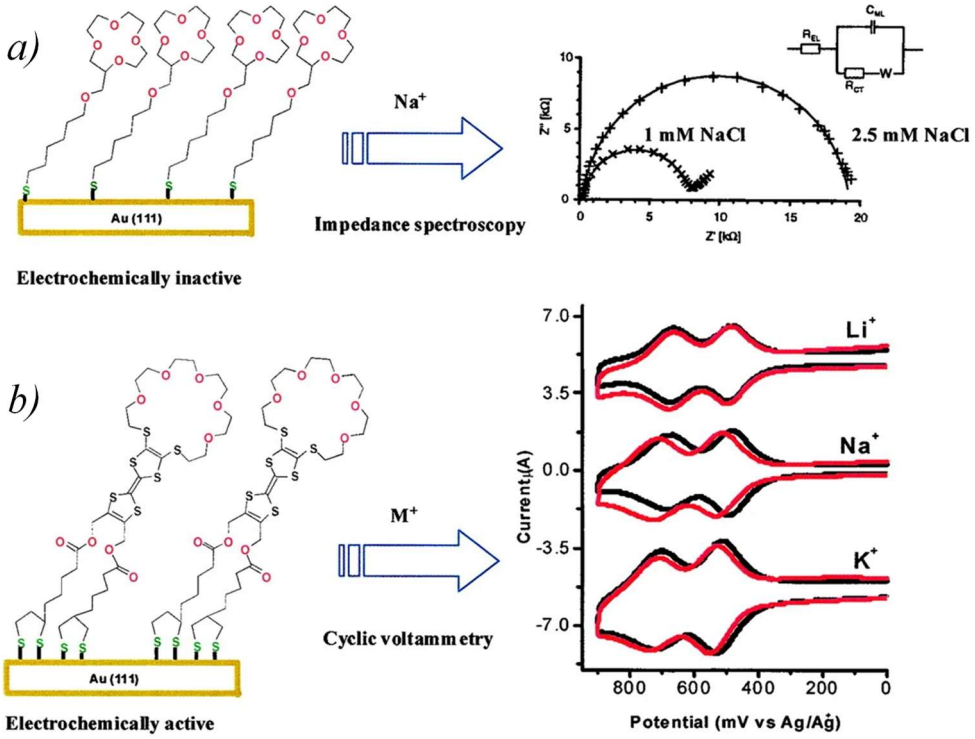

Figure 1.16: Comparison between an electrochemically *a)* inactive and *b)* active SAM. In the first case EIS using a redox probe is employed as readout, while in the second case, the redox properties of the SAM are exploited. Adapted from ref.[149]

Generally, these changes in the electrochemical measurements are originated from an increase in the monolayer thickness or steric hindrance upon the binding, typically

leading to a decrease in the electron transfer rate.[127,150] Then, from the plot of the electrochemical signal variation (current intensity, charge transfer resistance, etc.) versus the analyte concentration, a calibration curve can be performed, and the relevant parameters to determine the sensing performance can be extracted (i.e., the limit of detection, sensitivity, etc.).

Although Faradaic processes are more widely used for the development of electrochemical sensors, non-faradaic responses can also be exploited by analyzing the changes of the interfacial electrical capacitance upon the chemical interaction. In a non-faradaic electrochemical system, the imaginary part of the impedance is inversely proportional to the electrical double layer (EDL) capacitance.[151] Typically, the binding interactions within the EDL are captured at low frequencies (<1000 Hz), since at high frequencies (10000 Hz-1 MHz), a resistive response is commonly observed due to the bulk behaviour of the electrolyte system.

Electrochemical sensors have gained increasing attention in fields like pollutants detection, drug monitoring and biorecognition (especially in early diagnosis disease).[152] Here below, a few examples are described to illustrate the relevance of such types of devices and to show the diversity of strategies developed to obtain modified surfaces for sensing.

Regarding pollutants detection and quantification, Ait-Touchente *et al.*[153] developed a sensor for Cu^{2+} ions detection using ITO surfaces modified with multilayers of 4-mercaptophenyldiazonium tetrafluoroborate (4-MPD) SAMs and Au nanoparticles (AuNPs). This electrode design led to the right balance between the high specific surface for large receptor loading and low electrical resistance of the hybrid material grafted on

the electrode surface. Consequently, sensors with a low limit of detection in the pM range were realized using the square wave voltammetry (SWV) technique.

Regarding biosensing applications, following a similar approach as explained above, Jolly *et al*.[154] developed a biosensor to detect a prostate cancer biomarker using an array of AuNPs deposited on a SAM of 11-aminoundecanethiol on Au. Subsequently, the prostate-specific antibodies were anchored on the AuNPs together with a SAM of 6-mercapto-1-hexanol (MCH) or 6-(ferrocenyl)hexanethiol (FcSH) for both impedimetric or amperometry detection, respectively. In the first case, a redox marker was used in the electrochemical experiments, while in the second case, the response of the Fc SAM, which acted as an internal redox probe, was analyzed. In both cases, the sensors exhibited high sensitivity and selectivity towards the prostate-specific antigen, a wide dynamic range, and a low LOD (10 $pg \cdot mL^{-1}$), making this biosensor a promising tool for prostate cancer diagnosis and monitoring.

Finally, to highlight the feasibility of integrating these sensors in a device working with real samples (i.e., body fluids), the electrochemical biosensor developed by Upasham *et al*.[155] is described as a representative example. The authors developed an ultra-low volume, multi-bio fluid point-of-care (POC) device for cortisol sensing (Figure 1.18). Towards this goal, a gold electrode was modified through a two-step functionalization methodology by first grafting the cross-linker molecule dithiobis/ succinimidyl propionate (DSP) and attaching the α-cortisol antibody to the thiol linker. Interestingly, to improve the performance of the sensor in the presence of the bio-fluid matrixes, a room temperature ionic liquid (RTIL) (i.e., BMIM[BF_4]) was incorporated on the electrode as the buffer to modulate the EDL (Figure 1.18a). Here, non-faradaic label-free electrochemical impedance spectroscopy (EIS) was used as the detection modality by exploring changes in the interfacial capacitance at low frequency. Cortisol

concentration was measured in different human body fluids (blood, saliva and sweet), achieving excellent LODs and sensitivity (Figure 1.18b).

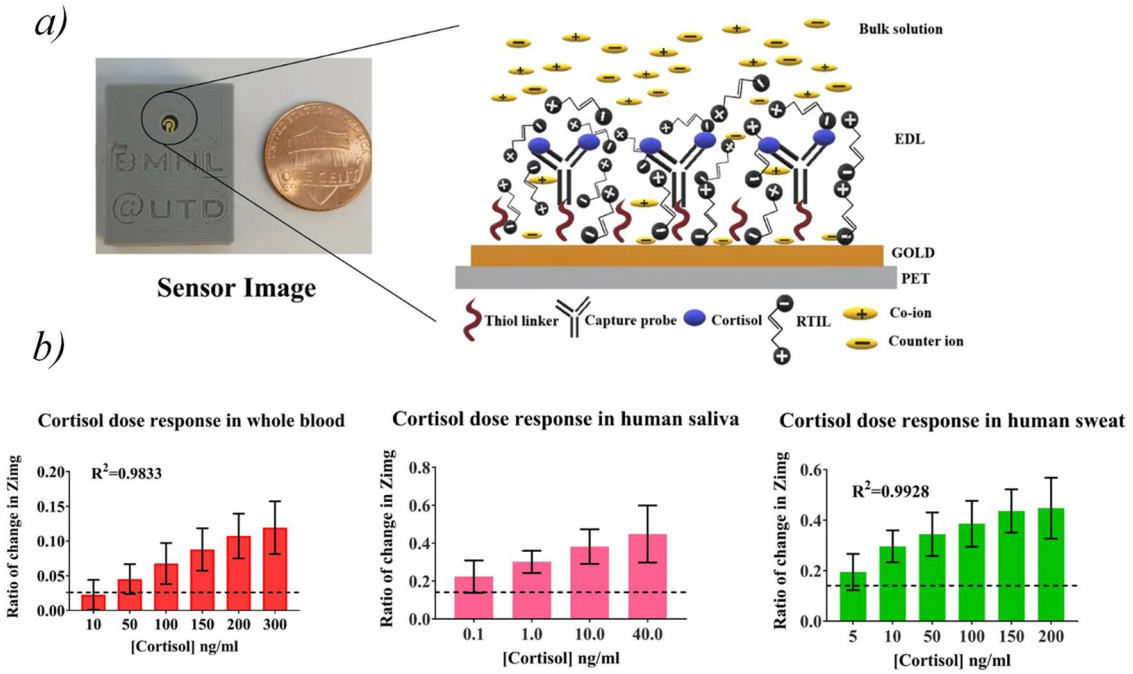

Figure 1.17: *a)* POC device for cortisol electrochemical sensor (left) and schematic representation of the electric double layer (EDL), including the SAM and the RTIL on the gold surface (right). *b)* Changes in imaginary impedance (Zimg), from baseline, against cortisol concentration using three different human fluids: blood, saliva and sweat. Adapted from ref.[155]

1.4.3 SAMs in Electrolyte-Gated Organic Field-Effect Transistors for Sensing Applications

Electrolyte-Gated Organic Field Effect Transistor (EGOFETs) are three-terminal devices that consist of an organic semiconductor (OSC) contacted between two electrodes (i.e., source and drain) and in contact with an electrolyte solution, where the third contact (i.e., gate) is immersed. The current through the OSC is modulated by applying a source-

gate voltage that causes the formation of two electrical double layers (EDLs) at the OSC/electrolyte and gate/electrolyte interfaces (see Figure 1.19a). As a result, the energy levels of the OSC are shifted, and charge carriers can accumulate in the semiconductor film.[156] The transfer characteristics of a typical EGOFET are shown in Figure 1.19b, in which the source-drain voltage is fixed whilst the source-gate voltage is swept. It can be observed that upon the application of a source-gate voltage above a threshold voltage value (V_{th}), the device is switched on, and electrical current starts to flow along the OSC.

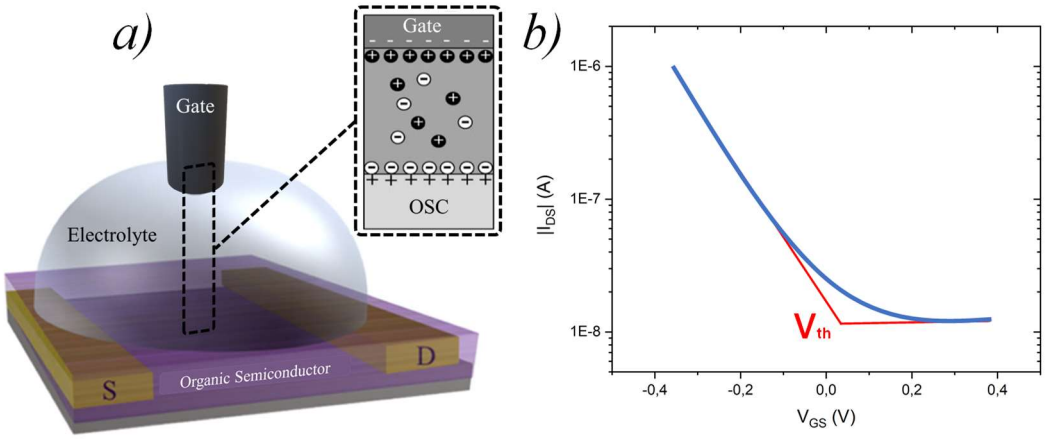

Figure 1.18: a) Scheme of a typical EGOFET showing the main components: top gate electrode, source (S) and drain (D) electrodes, the substrate with the organic semiconducting layer deposited on top and the electrolyte showing the formation of EDLs. b) Typical transfer curve for an EGOFET at a fixed source-drain voltage. Adapted from ref.[157]

These devices are raising much interest in developing (bio)sensors since they operate in aqueous media at low voltages and amplify the electric signals.[158] In fact, EGOFETs have been used to detect large and small molecular weight molecules, virus and biomarkers.[159,160]

The OSC/electrolyte and the electrolyte/gate interfaces represent the most sensitive parts of the device, and any tiny change in their surface potential and/or capacitance is amplified in the transistor electrical response.[161] Although several groups have worked on the functionalization of the OSC for this purpose, in this Thesis, we focus on the gate functionalization to incorporate the sensing units. Thus, similarly to the previously discussed electrochemical sensors, in an EGOFET, the gate electrode can also be functionalized with a specific SAM incorporating biological or chemical receptors.[162–167] After interaction with the analyte, potentiometric or capacitance changes occurring at the gate interface are translated into changes in the electrical characteristics of the transistor.

Previously in our group, a label-free sensor for α-synuclein, a protein associated with neurodegenerative disorders such as Parkinson's disease, was developed based on an EGOFET integrated in a microfluidics chip (Figure 1.20b and c).[168] The gate was functionalized with specific antibodies against α-synuclein, following two different approaches: *i)* using an amino-terminated self-assembled monolayer and *ii)* an His-tagged recombinant protein G (Figure 1.20a). The interaction of the antibodies with α-synuclein resulted in changes in the measured device current (Figure 1.20d). Both approaches gave high sensitivity and low LODs down to the sub-pM level. The reported devices combine the high sensitivity and short measurement tests with the electrical readout and the simplicity and upscaling compatibility of the fabrication methods employed. Thus, these devices are expected to contribute to personalized medicine and drug development advancements.

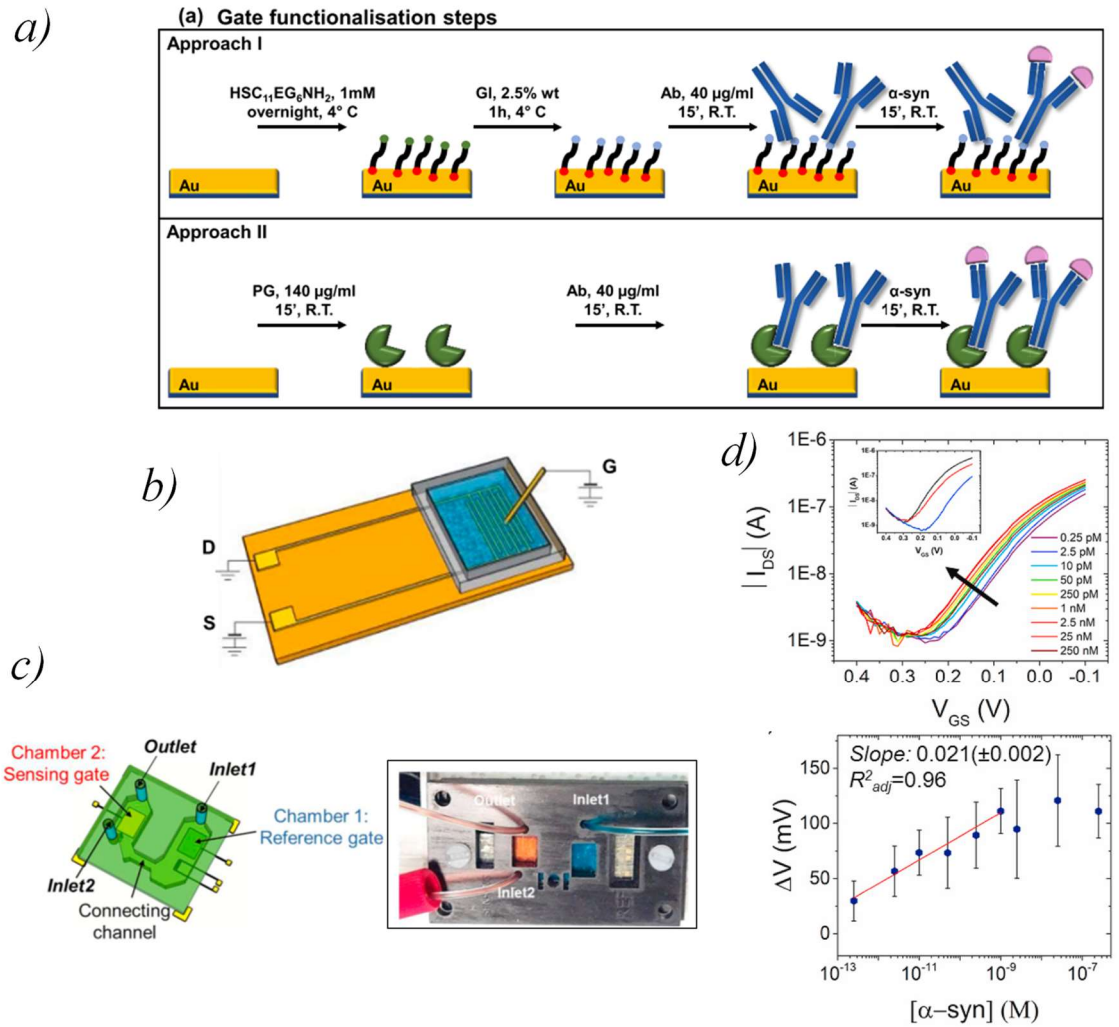

Figure 1.20: *a)* Gate electrode functionalization steps for the two different approaches. *b)* EGOFET scheme containing the gate, source and drain electrode. *c)* Microfluidic device layout employed (left) and integration in the microfluidic setup (right). d) (top) Electrical response of the EGOFET with an Ab-SAM-coated Au gate to the presence of α-synuclein at different concentrations. Inset: transfer curves relative to the bare Au (black), SAM (red) and Ab (blue). (bottom) Calibration curve obtained from the EGOFET sensing response. Adapted from ref.[168]

1.5. General Objectives

The present Doctoral Thesis is focused on the preparation of new molecular hybrid materials based on functionally stable SAMs grafted on electrodes or nanoparticles for the development of electrochemical sensors and switches. To achieve this main goal, the following specific objectives were proposed for this Thesis:

i. Fabrication of SAMs based on electroactive molecules in order to develop electrochemical switches. Specifically:
   A) Grafting an urazole organic radical on surface and investigating its redox and magnetic properties.
   B) Development of an electrochemical switch with a fluorescent response by functionalizing ITO substrates with quantum dots modified with an electroactive SAM.

ii. Exploiting supramolecular interactions as a strategy to develop sensing platforms that can be electrochemically read out using electrochemical impedance spectroscopy (EIS) and electrolyte-gated organic field-effect transistors (EGOFETs). In particular, the following sensors have been envisaged:

   A) Selective detection of toxic polycyclic aromatic molecules (PAHs) in water through π–π interactions.
   B) Development of a pH sensor by using the host-guest interactions between a cyclodextrin SAM and imidazole.

1.6. References

1. Kagdada, H. L., Bhojani, A. K. & Singh, D. K. An Overview of Nanomaterials: History, Fundamentals, and Applications. *Nanomaterials* 1–26 (2023).

2. Rymarczyk, J. The Change in the Traditional Paradigm of Production under the Influence of Industrial Revolution 4.0. *Businesses* **2**, 188–200 (2022).

3. Feynman, R. There's plenty of room at the bottom. in *Feynman and computation* 63–76 (CRC Press, 2018).

4. Baig, N., Kammakakam, I., Falath, W. & Kammakakam, I. Nanomaterials: A review of synthesis methods, properties, recent progress, and challenges. *Mater. Adv.* **2**, 1821–1871 (2021).

5. Abid, N. *et al.* Synthesis of nanomaterials using various top-down and bottom-up approaches, influencing factors, advantages, and disadvantages: A review. *Adv. Colloid Interface Sci.* **300**, 102597 (2022).

6. Thompson, S. E. & Parthasarathy, S. Moore's law: the future of Si microelectronics. *Mater. today* **9**, 20–25 (2006).

7. Balzani, V., Credi, A., Silvi, S. & Venturi, M. Artificial nanomachines based on interlocked molecular species: Recent advances. *Chem. Soc. Rev.* **35**, 1135–1149 (2006).

8. Komoto, Y., Fujii, S., Iwane, M. & Kiguchi, M. Single-molecule junctions for molecular electronics. *J. Mater. Chem. C* **4**, 8842–8858 (2016).

9. Huang, X. & Li, T. Recent progress in the development of molecular-scale electronics based on photoswitchable molecules. *J. Mater. Chem. C* **8**, 821–848 (2020).

10. Love, J. C., Estroff, L. A., Kriebel, J. K., Nuzzo, R. G. & Whitesides, G. M. Self-Assembled Monolayers of Thiolates on Metals as a Form of Nanotechnology. *Chem. Rev.* **105**, 1103–1169 (2005).

11. Love, J. C., Estroff, L. A., Kriebel, J. K., Nuzzo, R. G. & Whitesides, G. M. Self-assembled monolayers of thiolates on metals as a form of nanotechnology. *Chem. Rev.* **105**, 1103–1170 (2005).

12. Capitao, D., Limoges, B., Fave, C. & Schöllhorn, B. On the decisive role of the sulfur-based anchoring group in the electro-assisted formation of self-assembled monolayers on gold. *Electrochim. Acta* **257**, 165–171 (2017).

13. Herzer, N., Hoeppener, S. & Schubert, U. S. Fabrication of patterned silane based self-assembled monolayers by photolithography and surface reactions on silicon-

oxide substrates. *Chem. Commun.* **46**, 5634–5652 (2010).

14. Jadhav, S. A. Self-assembled monolayers (SAMs) of carboxylic acids: An overview. *Cent. Eur. J. Chem.* **9**, 369–378 (2011).

15. Sevrain, C. M., Berchel, M., Couthon, H. & Jaffrès, P. A. Phosphonic acid: Preparation and applications. *Beilstein J. Org. Chem.* **13**, 2186–2213 (2017).

16. Mutin, P. H., Guerrero, G. & Vioux, A. Hybrid materials from organophosphorus coupling molecules. *J. Mater. Chem.* **15**, 3761–3768 (2005).

17. Mesnage, A., Lefèvre, X., Jégou, P., Deniau, G. & Palacin, S. Spontaneous grafting of diazonium salts: Chemical mechanism on metallic surfaces. *Langmuir* **28**, 11767–11778 (2012).

18. Zaba, T. *et al.* Formation of highly ordered self-assembled monolayers of alkynes on Au(111) substrate. *J. Am. Chem. Soc.* **136**, 11918–11921 (2014).

19. Smith, R. K., Lewis, P. A. & Weiss, P. S. Patterning self-assembled monolayers. *Prog. Surf. Sci.* **75**, 1–68 (2004).

20. Feng, L., Zheng, S., Zhu, H., Ma, X. & Hu, Z. Detection of corrosion inhibition by dithiane self-assembled monolayers (SAMs) on copper. *J. Taiwan Inst. Chem. Eng.* **142**, 104610 (2023).

21. Sánchez-Obrero, G. *et al.* Surface Protection of Quaternary Gold Alloys by Thiol Self-Assembled Monolayers. *Int. J. Mol. Sci.* **23**, (2022).

22. Yi, R., Mao, Y., Shen, Y. & Chen, L. Self-Assembled Monolayers for Batteries. *J. Am. Chem. Soc.* **143**, 12897–12912 (2021).

23. Pieters, G. & Prins, L. J. Catalytic self-assembled monolayers on gold nanoparticles. *New J. Chem.* **36**, 1931–1939 (2012).

24. Samanta, D. & Sarkar, A. Immobilization of bio-macromolecules on self-assembled monolayers: Methods and sensor applications. *Chem. Soc. Rev.* **40**, 2567–2592 (2011).

25. Tan, D., Li, F. & Zhou, B. Antifouling self-assembled monolayers for designing of electrochemical biosensors. *Int. J. Electrochem. Sci.* **15**, 9446–9458 (2020).

26. Liu, K. & Jiang, L. Metallic surfaces with special wettability. *Nanoscale* **3**, 825–838 (2011).

27. Han, Y. & Uosaki, K. Effects of concentration and temperature on the formation process of decanethiol self-assembled monolayer on Au(1 1 1) followed by electrochemical reductive desorption. *Electrochim. Acta* **53**, 6196–6201 (2008).

28. Schwartz, D. K. Mechanisms and kinetics of self-assembled monolayer formation. *Annu. Rev. Phys. Chem.* **52**, 107–137 (2001).

29. Schreiber, F. Structure and growth of self-assembling monolayers. *Prog. Surf. Sci.*

65, 151–257 (2000).

30. Budz, H. A., Biesinger, M. C. & LaPierre, R. R. Passivation of GaAs by octadecanethiol self-assembled monolayers deposited from liquid and vapor phases. *J. Vac. Sci. Technol. B Microelectron. Nanom. Struct.* **27**, 637 (2009).

31. Ulman, A. Self-assembled monolayers of alkyltrichiorosilanes: Building blocks for future organic materials. *Adv. Mater.* **2**, 573–582 (1990).

32. Baccile, N., Derj, A., Boissière, C., Humblot, V. & Deniset-Besseau, A. Homogeneous supported monolayer from microbial glycolipid biosurfactant. *J. Mol. Liq.* **345**, 117827 (2022).

33. Gyepi-Garbrah, S. H. & Ŝilerová, R. The first direct comparison of self-assembly and Langmuir-Blodgett deposition techniques: Two routes to highly organized monolayers. *Phys. Chem. Chem. Phys.* **4**, 3436–3442 (2002).

34. Rouvière, L. *et al.* Silane-Based SAMs Deposited by Spin Coating as a Versatile Alternative Process to Solution Immersion. *Langmuir* **38**, 6464−6471 (2022).

35. Ali, F., Roldán-Carmona, C., Sohail, M. & Nazeeruddin, M. K. Applications of Self-Assembled Monolayers for Perovskite Solar Cells Interface Engineering to Address Efficiency and Stability. *Adv. Energy Mater.* **10**, 1–24 (2020).

36. Hong, Y. K. *et al.* Highly-ordered self-assembled monolayer of alkanethiol on thermally annealed polycrystalline gold films. *Chem. Phys.* **428**, 105–110 (2014).

37. Chen, J., Wang, Z., Oyola-Reynoso, S., Gathiaka, S. M. & Thuo, M. Limits to the Effect of Substrate Roughness or Smoothness on the Odd-Even Effect in Wetting Properties of n -Alkanethiolate Monolayers. *Langmuir* **31**, 7047–7054 (2015).

38. Carvalhal, R. F., Freire, R. S. & Kubota, L. T. Polycrystalline gold electrodes: A comparative study of pretreatment procedures used for cleaning and thiol self-assembly monolayer formation. *Electroanalysis* **17**, 1251–1259 (2005).

39. Kim, D., Lee, A. W. H., Eastcott, J. I. & Gates, B. D. Modifying the Surface Properties of Indium Tin Oxide with Alcohol-Based Monolayers for Use in Organic Electronics. *ACS Appl. Nano Mater.* **1**, 2237–2248 (2018).

40. Badv, M., Jaffer, I. H., Weitz, J. I. & Didar, T. F. An omniphobic lubricant-infused coating produced by chemical vapor deposition of hydrophobic organosilanes attenuates clotting on catheter surfaces. *Sci. Rep.* **7**, 1–10 (2017).

41. Badv, M., Imani, S. M., Weitz, J. I. & Didar, T. F. Lubricant-Infused Surfaces with Built-In Functional Biomolecules Exhibit Simultaneous Repellency and Tunable Cell Adhesion. *ACS Nano* **12**, 10890–10902 (2018).

42. Kang, J. & Rowntree, P. A. Gold film surface preparation for self-assembled monolayer studies. *Langmuir* **23**, 509–516 (2007).

43. Yang, Z. *et al.* Analytical application of self assembled monolayers on gold

electrodes: critical importance of surface pretreatment. *Biosens. Bioelectron.* **10**, 789–795 (1995).

44. Yamada, R., Sakai, H. & Uosaki, K. Solvent Effect on the Structure of the Self-Assembled Monolayer of Alkanethiol. *Chem. Lett.* **28**, 667–668 (1999).

45. Ulman, A. Formation and Structure of Self-Assembled Monolayers. *Chem. Rev.* **96**, 1533–1554 (1996).

46. Lee, N. S., Kang, H., Seong, S. & Noh, J. Effect of Immersion Time on the Structure of Octanethiol Self-Assembled Monolayers on Au(111) at an Elevated Solution Temperature. *Bull. Korean Chem. Soc.* **40**, 1152–1153 (2019).

47. Lee, S., Ishizaki, T., Saito, N. & Takai, O. Effect of reaction temperature on growth of organosilane self-assembled monolayers. *Jpn. J. Appl. Phys.* **47**, 6442–6447 (2008).

48. Kim, S. Y., Cho, S. J., Byeon, S. E., He, X. & Yoon, H. J. Self-Assembled Monolayers as Interface Engineering Nanomaterials in Perovskite Solar Cells. *Adv. Energy Mater.* **10**, 2002606 (2020).

49. Nuzzo, R. G. & Allara, D. L. Adsorption of bifunctional organic disulfides on gold surfaces. *J. Am. Chem. Soc.* **105**, 4481–4483 (1983).

50. Ederth, T., Claesson, P. & Liedberg, B. Self-assembled monolayers of alkanethiolates on thin gold films as substrates for surface force measurements. Long-range hydrophobic interactions and electrostatic double-layer interactions. *Langmuir* **14**, 4782–4789 (1998).

51. Schwartz, D. K., Steinberg, S., Israelachvili, J. & Zasadzinski, J. A. N. Growth of a self-assembled monolayer by fractal aggregation. *Phys. Rev. Lett.* **69**, 3354 (1992).

52. Andres, R. P. *et al.* Self-assembly of a two-dimensional superlattice of molecularly linked metal clusters. *Science* **273**, 1690–1693 (1996).

53. Yamada, R. & Uosaki, K. In situ, real time monitoring of the self-assembly process of decanethiol on Au (111) in liquid phase. A scanning tunneling microscopy investigation. *Langmuir* **13**, 5218–5221 (1997).

54. Vericat, C., Vela, M. E., Benitez, G., Carro, P. & Salvarezza, R. C. Self-assembled monolayers of thiols and dithiols on gold : new challenges for a well-known system. *Chem. Soc. Rev.* **39**, 1805–1834 (2010).

55. Iwasa, J. *et al.* In Situ Observation of a Self-Assembled Monolayer Formation of Octadecyltrimethoxysilane on a Silicon Oxide Surface Using a High-Speed Atomic Force Microscope. *J. Phys. Chem. C* **120**, 2807–2813 (2016).

56. Yasseri, A. A., Kobayashi, N. P. & Kamins, T. I. Formation and characterization of long-chained alkylsiloxane self-assembled monolayers on atomic-layer-

deposited aluminum oxide surfaces. *Appl. Phys. A* **84**, 1–5 (2006).

57. Wang, L., Schubert, U. S. & Hoeppener, S. Surface chemical reactions on self-assembled silane based monolayers. *Chem. Soc. Rev.* **50**, 6507–6540 (2021).

58. Issa, A. A. & Luyt, A. S. Kinetics of Alkoxysilanes and Organoalkoxysilanes Polymerization : A Review. *Polymers* **11**, 537 (2019).

59. Naik, V. V, Sta, R. & Spencer, N. D. Effect of Leaving Group on the Structures of Alkylsilane SAMs. *Langmuir* **30**, 14824–14831 (2014).

60. Richter, A. G., Yu, C. J., Datta, A., Kmetko, J. & Dutta, P. In situ and interrupted-growth studies of the self-assembly of octadecyltrichlorosilane monolayers. *Phys. Rev. E* **61**, 607–615 (2000).

61. Vallant, T., Kattner, J., Brunner, H., Mayer, U. & Hoffmann, H. Investigation of the formation and structure of self-assembled alkylsiloxane monolayers on silicon using in situ attenuated total reflection infrared spectroscopy. *Langmuir* **15**, 5339–5346 (1999).

62. Shakeri, A., Jarad, N. A., Leung, A., Soleymani, L. & Didar, T. F. Biofunctionalization of Glass and Paper-Based Microfluidic Devices: A Review. *Adv. Mater. Interfaces* **6**, 1900940 (2019).

63. Belman, N., Jin, K., Golan, Y., Israelachvili, J. N. & Pesika, N. S. Origin of the contact angle hysteresis of water on chemisorbed and physisorbed self-assembled monolayers. *Langmuir* **28**, 14609–14617 (2012).

64. Kind, M. & Wöll, C. Organic surfaces exposed by self-assembled organothiol monolayers: Preparation, characterization, and application. *Prog. Surf. Sci.* **84**, 230–278 (2009).

65. C. Julian Chen. *Introduction to Scanning Tunneling Microscopy 2nd Ed.* (Oxford University Press, 2007).

66. Yan, J. *et al.* Voltammetry and Single-Molecule In Situ Scanning Tunnelling Microscopy of the Redox Metalloenzyme Human Sulfite Oxidase. *ChemElectroChem* **8**, 164–171 (2021).

67. Liu, Y. F., Yang, Y. C. & Lee, Y. L. Assembly behavior and monolayer characteristics of OH-terminated alkanethiol on Au(111): In situ scanning tunneling microscopy and electrochemical studies. *Nanotechnology* **19**, 065609 (2008).

68. Zhang, C., Yi, Z. & Xu, W. Scanning probe microscopy in probing low-dimensional carbon-based nanostructures and nanomaterials. *Mater. Futur.* **1**, 032301 (2022).

69. Dufrêne, Y. F. Towards nanomicrobiology using atomic force microscopy. *Nat. Rev. Microbiol.* **6**, 674–680 (2008).

70. Rugar, D. & Hansma, P. Atomic force microscopy. *Phys. Today* **43**, 23–30 (1990).

71. Sinha Ray, S. Structure and Morphology Characterization Techniques. in *Clay-Containing Polymer Nanocomposites. From Fundamentals to Real Applications* 39–66 (Elsevier, 2013).

72. Interdigitated, M. *et al.* Electrochemical Detection of C-Reactive Protein in Human Serum Based on Self-Assembled. *Sensors* **19**, 5560 (2019).

73. Wu, Y. *et al.* Construction of Self-Assembled Polyelectrolyte/Cationic Microgel Multilayers and Their Interaction with Anionic Dyes Using Quartz Crystal Microbalance and Atomic Force Microscopy. *ACS Omega* **6**, 5764–5774 (2021).

74. Stevie, F. A. & Donley, C. L. Introduction to x-ray photoelectron spectroscopy. *J. Vac. Sci. Technol. A Vacuum, Surfaces, Film.* **38**, 63204 (2020).

75. Duwez, A.-S. Exploiting electron spectroscopies to probe the structure and organization of self-assembled monolayers: a review. *J. Electron Spectros. Relat. Phenomena* **134**, 97–138 (2004).

76. Kloprogge, J. T. & Wood, B. J. *Handbook of Mineral Spectroscopy. Volume 1: X-ray Photoelectron Spectra*. (Elsevier, 2020).

77. Konno, H. X-ray Photoelectron Spectroscopy. in *Materials Science and Engineering of Carbon: Characterization* 153–171 (Tsinghua University Press Limited, 2016).

78. Vlasov, I. I., Turner, S., Van Tendeloo, G. & Shiryaev, A. A. Chapter 9 - Recent Results on Characterization of Detonation Nanodiamonds. in *Ultananocrystalline Diamond 2sd Ed.* 291–326 (William Andrew Publishing, 2012).

79. Tao, F. & Bernasek, S. L. Understanding Odd−Even Effects in Organic Self-Assembled Monolayers. *Chem. Soc. Rev.* **107**, 1408–1453 (2007).

80. Steer, D., Kang, M. & Leal, C. Spectroscopic characterization of thiol-derived self-assembling monolayers. *J. Phys. Condens. Matter Spectrosc.* **13**, 11333–11365 (2001).

81. Gliboff, M. *et al.* Orientation of phenylphosphonic acid self-assembled monolayers on a transparent conductive oxide: A combined NEXAFS, PM-IRRAS, and DFT study. *Langmuir* **29**, 4176 (2013).

82. Diller, K., Maurer, R. J., Müller, M. & Reuter, K. Interpretation of x-ray absorption spectroscopy in the presence of surface hybridization. *J. Chem. Phys.* **146**, 214701 (2017).

83. Nie, H. Y. & Jahangiri-Famenini, H. R. Time-of-Flight Secondary Ion Mass Spectrometry Analyses of Self-Assembled Monolayers of Octadecyltrimethoxysilane on SiO2 Substrate. *Appl. Sci.* **12**, 4932 (2022).

84. Laskin, J., Wang, P. & Hadjar, O. Soft-landing of peptide ions onto self-assembled

monolayer surfaces: An overview. *Phys. Chem. Chem. Phys.* **10**, 1079–1090 (2008).

85. Chabal, Y. J. Surface Infrared Spectroscopy. *Surf. Sci. Rep.* **8**, 211–357 (1988).

86. Hollins, P. R. S. Infrared Reflection–Absorption Spectroscopy. in *Encyclopedia of Analytical Chemistry* (R.A. Meyers and M.L. McKelvy, 2006).

87. Akash, M. S. H. & Rehman, K. *Essentials of pharmaceutical analysis*. *Essentials of Pharmaceutical Analysis* (2019). doi:10.1007/978-981-15-1547-7.

88. Vecchi, A. *et al.* Tetraferrocenylporphyrins as active components of self-assembled monolayers on gold surface. *Chem. Commun.* **48**, 5145–5147 (2012).

89. Crivillers, N. *et al.* Self-Assembled Monolayers of a Multifunctional Organic Radical. *Angew. Chemie* **119**, 2265–2269 (2007).

90. Kondo, T. & Uosaki, K. Self-assembled monolayers (SAMs) with photo-functionalities. *J. Photochem. Photobiol. C Photochem. Rev.* **8**, 1–17 (2007).

91. Shin, S. K., Yoon, H. J., Jung, Y. J. & Park, J. W. Nanoscale controlled self-assembled monolayers and quantum dots. *Curr. Opin. Chem. Biol.* **10**, 423–429 (2006).

92. Ercole, F., Davis, T. P. & Evans, R. A. Photo-responsive systems and biomaterials: Photochromic polymers, light-triggered self-assembly, surface modification, fluorescence modulation and beyond. *Polym. Chem.* **1**, 37–54 (2010).

93. Crivillers, N., Mas-Torrent, M., Vidal-Gancedo, J., Veciana, J. & Rovira, C. Self-assembled monolayers of electroactive polychlorotriphenylmethyl radicals on Au(111). *J. Am. Chem. Soc.* **130**, 5499–5506 (2008).

94. Sahu, I. D. & Lorigan, G. A. Electron Paramagnetic Resonance as a Tool for Studying Membrane Proteins. *Biomolecules* **10**, 763 (2020).

95. Marcus, R. A. Theory of electron-transfer reaction rates of solvated electrons. *J. Chem. Phys.* **43**, 3477–3489 (1965).

96. Marcus, R. A. & Sutin, N. Electron transfers in chemistry and biology. *Biochim. Biophys. Acta* 265–322 (1985).

97. Inzelt, G., Lewenstam, A. & Scholz, F. *Handbook of Reference Electrodes*. (Springer Berlin Heidelberg, 2013).

98. Evans, D. H., O'Connell, K. M., Petersen, R. A. & Kelly, M. J. Cyclic voltammetry. *J. Chem. Educ.* **60**, 290–293 (1983).

99. Eckermann, A. L., Feld, D. J., Shaw, J. A. & Meade, T. J. Electrochemistry of redox-active self-assembled monolayers. *Coord. Chem. Rev.* **254**, 1769–1802 (2010).

100. Kingston, C. *et al.* A Survival Guide for the "Electro-curious". *Acc. Chem. Res.* **53**,

72–83 (2020).

101. Laviron, E. The use of linear potential sweep voltammetry and of a.c. voltammetry for the study of the surface electrochemical reaction of strongly adsorbed systems and of redox modified electrodes. *J. Electroanal. Chem.* **100**, 263–270 (1979).

102. Brown, A. P. & Anson, F. C. Cyclic and Differential Pulse Voltammetric Behavior of Reactants Confined to the Electrode Surface. *Anal. Chem.* **49**, 1589–1595 (1977).

103. Zanello, P., Nervi, C. & De Biani, F. F. *Inorganic electrochemistry: theory, practice and application*. (Royal Society of Chemistry, 2019).

104. Cecchet, F. *et al.* Redox Mediation at 11-Mercaptoundecanoic Acid Self-Assembled Monolayers on Gold. *J. Phys. Chem. B* **110**, 2241–2248 (2006).

105. Lasia, A. *Electrochemical Impedance Spectroscopy and its Applications*. (Springer Science & Business Media, 2011).

106. Muñoz, J., Montes, R. & Baeza, M. Trends in electrochemical impedance spectroscopy involving nanocomposite transducers: Characterization, architecture surface and bio-sensing. *Trends Anal. Chem.* **97**, 201–215 (2017).

107. Chang, B. Y. & Park, S. M. Electrochemical impedance spectroscopy. *Annu. Rev. Anal. Chem.* **3**, 207–229 (2010).

108. Barsoukov, E. & Macdonald, J. R. *Impedance Spectroscopy Theory, Experiment, and Applications, 2nd ed.* (John Wiley & Sons, 2005).

109. Maundy, B. & Elwakil, A. S. Extracting single dispersion Cole-Cole impedance model parameters using an integrator setup. *Analog Integr. Circuits Signal Process.* **71**, 107–110 (2012).

110. Tsai, Y. T. & Whitmore, D. H. Nonlinear least-squares analyses of complex impedance and admittance data for solid electrolytes. *Solid State Ionics* **7**, 129–139 (1982).

111. Amirudin, A. & Thieny, D. Application of electrochemical impedance spectroscopy to study the degradation of polymer-coated metals. *Prog. Org. Coatings* **26**, 1–28 (1995).

112. Bisquert, J., Garcia-Belmonte, G., Bueno, P., Longo, E. & Bulhões, L. O. S. Impedance of constant phase element (CPE)-blocked diffusion in film electrodes. *J. Electroanal. Chem.* **452**, 229–234 (1998).

113. Hirschorn, B. *et al.* Determination of effective capacitance and film thickness from constant-phase-element parameters. *Electrochim. Acta* **55**, 6218–6227 (2010).

114. Bisquert, J. Theory of the impedance of electron diffusion and recombination in a thin layer. *J. Phys. Chem. B* **106**, 325–333 (2002).

115. Facets, I. M. *et al.* Physical limits of silicon transistors and circuits. *Reports Prog. Phys.* **68**, 2701–2746 (2005).

116. Chen, F., Hihath, J., Huang, Z., Li, X. & Tao, N. J. Measurement of single-molecule conductance. *Annu. Rev. Phys. Chem.* **58**, 535–564 (2007).

117. Diehl, M. R. *et al.* Single-Walled Carbon Nanotube Based Molecular Switch Tunnel Junctions. *ChemPhysChem* **4**, 1335–1339 (2003).

118. Guo, X. *et al.* Covalently bridging gaps in single-walled carbon nanotubes with conducting molecules. *Science* **311**, 356–359 (2006).

119. Yates, J. T. & Campbell, C. T. Surface chemistry: Key to control and advance myriad technologies. *Proc. Natl. Acad. Sci. U. S. A.* **108**, 911–916 (2011).

120. Mathew, P. T. & Fang, F. Advances in Molecular Electronics: A Brief Review. *Engineering* **4**, 760–771 (2018).

121. Halik, M. & Hirsch, A. The Potential of Molecular Self-Assembled Monolayers in Organic Electronic Devices. *Adv. Mater.* **23**, 2689–2695 (2011).

122. Gooding, J. J., Mearns, F., Yang, W. & Liu, J. Self-assembled monolayers into the 21st century: Recent advances and applications. *Electroanalysis* **15**, 81–96 (2003).

123. Pathem, B. K., Claridge, S. A., Zheng, Y. B. & Weiss, P. S. Molecular switches and motors on surfaces. *Annu. Rev. Phys. Chem.* **64**, 605–630 (2013).

124. Katsonis, N., Lubomska, M., Pollard, M. M., Feringa, B. L. & Rudolf, P. Synthetic light-activated molecular switches and motors on surfaces. *Prog. Surf. Sci.* **82**, 407–434 (2007).

125. Campuzano, S., Pedrero, M., Yáñez-Sedeño, P. & Pingarrón, J. M. Antifouling (Bio)materials for electrochemical (bio)sensing. *Int. J. Mol. Sci.* **20**, 423 (2019).

126. Flink, S., Van Veggel, F. C. J. M. & Reinhoudt, D. N. Sensor functionalities in self-assembled monolayers. *Adv. Mater.* **12**, 1315–1328 (2000).

127. Arya, S. K., Solanki, P. R., Datta, M. & Malhotra, B. D. Recent advances in self-assembled monolayers based biomolecular electronic devices. *Biosens. Bioelectron.* **24**, 2810–2817 (2009).

128. Casalini, S., Bortolotti, C. A., Leonardi, F. & Biscarini, F. Self-assembled monolayers in organic electronics. *Chem. Soc. Rev.* **46**, 40–77 (2017).

129. Arndt, N. B. *et al.* Self-Assembled Monolayers of Arylazopyrazoles on Glass and Silicon Oxide: Photoisomerization and Photoresponsive Wettability. *Langmuir* **38**, 735–742 (2022).

130. Bian, Q. *et al.* Host-guest self-assembly toward reversible visible-light-responsive switching for bacterial adhesion. *Acta Biomater.* **76**, 39–45 (2018).

131. Han, Y. *et al.* Electric-field-driven dual-functional molecular switches in tunnel

junctions. *Nat. Mater.* **19**, 843–848 (2020).

132. Wen, J., Tian, Z. & Ma, J. Light- and electric-field-induced switching of thiolated azobenzene self-assembled monolayer. *J. Phys. Chem. C* **117**, 19934–19944 (2013).

133. Zareie, H. M., Boyer, C., Bulmus, V., Nateghi, E. & Davis, T. P. Temperature-Responsive Self-Assembled Monolayers of Oligo(ethylene glycol): Control ofBiomolecular Recognition. *ACS Nano* **2**, 757–765 (2008).

134. Leoni, T. *et al.* Controlling the charge state of a single redox molecular switch. *Phys. Rev. Lett.* **106**, 216103 (2011).

135. Jiang, Y., Wan, P., Smet, M., Wang, Z. & Zhang, X. Self-assembled monolayers of a malachite green derivative: Surfaces with pH- And UV-responsive wetting properties. *Adv. Mater.* **20**, 1972–1977 (2008).

136. Audi, H. *et al.* Electrical molecular switch addressed by chemical stimuli. *Nanoscale* **12**, 10127–10139 (2020).

137. Steen, J. D., Duijnstee, D. R. & Browne, W. R. Molecular switching on surfaces. *Surf. Sci. Rep.* **78**, 100596 (2023).

138. Marchante, E., Crivillers, N., Buhl, M., Veciana, J. & Mas-Torrent, M. An Electrically Driven and Readable Molecular Monolayer Switch Based on a Solid Electrolyte. *Angew. Chemie* **55**, 368–372 (2016).

139. Simão, C. *et al.* A three-state surface-confined molecular switch with multiple channel outputs. *J. Am. Chem. Soc.* **133**, 13256–13259 (2011).

140. Casado-Montenegro, J., Marchante, E., Crivillers, N., Rovira, C. & Mas-Torrent, M. Donor/Acceptor Mixed Self-Assembled Monolayers for Realizing a Multi-Redox-State Surface. *ChemPhysChem* **17**, 1810–1814 (2016).

141. Shokurov, A. V *et al.* Octopus-Type Crown-Bisphthalocyaninate Anchor for Bottom-Up Assembly of Supramolecular Bilayers with Expanded Redox-Switching Capability. *Small* **18**, 2104306 (2022).

142. Maglione, M. S. *et al.* Fluid Mixing for Low-Power' Digital Microfluidics' Using Electroactive Molecular Monolayers. *Small* **14**, 1–7 (2018).

143. Sharma, A. *et al.* Recent Advances in Tin Oxide Nanomaterials as Electrochemical/Chemiresistive Sensors. *J. Electrochem. Soc.* **168**, 027505 (2021).

144. Crespilho, F. N. *Advances in Bioelectrochemistry*. vol. 1 (Springer, 2022).

145. McEachern, F., Harvey, E. & Merle, G. Emerging Technologies for the Electrochemical Detection of Bacteria. *Biotechnol. J.* **15**, 2000140 (2020).

146. Mandler, D. & Kraus-Ophir, S. Self-assembled monolayers (SAMs) for

electrochemical sensing. *J. Solid State Electrochem.* **15**, 1535–1558 (2011).

147. Yuan, L. & Liu, L. Peptide-based electrochemical biosensing. *Sensors Actuators B Chem.* **344**, 130232 (2021).

148. Upasham, S. *et al.* Electrochemical impedimetric biosensors, featuring the use of Room Temperature Ionic Liquids (RTILs): Special focus on non-faradaic sensing. *Biosens. Bioelectron.* **177**, 112940 (2021).

149. Herranz, M. A., Colonna, B. & Echegoyen, L. Metal ion recognition and molecular templating in self-assembled monolayers of cyclic and acyclic polyethers. *Proc. Natl. Acad. Sci. U. S. A.* **99**, 5040–5047 (2002).

150. Zhang, S., Cardona, C. M. & Echegoyen, L. Ion recognition properties of self-assembled monolayers (SAMs). *Chem. Commun.* 4461–4473 (2006).

151. Tanak, A. S., Jagannath, B., Tamrakar, Y., Muthukumar, S. & Prasad, S. Non-faradaic electrochemical impedimetric profiling of procalcitonin and C-reactive protein as a dual marker biosensor for early sepsis detection. *Anal. Chim. Acta X* **3**, 100029 (2019).

152. Barhoum, A. & Altintas, Z. *Advanced Sensor Technology. Biomedical, Environmental, and Construction Applications. Elsevier*. (2022).

153. Ait-Touchente, Z. *et al.* Different electrochemical sensor designs based on diazonium salts and gold nanoparticles for pico molar detection of metals. *Molecules* **25**, 3903 (2020).

154. Jolly, P. *et al.* Self-assembled gold nanoparticles for impedimetric and amperometric detection of a prostate cancer biomarker. *Sensors Actuators, B Chem.* **251**, 637–643 (2017).

155. Upasham, S., Tanak, A., Jagannath, B. & Prasad, S. Development of ultra-low volume, multi-bio fluid, cortisol sensing platform. *Sci. Rep.* **8**, 1–12 (2018).

156. Zhang, Q. Electrolyte-gated organic field-effect transistors based on organic semiconductor: insulating polymer blends. (2019).

157. Zhang, Q., Tamayo, A., Leonardi, F. & Mas-Torrent, M. Interplay between Electrolyte-Gated Organic Field-Effect Transistors and Surfactants: A Surface Aggregation Tool and Protecting Semiconducting Layer. *ACS Appl. Mater. Interfaces* **13**, 30902–30909 (2021).

158. Adrahtas, D. Z. *et al.* Electrolyte-gated transistors for enhanced performance bioelectronics. *Nat. Rev. Methods Prim.* **1**, 66 (2021).

159. Li, L., Wang, S., Xiao, Y. & Wang, Y. Recent Advances in Immobilization Strategies for Biomolecules in Sensors Using Organic Field-Effect Transistors. *Trans. Tianjin Univ.* **26**, 424–440 (2020).

160. Burtscher, B. *et al.* Sensing Inflammation Biomarkers with Electrolyte-Gated

Organic Electronic Transistors. *Adv. Healthc. Mater.* **10**, (2021).

161. Cramer, T. *et al.* Water-gated organic field effect transistors-opportunities for biochemical sensing and extracellular signal transduction. *J. Mater. Chem. B* **1**, 3728–3741 (2013).

162. Casalini, S., Bortolotti, C. A., Leonardi, F. & Biscarini, F. Self-assembled monolayers in organic electronics. *Chem. Soc. Rev.* **46**, 40–71 (2017).

163. Guo, K. *et al.* Rapid single-molecule detection of COVID-19 and MERS antigens via nanobody-functionalized organic electrochemical transistors. *Nat. Biomed. Eng.* **5**, 666–677 (2021).

164. Parkula, V. *et al.* Harnessing selectivity and sensitivity in electronic biosensing: A Novel Lab-on-Chip Multigate Organic Transistor. *Anal. Chem.* **92**, 9330–9337 (2020).

165. Solodka, K. *et al.* Detection of Neurofilament Light Chain with Label-Free Electrolyte-Gated Organic Field-Effect Transistors. *Adv. Mater. Interfaces* **9**, (2022).

166. Sailapu, S. K. *et al.* Standalone operation of an EGOFET for ultra-sensitive detection of HIV. *Biosens. Bioelectron.* **156**, 1–7 (2020).

167. Piro, B. *et al.* Versatile transduction scheme based on electrolyte-gated organic field-effect transistor used as immunoassay readout system. *Biosens. Bioelectron.* **92**, 215–220 (2017).

168. Ricci, S. *et al.* Label-free immunodetection of α-synuclein by using a microfluidics coplanar electrolyte-gated organic field-effect transistor. *Biosens. Bioelectron.* **167**, 112433 (2020).

CHAPTER 2:

Electrochemically triggered switches based on SAMs of redox-active molecules

This Chapter is composed of two scientific articles related to the development of switchable surfaces based on the redox activity of two molecular systems, the urazole radical and the ferrocene.

Article I: Efficient Routes for the Preparation of Urazole Radical Self-Assembled Monolayers on Gold Surfaces

Article II: Fluorescent Switchable Surfaces Based on Quantum Dots Modified With Redox-Active Molecules

2.1 Introduction

As mentioned in the general introduction, the immobilization of molecular switches on surfaces is required to develop platforms for practical applications. The surface confinement of electrochemical switches through the preparation of robust self-assembled monolayers (SAMs) is a versatile approach to achieve this objective. The modulation of the surface properties of this type of SAM is accomplished by applying a voltage (electrical input) to change the redox state of the grafted molecules. The oxidized and reduced species can display different physicochemical characteristics (electrical, optical, magnetic, chemical, etc.) that are used as the output of the switch. In order to promote the stability of the hybrid system (i.e., SAM/surface), it is desired that the redox potential, the voltage at which a redox process occurs, is low enough to avoid the monolayer desorption.[1,2] It is key that the switching process is highly stable and reversible.

The most common case is a bistable system showing two commutable redox states. Here, the SAM can be considered a binary memory displaying "0" and "1" states associated with the two redox-accessible species. This can be extended to ternary or multilevel memories if the system has richer electrochemistry and shows three or more well-differentiated stable redox states.[3–5] For the electrical readout, the states can be directly correlated with the formal charges generated at the SAM in contact with the electrolyte, which determines the interfacial double-layer capacitance. This can be measured by EIS. However, as mentioned above, in the case that the various redox states show different physicochemical properties, such as optical and magnetic properties, they can also be used to identify the state of the switch (measured by EPR, UV-vis, fluorescence, etc.) (Figure 2.1).

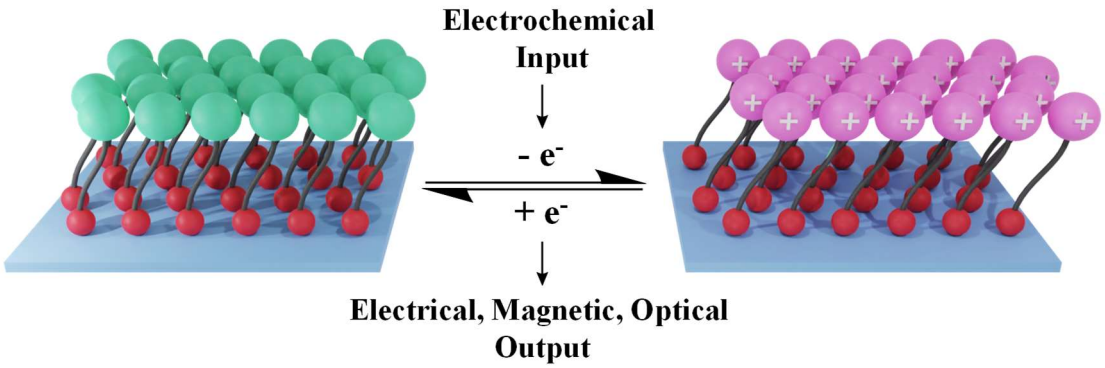

Figure 2.1: Illustration of a switchable SAM triggered by an electrochemical input with an electrical, optical and/or magnetic output response.

Some of the redox-active molecules that have been employed to prepare electrochemically switchable surfaces are metallocenes (such as ferrocene and derivatives), viologens, porphyrins, phthalocyanines, other metal-organic complexes, as well as stable organic radicals.[6–13] Further, single monolayers and multicomponent molecular assemblies can be synthesized to generate advanced molecular logic functions. For instance, van der Boom and co-workers prepared such structures by step-wise immobilizing redox-active metal complexes on ITO.[14] This system was operated with an electrical input to change the metal oxidation states ($M^{2+/3+}$), addressing the logic elements individually, and the output was read optically by UV-vis absorption spectroscopy.

Focusing on stable organic radicals, they are particularly interesting systems because they show paramagnetic and redox properties and, in some cases, interesting optical characteristics.[15,16] Organic radicals are open-shell species with one or more unpaired electrons in the molecular structure. The existence of these unpaired electrons endows them with some unique physicochemical properties related to their open-shell electronic structure. Several stable organic radicals are known in the literature, like nitroxides (such as the prototypical 2,2,6,6,-tetramethylpiperidin-N-oxyl (TEMPO) radical), phenoxyl,

nitronyl nitroxides, verdazyl or chlorinated trityl radicals.[17] Hence, taking advantage of the open-shell configuration and the versatile organic radical chemistry, which permits modulating spin-spin interactions and further control of their physical and chemical properties, great efforts have been devoted to boost their potential integration into magnetic, (opto)electronic and biological devices.[17,18] One methodology explored to advance in this direction is the preparation of stable organic radical-based SAMs, as explained below in the Article I description.

As mentioned above, metallocenes belong to another type of redox system that has been widely studied in fabricating molecular switches. In particular, the well-known electrochemical properties and stability of ferrocene (Fc) make it an ideal system for this purpose. A large variety of switchable materials based on Fc have been reported, including Fc SAMs, Fc-containing polymers, graphene/Fc composites, etc.[19–22] Quantum dots (QDs) have also been chemically modified with Fc showing clear synergistic characteristics since the redox properties of Fc influences the QD features and vice versa.[23] This is the focus of discussion for Article II.

Therefore, this Chapter includes two works describing the development of novel strategies to prepare electrochemically triggered switchable surfaces based on an organic radical and Fc, respectively. In Article I, the preparation of SAMs based on an urazole radical was successfully achieved, pursuing higher stability of the electrochemical and magnetic properties of the grafted radical compared to its behaviour in solution. In Article II, monolayers of Quantum Dots functionalized with Fc on ITO electrodes have been prepared. The covalent anchoring of Fc units on the QDs shell has permitted tuning the fluorescence properties of the system by changing the redox state of Fc. Only by grafting this system on a surface a stable switch was realized, since the nanoparticle aggregation observed in suspension hinders the reversibility of the switch.

2.1.1. *Article I*: Efficient Routes for the Preparation of Urazole Radical Self-Assembled Monolayers on Gold Surfaces

As commented above, stable organic radicals are appealing molecular building blocks for synthesizing functional (hybrid)materials mainly due to their inherent magnetic moment. Because of this, they are currently being investigated for their application in different fields, such as molecular quantum computing, molecular (opto)electronics and spintronics, energy storage conversion and (bio)imaging.[24–28] Towards device integration, the deposition of stable organic radicals on surfaces (physi- and chemisorbed) has been pursued by several groups.[26,29–33] Stable neutral organic radicals have been physisorbed on surface showing interesting properties such as the Kondo effect.[33–35] However, to better stabilize such systems, direct chemical bonding of the molecules with the surface can be realized by modifying them with surface anchoring groups (thiols, disulfides, silanes, etc.). Alternatively, if required, a two-step functionalization approach can be followed by using a SAM of a linker with a functional group able to react with the organic radical derivative.[29] Following one or the other methodology, radicals such as TEMPO, nitronyl nitroxides, and perchlorotriphenyl methyl (PTM) derivatives have been successfully grafted on different substrates like metals (i.e., gold), inorganic semiconductors, glass/quartz, metal oxides (i.e., TiO_2, ITO) and silicon.[26,29,36] Besides, Au nanoparticles (NPs) have also been functionalized with organic radicals and employed to investigate intramolecular spin exchange interactions between radicals covering the NP surface[37] or applied in electrocatalysis.[38]

In addition to the spin moment, the electrochemical switchability of organic radical SAMs is also a highly appealing characteristic. In our group, SAMs of chlorinated trityl radicals, particularly the polychlorotriphenylmethyl (PTM) radical, have been extensively

studied for the development of electrically triggered multi-responsive surfaces. C. Simao *et al.*[39] have reported the preparation of robust PTM SAMs on ITO as non-volatile memories (Figure 2.2). A reversible redox wave, with oxidation and a reduction peak at +53 mV and -32 mV, respectively (at 100 $mV \cdot s^{-1}$), was observed by CV. This was associated with the radical/anion reversible redox process. The different optical absorption, emission, and magnetic responses were used to determine the state of this multi-channel switch. The absorption and emission bands were reversibly modified during the write/erase cycles (+0.3V and -0.3V, respectively). The PTM radical state showed an absorption band at 365 nm and an emission one-centred at 688 nm.

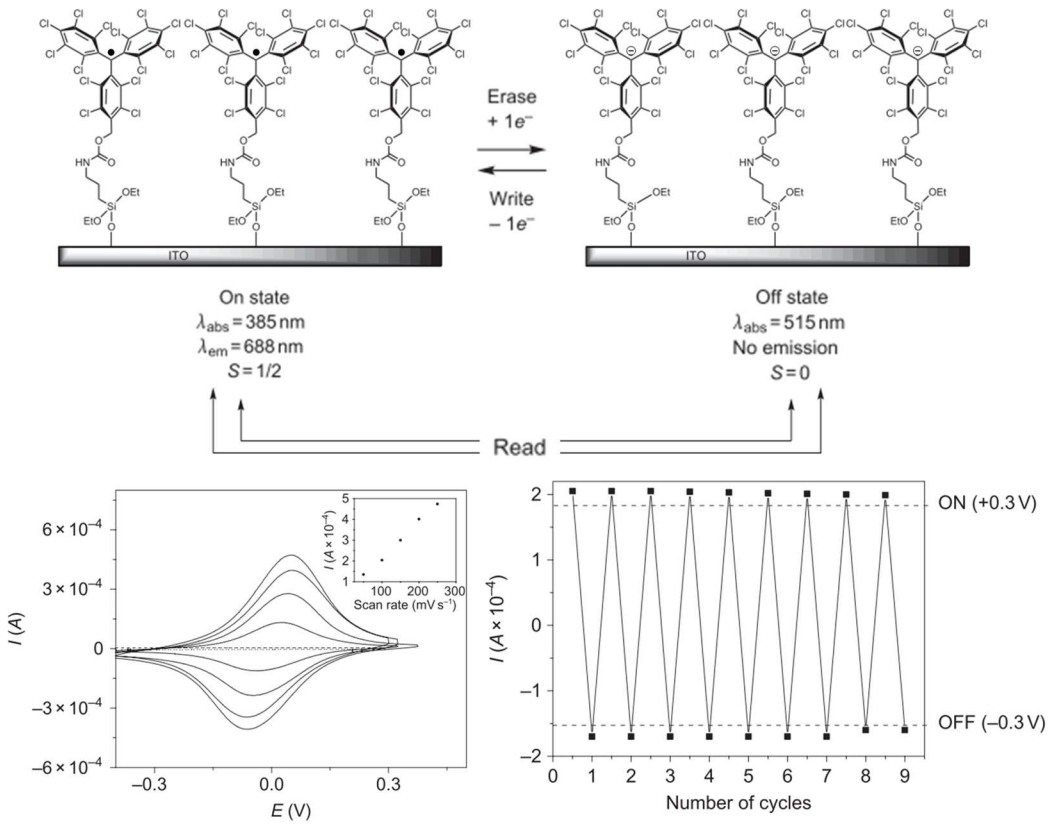

Figure 2.2: PTM radical SAM grafted on ITO (top left) that can be reversibly reduced to the anion form (top right). (bottom-left) CV voltammograms at different scan rates. Inset: plot of the current intensity *vs.* scan rate; (bottom-right) Reversible current modulation in the ON (+0.3 V) and OFF (-0.3 V) states. Ag wire was used as reference electrode. Adapted from ref.[39]

On the other hand, in the PTM anion state, the absorption band was observed at 515 nm, and no emission was detected. Furthermore, the EPR signal observed in the PTM radical SAM vanished upon reduction to the anionic form. Hence, the optical and magnetic outputs were suitable readout tools for determining the state of the switch (Figure 2.2).

A much less explored family of organic free radicals is the one derived from heterocyclic triazolidine, named after urazole. N-aryl substituted urazolyl radicals are persistent nitrogen-centred radicals.[40] Urazole radicals are stable when exposed to air;[41] nevertheless, they maintain an equilibrium with the N-N tetrazane dimer. The intermolecular interactions play an important role in this equilibrium process (Figure 2.3).[42] If the urazole core is functionalized with an aromatic ring, the presence of *ortho* substituents on this ring hinders the resonance stabilization of the radical spin because of the urazole ring's inability to achieve coplanarity with the benzene ring (Figure 2.3b).[41] On the contrary, in the absence of the substituents on the aromatic ring, the presence of radical species is favoured (Figure 2.3a).[43] In addition, urazole radicals can also self-react, forming a C-N bond (Figure 2.3c).[40]

Urazole radicals are generated in solution from their precursors by oxidation. Due to the dimerization reactions mentioned above, they cannot be isolated in the solid state; hence, they have been mainly studied in solution. Hence, the work carried out in this Thesis aimed to develop novel strategies to immobilize covalently urazole radicals on gold surfaces as described below.

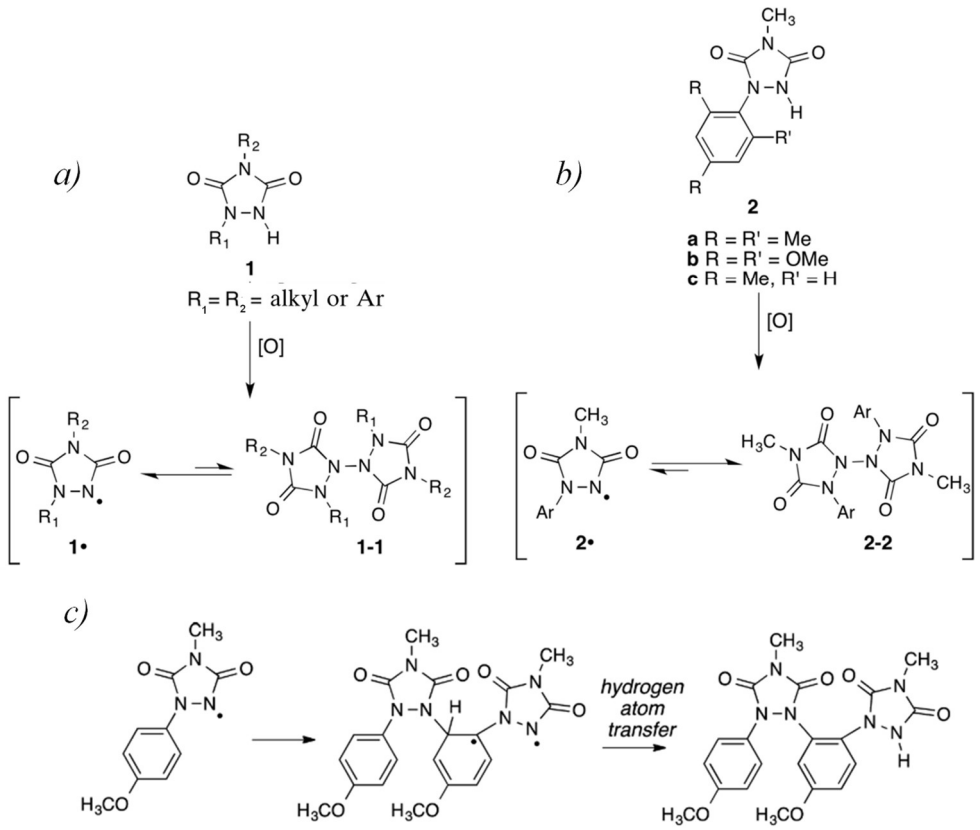

Figure 2.3: Oxidation of urazole to form N-centered urazolyl radical that exists in equilibrium with N-N dimer in solution: a) in the absence and b) presence of *ortho* substitution on the aromatic ring. c) Urazole radical dimerization through self-reaction forming a C-N bond. Adapted from ref.[40,41]

The work reported in Article I was done in collaboration with Prof. Gary Breton from Berry College (Georgia, USA), who synthesized the employed derivatives. The urazole radical precursor was designed to include aryl-substitution with a short alkoxy chain and a terminal alkyne group responsible for the interaction with the gold surface through a C-Au bond formation. In short, the urazole derivatives were synthesized by reacting 5-chloro-1-butyne with potassium phenoxide in dry DMF that afforded the aryl ether. The reaction of the resulting compound with N-methyl-1,2,4-triazoline-3,5-dione

(MeTAD) in the presence of trifluoroacetic acid as a catalyst led to the urazole derivative employed in this work (Figure 2.4).

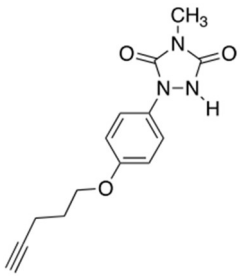

Figure 2.4: Urazole derivative employed in Article I for the preparation of SAMs on gold.

Prior to the SAMs preparation, the formation and stability of the urazole radical derivative were deeply investigated in solution. First, the generation of the radical was carried out following reported methodologies. EPR and UV-vis characterization showed that the radical was stable over 5 hours in solution. However, after 24 hours, the radical self-reacted dimerizing, forming a C-N bond.

Then, two approaches were employed for the SAMs formation, considering that the radical in solution was only stable for a few hours. In the first one, the radical urazole precursor was grafted on the surface, and the radical was in situ generated under oxidizing conditions. In the second approach, the radical was formed in solution and subsequently attached to the gold surface. The functionalized surfaces were fully characterized by EPR and CV, demonstrating the successful immobilization of the urazole radical derivatives. Density functional theory calculations showed that the molecules tend to be vertically oriented concerning the surface, which helped to estimate the surface coverage. The results showed that the first approach was more effective, although it could be expected that for longer-lived urazole radicals in solution the second approach could be more suitable.

2.1.2. *Article II*: Fluorescent Switchable Surfaces Based on Quantum Dots Modified with Redox-Active Molecules

Quantum Dots (QDs) are zero-dimensional nanostructures with shape-dependent optoelectronic properties showing size-tunable emission wavelength.[44] Owing to their luminescence properties,[45,46] QDs have attracted attention in biomedical imaging,[47] optical quantum computing,[48] light-emitting diodes (LEDs),[49] displays,[50,51] solar cells,[52] and sensors.[53,54]

Nevertheless, QDs are extremely vulnerable to some external stimuli, such as oxidation,[55–57] moisture[58] or heat,[59–61] and because of that, they are often chemically and thermally stabilized by a semiconductor shell[62–65] fabricated with heavy or inorganic materials (i.e., Cd, Se, ZnO, silica, etc.).[66] This shell helps to maintain or improve their optical properties.[67–69] Additionally, usually these core/shell QDs are synthesized having a protecting or passivating surface molecular layer (e.g., trioctylphosphine oxide (TOPO) or trioctylphosphine (TOP), which increases their colloidal stability (Figure 2.5a). Interestingly, this organic layer can be substituted with another monolayer through a ligand-exchange reaction, allowing it to incorporate other functional molecules on the QD surface. Following this methodology, QDs have been functionalized with ligands acting as protecting[70,71] and recognition groups [72] or with molecules that can modulate their optical properties (Figure 2.5b).[73,74] In this latter case, the QDs have been investigated at the fundamental level in order to gain insights into the mechanisms driving the quenching or enhancement of the emission properties upon the ligands grafting. For example, this phenomenon has been reported for CdSe/ZnS core/shell QDs modified with alkane thiol derivatives.[75] Thiol groups play a crucial role as hole trap states, affecting the relaxation of excited electrons from the conduction to the valence band and leading to non-radiative recombination processes, which results in emission quenching.

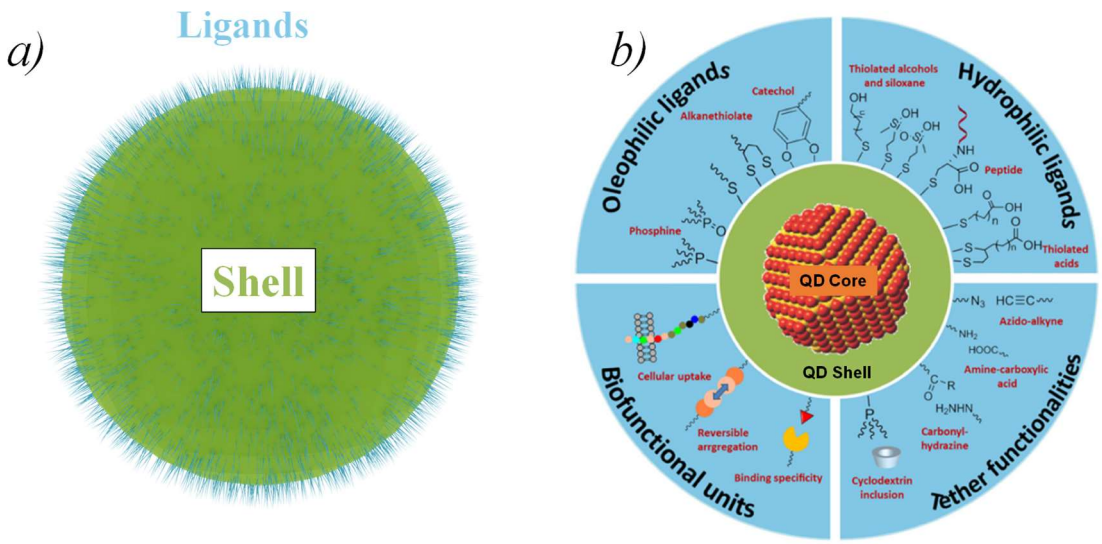

Figure 2.5: a) Illustration of a QD functionalized with an organic ligand-based monolayer. b) Surface engineering strategies of QDs with capping layers using oleophilic ligands, water-soluble surface layers using hydrophilic ligands, versatile tether functionalities via selective reactions or interactions, and biofunctionalities for targeting or therapeutic applications. Adapted from ref.[72]

Molecules with electron donor or electron acceptor character have been employed to covalently modify the QDs shell in order to study the charge transfer processes between the molecule and the QD.[76] The quenching mechanism depends on the species attached to the QD surface. For instance, when an electron acceptor grafted to a QD surface has the lowest unoccupied molecular orbital (LUMO) at lower energy compared to the QD conduction band edge, a photoinduced electron transfer from the QD to the electron acceptor takes place (see Figure 2.6a). As a result, the luminescence of the QD is quenched. Conversely, if an electron donor species is grafted on the nanocrystal surface with the highest occupied molecular orbital (HOMO) at higher energy with respect to the valence band, an electron transfer from the molecular donor to the photoexcited QD is promoted, also resulting in luminescence quenching (see Figure 2.6b).[77]

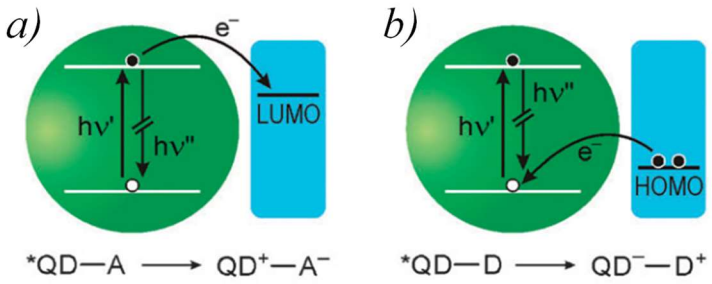

Figure 2.6. Schematic representation of the electron transfer a) from the photoexcited QD to an electron acceptor molecule and b) from an electron donor molecule to a photoexcited QD. Adapted from ref.[77]

Previously to the work done in this Thesis, other authors have investigated the QD surface modification with ferrocene (an excellent electron donor). Dorokhin *et al.*[78] demonstrated that the photoluminescence of CdSe/ZnS core/shell QDs could be tuned by grafting ferrocenyl alkane thiols of different lengths (Figure 2.7a). They observed that the quenching efficiency increased by decreasing the alkyl spacer length (Figure 2.7b). The proposed mechanism involved a hole transfer between the photoexcited QD and the ferrocene.

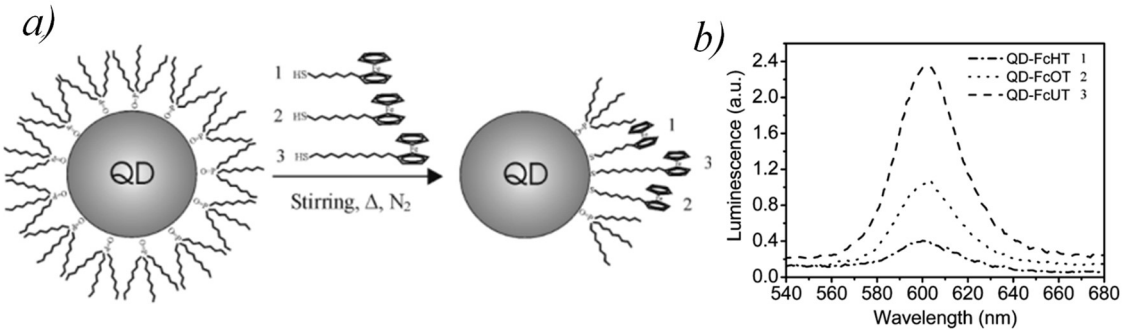

Figure 2.7: a) Ligand exchange reaction between a CdSe/ZnS core/shell QDs stabilized with a surfactant and the Fc thiolated ligands. b) QDs luminescence quenching depending on the length of the Fc ligand. The graph shows a decrease in the luminescence intensity by decreasing the Fc-QD distance. Adapted from ref. [78]

However, despite the great progress and stability improvement upon incorporating the organic shell, the QDs colloidal suspensions tend to aggregate over time, which promotes self-quenching and limits their potential applications.[79] Different strategies based on increasing the distance between nanoparticles have been explored to circumvent this issue, for example, by using long alkyl chain molecules as ligands.[80] Another route is the surface deposition of QDs, which has opened new perspectives for the fabrication of advanced optoelectronic devices.[81] The most common approaches to deposit QDs on surfaces are spin-coating[82–84] and inkjet printing.[85,86] Nevertheless, with these techniques, the obtained thin films are usually composed of multilayers and the QDs are not covalently attached to the surface.

Based on all these precedents, the main goal of the second work included in this Chapter (Article II) was to design and fabricate robust electrochemically switchable Fc@QDs-based monolayers on ITO. In particular, CdSe/ZnS core/shell QDs were employed. For this purpose, a three-step approach was optimized to obtain the covalently anchored QDs: 1) formation of a thiol-terminated SAM on ITO, 2) on-surface ligand exchange reaction to link the QDs/octadecylamine to the modified ITO surface and 3) on-surface ligand exchange between the amine and the ferrocenyl alkane thiols. The resulting surface combined the fluorescence properties of CdSe/ZnS QDs and the redox activity of the Fc. First, the SAMs were characterized by XPS. Then, the redox activity of the grafted Fc/QDs was proved by cyclic voltammetry. Based on the redox peak position, the reversible modulation of the luminescent properties was carried out by applying the voltage needed to oxidize or reduce the Fc molecules (+0.6 V and 0 V, respectively). The oxidation of the Fc to ferrocenium (Fc^+) induced a decrease in the luminescence intensity ("OFF" state), which was recovered upon the reduction back to Fc ("ON" state). The application of consecutive switching cycles without losing the response demonstrated the high stability and reversibility of this system. Moreover, to modulate the ON/OFF ratio

of the switch, the spacer distance between the QDs and Fc molecules was adjusted using ligands with different spacers. The maximum ON/OFF ratio of 27% was realized with the shorter spacer.

Remarkably, the partial oxidation/reduction of the grafted Fc molecules was achieved by applying an intermediate voltage (+0.3 V), giving rise to an additional intermediate fluorescence state and, hence, a ternary optical switch. Importantly, our work showcases an efficient and novel approach to fabricate robust fluorescent redox switches by harnessing the luminescence properties of QDs. By immobilizing the QDs on the surface, we have effectively prevented their aggregation and self-quenching, enhancing their switching performance.

2.2. Summary

In summary, two novel switchable surfaces have been developed employing redox-active molecules. First, the preparation of SAMs on gold based on a new urazole radical derivative has been achieved, proving that these radicals can be stabilized on surface. The electrochemical and paramagnetic activity of the modified surfaces was demonstrated. The obtained results could serve as a seed for the design and preparation of more robust surfaces based on these radicals, which until now have been hardly explored due to the inability of urazole radicals to be isolated in solid state and their sometimes-limited stability in solution.

Further, it has been demonstrated that QDs can be covalently linked to ITO substrates with a proper surface functionalization strategy. The stable QDs SAMs were modified with Fc through an on-surface ligand-exchange. The redox state of the Fc was exploited to reversibly modulate the fluorescence of the system. Furthermore, it was shown that controlling the ratio of oxidized/reduced Fc species on the QD surface can also be used to fine-tune the substrate luminescence, leading to a multistate switch.

2.3. References

1. Simão, C. *et al.* A three-state surface-confined molecular switch with multiple channel outputs. *J. Am. Chem. Soc.* **133**, 13256–13259 (2011).
2. Parkula, V. *et al.* EGOFET Gated by a Molecular Electronic Switch: A Single-Device Memory Cell. *Adv. Electron. Mater.* **5**, 1–8 (2019).
3. Han, B., Li, Z., Wandlowski, T., Błaszczyk, A. & Mayor, M. Potential-induced redox switching in viologen self-assembled monolayers: An ATR-SEIRAS approach. *J. Phys. Chem. C* **111**, 13855–13863 (2007).
4. Li, Y. *et al.* Recent advances in organic-based materials for resistive memory applications. *InfoMat* **2**, 995–1033 (2020).
5. Mas-Torrent, M., Rovira, C. & Veciana, J. Surface-confined electroactive molecules for multistate charge storage information. *Adv. Mater.* **25**, 462–468 (2013).
6. Wong, R. A., Yokota, Y., Wakisaka, M., Inukai, J. & Kim, Y. Probing the Redox-Dependent Electronic and Interfacial Structures in Ferrocene-Terminated Self-Assembled Monolayers with Photoelectron Spectroscopy. in *Electrochemical Society Meeting Abstracts 236* 2123 (The Electrochemical Society, Inc., 2019).
7. Marchante, E., Crivillers, N., Buhl, M., Veciana, J. & Mas-Torrent, M. An electrically driven and readable molecular monolayer switch based on a solid electrolyte. *Angew. Chemie* **128**, 376–380 (2016).
8. Fave, C. & Schöllhorn, B. Electrochemical activation of halogen bonding. *Curr. Opin. Electrochem.* **15**, 89–96 (2019).
9. Li, J. *et al.* Reversible switching of molecular conductance in viologens is controlled by the electrochemical environment. *J. Phys. Chem. C* **125**, 21862–21872 (2021).
10. Marchante, E., Maglione, M. S., Crivillers, N. & Rovira, C. RSC Advances A four-state capacitance molecular switch based on a redox active tetrathiafulvalene self-assembled. *RSC Adv.* **7**, 5636–5641 (2017).
11. Xu, K. & Xie, S. Self-assembled molecular devices: a minireview. *Instrum. Sci. Technol.* **48**, 86–111 (2020).
12. Alcon, I., Gonidec, M., Ajayakumar, M. R., Mas-Torrent, M. & Veciana, J. A surface confined yttrium(III) bis-phthalocyaninato complex: a colourful switch controlled by electrons. *Chem. Sci.* **7**, 4940–4944 (2016).
13. Ivashenko, O., Herpt, J. T. Van, Feringa, B. L., Rudolf, P. & Browne, W. R. Electrochemical Write and Read Functionality through Oxidative Dimerization of

Spiropyran Self-Assembled Monolayers on Gold. *J. Phys. Chem. C* **117**, 18567–18577 (2013).

14. Keisar, H., Lahav, M. & van der Boom, M. E. Integrated Molecular Logic Using a Multistate Electrochromic Platform. *ChemPhysChem* **20**, 2403–2407 (2019).

15. Ratera, I. *et al.* Perspectives for polychlorinated trityl radicals. *J. Mater. Chem. C* **9**, 10610–10623 (2021).

16. Lloveras, V. *et al.* Multifunctional Switch Based on Spin-Labeled Gold Nanoparticles. *Nano Lett.* **22**, 768–774 (2022).

17. Chen, Z. X., Li, Y. & Huang, F. Persistent and Stable Organic Radicals: Design, Synthesis, and Applications. *Chem* **7**, 288–332 (2021).

18. Ji, L., Shi, J., Wei, J., Yu, T. & Huang, W. Air-Stable Organic Radicals: New-Generation Materials for Flexible Electronics? *Adv. Mater.* **32**, 1–15 (2020).

19. Wu, Z. *et al.* Nanoparticles functionalized with supramolecular host–guest systems for nanomedicine and healthcare. *Nanomedicine* **10**, 1493–1514 (2015).

20. Xia, N., Liu, L., Sun, Z. & Zhou, B. Nanocomposites of Graphene with Ferrocene or Hemin: Preparation and Application in Electrochemical Sensing. *J. Nanomater.* **2015**, 1–9 (2015).

21. Gallei, M. & Christian, R. Recent Trends in Metallopolymer Design:Redox-Controlled Surfaces, Porous Membranes, and Switchable Optical Materials Using Ferrocene-Containing Polymers. *Chem. - A Eur. J.* **24**, 10006–10021 (2018).

22. Hu, M. *et al.* Electrochemical Applications of Ferrocene-Based Coordination Polymers. *Chempluschem* **85**, 2397–2418 (2020).

23. Dorokhin, D., Tomczak, N., Reinhoudt, D. N., Velders, A. H. & Vancso, G. J. Ferrocene-coated CdSe/ZnS quantum dots as electroactive nanoparticles hybrids. *Nanotechnology* **21**, 285703 (2010).

24. Nakahara, K., Oyaizu, K. & Nishide, H. Organic radical battery approaching practical use. *Chem. Lett.* **40**, 222–227 (2011).

25. Cui, X., Zhang, Z., Yang, Y., Li, S. & Lee, C. Organic radical materials in biomedical applications: State of the art and perspectives. *Exploration* **2**, 20210264 (2022).

26. Mas-Torrent, M. *et al.* Organic radicals on surfaces: Towards molecular spintronics. *J. Mater. Chem.* **19**, 1691–1695 (2009).

27. Sun, L. *et al.* Room-Temperature Quantitative Quantum Sensing of Lithium Ions with a Radical-Embedded Metal-Organic Framework. *J. Am. Chem. Soc.* **144**, 19008–19016 (2022).

28. Tan, Y. *et al.* Electronic and Spintronic Open-Shell Macromolecules, Quo Vadis? *J. Am. Chem. Soc.* **144**, 626–647 (2022).

29. Mas-Torrent, M., Crivillers, N., Rovira, C. & Veciana, J. Attaching persistent organic free radicals to surfaces: How and why. *Chem. Rev.* **112**, 2506–2527 (2012).

30. Alévêque, O. *et al.* Nitroxyl radical self-assembled monolayers on gold: Versatile electroactive centers in aqueous and organic media. *ChemPhysChem* **10**, 2401–2404 (2009).

31. Mannini, M. *et al.* Self-assembled organic radicals on Au(111) surfaces: A combined ToF-SIMS, STM, and ESR study. *Langmuir* **23**, 2389–2397 (2007).

32. Matsushita, M. M., Ozaki, N., Sugawara, T., Nakamura, F. & Hara, M. Formation of self-assembled monolayer of phenylthiol carrying nitronyl nitroxide on gold surface. *Chem. Lett.* **31**, 596–597 (2002).

33. Liu, J. *et al.* First observation of a Kondo resonance for a stable neutral pure organic radical, 1,3,5-triphenyl-6-oxoverdazyl, adsorbed on the Au(111) surface. *J. Am. Chem. Soc.* **135**, 651–658 (2013).

34. Müllegger, S., Rashidi, M., Fattinger, M. & Koch, R. Surface-supported hydrocarbon π radicals show Kondo behavior. *J. Phys. Chem. C* **117**, 5718–5721 (2013).

35. Zhang, Y. H. *et al.* Temperature and magnetic field dependence of a Kondo system in the weak coupling regime. *Nat. Commun.* **4**, 1–6 (2013).

36. Shekhah, O. *et al.* Grafting of monocarboxylic substituted polychlorotriphenylmethyl radicals onto a COOH-functionalized self-assembled monolayer through copper (II) metal ions. *Langmuir* **24**, 6640–6648 (2008).

37. Lloveras, V., Badetti, E., Veciana, J. & Vidal-Gancedo, J. Dynamics of intramolecular spin exchange interaction of a nitronyl nitroxide diradical in solution and on surfaces. *Nanoscale* **8**, 5049–5058 (2016).

38. Swiech, O., Bilewicz, R. & Megiel, E. TEMPO coated Au nanoparticles: Synthesis and tethering to gold surfaces. *RSC Adv.* **3**, 5979–5986 (2013).

39. Simão, C. *et al.* A robust molecular platform for non-volatile memory devices with optical and magnetic responses. *Nat. Chem.* **3**, 359–364 (2011).

40. Breton, G. W. & Suroviec, A. H. Intermediacy of a Persistent Urazole Radical and an Electrophilic Diazenium Species in the Acid-Catalyzed Reaction of MeTAD with Anisole. *J. Org. Chem.* **81**, 206–214 (2016).

41. Martin, K. L. & Breton, G. W. Computational, 1H NMR, and X-ray structural studies on 1-Arylurazole tetrazane dimers. *Acta Crystallogr.* **C73**, 660–666 (2017).

42. Breton, G. W. Factors affecting the dimerization of persistent nitrogen-centered 1-phenyl urazole radicals to tetrazanes. *J. Phys. Org. Chem.* **31**, 1–9 (2018).

43. Breton, G. W. & Bowron, J. A. 1-(4-{[3,5-bis({[3,5-Dimethyl-4-(4-methyl-3,5-

dioxo-1,2,4- triazolidin-1-yl)-phenoxy]methyl})phenyl]methoxy}-2,6- dimethyl-phenyl)-4-methyl-1,2,4-triazolidine-3,5-dione. *Molbank* 3–7 (2023).

44. Bera, D., Qian, L., Tseng, T. K. & Holloway, P. H. Quantum dots and their multimodal applications: A review. *Materials (Basel).* **3**, 2260–2345 (2010).

45. Cotta, M. A. Quantum Dots and Their Applications: What Lies Ahead? *ACS Appl. Nano Mater.* **3**, 4920–4924 (2020).

46. Wang, X., Feng, Y., Dong, P. & Huang, J. A Mini Review on Carbon Quantum Dots: Preparation, Properties, and Electrocatalytic Application. *Front. Chem.* **7**, 1–9 (2019).

47. Wagner, A. M., Knipe, J. M., Orive, G. & Peppas, N. A. Quantum dots in biomedical applications. *Acta Biomater.* **94**, 44–63 (2019).

48. Arakawa, Y. & Holmes, M. J. Progress in quantum-dot single photon sources for quantum information technologies: A broad spectrum overview. *Appl. Phys. Rev.* **7**, 21309 (2020).

49. Onal, A. *et al.* High-Performance White Light-Emitting Diodes over 150 lm/W Using Near-Unity-Emitting Quantum Dots in a Liquid Matrix. *ACS Photonics* **9**, 1304−1314 (2022).

50. Lee, Y. *et al.* Stretchable array of CdSe/ZnS quantum-dot light emitting diodes for visual display of bio-signals. *Chem. Eng. J.* **427**, 130858 (2021).

51. Huang, Y. M. *et al.* Advances in quantum-dot-based displays. *Nanomaterials* **10**, 1–29 (2020).

52. Sahu, A., Garg, A. & Dixit, A. A review on quantum dot sensitized solar cells: Past, present and future towards carrier multiplication with a possibility for higher efficiency. *Sol. Energy* **203**, 210–239 (2020).

53. Lesiak, A. *et al.* Optical sensors based on II-VI quantum dots. *Nanomaterials* **9**, 1–24 (2019).

54. Maluleke, R. & Oluwafemi, O. S. Synthetic approaches, modification strategies and the application of quantum dots in the sensing of priority pollutants. *Appl. Sci.* **11**, 11580 (2021).

55. Dabbousi, B. O. *et al.* (CdSe)ZnS core-shell quantum dots: Synthesis and characterization of a size series of highly luminescent nanocrystallites. *J. Phys. Chem. B* **101**, 9463–9475 (1997).

56. Katari, J. E. B., Colvin, V. L. & Alivisatos, A. P. X-ray photoelectron spectroscopy of CdSe nanocrystals with applications to studies of the nanocrystal surface. *J. Phys. Chem.* **98**, 4109–4117 (1994).

57. Inerbaev, T. M. *et al.* Quantum chemistry of quantum dots: Effects of ligands and oxidation. *J. Chem. Phys.* **131**, 044106 (2009).

58. Tata, M., Banerjee, S., John, V. T., Waguespack, Y. & McPherson, G. L. Fluorescence quenching of CdS nanocrystallites in AOT water-in-oil microemulsions. *Colloids Surfaces A Physicochem. Eng. Asp.* **127**, 39–46 (1997).

59. Chen, K. J. *et al.* The influence of the thermal effect on CdSe/ZnS quantum dots in light-emitting diodes. *J. Light. Technol.* **30**, 2256–2261 (2012).

60. Woo, J. Y., Kim, K. N., Jeong, S. & Han, C. S. Thermal behavior of a quantum dot nanocomposite as a color converting material and its application to white LED. *Nanotechnology* **21**, 495704 (2010).

61. Zhao, Y. *et al.* High-temperature luminescence quenching of colloidal quantum dots. *ACS Nano* **6**, 9058–9067 (2012).

62. Fu, Y. *et al.* Excellent stability of thicker shell CdSe@ZnS/ZnS quantum dots. *RSC Adv.* **7**, 40866–40872 (2017).

63. Chen, Y. *et al.* 'Giant' multishell CdSe nanocrystal quantum dots with suppressed blinking. *J. Am. Chem. Soc.* **130**, 5026–5027 (2008).

64. Wang, N. *et al.* Highly luminescent silica-coated CdS/CdSe/CdS nanoparticles with strong chemical robustness and excellent thermal stability. *Nanotechnology* **28**, 185603 (2017).

65. Lim, J. *et al.* Influence of shell thickness on the performance of light-emitting devices based on CdSe/Zn 1- X Cd x S core/shell heterostructured quantum dots. *Adv. Mater.* **26**, 8034–8040 (2014).

66. Gidwani, B., Sahu, V., Shankar, S., Pandey, R. & Joshi, V. Journal of Drug Delivery Science and Technology Quantum dots : Prospectives , toxicity , advances and applications. *J. Drug Deliv. Sci. Technol.* **61**, 102308 (2021).

67. Kim, J. *et al.* High-quantum yield alloy-typed core/shell CdSeZnS/ZnS quantum dots for bio-applications. *J. Nanobiotechnology* **20**, 1–12 (2022).

68. Jeong, S. *et al.* Enhancement Mechanism of the Photoluminescence Quantum Yield in Highly Efficient ZnS-AgIn5S8 Quantum Dots with Core/Shell Structures. *J. Phys. Chem. C* **122**, 10125–10132 (2018).

69. Ko, J. *et al.* Chemically resistant and thermally stable quantum dots prepared by shell encapsulation with cross-linkable block copolymer ligands. *NPG Asia Mater.* **12**, (2020).

70. Hostetler, M. J. & Murray, R. W. Colloids and self-assembled monolayers. *Curr. Opin. Colloid Interface Sci.* **2**, 42–50 (1997).

71. Hines, D. A. & Kamat, P. V. Recent advances in quantum dot surface chemistry. *ACS Appl. Mater. Interfaces* **6**, 3041–3057 (2014).

72. Zhou, J., Liu, Y., Tang, J. & Tang, W. Surface ligands engineering of semiconductor quantum dots for chemosensory and biological applications.

Biochem. Pharmacol. **20**, 360–376 (2017).

73. Kalyuzhny, G. & Murray, R. W. Ligand Effects on Optical Properties of CdSe Nanocrystals. *J. Phys. Chem. B* **109**, 7012–7021 (2005).

74. Jeong, S. *et al.* Effect of the thiol-thiolate equilibrium on the photophysical properties of aqueous CdSe/ZnS nanocrystal quantum dots. *J. Am. Chem. Soc.* **127**, 10126–10127 (2005).

75. Lystrom, L., Roberts, A., Dandu, N. & Kilina, S. Surface-Induced Deprotonation of Thiol Ligands Impacts the Optical Response of CdS Quantum Dots. *Chem. Mater.* **33**, 892–901 (2021).

76. Olshansky, J. H., Ding, T. X., Lee, Y. V., Leone, S. R. & Alivisatos, A. P. Hole Transfer from Photoexcited Quantum Dots: The Relationship between Driving Force and Rate. *J. Am. Chem. Soc.* **137**, 15567–15575 (2015).

77. Credi, A. Quantum dot–molecule hybrids: a paradigm for light-responsive nanodevices. *New J. Chem.* **36**, 1925–1930 (2012).

78. Dorokhin, D., Tomczak, N., Velders, A. H., Reinhoudt, D. N. & Vancso, G. J. Photoluminescence quenching of CdSe/ZnS quantum dots by molecular ferrocene and ferrocenyl thiol ligands. *J. Phys. Chem. C* **113**, 18676–18680 (2009).

79. Zhou, Q. *et al.* Polymer-capped CdSe/ZnS quantum dots for the sensitive detection of Cu2+and Hg2+and the quenching mechanism. *Anal. Methods* **13**, 2305–2312 (2021).

80. Jiang, B. P. *et al.* White-emitting carbon dots with long alkyl-chain structure: Effective inhibition of aggregation caused quenching effect for label-free imaging of latent fingerprint. *Carbon N. Y.* **128**, 12–20 (2018).

81. García de Arquer, F. P. *et al.* Semiconductor quantum dots: Technological progress and future challenges. *Science* **373**, eaaz8541 (2021).

82. Gao, Z. W. *et al.* Tailoring the Interface in FAPbI3 Planar Perovskite Solar Cells by Imidazole-Graphene-Quantum-Dots. *Adv. Funct. Mater.* **31**, 1–7 (2021).

83. Cao, W. *et al.* Highly stable QLEDs with improved hole injection via quantum dot structure tailoring. *Nat. Commun.* **9**, 2–7 (2018).

84. Lee, T. *et al.* Bright and Stable Quantum Dot Light-Emitting Diodes. *Adv. Mater.* **34**, 1–9 (2022).

85. Wei, C. *et al.* A Universal Ternary-Solvent-Ink Strategy toward Efficient Inkjet-Printed Perovskite Quantum Dot Light-Emitting Diodes. *Adv. Mater.* **34**, 1–12 (2022).

86. Zhan, S. *et al.* Inkjet-printed multi-color arrays based on eco-friendly quantum dot light emitting diodes with tailored hole transport layer. *J. Soc. Inf. Disp.* **30**, 748–757 (2022).

ARTICLE I

Efficient Routes for the Preparation of Urazole Radical Self-Assembled Monolayers on Gold Surfaces

AUTHORS: Ángel Campos-Lendinez, † Núria Crivillers,* Stefan T. Bromley, Concepció Rovira, Gary W. Breton,* and Marta Mas-Torrent*

PUBLICATION: The Journal of Physical Chemistry C, 2022, 126, 31, 13358–13365

THE JOURNAL OF PHYSICAL CHEMISTRY C
A JOURNAL OF THE AMERICAN CHEMICAL SOCIETY

pubs.acs.org/JPCC

Article

Efficient Routes for the Preparation of Urazole Radical Self-Assembled Monolayers on Gold Surfaces

Ángel Campos-Lendinez, Núria Crivillers,* Stefan T. Bromley, Concepció Rovira, Gary W. Breton,* and Marta Mas-Torrent*

Cite This: J. Phys. Chem. C 2022, 126, 13358−13365

Read Online

ACCESS | Metrics & More | Article Recommendations | Supporting Information

ABSTRACT: The functionalization of substrates with radical species has been shown to be a promising strategy to confer novel physical and chemical properties to a surface. Urazole radicals are persistent nitrogen-centered radicals that are insensitive to oxygen, making them desirable targets for the functionalization of surfaces. Here, we succeed in the preparation of self-assembled monolayers (SAMs) of a 1-arylurazole radical on Au surfaces using two different approaches. In the first approach, a SAM of a radical precursor on the gold surface is prepared followed by its chemical oxidation to generate the active urazole radical. In the second route, the radical is generated in solution and subsequently grafted on the Au surface. In both cases, the SAMs exhibit active radical behavior, but the SAM prepared by the first approach demonstrates greater surface coverage of the electroactive urazole radical species.

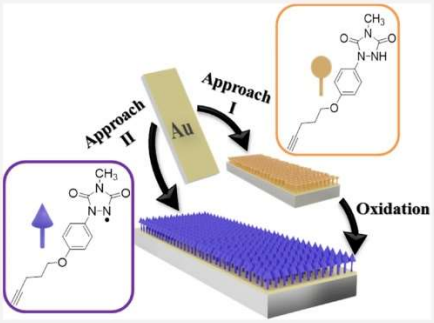

INTRODUCTION

The functionalization of substrates with organic molecules has proven to be a promising strategy to confer novel physical and chemical properties to surfaces. This route has been successfully exploited for the fabrication of chemical sensors,[1−3] for immobilizing biomolecules,[4−6] and for tuning surface wettability[7,8] or metal work function,[9] among other applications. In particular, surface modification with stable neutral organic radicals with one or more unpaired electrons has recently attracted great attention in the fields of molecular electronics and spintronics.[9−12]

Stable neutral organic radicals have been physisorbed on surface showing the Kondo effect.[13−15] However, to better stabilize such systems for potential applications, the preparation of self-assembled monolayers (SAMs) chemically bonded to the surface is often preferred.[16,17] This has been mainly realized by designing and synthesizing neutral organic radicals bearing appropriate surface anchors, for example, thiol or silane groups to graft the molecules onto Au or oxide substrates, respectively. In this way, SAMs of polychlorinated trityl radicals,[16,18] nitroxyls,[19,20] and α-nitronyl nitroxyls[21,22] have been widely investigated. Importantly, all of these radicals need to be highly stable to survive the reaction conditions required to prepare the SAMs and, further, the radical character needs to be preserved after the surface self-assembly process. To date, very few examples have been reported regarding the preparation of SAMs using precursors to radical species that are subsequently converted to their corresponding neutral radical analogues by performing surface chemical reactions[23] or by interaction with a metallic surface.[24]

Urazole radicals, **2**, which are readily accessible by oxidation of urazole precursors **1**, were first reported by Pirkle as early as 1978 (Scheme 1).[25] Many of these nitrogen-centered radicals are indefinitely persistent in solution.[25] While they are known to be in equilibrium with the corresponding N−N dimers **3** (Scheme 1), significant concentrations of the radical species remain present in the solution.[25−27] The unusual stability of these radicals, coupled with their lack of sensitivity to oxygen, make them desirable targets for the functionalization of surfaces. 1-Arylurazoles radicals are easily synthesized by established means and, therefore, in this paper have been selected as initial targets for studying the feasibility of SAM preparation.[25,26] Although 1-arylurazoles radicals such as **2b** are persistent in solution for many hours like other urazole radicals, they eventually succumb to a self-reaction to form urazole **4**.[25,26] Therefore, suitable methodologies have to be applied to successfully achieve radical urazole SAMs.

In this work, we report the preparation and characterization of urazole radical SAMs employing two different approaches. The first route is based on prior preparation of a SAM using the precursor to the radical species, followed by oxidization to the corresponding radical form. In the second approach, the radical is first generated in solution and then self-assembled on

Received: April 10, 2022
Revised: July 14, 2022
Published: July 27, 2022

https://doi.org/10.1021/acs.jpcc.2c02453
J. Phys. Chem. C 2022, 126, 13358−13365

Scheme 1. Formation of Urazole Radicals 2 from Urazole Precursors 1[a,b]

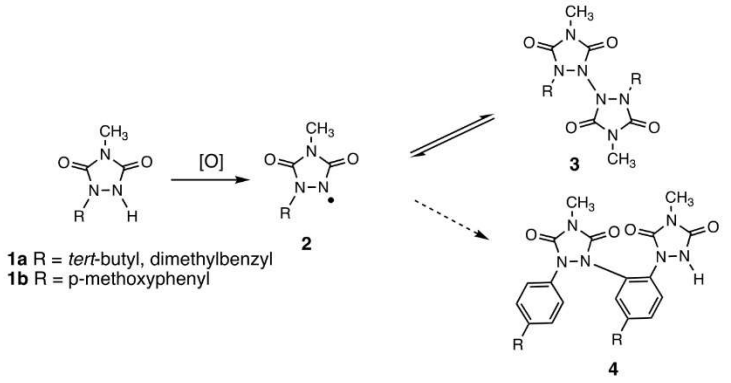

[a]The radicals are in equilibrium with N−N dimers **3** in solution. [b]Urazole radical **2b** undergoes a slow self-reaction to form **4**.

the surface. Both approaches successfully lead to urazole radical SAMs, as demonstrated by means of electrochemical and electron paramagnetic resonance (EPR) detection.

EXPERIMENTAL SECTION

General Methods for the Synthesis. Column chromatography was conducted on a silica gel (234−400 mesh). Thin-layer chromatography was performed on precoated silica gel plates and visualized by ultraviolet light. ^{1}H and ^{13}C NMR spectra were obtained on a 400 MHz NMR spectrometer. Chemical shifts are reported in units of parts per million downfield from TMS. High-resolution mass spectra (HRMS) were acquired via electron spray ionization on a Linear ion trap-Fourier transform hybrid mass spectrometer (LTQ-FTMS). *N*-methyl-1,3,5-triazoline-3,5-dione (**2**) was synthesized via oxidation of *N*-methylurazole with DABCO-Br_2 as described in the literature.[28,29] All other chemicals and solvents were obtained from commercial sources and used without further purification unless otherwise noted.

*(Pent-4-yn-1-yloxy)benzene (**5**).* To a solution of 1 g (10.6 mmol) of phenol in 25 mL of dry DMF, 1.19 g (1 equiv) of potassium *tert*-butoxide was added as a solid, at once, and stirred for 0.5 h. To the resulting pale green solution, 1.0 g (1 equiv) of 5-chloro-1-pentyne was added dropwise, and the reaction mixture was stirred overnight. The resulting pale brown mixture was poured into 50 mL of EtOAc, and the combined organic layer was washed with 2 × 50 mL of H_2O and 2 × 20 mL of sat. aq. NaCl, dried over Na_2SO_4, and concentrated. Column chromatography (SiO_2, 6:1 hexanes/EtOAc) afforded 1.12 g (60% yield) of **5** as a clear colorless liquid: ^{1}H NMR ($CDCl_3$) δ 7.26 (dt, J = 7.3, 8.5 Hz, 2H), 6.92 (t, J = 7.3 Hz, 1H), 6.89 (d, J = 8.5 Hz, 2H), 4.03 (t, J = 6.2 Hz, 2H), 2.38 (dt, J = 2.7, 6.9 Hz, 2H), 1.95−2.04 (m, 3H); ^{13}C NMR ($CDCl_3$) δ 158.9, 129.5, 120.8, 114.5, 83.6, 69.0, 66.0, 28.3, 15.3. HRMS [ESI] m/z [M + H]+ Calcd for $C_{11}H_{13}O$: 161.09609; Found 161.09616.

*4-Methyl-1-[4-(pent-4-yn-1-yloxy)phenyl]-1,2,4-triazolidine-3,5-dione (**6**).* To a stirring solution of 0.92 g (5.75 mmol) of compound **5** (neat) and 0.113 g (1 mmol) of MeTAD, 155 μL (2 mmol) of CF_3CO_2H was added via syringe. The solution initially turned deep red-purple in color, but then a thick white precipitate was formed. The precipitate was suspended in 10 mL of CH_2Cl_2 in a separatory funnel, and 2 mL of 1 M NaOH was added, which dissolved the precipitate. The aqueous layer was washed with 1 × 2 mL of CH_2Cl_2 and then acidified with conc. aq. HCl, forming a thick white precipitate. Washing with 3 × 50 mL of CH_2Cl_2, drying over Na_2SO_4, and concentration afforded 0.134 g (49% yield) of **6** as a white solid: ^{1}H NMR (DMSO-d_6) δ 11.05 (s, 1H, NH), 7.43 (d, J = 9.1 Hz, 2H), 7.01 (d, J = 9.1 Hz, 2H), 4.03 (t, J = 6.9 Hz, 2H), 2.96 (s, 3H), 2.83 (t, J = 2.6 Hz, 1H), 2.32 (dt, J = 2.6, 6.9 Hz, 2H), 1.88 (p, J = 6.9 Hz, 2H); ^{13}C NMR ($CDCl_3$) δ 156.4, 154.2, 151.6, 130.5, 121.3, 115.4, 84.2, 72.2, 66.7, 28.2, 25.4, 15.0. HRMS [ESI] m/z [M + H]+ Calcd for $C_{14}H_{16}N_3O_3$: 274.11862; Found 274.11824.

*Generation of a Urazole Radical (**7**).* To a stirring mixture of 3.35 mg of **6**, 13.65 mg of sodium sulfate (Na_2SO_4, 99.5%, Sigma) and 6.82 mg of nickel peroxide (Ni_2O_3 99%, Sigma) in 10 mL of acetonitrile was added. The solution, kept in inert conditions, turned blue after a few minutes. The mixture was stirred for 30 min and then filtered, resulting in a deep purple solution of radical 7.

SAMs' Preparation and Characterization. SAMs were prepared on Au substrates (50 nm thick) evaporated on glass, purchased from Phasis Sàrl.

Approach I. The gold surface was cleaned in a piranha bath 1:1 (H_2SO_4/H_2O_2) for a minute and subsequently rinsed with plenty of Milli-Q water and ethanol, and dried with a N_2 stream. Afterward, the substrate was immersed in a 10^{-4} M solution of **6** in dry acetonitrile and was left for 48 h under stirring and inert conditions. Then, the substrates were rinsed with acetonitrile and ethanol to remove the physisorbed molecules, and dried with N_2, giving SAM **S6**. The resulting substrate was immersed in a previously prepared oxidant dispersion (6.82 mg of NiO_2 and 13.65 mg of Na_2SO_4 in 10 mL of acetonitrile heated at 50 °C for 30 min. in an ultrasound bath and in inert conditions) while stirring at low rpm. for 45 min. Afterward, the substrate was rinsed with plenty of acetonitrile, and ethanol and dried with a N_2 stream, affording SAM **S7-I**.

Approach II. The Au surface was cleaned as in approach I. Subsequently, the substrate was directly immersed into a 10^{-4} M solution of **7** in acetonitrile. After 2 h, the substrate was removed and rinsed with acetonitrile and ethanol, and dried with N_2. This process led to the formation of **S7-II**.

Cyclic voltammetry (CV) was carried out using an Autolab PGSTAT101 with NOVA Advanced Electrochemical Software. For the electrochemical experiments, a solution of 0.1 M of

https://doi.org/10.1021/acs.jpcc.2c02453
J. Phys. Chem. C 2022, 126, 13358−13365

Scheme 2. Synthesis of Urazole Precursor 6

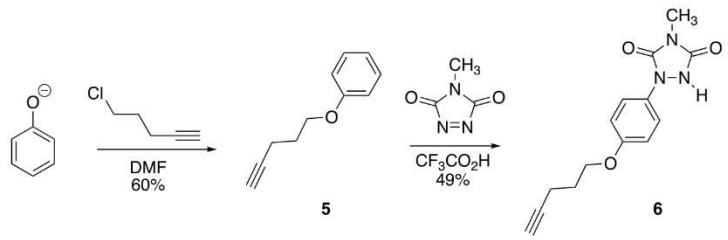

Scheme 3. Generation of Urazole Radical 7 and the Decomposition Pathway toward Dimer 8

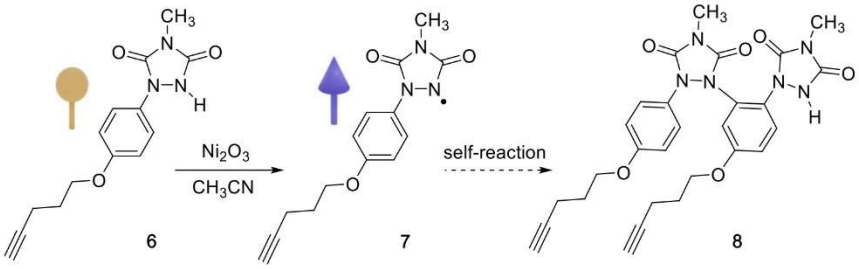

tetrabutylammonium hexafluorophosphate ($TBAPF_6$, 98%, Sigma) in dried acetonitrile was used as an electrolyte. The experiments were performed under inert conditions. For the characterization of the SAMs using a redox probe, we used a solution of 0.1 M KCl in Milli-Q water as electrolyte, containing 0.01 M of $[Fe(CN)_6]^{3-/4-}$ as redox marker. The bare Au or the functionalized surfaces were used as working electrodes. Finally, for characterizing the redox activity of **S7** SAMs, the functionalized substrates were used as a working electrode and Pt wires as counter and reference electrodes. The SAMs' coverage (Γ) was then calculated as follows[30]

$$\Gamma = \frac{Q}{n \cdot F \cdot A}$$

$$Q = \frac{A_{uc}}{SR}$$

where Q is the charge transferred, n is the number of electrons transferred, F is the Faraday constant, and A is the electrode area immersed in the solution. The charge transferred Q is obtained by the quotient of the area under the curve (A_{uc}) in the redox process through integration and the scan rate (SR).

Ultraviolet−visible (UV−vis) measurements were performed using a JASCO V-780 Spectrophotometer recorded at a 400 nm/s scan speed. Solutions with a concentration of 10^{-4} M of the urazole derivatives in acetonitrile were prepared.

Electron paramagnetic resonance spectroscopy (EPR) spectra were obtained using an X-Band (9.7 GHz) Bruker ELEXSYS E500 spectrometer equipped with a Bruker variable temperature unit, an ST8911 microwave cavity, a field frequency lock system Bruker ER 033 M, and a NMR Gaussmeter Bruker ER 035 M. The solutions containing 10^{-4} M urazole derivatives in acetonitrile were previously degassed with argon and measured in thin quartz tubes. SAM samples were measured in a Suprasil tissue cell.

Contact angle characterization was performed using a DSA100 System (KRÜSS) by automatically dispensing 3 μL of Milli-Q water drops. The measurements were carried out in triplicate.

X-ray photoelectron spectroscopy (XPS) measurements were performed at room temperature with a SPECS PHOIBOS 150 hemispherical analyzer (SPECS GmbH, Berlin, Germany) with a base pressure of 5×10^{-10} mbar using monochromatic Al Kα radiation (1486.74 eV) as an excitation source operated at 300 W. The energy resolution as measured by the full width at half maximum (FWHM) of the Ag $3d_{5/2}$ peak for a sputtered silver foil was 0.62 eV.

■ RESULTS AND DISCUSSION

Urazole radical precursor **6** (Scheme 2) was designed to include aryl-substitution similar to the previously investigated urazole **1b** but with the addition of a short alkoxy chain and a terminal alkyne group. The former provides some flexibility to the system, whereas the alkyne group has been previously shown to be a suitable Au surface anchor group that leads to a robust Au−C covalent bond.[31,32] Urazole **6** was synthesized according to Scheme 2. The reaction of 5-chloro-1-butyne with potassium phenoxide in dry DMF afforded aryl ether **5** in a 60% yield. The neat reaction of **5** with *N*-methyl-1,2,4-triazoline-3,5-dione (MeTAD) in the presence of trifluoroacetic acid as a catalyst, according to the procedure previously described for the reaction of MeTAD with anisole,[33] afforded the desired 1-substituted urazole **6** in a 49% yield (Figures S1−S4).

The formation of the radical derived from **6** was studied in solution following the previously reported methodology (Scheme 3).[26] Oxidation of **6** with the commercially available heterogeneous oxidant Ni_2O_3 in CH_3CN or $CDCl_3$ followed by filtration afforded a deep blue solution of radical **7**. The paramagnetic nature of the radical prevented direct observation of **7** by ^{1}H NMR spectroscopy, but over the course of several hours the signals for a new compound, dimer **8** began to appear (see Scheme 3). Complete consumption of **7** over several days, with a concomitant loss of the characteristic deep blue color, led primarily to the formation of **8**, which could be isolated in a 32% yield (Figures S5 and S6). Furthermore, attempts at isolating radical **7** via the concentration of

https://doi.org/10.1021/acs.jpcc.2c02453
J. Phys. Chem. C 2022, 126, 13358−13365

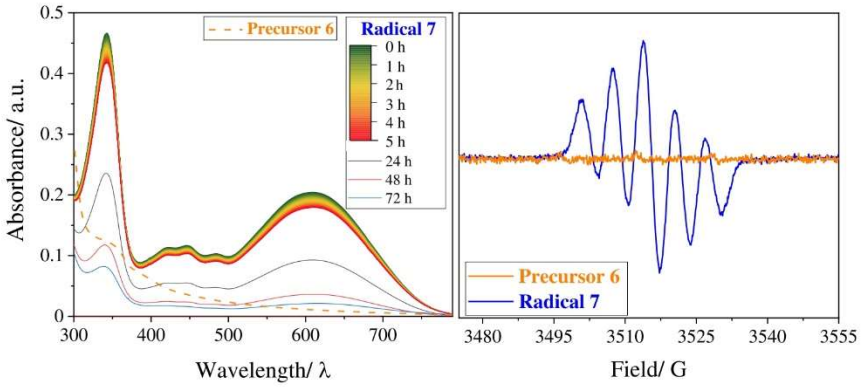

Figure 1. Left. UV−vis spectra of **6** and **7** in acetonitrile. The spectrum of **7** was registered over time ($c = 10^{-4}$ M). Right. EPR spectra of **6** and **7** in acetonitrile ($c = 10^{-4}$ M).

solutions promoted the formation of **8** (see Supporting Information).

The UV−vis spectrum of a freshly prepared solution of **7** in CH_3CN showed the characteristic absorption bands of this family of radicals (Figure 1, left).[25−27] Intense absorption bands at 343 and 609 nm are observed, accompanied by less intense bands centered at 420, 445, and 485 nm. The stability of the radical was assessed by following the UV−vis spectrum with time. The radical was found to be stable in solution for more than 5 h, observing only a small decrease in the absorption bands' intensity. However, in line with what had been observed via ^{1}H NMR spectroscopy, after 24 h, a significant drop in the absorption bands indicated the depletion of the radical due to the self-reaction of **7** to afford dimer **8** (Scheme 3).

The radical formation was also investigated by EPR spectroscopy in solution. As expected, precursor **6** was EPR silent due to its diamagnetic character (Figure 1, right). In contrast, radical **7** exhibited a five-line spectrum centered at g = 2.0034, close to the value of the free electron. The hyperfine splitting comes from the interaction of the radical with two equivalent ^{14}N nuclei, with coupling constant and bandwidth of a = 6.5 G and ΔH_{pp} = 3.1 G, respectively.[34]

CV characterization was performed employing a three-electrode electrochemical cell and using platinum wires as working and counter electrodes, and a Ag/AgCl reference electrode (Figure 2). In the case of radical **7**, a redox peak at $E^{1/2}$ = 227 mV, ascribed to the reduction of the radical to the anion form, was clearly observed (Scheme 4). At higher voltages, the CV exhibited an oxidation peak at $E^{1/2}$ = 1148 mV attributed to the oxidation of the radical to the diazonium species (Scheme 4).[26] In contrast, the CV of the radical precursor **6** only showed the oxidation peak to the diazonium form at $E^{1/2}$ = 1143 mV. These behaviors were consistent with what had been previously reported for urazole radical **2b**.[26]

Once we confirmed the successful formation of radical **7** and confirmed its stability over a time period of several hours in solution, we proceeded to the preparation of self-assembled monolayers of **7** on Au. With this aim, we followed two distinct routes (Figure 3). Approach I was focused on the formation of a SAM of urazole precursor **6** on the gold surface over 48 h. Following this, the SAM was then oxidized to generate radical **7** (**S7-I**) directly on the surface. Alternatively, in approach II, the radical was first separately generated in solution, and then the Au substrate was immersed in the radical solution for 2 h

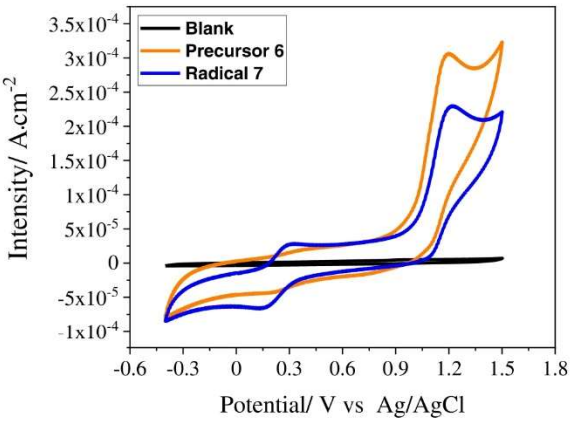

Figure 2. Cyclic voltammograms of **6** and **7** (10^{-4} M) in acetonitrile containing tetrabutylammonium hexafluorophosphate ($TBAPF_6$) 0.1 M. The Ag/AgCl electrode was used as reference and platinum wires as working and counter electrodes. Scan rate: 0.1 V s^{-1}. A blank acquired using a Pt wire is also included.

Scheme 4. Electrochemical Oxidation and Reduction Events of Urazole Radical 7 As Observed by Cyclic Voltammetry

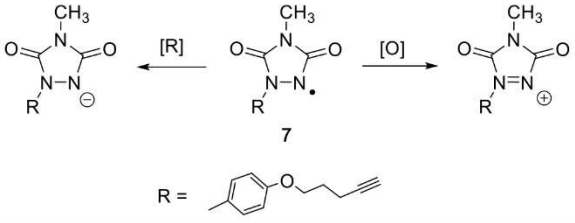

to form the corresponding radical SAM (**S7-II**). In both cases, the SAM formation processes were adjusted to find optimum conditions.

The SAMs from both approaches were fully characterized by X-ray photoelectron spectroscopy (XPS), water contact angle, EPR, and CV. C 1s and N 1s XPS data confirmed the presence of molecules **6** and **7** on the gold surface (Figure S7). By water contact angle, we observed a decrease in the angle from the bare gold substrate (84.8° ± 1.8°) to the functionalized substrates, giving a value of 52.4° ± 2.0° for **S6** and 49.7° ±

https://doi.org/10.1021/acs.jpcc.2c02453
J. Phys. Chem. C 2022, 126, 13358−13365

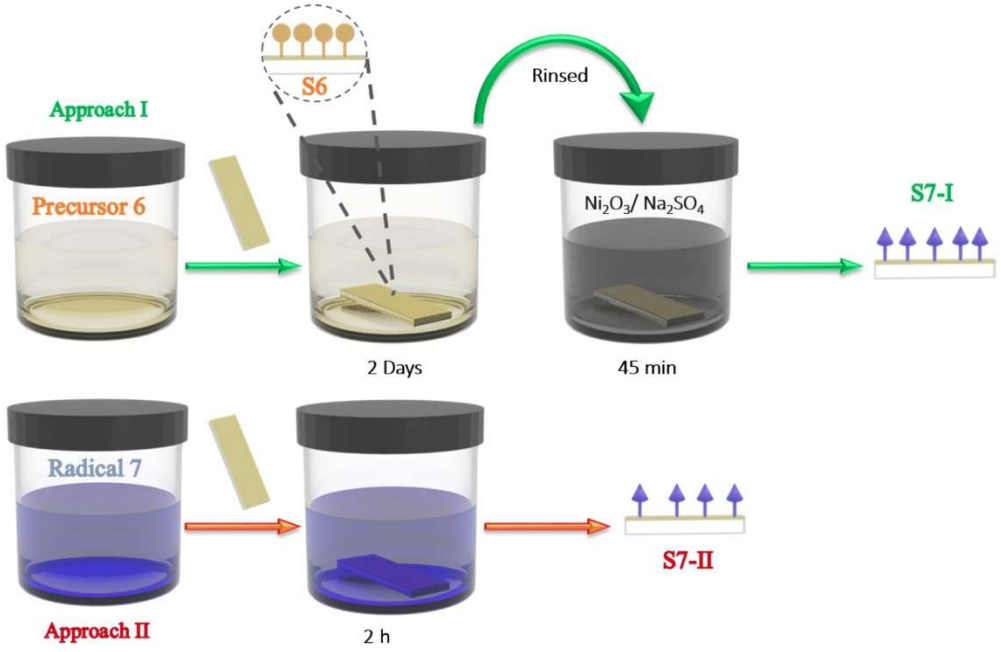

Figure 3. Schematic representation of the approaches used to prepare SAMs of radical 7.

1.2° for **S7** (Figure S8). This behavior is consistent with the hydrophilic character of the surface-bound molecules.

EPR characterization was also carried out since it is a powerful tool for the identification of radicals on surfaces.[35] Figure 4 shows the spectra collected for the SAMs of 7 prepared according to the two approaches together with the EPR of the same molecule in solution. The SAMs show a weak but distinguishable line with a *g*-factor value (g = 2.0075) similar to that of the unbound radical in solution (g = 2.0034). Due to the low intensity of the signals and also their larger linewidth typical of solid-state measurements, the hyperfine couplings were not clearly observed. Nonetheless, this data proves unambiguously the presence of an unpaired spin on the functionalized gold surfaces.

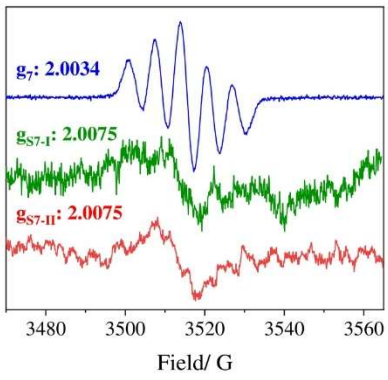

Figure 4. EPR spectra of 7 (blue) in solution and SAMs **S7-I** (green) and **S7-II** (red).

CV was also used to verify the SAM formation. First, electrochemical experiments were carried out in a three-electrode configuration cell, using a Pt wire and an Ag/AgCl electrode as counter and reference electrodes, respectively. As working electrodes, a bare Au electrode and the functionalized substrates (**S7-I, II**) were employed. The electrolyte consisted of a 0.1 M KCl aqueous solution containing 10 mM $[Fe(CN)_6]^{3-/4-}$ as benchmark redox marker. As observed in Figure 5a, a decrease in the redox peak current intensity accompanied by a larger peak-to-peak separation (ΔE) is observed when the Au substrates covered with the SAMs are used instead of the bare Au electrode. This is rationalized by the passivation of the electrode with the surface-bound molecules that hinder the electron transfer process from the redox probe in solution to the electrode. It is noted that the $[Fe(CN)_6]^{3-/4-}$ redox peak is more inhibited with the **S7-I** substrate, which suggests that approach I leads to greater surface coverage.

CV experiments were also carried out with the aim of detecting the redox activity of the radical SAM. In this case, we registered the electrochemical response of the **S7** SAMs. We used a 10^{-4} M $TBAPF_6$ solution in acetonitrile as an electrolyte, a Pt wire as a pseudo-reference electrode, and **S7-I, II** as working electrodes. For both approaches, a reversible redox peak attributed to the reduction of the radical to the anion (see Scheme 4) was detected at $E^{1/2}$ = 21 mV and $E^{1/2}$ = −40 mV, for **S7-I, II**, respectively (Figure 5b). Notice that the oxidation redox process to the diazonium species (see Scheme 4) could not be investigated since the SAMs are not stable under the application of very high voltage values.[36] The intensity of the redox peaks linearly increased with the scan rate (Figure S9), which is characteristic of surface-confined species.[23] The differences in shape and redox potential values between the two substrates may be attributed to the distinct molecular organizations resulting from the two different methods of SAM preparation.[37] It has been reported that changes in the local intermolecular and electrostatic interactions induced by the supramolecular organization and

https://doi.org/10.1021/acs.jpcc.2c02453
J. Phys. Chem. C 2022, 126, 13358−13365

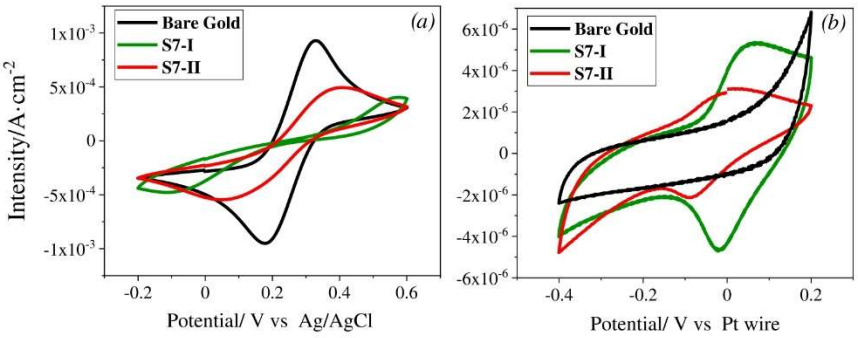

Figure 5. Electrochemical characterization of **S7-I** (green) and **S7-II** (red). (a) Redox probe experiment carried out using a solution of 0.1 M KCl as an electrolyte in Milli-Q water with 0.01 M $[Fe(CN)_6]^{3-/4-}$ as a redox marker. The bare Au or the functionalized surfaces were used as working electrodes, a Pt wire as a counter electrode, and a Ag/AgCl electrode as a reference. (b) CV measurements performed by immersion of the modified electrodes in acetonitrile containing 10^{-4} M $TBAPF_6$ and using Pt wires as counter and pseudo-reference. Scan rate: 0.1 V s^{-1}.

distribution of the redox active species within the layer may lead to different electrochemical voltammograms (e.g., peak shifting, peak splitting, or peak broadening).[37−39] By integration of the redox peaks (see the Experimental Section), surface coverages of 5.0×10^{-10} and 1.2×10^{-11} mol cm^{-2} were estimated for **S7-I** and **S7-II**, respectively. The greater surface coverage measured for **S7-I** agrees with the results using the redox marker as discussed earlier. While the lower surface coverage of **S7-II** might at first glance be rationalized by the shorter time period allowed for SAM formation in approach II than that provided in approach I, it was observed that longer incubation times did not increase the radical density on the surface, as determined by CV. Likely, the self-reaction of radical **7** in solution during SAM formation (see Scheme 2) resulted in competing grafting of dimer **8** onto the surface. Such dimerized molecules would not be electroactive in this region and, hence, are not considered in the estimation of the surface coverage.

Finally, density functional theory calculations were performed to understand the configuration of the molecules adsorbed on the surface (see Supporting Information for computational details). It was found that the molecules tend to be vertical with respect to the surface and, as a first approximation, the maximum molecular density calculated (approx. 7×10^{-10} mol cm^{-2}) was found to be slightly higher than the value estimated in approach I by CV (Figure S10).

■ CONCLUSIONS

In summary, we have demonstrated that SAMs of 1-arylurazole radicals can be successfully prepared by two different approaches despite their limited lifetimes in solution and inability to isolate them in the solid state. The SAM with greater urazole radical surface coverage and, thus, electrochemical activity was achieved by first grafting the urazole precursor to the gold surface prior to oxidation of the precursor to the active radical species. In both instances, however, analysis by both EPR and CV clearly demonstrates radical behavior similar to that exhibited by the urazole radical in solution. In this investigation, therefore, we have successfully developed and optimized the conditions for future studies of other urazole radical SAMs. Of particular interest would be the investigation of urazole radicals known to be longer-lived in solution.[25]

■ ASSOCIATED CONTENT

Supporting Information

The Supporting Information is available free of charge at https://pubs.acs.org/doi/10.1021/acs.jpcc.2c02453.

^{1}H and ^{13}C NMR spectra of **5**, **6**, and **8**, XPS and contact angle of **S6** and **S7**, and CV measurements at different scan rates of **S7-I**, **II** (PDF)

■ AUTHOR INFORMATION

Corresponding Authors

Núria Crivillers − *Institut de Ciència de Materials de Barcelona, ICMAB-CSIC, 08193 Bellaterra, Spain;* orcid.org/0000-0001-6538-2482; Email: ncrivillers@icmab.es

Gary W. Breton − *Department of Chemistry and Biochemistry, Berry College, Mount Berry, Georgia 30149, United States;* orcid.org/0000-0001-5760-7071; Email: gbreton@berry.edu

Marta Mas-Torrent − *Institut de Ciència de Materials de Barcelona, ICMAB-CSIC, 08193 Bellaterra, Spain;* orcid.org/0000-0002-1586-005X; Email: mmas@icmab.es

Authors

Àngel Campos-Lendinez − *Institut de Ciència de Materials de Barcelona, ICMAB-CSIC, 08193 Bellaterra, Spain*

Stefan T. Bromley − *Departament de Ciència de Materials i Física Química & Institut de Química Teòrica i Computacional (IQTCUB), Universitat de Barcelona, E-08028 Barcelona, Spain; Institució Catalana de Recerca i Estudis Avançats (ICREA), E-08010 Barcelona, Spain;* orcid.org/0000-0002-7037-0475

Concepció Rovira − *Institut de Ciència de Materials de Barcelona, ICMAB-CSIC, 08193 Bellaterra, Spain;* orcid.org/0000-0002-2365-9479

Complete contact information is available at: https://pubs.acs.org/10.1021/acs.jpcc.2c02453

Notes

The authors declare no competing financial interest.

■ ACKNOWLEDGMENTS

This work was funded by the Spanish Ministry with the project GENESIS PID2019-111682RB-I00 and through the "Severo

Ochoa" Programme for Centers of Excellence in R&D (FUNFUTURE CEX2019-000917-S) and the Generalitat de Catalunya (2017-SGR-918). Á.C.-L. is enrolled in the UAB Materials Science PhD program. G.B. thanks Berry College for generous financial support. S.T.B. acknowledges financial support from the Spanish Ministerio de Ciencia, Innnovación y Universidades (RTI2018-095460-B-100, and MDM-2017-0767 via the Spanish Structures of Excellence María de Maeztu program), the Generalitat de Catalunya (2017SGR13), and the Red Espanola de Supercomputación (RES) for the provision of supercomputing time.

■ REFERENCES

(1) De Ruiter, G.; Gupta, T.; Van Der Boom, M. E. Selective Optical Recognition and Quantification of Parts per Million Levels of Cr6+ in Aqueous and Organic Media by Immobilized Polypyridyl Complexes on Glass. *J. Am. Chem. Soc.* **2008**, *130*, 2744−2745.

(2) Basabe-Desmonts, L.; Beld, J.; Zimmerman, R. S.; Hernando, J.; Mela, P.; García Parajó, M. F.; Van Hulst, N. F.; Van Den Berg, A.; Reinhoudt, D. N.; Crego-Calama, M. A Simple Approach to Sensor Discovery and Fabrication on Self-Assembled Monolayers on Glass. *J. Am. Chem. Soc.* **2004**, *126*, 7293−7299.

(3) Muñoz, J.; Campos-Lendinez, Á.; Crivillers, N.; Mas-Torrent, M. Selective Discrimination of Toxic Polycyclic Aromatic Hydrocarbons in Water by Targeting π-Stacking Interactions. *ACS Appl. Mater. Interfaces* **2020**, *12*, 26688−26693.

(4) Ricci, S.; Casalini, S.; Parkula, V.; Selvaraj, M.; Saygin, G. D.; Greco, P.; Biscarini, F.; Mas-Torrent, M. Label-Free Immunodetection of α-Synuclein by Using a Microfluidics Coplanar Electrolyte-Gated Organic Field-Effect Transistor. *Biosens. Bioelectron.* **2020**, *167*, No. 112433.

(5) Mendes, P. M. Stimuli-Responsive Surfaces for Bio-Applications. *Chem. Soc. Rev.* **2008**, *37*, 2512−2529.

(6) Artzy-Schnirman, A.; Brod, E.; Epel, M.; Dines, M.; Hammer, T.; Benhar, I.; Reiter, Y.; Sivan, U. A Two-State Electronic Antigen and an Antibody Selected to Discriminate between These States. *Nano Lett.* **2008**, *8*, 3398−3403.

(7) Simão, C.; Mas-Torrent, M.; Veciana, J.; Rovira, C. Multichannel Molecular Switch with a Surface-Confined Electroactive Radical Exhibiting Tunable Wetting Properties. *Nano Lett.* **2011**, *11*, 4382−4385.

(8) Colorado, R.; Lee, T. R. Wettabilities of Self-Assembled Monolayers on Gold Generated from Progressively Fluorinated Alkanethiols. *Langmuir* **2003**, *19*, 3288−3296.

(9) Heimel, G.; Romaner, L.; Zojer, E.; Bredas, J. L. The Interface Energetics of Self-Assembled Monolayers on Metals. *Acc. Chem. Res.* **2008**, *41*, 721−729.

(10) Herrmann, C.; Solomon, G. C.; Ratner, M. A. Organic Radicals As Spin Filters. *J. Am. Chem. Soc.* **2010**, *132*, 3682−3684.

(11) Mas-Torrent, M.; Crivillers, N.; Rovira, C.; Veciana, J. Attaching Persistent Organic Free Radicals to Surfaces: How and Why. *Chem. Rev.* **2012**, *112*, 2506−2527.

(12) Ratera, I.; Vidal-Gancedo, J.; Maspoch, D.; Bromley, S. T.; Crivillers, N.; Mas-Torrent, M. Perspectives for Polychlorinated Trityl Radicals. *J. Mater. Chem. C* **2021**, *9*, 10610−10623.

(13) Zhang, Y. H.; Kahle, S.; Herden, T.; Stroh, C.; Mayor, M.; Schlickum, U.; Ternes, M.; Wahl, P.; Kern, K. Temperature and Magnetic Field Dependence of a Kondo System in the Weak Coupling Regime. *Nat. Commun.* **2013**, *4*, No. 2110.

(14) Liu, J.; Isshiki, H.; Katoh, K.; Morita, T.; Breedlove, B. K.; Yamashita, M.; Komeda, T. First Observation of a Kondo Resonance for a Stable Neutral Pure Organic Radical, 1,3,5-Triphenyl-6-Oxoverdazyl, Adsorbed on the Au(111) Surface. *J. Am. Chem. Soc.* **2013**, *135*, 651−658.

(15) Müllegger, S.; Rashidi, M.; Fattinger, M.; Koch, R. Surface-Supported Hydrocarbon π Radicals Show Kondo Behavior. *J. Phys. Chem. C* **2013**, *117*, 5718−5721.

(16) Mas-Torrent, M.; Crivillers, N.; Mugnaini, V.; Ratera, I.; Rovira, C.; Veciana, J. Organic Radicals on Surfaces: Towards Molecular Spintronics. *J. Mater. Chem.* **2009**, *19*, 1691−1695.

(17) Poggini, L.; Cucinotta, G.; Pradipto, A. M.; Scarrozza, M.; Barone, P.; Caneschi, A.; Graziosi, P.; Calbucci, M.; Cecchini, R.; Dediu, V. A.; et al. An Organic Spin Valve Embedding a Self-Assembled Monolayer of Organic Radicals. *Adv. Mater. Interfaces* **2016**, *3*, No. 1500855.

(18) Simão, C.; Mas-Torrent, M.; Crivillers, N.; Lloveras, V.; Artés, J. M.; Gorostiza, P.; Veciana, J.; Rovira, C. A Robust Molecular Platform for Non-Volatile Memory Devices with Optical and Magnetic Responses. *Nat. Chem.* **2011**, *3*, 359−364.

(19) Finklea, H. O.; Madhiri, N. Reorganization Energies of TEMPO{radical Dot}/TEMPO+ in Water. *J. Electroanal. Chem.* **2008**, *621*, 129−133.

(20) Alévêque, O.; Seladji, F.; Gautier, C.; Dias, M.; Breton, T.; Levillain, E. Nitroxyl Radical Self-Assembled Monolayers on Gold: Versatile Electroactive Centers in Aqueous and Organic Media. *ChemPhysChem* **2009**, *10*, 2401−2404.

(21) Matsushita, M. M.; Ozaki, N.; Sugawara, T.; Nakamura, F.; Hara, M. Formation of Self-Assembled Monolayer of Phenylthiol Carrying Nitronyl Nitroxide on Gold Surface. *Chem. Lett.* **2002**, *31*, 596−597.

(22) Mannini, M.; Sorace, L.; Gorini, L.; Piras, F. M.; Caneschi, A.; Magnani, A.; Menichetti, S.; Gatteschi, D. Self-Assembled Organic Radicals on Au(111) Surfaces: A Combined ToF-SIMS, STM, and ESR Study. *Langmuir* **2007**, *23*, 2389−2397.

(23) Crivillers, N.; Mas-Torrent, M.; Vidal-Gancedo, J.; Veciana, J.; Rovira, C. Self-Assembled Monolayers of Electroactive Polychlorotriphenylmethyl Radicals on Au(111). *J. Am. Chem. Soc.* **2008**, *130*, 5499−5506.

(24) Ajayakumar, M. R.; Moreno, C.; Alcón, I.; Illas, F.; Rovira, C.; Veciana, J.; Bromley, S. T.; Mugarza, A.; Mas-Torrent, M. Neutral Organic Radical Formation by Chemisorption on Metal Surfaces. *J. Phys. Chem. Lett.* **2020**, *11*, 3897−3904.

(25) Pirkle, W. H.; Gravel, P. L. Persistent Cyclic Diacylhydrazyl Radicals from Urazoles and Pyrazolidine-3,5-Diones. *J. Org. Chem.* **1978**, *43*, 808−815.

(26) Breton, G. W.; Suroviec, A. H. Intermediacy of a Persistent Urazole Radical and an Electrophilic Diazenium Species in the Acid-Catalyzed Reaction of MeTAD with Anisole. *J. Org. Chem.* **2016**, *81*, 206−214.

(27) Breton, G. W. Factors Affecting the Dimerization of Persistent Nitrogen - Centered 1 - Phenyl Urazole Radicals to Tetrazanes. *J. Phys. Org. Chem.* **2018**, *31*, No. e3808.

(28) Billiet, S.; De Bruycker, K.; Driessen, F.; Goossens, H.; Van Speybroeck, V.; Winne, J. M.; Du Prez, F. E. Triazolinediones Enable Ultrafast and Reversible Click Chemistry for the Design of Dynamic Polymer Systems. *Nat. Chem.* **2014**, *6*, 815−821.

(29) Breton, G. W.; Turlington, M. Alternative Synthetic Routes to N-Methyl-1,2,4-Triazoline-3,5-Dione (MeTAD) and Other Triazolinedione Derivatives. *Tetrahedron Lett.* **2014**, *55*, 4661−4663.

(30) Haag, A. L.; Toader, V.; Lennox, R. B.; Grutter, P. Selective in Situ Potential-Assisted SAM Formation on Multi Electrode Arrays. *Nanotechnology* **2016**, *27*, No. 455501.

(31) Li, Q.; Han, C.; Fuentes-Cabrera, M.; Terrones, H.; Sumpter, B. G.; Lu, W.; Bernholc, J.; Yi, J.; Gai, Z.; Baddorf, A. P.; et al. Electronic Control over Attachment and Self-Assembly of Alkyne Groups on Gold. *ACS Nano* **2012**, *6*, 9267−9275.

(32) De Sousa, J. A.; Bejarano, F.; Gutiérrez, D.; Leroux, Y. R.; Nowik-Boltyk, E. M.; Junghoefer, T.; Giangrisostomi, E.; Ovsyannikov, R.; Casu, M. B.; Veciana, J.; et al. Exploiting the Versatile Alkyne-Based Chemistry for Expanding the Applications of a Stable Triphenylmethyl Organic Radical on Surfaces. *Chem. Sci.* **2020**, *11*, 516−524.

(33) Breton, G. W. Acid-Catalyzed Reaction of 4-Methyl-1,2,4-Triazoline-3,5-Dione (MeTAD) with Substituted Benzenes. *Tetrahedron Lett.* **2011**, *52*, 733−735.

https://doi.org/10.1021/acs.jpcc.2c02453
J. Phys. Chem. C 2022, 126, 13358−13365

(34) Sahu, I. D.; Lorigan, G. A.; States, U. *EPR Techniques, Spin Labeling, and Spin Trapping*, 3rd ed.; Elsevier Ltd.: Amsterdam, The Netherlands, 2019.
(35) Crivillers, N.; Mas-Torrent, M.; Perruchas, S.; Roques, N.; Vidal-Gancedo, J.; Veciana, J.; Rovira, C.; Basabe-Desmonts, L.; Ravoo, B. J.; Crego-Calama, M.; Reinhoudt, D. N. Self-Assembled Monolayers of a Multifunctional Organic Radical. *Angew. Chem.* **2007**, *119*, 2265−2269.
(36) Casado-Montenegro, J.; Marchante, E.; Crivillers, N.; Rovira, C.; Mas-Torrent, M. Donor/Acceptor Mixed Self-Assembled Monolayers for Realising a Multi-Redox-State Surface. *ChemPhysChem* **2016**, *17*, 1810−1814.
(37) Alévêque, O.; Blanchard, P. Y.; Breton, T.; Dias, M.; Gautier, C.; Levillain, E.; Seladji, F. Nitroxyl Radical Self-Assembled Monolayers on Gold: Experimental Data vs. Laviron's Interaction Model. *Electrochem. Commun.* **2009**, *11*, 1776−1780.
(38) Duffin, T. J.; Nerngchamnong, N.; Thompson, D.; Nijhuis, C. A. Direct Measurement of the Local Field within Alkyl-Ferrocenyl-Alkanethiolate Monolayers: Importance of the Supramolecular and Electronic Structure on the Voltammetric Response and Potential Profile. *Electrochim. Acta* **2019**, *311*, 92−102.
(39) Guo, Y.; Zhao, J.; Zhu, J. Study on the Intermolecular Interactions between the Functional Moieties in Ferrocene-Terminated Alkanethiol Self-Assembled Monolayer on Gold. *Thin Solid Films* **2008**, *516*, 3051−3057.

https://doi.org/10.1021/acs.jpcc.2c02453
J. Phys. Chem. C 2022, 126, 13358−13365

Supporting Information

Efficient Routes for the Preparation of Urazole Radical Self-Assembled Monolayers on Gold Surfaces

Ángel Campos-Lendinez,[a] Núria Crivillers,[a,*] Stefan T. Bromley,[c] Concepció Rovira,[a] Gary W. Breton,[b,*] Marta Mas-Torrent [a,*]

[a]*Institut de Ciència de Materials de Barcelona, ICMAB-CSIC, Campus UAB, 08193 Bellaterra, Spain*

[b]*Department of Chemistry and Biochemistry, Berry College, Mount Berry, GA 30149, USA*

[c] *Departament de Ciència de Materials i Física Química & Institut de Química Teòrica i Computacional (IQTCUB), Universitat de Barcelona, E-08028 Barcelona, Spain: Institució Catalana de Recerca i Estudis Avançats (ICREA), E-08010 Barcelona, Spain.*

Table of contents

Synthesis of Dimer 8

Self-Reaction of Urazole Radical 7 to form Dimer 8. To a stirring mixture of 70 mg of compound 6 and 50 mg of sodium sulfate (Na_2SO_4, 99.5%, Sigma) in 5 mL $CDCl_3$ was added 175 mg of nickel peroxide (Ni_2O_3 99%, Sigma). The mixture was stirred for 30 minutes and then filtered through a fine glass frit under N_2 pressure. The resulting deep purple solution of radical 7 was periodically analyzed by ^1H NMR spectroscopy. Over the course of several days, the color significantly lightened. The solution was concentrated, and the residue chromatographed on SiO_2 using a 95/5 mixture of ethyl acetate and methanol to afford 23 mg (33% yield) of 8 as a pale brown thin film: ^1H NMR ($CDCl_3$) δ 8.55 (br s, 1H, NH), 7.34 (m, 3H), 6.91-6.87 (m, 3H), 6.73 (d, J = 2.3 Hz, 1H), 4.00 (t, J = 6.2 Hz, 2H), 3.96 (br t, J = 6.2 Hz, 2H), 3.21 (s, 3H), 3.20 (s, 3H), 2.39-2.29 (m, 4H), 1.99-1.87 (m, 6H); ^{13}C NMR ($CDCl_3$) δ 160.6, 157.9, 155.4, 153.8, 153.6, 152.6, 136.3, 131.5, 128.1, 125.4, 124.0, 115.9, 115.3, 109,7, 83.4, 83.0, 69.4, 69.1, 66.8, 66.4, 28.2, 27.7, 26.3, 25.6, 15.2, 15.1. HRMS [ESI] m/z [M+H]+ Calcd for $C_{28}H_{29}N_6O_6$: 545.21431; Found: 545.21418.

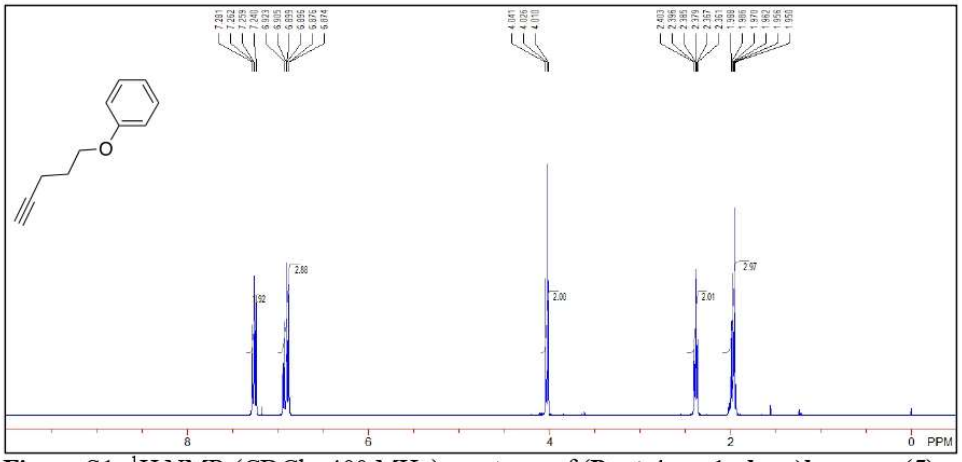

Figure S1: ^{1}H NMR ($CDCl_3$, 400 MHz) spectrum of (**Pent-4-yn-1-yloxy)benzene** (**5**).

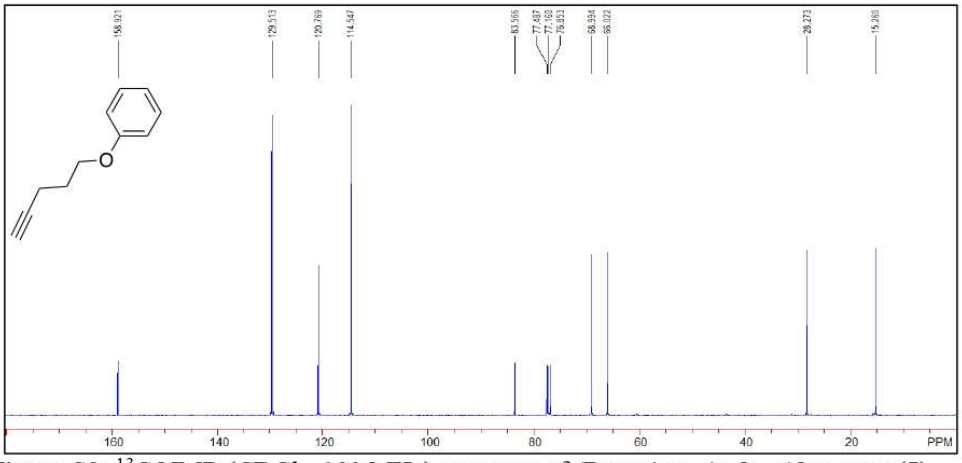

Figure S2: ^{13}C NMR ($CDCl_3$, 100 MHz) spectrum of **(Pent-4-yn-1-yloxy)benzene** (**5**).

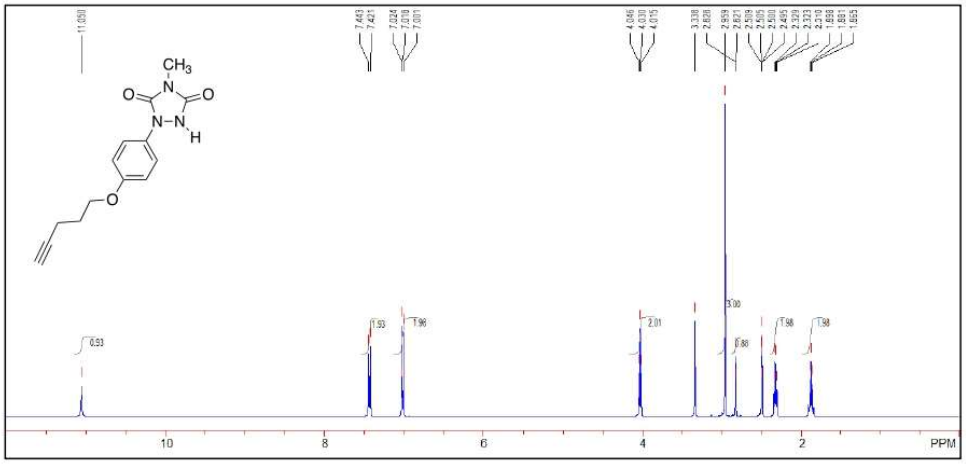

Figure S3: ^{1}H NMR (DMSO-d_6, 400 MHz) spectrum of **4-Methyl-1-[4-(pent-4-yn-1-yloxy)phenyl]-1,2,4-triazolidine-3,5-dione (6)**.

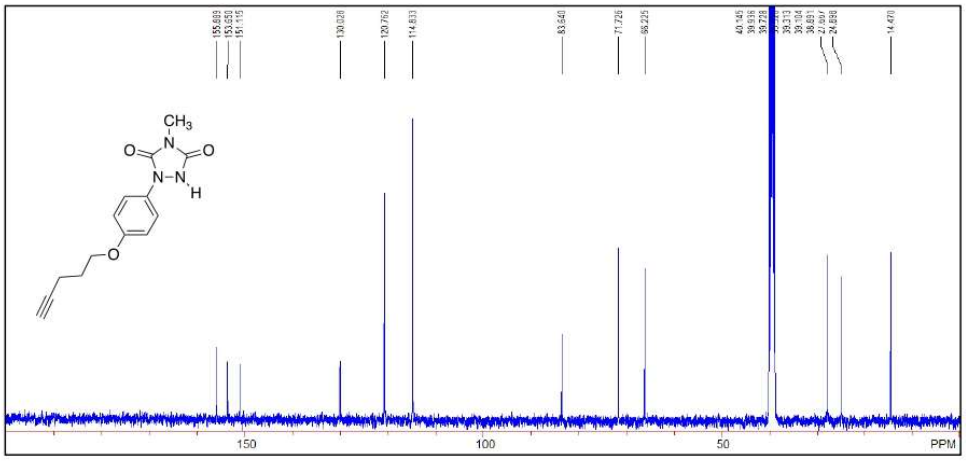

Figure S4: ^{13}C NMR (DMSO-d_6, 100 MHz) spectrum of **4-Methyl-1-[4-(pent-4-yn-1-yloxy)phenyl]-1,2,4-triazolidine-3,5-dione (6)**.

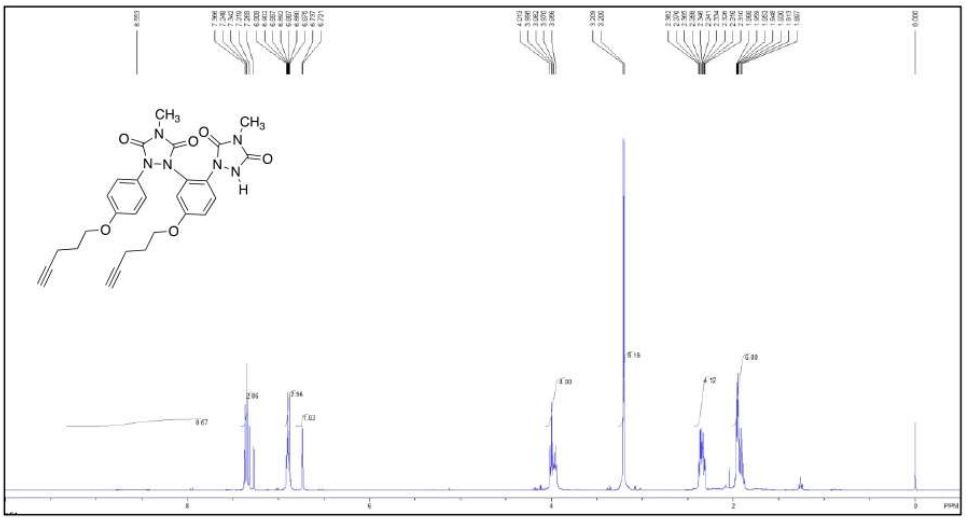

Figure S5: ^{1}H NMR ($CDCl_3$, 400 MHz) spectrum of self-reaction dimer **8**.

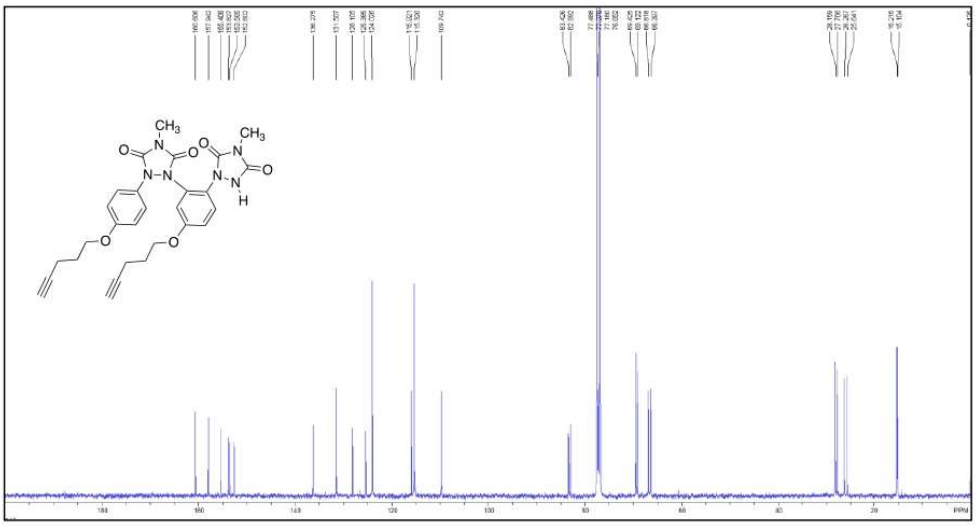

Figure S6: ^{13}C NMR ($CDCl_3$, 400 MHz) spectrum of self-reaction dimer **8**.

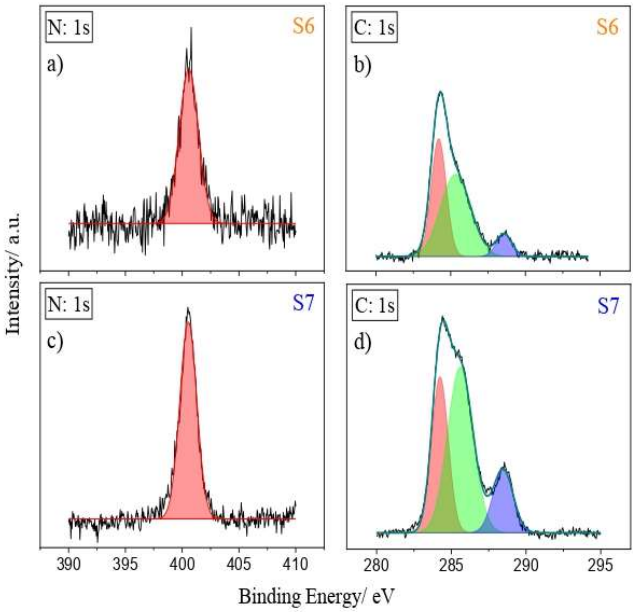

Figure S7: Carbon C1s and nitrogen N1s high resolution XPS spectra SAMs of the urazole precursor **6** (**a,b**) and the radical urazole **7** (**c,d**) on gold surface. Binding energies N1s: 400.5 eV (N-C bond); C1s: 284.2eV (C-H), 285.3 eV (C=C), and 288.5 eV (N-C=O).

A peak of N1s is observed at 400.56 eV for both species corresponding to the nitrogen atoms in the urazole ring. Additionally, C1s spectra are presented exhibiting peaks at 288.54, 285.36 and 284.21 eV related to N-C=O, C=C and C-H bindings, respectively.[1]

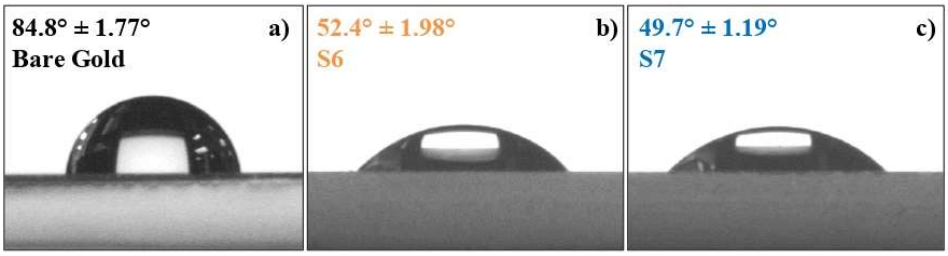

Figure S8: Contact angle measurements of **a)** bare gold, **b) S6** and **c) S7**. A drop of 3µL of Milli-Q water was used for these experiments.

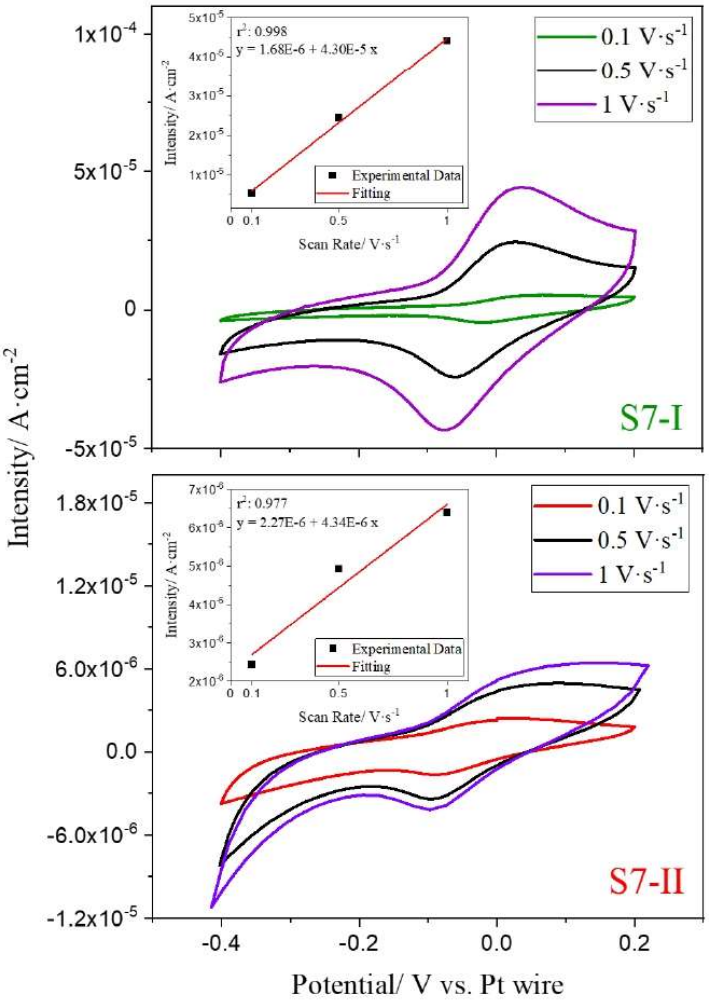

Figure S9: CV of **S7-I** and **S7-II** performed at different scan rates (0.1, 0.5 and 1 $V \cdot s^{-1}$). The measurements were performed using a 0.1 M $TBAPF_6$ solution in acetonitrile and Pt wires as pseudo-reference electrode. Inset: plots of the maximum current intensity vs. scan rate.

The maximum of the intensity of the redox peak current density for each scan rate is plotted against the scan rate. The linear relationship (as shown in the inset) is characteristic of immobilized redox species on a surface. This tendency is followed for both SAMs.

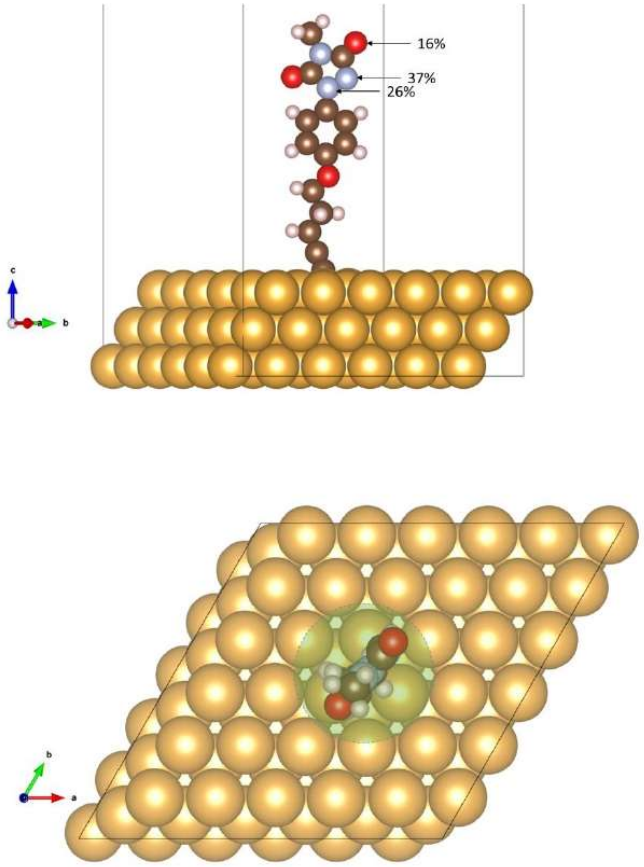

Figure S10: Top. Side (in surface plane) view of radical **7** bound to the Au(111) surface. Labelled percentages indicate where approximately 80% of the spin is localised. Atom colour key: C – brown, N – blue, O – red, H – light gray, Au – gold. **Bottom**. Top (perpendicular to surface plane) view of **7** bound to the Au(111) surface. Using the shaded circular region (area of approx. 21 Å^2) and assuming a hexagonal close packing, an approximate maximum upper limit to the surface coverage of four molecules per 100 Å^2 is obtained. Atom colour key: C – brown, N – blue, O – red, H – light gray, Au – gold.

We investigated the adsorption of **7** on the Au(111) surface by periodic density functional theory (DFT) based calculations employing the VASP code.[2] In all cases the PBE[3] generalised gradient approximation functional together with Tkatchenko-Scheffler van der Waals corrections[4] was used. The electron density was expanded in a plane wave basis set with a 500 eV energy cut-off with the effect of inner cores on the valence electron density described through the Projector Augmented Wave method.[5] Vacuum 6×6×3 slabs (separated by 25 Å in the *z* direction) consisting

of 108 Au atoms cut from fully optimised PBE-DFT calculations of bulk Au were used to represent the Au(111) surface, with atoms in the lowest layer fixed to their respective optimised bulk crystalline positions. The lateral size of the slab (17.8 Å) was chosen as to minimise intermolecular interactions. Gamma point calculations were employed due to relatively large unit cell sizes used. All calculations were carried with fixed lattice parameters and with explicit consideration of spin polarization. The positions of all unconstrained atoms in the system were optimised until forces were less than 0.02 eV/Å.

[1] Laure, W.; De Bruycker, K.; Espeel, P.; Fournier, D.; Woisel, P.; Du Prez, F. E.; Lyskawa, J. Ultrafast Tailoring of Carbon Surfaces via Electrochemically Attached Triazolinediones. Langmuir 2018, 34 (7), 2397.
[2] Perdew, J. P., Burke, K.; Ernzerhof, M. Generalized gradient approximation made simple, Phys. Rev. Lett. 1996, 77, 3865.
[3] Tkatchenko, A.; Scheffler, M. Accurate molecular Van der Waals interactions from ground-state electron density and free-atom reference data, Phys. Rev. Lett. 2009, 102, 073005.
[4] Blöchl, P. E. Projector augmented-wave method, Phys. Rev. B 1994, 50, 17953.

ARTICLE II

Fluorescent Switchable Surfaces Based on Quantum Dots Modified with Redox-Active Molecules

AUTHORS: Ángel Campos-Lendinez, † Jose Muñoz, Núria Crivillers * and Marta Mas-Torrent *

PUBLICATION: *Submitted* (2023)

WILEY-VCH

RESEARCH ARTICLE

Fluorescent switchable surfaces based on quantum dots modified with redox-active molecules

Ángel Campos-Lendinez, [a] Jose Muñoz, [a] Núria Crivillers *[a] and Marta Mas-Torrent *[a]

[a] Á. Campos-Lendinez, J. Muñoz, N. Crivillers, M. Mas-Torrent
Institut de Ciència de Materials de Barcelona, ICMAB-CSIC.
Campus UAB, 08193 Bellaterra, Spain.
E-mail: ncrivillers@icmab.es, mmas@icmab.es.

Abstract: By combining the switching ability of redox molecules with the unique fluorescence properties of quantum dots (QDs), we develop here a robust electrochemical fluorescence switch. This is realised by grafting CdSe/ZnS QDs on transparent indium tin oxide (ITO) substrates and, subsequently, modifying them with a Ferrocene (Fc) molecular monolayer. The application of oxidation/reduction voltage pulses to tune the Fc redox state leads to the tuning of the surface fluorescence output. Interestingly, the ON/OF ratio can be enhanced by reducing the distance between the redox active unit and the QD due to a more efficient electronic coupling. Remarkably, by defining a mixed-valence state a ternary switch has also been achieved. We highlight that the QD surface immobilisation is key to realise this switch to avoid aggregation and fluorescence quenching in suspension. Hence, an efficient and versatile novel route to fabricate robust fluorescent redox switches is demonstrated, opening a wide avenue of possibilities to be explored in the field of sensing and information storage.

Introduction

Engineering smart surfaces, whose properties can be reversibly tuned under an external stimulus (e.g., chemical, temperature, light, electric, etc.), has attracted much attention over the last years for the development of a wide range of applications, such as self-cleaning surfaces, smart windows or data storage and microfluidic devices.[1–4] As an external stimulus, using electric or electrochemical inputs to trigger the switching function is technologically relevant for the fabrication of electronic and optoelectronic devices. The preparation of electrically/electrochemically switchable surfaces has successfully been realised by surface-grafting redox-active molecular systems as thin films or self-assembled monolayers (SAMs).[5–11] In these systems, the application of an electrical signal has been translated into changes in the capacitance,[12,13] magnetic,[14] chemical,[5,16] absorption,[11,17] or fluorescence[14] surface properties. In particular, fluorescent electrical switches are highly appealing as fluorescent probes for imaging or sensing, in fluorescent displays or in memory and information processing devices.[18]

Semiconductor Quantum Dots (QDs) are zero-dimensional nanostructures with quantum confinement. They possess unique size and shape-dependent optoelectronic properties showing size-tunable emission wavelength.[19] QDs have attracted attention in applications such as biomedical imaging,[20] optical quantum computing,[21] light-emitting diodes (LEDs),[22] displays,[23,24] solar cells,[25,26] and in sensors exploiting their emission properties as read-out.[27,28] QDs are often thermally and chemically stabilised with a semiconductor shell. Interestingly, this shell can also be used for the grafting of recognition groups or functional molecules that can tune the QD luminescent properties,[29–32] including redox-active molecular units.[33,34] Nevertheless, their poor colloidal stability (i.e., aggregation) typically results in their fluorescence self-quenching over time, which limits the potential exploitation of these systems.[35] To circumvent this issue, QDs can be grafted on surface, providing new perspectives for the fabrication of multiple optoelectronic devices.[29,39]

In this work, we fabricate surfaces that behave as fluorescence electrochemical switches by combining the switching ability of redox molecules with the unique fluorescence properties of CdSe/ZnS QDs. Specifically, a novel methodology has been developed to prepare thiol-terminated SAMs on transparent indium tin oxide (ITO) substrates that can subsequently interact through the formation of a robust covalent bond with the CdSe/ZnS QDs shell. Following, the QDs were modified with a ferrocene (Fc) molecular monolayer. Applying the redox potential required to oxidise/reduce the Fc moiety, a stable reversible luminescent switch with two distinguishable states operating in a low potential window range (from 0 V to +0.6 V) is demonstrated. Furthermore, the ON/OFF ratio is modulated by the spacer distance between the QD and Fc. Ultimately, the partial oxidation/reduction of the grafted Fc moieties has permitted to write an additional intermediate fluorescence state, giving rise to a ternary optical switch, highly appealing for information processing.[37] Hence, this work shows an efficient novel route to fabricate robust fluorescent

redox switches exploiting QDs luminescence, which has been realised thanks to the QDs surface immobilisation that avoids their aggregation and self-quenching.

Results and Discussion

Scheme 1 summarises the two-step surface functionalisation procedure developed to obtain the functional layers on ITO. First, the previously activated ITO substrate (**S0**) was functionalised with (3-mercaptopropyl)trimethoxysilane (MPS), resulting in **S1**. Subsequently, **S1** was modified with CdSe/ZnS core/shell QDs passivated with a octadecylamine layer by an on-surface ligand-exchange reaction between the amine molecules molecules and the terminal thiol of the SAM, giving **S2**.[38,39] Finally, a second on-surface ligand-exchange reaction step was carried out using two Fc alkane thiols of different lengths (i.e., 6-(ferrocenyl)hexanethiol and 11-(ferrocenyl)undecanethiol) to form **S3-Fc6** and **S3-Fc11**, respectively. Additionally, to elucidate the role of Fc on the switching performance, the surface-grafted QDs were also functionalised with the non-redox active 1-hexanethiol molecule (i.e., **S3-Hx**). All the samples were fully characterised employing several techniques described below (see also Supporting Information).

For the preparation of **S2**, the incubation time of **S1** substrates in the QD suspension was optimised. As shown in the Scanning Electronic Microscopy (SEM) images of Figure S1, the surface density of QDs increases during the first 8 hours of incubation, but afterwards, no significant improvement is observed (Figure S2). Thus, the minimum incubation time (i.e., 8 h) was used for all the experiments (Figure 1c).

X-Ray Photoelectron Spectroscopy (XPS) spectra of Si2p, S2p, Zn2p and Fe2p were acquired, confirming the successful two-step modification of ITO (Figure S3). The Si2p spectra indicate the presence of thiolated silane SAM (**S1**-**S3**). Two peaks are clearly observed at 102.1 and 103.2 eV, attributed to Si-C and Si-O.[40,41] In addition, the S2p spectrum of **S1** shows a doublet at 163.2 eV ($S2p_{3/2}$) and 164.5 eV ($S2p_{1/2}$) assigned to the terminal -SH.[42,43] Two additional peaks at 167.8 and 169.1 eV are attributed to some oxidised thiols.[44,45] Further, for samples **S2**, **S3-Hx**, **S3-Fc6**, and **S3-Fc11**, a Zn-S doublet is observed at 160.8 and 162.2 eV ascribed to the presence of the QD.[44,46] Finally, the S_x/SO_x peak is found at 165.8 eV, related to sulfur binding energy from the QD shell.[46] In the Zn2p spectra, the expected doublet is observed at 1022.3 and 1045.3 eV for **S2**, while a shift in this binding energy is found in **S3-Hx**, **S3-Fc6** and **S3-Fc11** owing to the existence of sulfur vacancies filled by the thiolated ligands.[47] The highest shift is found in **S3-Hx**, suggesting that the alkane chain promotes a better surface coverage due to less lateral steric constraints than the Fc-containing thiols. Finally, the presence of Fc in **S3-Fc6** and **S3-Fc11** is demonstrated by a doublet at 708.2 eV and 720.1 eV, ascribed to Fe^{2+} $2p_{3/2}$ and Fe^{2+} $2p_{1/2}$, respectively.[48] A lower intensity peak at 711.9 eV is assigned to Fe^{3+} $2p_{3/2}$,[49] indicating a partial oxidation of the metal ion.[50]

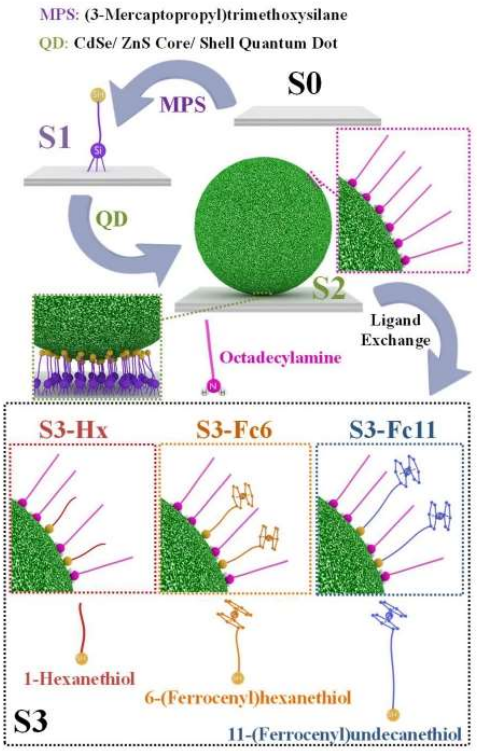

Scheme 1. Scheme of the preparation of the three functionalised QDs-based SAMs: **S3-Fc6**, **S3-Fc11** and **S3-Hx**.

The measured water contact angle on the different samples varied from 38.3º (**S0**), 67.8º (**S1**) to 102.9º (**S2**), showing an increase in the hydrophobic character of the surface (Figure S5). Upon the last modification step, the **S3** surfaces showed different wettabilities, with contact angles of 88.2º, 96.9º and 118.1º for **S3-Fc6**, **S3-Fc11** and **S3-Hx**, respectively. As expected, the larger contact angle corresponds to the most hydrophobic $-CH_3$ terminated **S3-Hx** surface.

All the samples were also characterised by electrochemical means. Cyclic voltammetry (CV) and electrochemical impedance spectroscopy (EIS) measurements were performed using the ITO substrates as working electrodes and a 0.1 M KCl electrolyte solution containing $[Fe(CN)_6]^{3-/4-}$ as redox probe (Figure S6). As expected, the CV of **S0** clearly shows the peak of the $[Fe(CN)_6]^{3-}/[Fe(CN)_6]^{4-}$ redox couple. For **S1** to **S3,** the peak is almost or entirely vanished, ascribed to a poor electron transfer efficiency (from the solution to the electrode) through the monolayers. In agreement with the CV results, EIS measurements show increasing values for the charge transfer resistance (R_{ct}) from **S0** to **S3**, except the Fc-terminated SAM with the short alkane chain that does hardly alter the electron transfer rate with

respect to **S2** (R_{CT}: 0.3 (**S0**), 8.7 (**S1**), 52.2 (**S2**), 151.0 (**S3-Hx**), 138.0 (**S3-Fc11**) and 56.2 (**S3-Fc6**) kΩ·cm^{-2}).

Electrochemical measurements were also carried out to investigate the surface redox activity using the functionalized surfaces as working electrode (WE) and a 0.1 M of tetrabutylammonium hexafluorophosphate ($TBAPF_6$) CH_3CN solution as electrolyte (Figure S7). For **S1,** only capacitive currents were found, owing to the absence of an electroactive group. A small broad faradaic peak was noticed for **S2,** which was ascribed to defect states in the QD nanocrystal ($E^{1/2}$ = 0.36 V).[51,52] Similarly and as expected, **S3-Hx** did not show any redox process (Figure 1a). On the contrary, **S3-Fc6** and **S3-Fc11** clearly exhibit the redox peak associated with the Fc/Fc$^+$ pair ($E^{1/2}$ = 0.37 V and $E^{1/2}$ = 0.35 V *vs* Ag/AgCl, respectively) (Figure 1b and Figure S7), further corroborating the incorporation of the Fc unit on the QDs surface. Additionally, a low voltage difference between the anodic and cathodic process ($\Delta E = E_{anodic}-E_{cathodic}$) of 0.058 V for **S3-Fc6** and 0.051 V for **S3-Fc11**, along with a linear relationship between the scan rate and the peak intensity were observed, in agreement with the surface-confinement of the redox molecules (Figure S8). Similar coverages, 1.2·10^{-10} mol·cm^{-2} (**S3-Fc6**) and 1.8·10^{-10} mol·cm^{-2} (**S3-Fc11)**, were estimated for both systems by the integration of the redox peaks. Finally, consecutive cycles (up to 30) sweeping the applied voltage between 0.2 and 0.7 V were recorded, supporting the robust grafting of the redox molecules on the QDs, and these on the ITO electrode (Figure S7).

Next, the fluorescence properties of the surfaces were explored for **S2** and **S3**. Fluorescence emission bands centered at 527 nm were observed in all the cases (excitation at 390 nm), although with remarkable intensity differences (Figure 1d). The modification of **S2** with thiol ligands diminishes the substrate fluorescence emission in all cases. As previously reported, thiol groups act as hole trap states, affecting the electron relaxation from the conduction to the valence band after electron excitation and resulting in non-radiative recombination.[53,54] Furthermore, the surfaces containing Fc (i.e., **S3-Fc6** and **S3-Fc11**) show a higher fluorescence quenching compared to **S3-Hx**, which is also visible in the confocal microscopy images of the surfaces (Figure S9). In fact, when the Fc unit is closer to the QD (i.e., **S3-Fc6**), the quenching is even more enhanced. This is ascribed, as previously reported, to the electron transfer promoted by the high hole-acceptor efficiency of Fc units, which, according to tunneling transfer, decreases at larger distances due to lower electronic coupling.[34]

Based on the above-described results, the QDs-based SAMs **S3-Fc6** and **S3-Fc11** were then interrogated as fluorescence switches using the electrochemical input to tune the redox state of the QD-Fc nanoparticle, i.e. to write the state of the switch. As reference, the non-electroactive **S3-Hx** surface was also investigated. For this purpose, a customised fluorescence cuvette was designed to perform spectro-electrochemistry experiments, where the modified ITO was used as a WE and two platinum wires as counter and pseudo-reference electrodes (CE and RE). The cuvette was then filled up with an acetonitrile solution containing 0.1 M of $TBAPF_6$ as electrolyte. Write/erase switching steps were recorded by applying oxidation potential pulses of + 0.6 V (Fc → Fc$^+$) and reduction potential pulses of 0 V (Fc$^+$ → Fc) for 40 seconds each. The fluorescence spectra were immediately acquired after each oxidation/reduction step, denoted as I_O (oxidised) and I_R (reduced) (Figure 2). The initial spectra acquired before applying any voltage are also displayed in dashed lines. Interestingly, for **S3-Fc6** this initial spectrum is close in intensity to I_O, indicating a spontaneous electron transfer between the QD and the Fc moiety generating the charged Fc$^+$ species. This effect is less pronounced for the **S3-Fc11** were the initial spectrum lies between the I_O and I_R, in agreement with a less efficient electron transfer due to the longer distance.

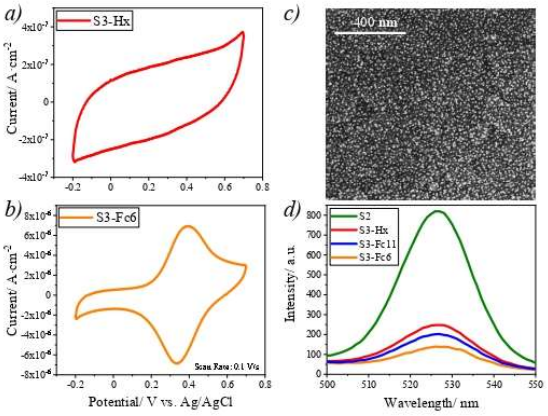

Figure 1. CV of a) **S3-Hx** and b) **S3-Fc6** samples. Voltammograms were recorded in a typical three electrode-configuration cell using the functionalized surfaces as WE, Pt wire as CE and Ag/AgCl electrode as reference. As electrolyte, an acetonitrile solution containing 0.1 M $TBAPF_6$ was used. The CVs were recorded at a scan rate 0.1 V·s^{-1} in a voltage window -0.2 V - +0.7 V. c) SEM image of **S2** and d) fluorescence emission spectra of all the surfaces investigated (excitation at 390 nm).

A significant reduction in the fluorescence intensity was observed for **S3-Fc6** and a more moderate one for **S3-Fc11** upon oxidation, which increased again after applying the reduction potential. These two distinguishable fluorescence spectra permitted to define two states, the "ON" state for the reduced Fc and the "OFF" state for the oxidised Fc$^+$. Remarkably, **S3-Hx** did not respond to the

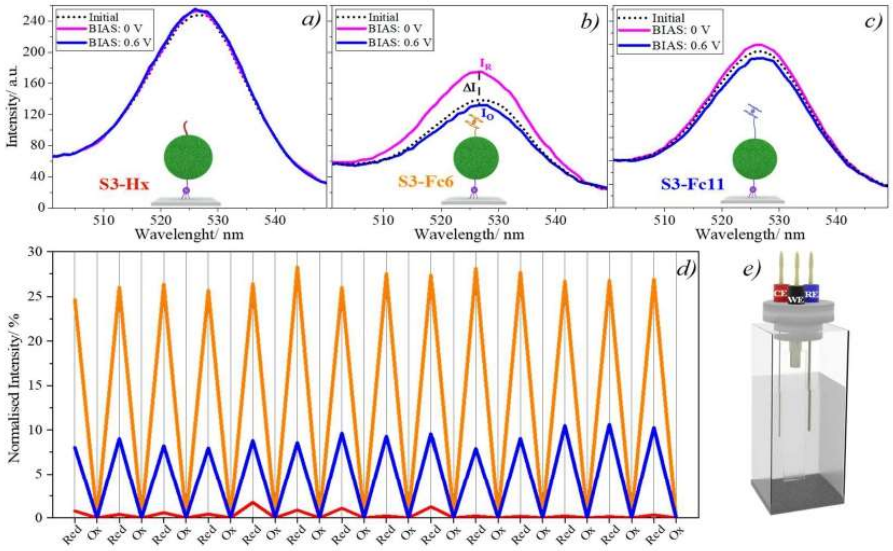

Figure 2. Fluorescence spectra of the modified substrates acquired during the spectro-electrochemical switching experiments for a) **S3-Hx**, b) **S3-Fc6** and c) **S3-Fc11** recorded initially before starting the experiment (dashed lines) and after applying a reduction pulse of 0 V (I_R) and an oxidation voltage of +0.6 V (I_O). d) Consecutive fluorescence switching cycles between the "ON" (reduced) and "OFF" (oxidised) states for **S3-Hx** (in red), **S3-Fc11** (in blue) and **S3-Fc6** (in orange). e) Scheme of the three-electrode configuration cell used in spectro-electrochemical experiments with the modified substrates as WE and platinum wires, as RE and CE, immersed in a 0.1 M $TBAPF_6$ solution in CH_3CN.

applied potentials, confirming that the switching behaviour is solely attributed to the effect of the redox state of the Fc unit.

The relative ON/OFF fluorescence intensity ratio (at 527 nm) was calculated as follows:

$$\%\, fluorescence\ intensity = \frac{I_R - I_O}{I_R} \cdot 100$$

where I_O and I_R correspond to the fluorescence intensity at + 0.6 V and 0 V bias, respectively. **S3-Fc6** exhibits a remarkable ON/OFF ratio of 27 %, while for the longer Fc SAM, the ratio is reduced to 9 %. Hence, the switching ability is more efficient for the shorter Fc SAM. This could be attributed mainly to exciton dissociation via electron transfer from the CdSe QD to Fc^+, which is again more efficient in the short Fc SAM.[55–58] The stability and reversibility of the switches were corroborated by performing 14 consecutive cycles, where no significant degradation was observed (Figure 2d).

The relevance of our reported strategy to obtain a robust QD-based switch on surface is reinforced when the same experiment was performed using a suspension of the QDs functionalised with the Fc6-SAM. In this case, a continuous decrease in the fluorescence intensity was observed while applying alternating oxidation and reduction potentials (Figure S10). Dynamic light scattering (DLS) analysis indicated continuous nanoparticle aggregation after applying the voltage pulses, leading to self-quenching.[59] Thus, this material in suspension could not operate as a fluorescent switch.

As previously mentioned, the initial fluorescence spectra recorded for **S3-Fc6** and **S3-Fc11** showed an intermediate fluoresce intensity with respect to the oxidized and reduced states, pointing out the existence of a mixed-valence state (Figure 2). This encouraged us to go a step further by defining a third additional intermediate state applying an intermediate voltage pulse of + 0.3 V. At this potential, only partial oxidation of the Fc moieties is expected. Again, upon applying three-step voltage pulses (i.e., 0, + 0.3, + 0.6 V), the fluorescence intensity of **S3-Hx** did not show any variation over time owing to the absence of electroactive groups. On the contrary, the fluorescence intensity for **S3-Fc6** and **S3-Fc11** could be continuously modified and controlled by the applied voltage, displaying both substrates three well-characteristic optical read-out states. As expected from the above data, the intensity ratio between the states is higher for **S3-Fc6**. Thus, these results suggest that a multistate (or multilevel) switch could be achieved by controlling the ratio of oxidised/reduced Fc units at the QD shell. Impressively, the fluorescence switching platforms **S3-Fc6** and **S3-Fc11** did not show fatigue in the time range investigated, demonstrating the robustness of the modified surfaces.

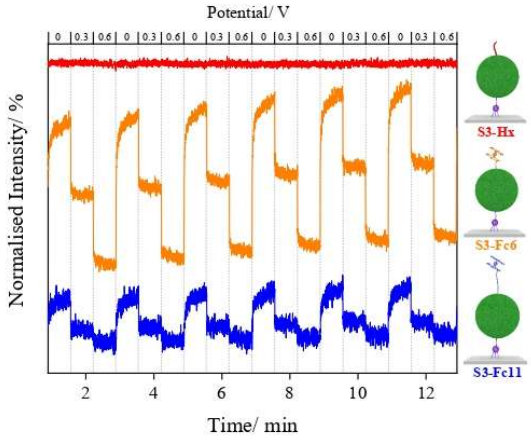

Figure 3. Fluorescence intensity spectra monitored over time after applying 45 s voltage pulses of 0, + 0.3 and + 0.6 V for **S3-Hx**, **S3-Fc6** and **S3-Fc11**.

Conclusion

In summary, the preparation of ITO surfaces behaving as robust fluorescent electrochemical switches is successfully achieved by grafting CdSe/ZnS QDs modified with a redox-active Fc unit. This approach takes advantage of the unique fluorescence properties of QDs and the switching ability of electroactive molecular units. The optimization of the on-surface ligand exchange reactions has been key for the effective development of the reported switchable platform.

Spectro-electrochemical experiments have clearly demonstrated the role of the redox active center, which triggers the fluorescence quenching proportionally to the ratio of oxidized Fc+ units and to the lower distance between the Fc and the QD. A maximum ON/OFF fluorescence intensity ratio of 27 % was obtained for the shorter Fc derivative. Remarkably, by defining a mixed valence state, a ternary switch was also proven.

We believe that the approach reported here can be extended to other functional molecules of interest, which may interfere or participate differently in the optical response of QDs thus, opening a wide avenue of possibilities to be explored in the field of sensing and information storage. Main Text Paragraph.

Supporting Information

Supporting Information: Surface functionalization details and additional surface characterization (SEM, XPS, electrochemical and contact angle). pdf

Acknowledgements

This work was funded by the Spanish Ministry with the project GENESIS PID2019-111682RB-I00 and through the "Severo Ochoa" Programme for Centers of Excellence in R&D (FUNFUTURE CEX2019-000917-S) and the Generalitat de Catalunya (2021-SGR-00443). Á. C.-L. is enrolled in the UAB Materials Science PhD program.

Keywords: self-assembled monolayer • molecular switch • quantum dot • electrochemistry • ferrocene

[1] J. Drelich, E. Chibowski, D. D. Meng, K. Terpilowski, *Soft Matter* **2011**, *7*, 9804–9828.
[2] H. J. Yoon, D. Lee, J. Yang, J. K. Song, *J. Mol. Liq.* **2022**, *348*, 118014.
[3] A. R. Naik, B. Warren, A. Burns, R. Lenigk, J. Morse, A. Alizadeh, J. J. Watkins, *Microfluid. Nanofluidics* **2021**, *25*, 1–9.
[4] C. Chen, S. Yang, G. Su, J. Li, J. C. Ren, W. Liu, *J. Phys. Chem. C* **2021**, *125*, 1069–1074.
[5] M. S. Maglione, S. Casalini, S. Georgakopoulos, M. Barbalinardo, V. Parkula, N. Crivillers, C. Rovira, P. Greco, M. Mas-Torrent, *Small* **2018**, *14*, 1703344.
[6] C. Simao, M. Mas-Torrent, J. Veciana, C. Rovira, *Nano Lett.* **2011**, *11*, 4382–4385.
[7] P. M. Mendes, *Chem. Soc. Rev.* **2008**, *37*, 2512–2529.
[8] X. Lv, L. Zha, L. Qian, X. Xu, Q. Bi, Z. Xu, D. S. Wright, C. Zhang, *Chem. Eng. J.* **2020**, *386*, 123939.
[9] S. Sortino, S. Di Bella, S. Conoci, S. Petralia, M. Tomasulo, E. J. Pacsial, F. M. Raymo, *Adv. Mater.* **2005**, *17*, 1390–1393.
[10] J. Peng, H.-H. Jeong, Q. Lin, S. Cormier, H.-L. Liang, M. F. L. De Volder, S. Vignolini, J. J. Baumberg, *Sci. Adv.* **2019**, *5*, eaaw2205.
[11] I. Alcón, M. Gonidec, M. R. Ajayakumar, M. Mas-Torrent, J. Veciana, *Chem. Sci.* **2016**, *7*, 4940–4944.
[12] J. Rivera-Gandía, C. R. Cabrera, *J. Electroanal. Chem.* **2007**, *605*, 145–150.
[13] E. Marchante, M. S. Maglione, N. Crivillers, C. Rovira, M. Mas-Torrent, *RSC Adv.* **2017**, *7*, 5636–5641.
[14] C. Simão, M. Mas-Torrent, N. Crivillers, V. Lloveras, J. M. Artés, P. Gorostiza, J. Veciana, C. Rovira, *Nat. Chem.* **2011**, *3*, 359–364.
[15] V. Lloveras, P. Elías-Rodríguez, L. Bursi, E. Shirdel, A. R. Goñi, A. Calzolari, J. Vidal-Gancedo, *Nano Lett.* **2022**, *22*, 768–774.
[16] A. Wieckowska, A. B. Braunschweig, I. Willner, *Chem. Commun.* **2007**, 3918–3920.
[17] S. Shankar, M. Lahav, M. E. Van Der Boom, *J. Am. Chem. Soc.* **2015**, *137*, 4050–4053.
[18] M. Guille-Collignon, J. Delacotte, F. Lemaître, E. Labbé, O. Buriez, *Chem. Rec.* **2021**, *21*, 2193–2202.
[19] D. Bera, L. Qian, T. K. Tseng, P. H. Holloway, *Materials (Basel).* **2010**, *3*, 2260–2345.
[20] A. M. Wagner, J. M. Knipe, G. Orive, N. A. Peppas, *Acta*

Biomater. **2019**, *94*, 44–63.
[21] Y. Arakawa, M. J. Holmes, *Appl. Phys. Rev.* **2020**, *7*, 21309.
[22] A. Onal, G. O. Eren, S. Sadeghi, R. Melikov, M. Han, O. Karatum, M. S. Ozer, H. B. Jalali, I. B. Dogru-yuksel, I. Yilgor, O. Metin, S. Nizamoglu, *ACS Photonics* **2022**, *9*, 1304−1314.
[23] Y. Lee, D. S. Kim, S. W. Jin, H. Lee, Y. R. Jeong, I. You, G. Zi, J. S. Ha, *Chem. Eng. J.* **2021**, *427*, 130858.
[24] Y. M. Huang, K. J. Singh, A. C. Liu, C. C. Lin, Z. Chen, K. Wang, Y. Lin, Z. Liu, T. Wu, H. C. Kuo, *Nanomaterials* **2020**, *10*, 1–29.
[25] A. Sahu, A. Garg, A. Dixit, *Sol. Energy* **2020**, *203*, 210–239.
[26] F. P. García de Arquer, D. V. Talapin, V. I. Klimov, Y. Arakawa, M. Bayer, E. H. Sargent, *Science (80-.).* **2021**, *373*, eaaz8541.
[27] A. Lesiak, K. Drzozga, J. Cabaj, M. Bański, K. Malecha, A. Podhorodecki, *Nanomaterials* **2019**, *9*, 1–24.
[28] R. Maluleke, O. S. Oluwafemi, *Appl. Sci.* **2021**, *11*, 11580.
[29] J. Zhou, Y. Liu, J. Tang, W. Tang, *Biochem. Pharmacol.* **2017**, *20*, 360–376.
[30] G. Kalyuzhny, R. W. Murray, *J. Phys. Chem. B* **2005**, *109*, 7012–7021.
[31] S. Jeong, M. Achermann, J. Nanda, S. Ivanov, V. I. Klimov, J. A. Hollingsworth, *J. Am. Chem. Soc.* **2005**, *127*, 10126–10127.
[32] S. Hohng, T. Ha, *J. Am. Chem. Soc.* **2004**, *126*, 1324–1325.
[33] D. Dorokhin, N. Tomczak, A. H. Velders, D. N. Reinhoudt, G. J. Vancso, *J. Phys. Chem. C* **2009**, *113*, 18676–18680.
[34] T. X. Ding, J. H. Olshansky, S. R. Leone, A. P. Alivisatos, *J. Am. Chem. Soc.* **2015**, *137*, 2021–2029.
[35] Q. Zhou, Z. Li, Q. Wang, L. Peng, S. Luo, F. L. Gu, *Anal. Methods* **2021**, *13*, 2305–2312.
[36] T. Lee, K. Enomoto, K. Ohshiro, D. Inoue, T. Kikitsu, K. Hyeon-Deuk, Y.-J. Pu, D. Kim, *Nat. Commun.* **2020**, *11*, 5471.
[37] M. Mas-Torrent, C. Rovira, J. Veciana, *Adv. Mater.* **2013**, *25*, 462–468.
[38] A. Farmonovih, I. Kadriddin, F. Khalilov, R. Rashidovich, *J. Sol-Gel Sci. Technol.* **2023**, 1–6.
[39] J. H. Dunlap, N. P. Jayaweera, P. J. Pellechia, A. B. Greytak, *J. Phys. Chem. C* **2022**, *126*, 17635–17646.
[40] N. H. Khdary, A. E. H. Gassim, A. G. Howard, T. S. Sakthivel, S. Seal, *Anal. Methods* **2018**, *10*, 245–255.
[41] P. M. Dietrich, S. Glamsch, C. Ehlert, A. Lippitz, N. Kulak, W. E. S. Unger, *Appl. Surf. Sci.* **2016**, *363*, 406–411.
[42] Y. C. Liang, C. C. Wang, *RSC Adv.* **2018**, *8*, 5063–5070.
[43] H. Peisert, T. Chassé, P. Streubel, A. Meisel, R. Szargan, *J. Electron Spectros. Relat. Phenomena* **1994**, *68*, 321–328.
[44] H. Mekaru, A. Yoshigoe, M. Nakamura, T. Doura, F. Tamanoi, *ACS Appl. Nano Mater.* **2019**, *2*, 479–488.
[45] Q. Lin, X. Dong, Y. Wang, N. Zheng, Y. Zhao, W. Xu, T. Ding, *J. Mater. Sci.* **2020**, *55*, 6637–6647.
[46] A. E. Raevskaya, O. L. Stroyuk, Y. V. Panasiuk, V. M. Dzhagan, D. I. Solonenko, S. Schulze, D. R. T. Zahn, *Nano-Structures and Nano-Objects* **2018**, *13*, 146–154.
[47] J. Choi, W. Choi, D. Y. Jeon, *ACS Appl. Nano Mater.* **2019**, *2*, 5504–5511.
[48] A. Le Goff, V. Artero, R. Metayé, F. Moggia, B. Jousselme, M. Razavet, P. D. Tran, S. Palacin, M. Fontecave, *Int. J. Hydrogen Energy* **2010**, *35*, 10790–10796.
[49] A. Rajan, M. Sharma, N. K. Sahu, *Sci. Rep.* **2020**, *10*, 1–15.
[50] G. Riveros, S. Meneses, S. Escobar, C. Garín, B. Chornik, *J. Chil. Chem. Soc.* **2010**, *55*, 61–66.
[51] E. Kuçur, W. Bücking, R. Giernoth, T. Nann, *J. Phys. Chem. B* **2005**, *109*, 20355–20360.
[52] D. Dorokhin, N. Tomczak, D. N. Reinhoudt, A. H. Velders, G. J. Vancso, *Nanotechnology* **2010**, *21*, 285703.
[53] L. Lystrom, A. Roberts, N. Dandu, S. Kilina, *Chem. Mater.* **2021**, *33*, 892–901.
[54] C. H. R, J. D. Schiffman, R. G. Balakrishna, *Sensors Actuators, B Chem.* **2018**, *258*, 1191–1214.
[55] H. Zhu, Y. Yang, K. Hyeon-Deuk, M. Califano, N. Song, Y. Wang, W. Zhang, O. V. Prezhdo, T. Lian, *Nano Lett.* **2014**, *14*, 1263–1269.
[56] A. J. Morris-Cohen, M. T. Frederick, L. C. Cass, E. A. Weiss, *J. Am. Chem. Soc.* **2011**, *133*, 10146–10154.
[57] A. Boulesbaa, Z. Huang, D. Wu, T. Lian, *J. Phys. Chem. C* **2010**, *114*, 962–969.
[58] A. Boulesbaa, A. Issac, D. Stockwell, Z. Huang, J. Huang, J. Guo, T. Lian, *J. Am. Chem. Soc.* **2007**, *129*, 15132–15133.
[59] T. Kang, K. Um, J. Park, H. Chang, D. C. Lee, C. K. Kim, K. Lee, *Sensors Actuators, B Chem.* **2016**, *222*, 871–878.

Supporting Information

Fluorescent switchable surfaces based on quantum dots modified with redox-active molecules

Ángel Campos-Lendinez,[a] José Muñoz,[Ω] Núria Crivillers,[a,*] and Marta Mas-Torrent [a,*]

[a]*Institut de Ciència de Materials de Barcelona, ICMAB-CSIC, Campus UAB, 08193 Bellaterra, Spain*

Table of contents

MATERIALS AND METHODS

Substrates, Chemicals and Reagents:

Indium Thin Oxide substrates (ITO over unpolished float glass, resistance: 15–25 Ω) were purchased from Delta Technologies. Fluorescence CdSe/ZnS core/shell colloidal nanoparticles in toluene (c = 1 $mg \cdot mL^{-1}$) stabilized with Trioctylphosphine oxide (TOPO), and reagents 6-(Ferrocenyl)hexanethiol (> 99 %), 11-(Ferrocenyl)undecanethiol (> 99 %) and 1-Hexanethiol (> 99 %) were acquired from Sigma-Aldrich. Tetrabuthyl ammonium hexafluorophosphate ($TBAPF_6$), ammonium hydroxide (NH_4OH, 5 N), hydrogen peroxide (H_2O_2, 30% wt), potassium ferricyanide/ferrocyanide ($K_3[Fe(CN)_6]/K_4[Fe(CN)_6]$, 99.8%) and potassium chloride (KCl, 99.5%) were also supplied by Sigma-Aldrich. The high-performance liquid chromatography grade organic solvents (toluene, dichloromethane, acetone and ethanol) used were purchased from Teknokroma. Aqueous solutions were prepared using ultrapure water from a Milli-Q system (Millipore).

Samples Preparation:

Preparation of QD-Fc6 suspension: a deoxygenated toluene suspension containing of 0.1 mg/mL CdSe/ ZnS QDs (stabilized with TOPO) were placed in a vial. Then, the thiol ligand (i.e., 6-(Ferrocenyl)hexanethiol) was added with a final concentration of 1 mM. Subsequently, the colloidal suspension was stirred at 60°C under an inert atmosphere and in the dark for 5 days. Afterwards, 5 ml of ethanol was added, and the suspension was centrifuged at 5000 rpm for 3 hours. The free ligand supernatant was discarded, and the precipitated particles were collected and washed three times with 5 mL of ethanol. Finally, 5 mL of ethanol was added, and the mixture was ultra-sonicated for 1 hour, leading to **QD-Fc6**.

*ITO functionalization***:** Indium Tin Oxide (ITO) substrates were cleaned under sonication with solvents with increased polarity (dichloromethane, acetone, and ethanol)

for 15 min each. Subsequently, the cleaned substrates were dipped in a basic piranha solution (NH_4OH /H_2O_2 /H_2O, 1:1:5) for 30 min at 80°C to promote the hydroxyl group formation on the surface. Immediately after, the activated surfaces were rinsed with Milli-Q water and ethanol, dried with a N_2 stream and quickly immersed in a deoxygenated toluene solution containing of 3-Mercaptopropyl)trimethoxysilane (MPS) [1% (v/v)] for 12 hours. The reaction was kept in the absence of light, under an inert atmosphere and stirring conditions at 60°C. Then, surfaces were rinsed with toluene and ethanol and dried with N_2 stream, giving **S1**. **S1** was then immersed in a deoxygenated 0.1 mg/mL toluene suspension of CdSe/ZnS QDs (stabilized with TOPO). After 8 hours, the substrates were removed, rinsed with toluene and ethanol, and dried under an N_2 stream, obtaining **S2**. Finally, to prepare **S3-Hx**, **S3-Fc6** and **S3-Fc11**, **S2** was immersed for 24 hours at 60°C under mild stirring in deoxygenated 1 mM toluene solutions of 1-Hexanethiol, 6-(Ferrocenyl)hexanethiol, 11-(Ferrocenyl)undecanethiol, respectively. The reaction was carried out without light and under inert conditions. Afterwards, the substrates were also rinsed with plenty of toluene and ethanol, and dried with N_2 stream.

Characterization

Cyclic Voltammetry (CV) and *Electrochemical Impedance Spectroscopy (EIS)* were carried out with an Autolab PGSTAT101 with NOVA Advanced Electrochemical Software. The experiments were performed under inert conditions using 0.1 M $TBAPF_6$ (98%, Sigma-Aldrich), in dried acetonitrile as electrolyte. For EIS measurements, the bias was 0.21 V in a frequency range of $1 \cdot 10^5$ to 0.1 Hz. To characterize the SAMs using a redox probe, a solution of 0.1 M of KCl in Milli-Q water containing 0.01 M of $[Fe(CN)_6]^{3-/4-}$ as a redox marker was used as electrolyte. The bare or functionalized ITO

surfaces were used as working electrodes, Pt wire as counter, and Ag/AgCl as reference electrodes. The Fc content (i.e. surface coverage (Γ), was calculated as follows:

$$\Gamma = \frac{Q}{n \cdot F \cdot A}$$

$$Q = \frac{Auc}{SR}$$

where Q is the charge transferred, n corresponds to the number of electrons transferred, F is the Faraday constant, and A is the electrode area immersed in the solution. The charge transferred Q is obtained by the quotient of the area under the curve (Auc) of the redox peak through integration and the scan rate (SR).

Spectro-electrochemical assays were recorded using a Cary Eclipse Fluorimeter. The excitation wavelength was 390 nm, and the fluorescence spectra were recorded from 500 to 550 nm in a quartz fluorescence cuvette containing an electrolyte solution of 0.1 M $TBAPF_6$ in acetonitrile. For the experiments of the QD in suspension, **QD-Fc6** (c= 0.5 mg/ mL) suspensions were prepared as indicated above, and a homemade cell was used, where a platinum mesh was applied as a working electrode and platinum wires were used as counter and reference electrodes. These experiments were performed under stirring (400 rpm). On the other hand, in the experiments performed with the ITO-modified substrates, **S2** and **S3** were used as working electrodes and platinum wires as reference and counter electrodes.

Contact angle characterization was performed with a DSA100 System (KRÜSS) by automatically dispensing 3 µL of Milli-Q water drops. The measurements were carried out by triplicate.

X-Ray Photoelectron spectroscopy (XPS) measurements were performed at room temperature with a SPECS PHOIBOS 150 hemispherical analyzer (SPECS GmbH, Berlin, Germany) in a base pressure of $5x10^{-10}$ mbar using monochromatic Al K alpha

radiation (1486.74 eV) as excitation source operated at 300W. The energy resolution measured by the FWHM of the Ag 3d5/2 peak for a sputtered silver foil was 0.62 eV.

Scanning electron microscopy (SEM) was performed using a FEI Magellan 400 L XHR SE microscope equipped with a newly developed electron column with a monochromator, UC (UniColore) Technology. Landing energy of 2.00 kV and beam current of 0.10 nA were used and the signal was acquired with secondary electrons through-lens detector (TLD). Image J software was used for particle density calculations.

Confocal images were acquired with an Olympus FV1000 with a 488 nm excitation wavelength recording the emission from 500 to 600 nm. The lamp voltage was 644 V with a step size of 1.1 microns.

Dynamic Light Scattering (DLS) measurements were carried out by a Zetasizer Nano ZS using a plastic micro cuvette from Malvern Panalytical.

SUPPORTING INFORMATION FIGURES

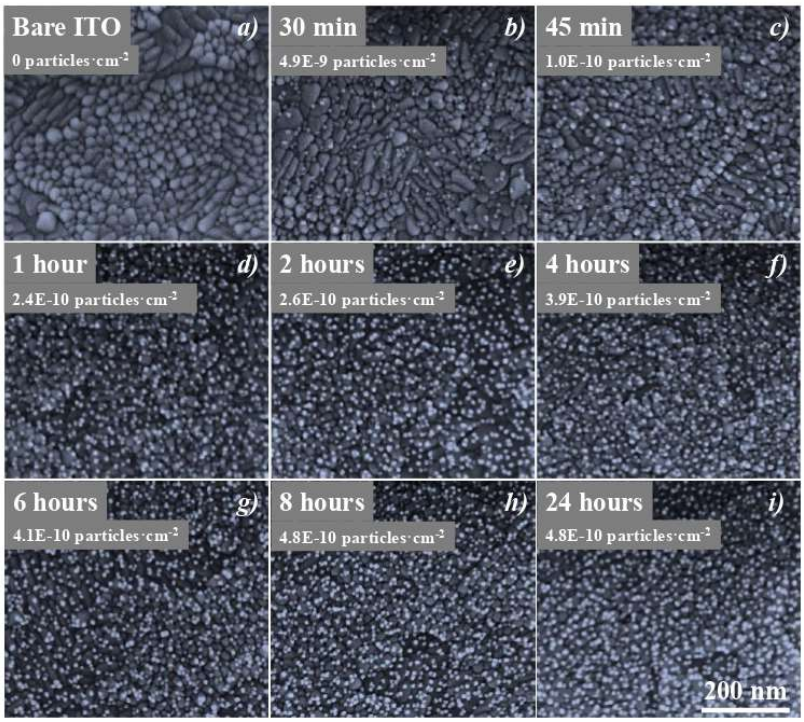

Figure S1: SEM images of **S2** prepared at different incubation times (0, 30 and 45 min, 1, 2, 4, 6, 8 and 24 hours) and their respective particle density using ImageJ software.

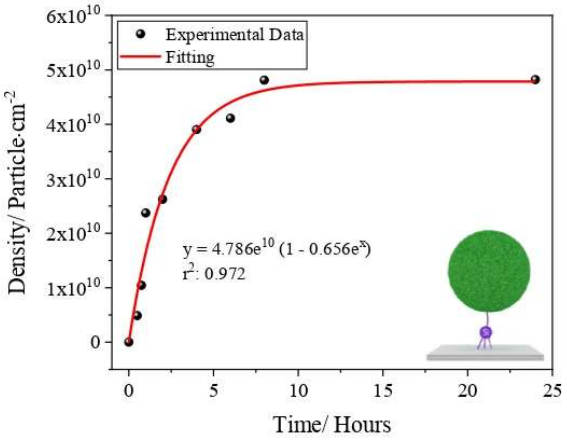

Figure S2: Particle density vs. incubation time plot for **S2**. Data extracted from Figure S1.

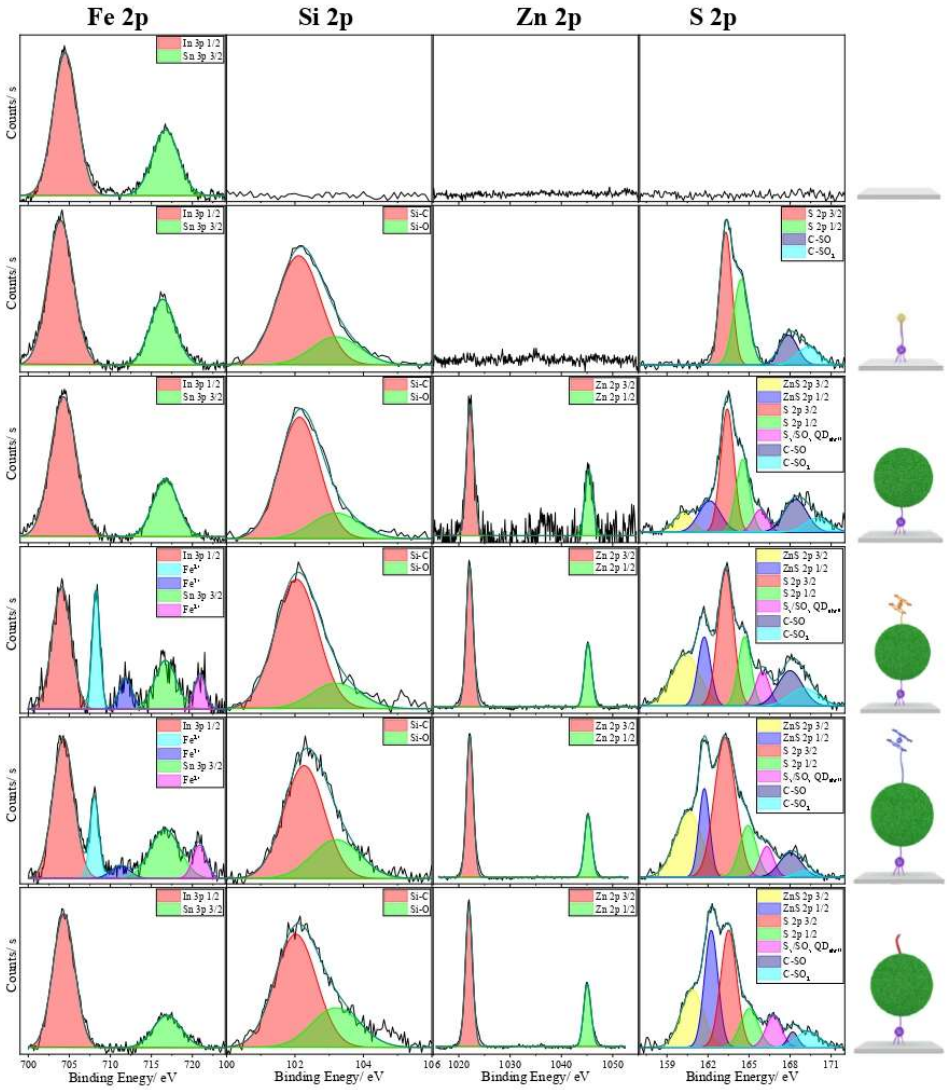

Figure S3: Fe 2p, Si 2p, Zn 2p and S 2p XPS spectra for **S0**, **S1**, **S2** and **S3** samples.

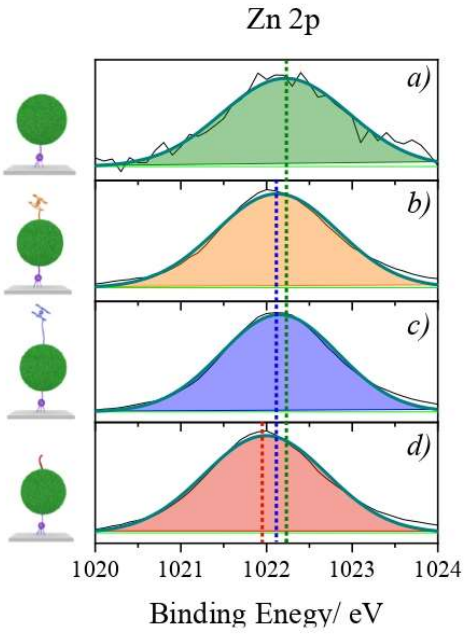

Figure S4: Binding energy shift of Zn 2p XPS spectra for *a)* **S2**, *b)* **S3-Fc6**, *c)* **S3-Fc11** and *d)* **S3-Hx**.

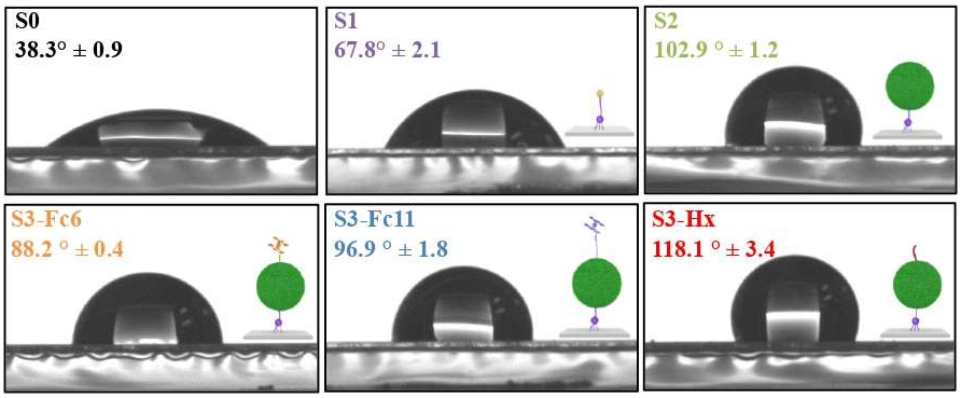

Figure S5: Contact angle images of **S0**, **S1**, **S2** and **S3** samples.

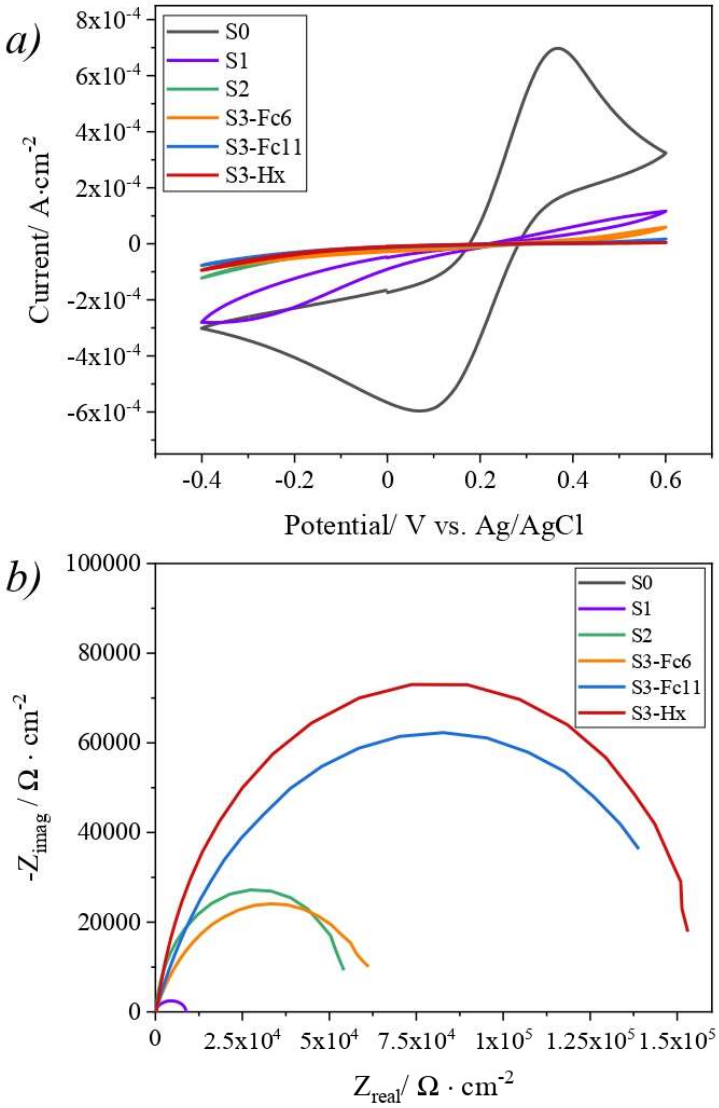

Figure S6: Electrochemical experiments using a solution of 0.1 M KCl as electrolyte in Milli-Q water with 0.01 M of $[Fe(CN)_6]^{3-/4-}$ as redox marker. Bare ITO (**S0**) and functionalized substrates (**S1**, **S2** and **S3**) were used as WE, Pt wire as CE and an Ag/AgCl electrode as reference. *a)* CV recorded at 0.1 $V \cdot s^{-1}$ scan rate from -0.4 V to 0.7 V and *b)* Nyquist plots for the different surfaces.

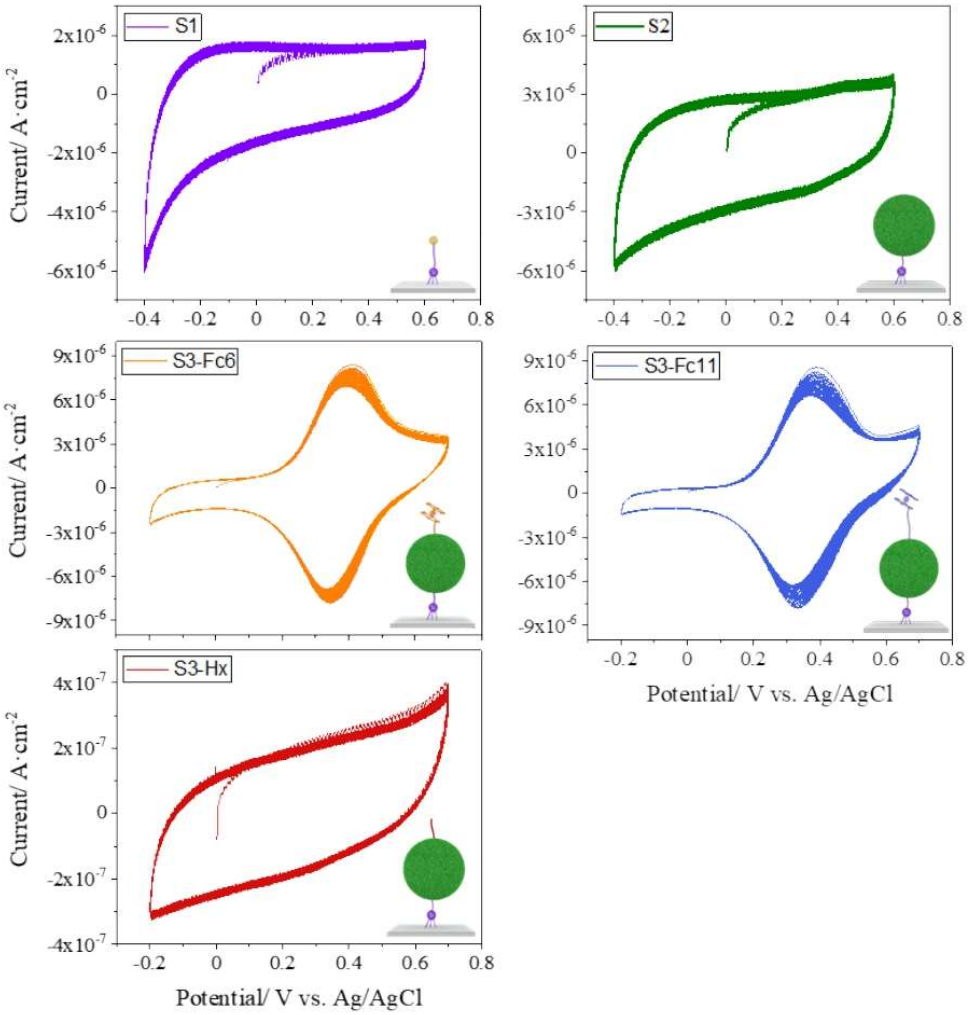

Figure S7: Voltammograms recorded in a typical three-electrode configuration cell using functionalized surfaces (**S1**, **S2** and **S3**) as working electrodes, Pt wire as counter electrode, Ag/AgCl as reference electrode. An acetonitrile solution containing 0.1 M $TBAPF_6$ as was used as electrolyte. Measurements were performed at a scan rate of 0.1 $V \cdot s^{-1}$ and 30 sweeping voltage cycles were measured.

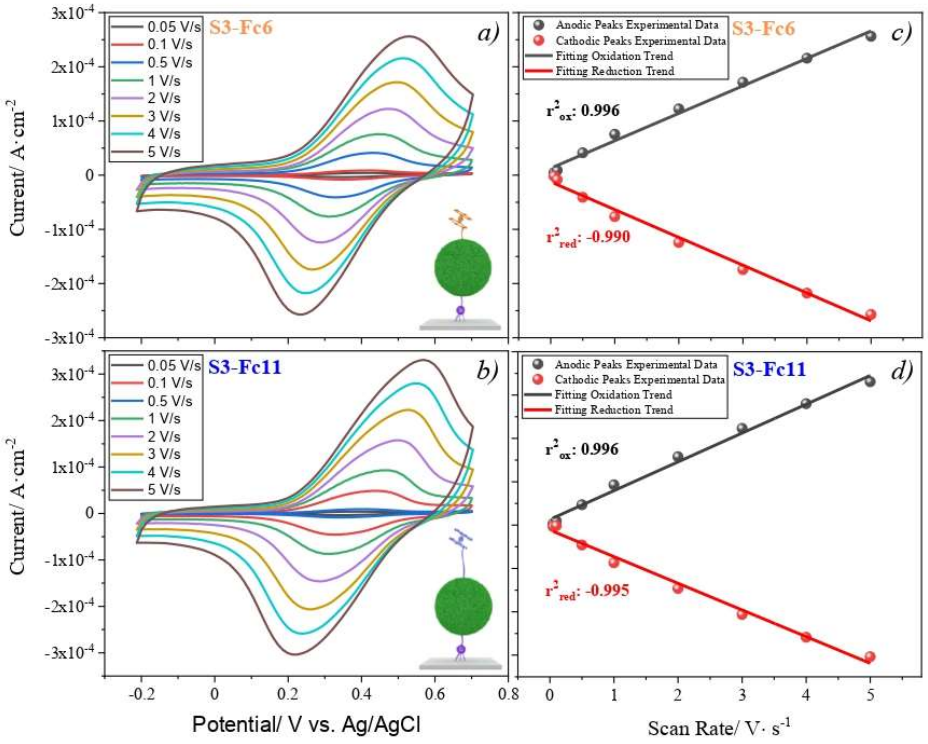

Figure S8: *a) b)* CV at different scan rates (0.05, 0.1, 0.5, 1, 2, 3, 4 and 5 $V \cdot s^{-1}$) and *c) d)* current versus scan rate plots and linear fitting for **S3-Fc6** and **S3-Fc11.** The functionalised surfaces were used as WE, Pt wire as CE and Ag/AgCl as reference electrode. Electrolyte: 0.1 M $TBAPF_6$ acetonitrile solution.

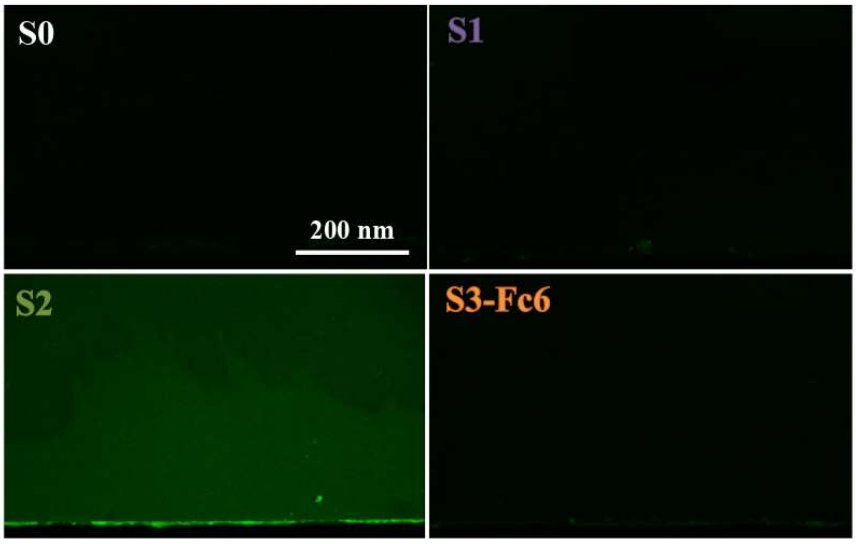

Figure S9: Confocal images for **S0** (top-left), **S1** (top-right), **S2** (bottom-left) and **S3-Fc6** (bottom-right).

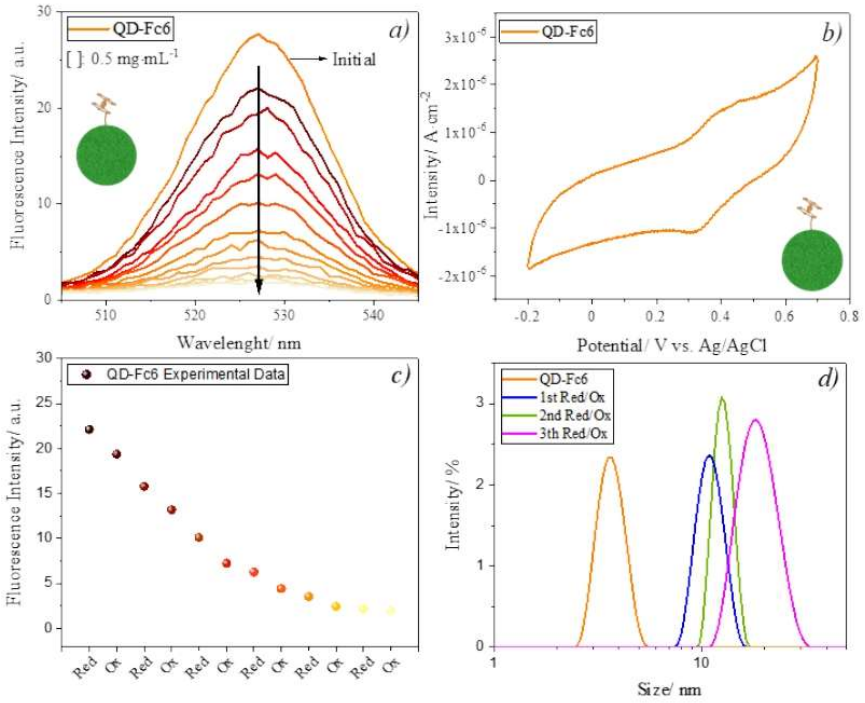

Figure S10: *a)* Fluorescence spectra for 0.5 mg·mL^{-1} **QD-Fc6** suspension in acetonitrile containing 0.1 M $TBAPF_6$ as electrolyte, acquired after subsequent applied voltages (Red/Ox at 0 V/ + 0.6 V; using a Pt mesh as WE, and Pt wire as CE and RE electrode). b) corresponding CV spectra of the suspension. *c)* Fluorescence intensity quenching upon applying consecutive switching cycles. *d)* DLS measurements before (orange) after the first (blue), second (green) and third (magenta) reduction-oxidation cycles (Red/Ox) cycles. The Red/Ox cycles consisted in applying Oxidation (+0.6 V) and reduction (0 V) potentials for 40 seconds each.

CHAPTER 3:
SAMs for Electrochemical Sensing Applications

This Chapter includes two scientific papers related to the use of molecular SAMs acting as recognition units for sensing applications. In these works, the SAM/analyte binding is driven by either supramolecular π-π or host-guest interactions, and the readout is performed using impedance electrochemical spectroscopy or an electrolyte-gated field-effect transistor.

Article III: Selective Discrimination of Toxic Polycyclic Aromatic Hydrocarbons in Water by Targeting π-Stacking Interactions

Article IV: pH Sensor Based on Supramolecular Host-Guest Interactions and an Organic Field-Effect Transistor with a Magnetic Carbon Gate Electrode

3.1 Introduction

Electrochemical sensors based on SAMs are appealing devices because the tailored interface promotes selective molecular recognition enhancing the sensor performance. Importantly, the use of an electrical transducer is particularly suitable for device integration. These devices can be easily miniaturized and integrated with an electronic acquisition module. In addition, electrochemical signals can be collected by simple, portable, low-cost instruments with low power consumption, making these sensors attractive for point-of-care (POC) tests or in-field analysis.[1,2]

Upon the SAM/analyte interaction, the electrode/electrolyte interface is modified. As mentioned in the Introduction, one method to monitor these interfacial changes is by studying the capability of the electrode to transfer electrons to/from a redox probe present in the electrolyte solution. Changes in the current intensity and/or redox peak position in the cyclic voltammogram plot as well as the modification of the charge transfer resistance (R_{CT}) measured by Electrochemical Impedance Spectroscopy (EIS) (Figure 3.1a), are commonly used to evaluate the response of the sensing SAM. From the plot of the electrical signal variation *vs.* the analyte concentration, the characteristic parameters of the sensor can be determined. These are sensitivity, selectivity, limit of detection (LOD), response time and stability.[2] These, together with the repeatability and reproducibility, are the figures of merit to be considered for validating the sensor. In the case that undesirable interferences cannot be screened from the target analyte, i.e., the impossibility of discriminating between other similar molecules, the applicability of the sensor is reduced due to the poor selectivity capacity.[3,4] Figure 3.1a-c shows the expected behaviour of an ideal sensor measured by EIS. A brief description of the main parameters that determine the operation of the sensor is given below.

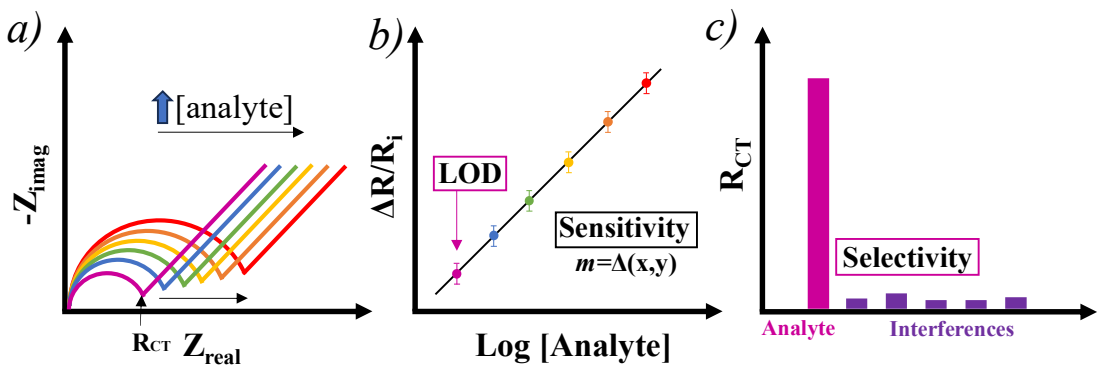

Figure 3.1: Ideal behaviour of an impedimetric sensor: a) R_{CT} changes with the analyte concentration increase; b) calibration curve, and c) selectivity illustrated by a high R_{CT}, for the analyte detection in comparison with the one obtained for the interferences.

The sensitivity is calculated from the slope (*m,* Figure 3.1b) of the calibration curve, and it refers to the change in electrical signal (current, potential, impedance, etc.) per unit change of analyte concentration.[5] The calibration curve is performed in the concentration range where the sensor responds typically linearly or logarithmically. The LOD is the lowest analyte concentration derived from a detectable signal change acquired with an acceptable degree of certainty.[6]

In order to compare data coming from different experiments, the calibration curve is often plotted using normalized values. Each point in the plot in Figure 3.1b is calculated as follows:

$$\frac{R_i - R_f}{R_i} = \frac{\Delta R}{R_i} = R_{CT'} \qquad (16)$$

where ΔR is the difference between the electron transfer resistance before (R_i) and after (R_f) each measurement, and $R_{CT'}$ is the normalized electron transfer resistance. In Figure 3.1c, the selectivity is illustrated by an electrochemical anti-interference plot, where a high $R_{CT'}$ value is measured for the target analyte, while this value is very low for the

interferences. The effect of the presence of interferences together with the analyte or the effect of a specific matrix on the sensor performance can also be evaluated by estimating the percentage of recovery, that is, by comparing the measured R_{CT}' at a specific analyte concentration ($R_{CT'analyte}$) with the value calculated from the calibration curve ($R_{CT'curve}$):

$$Recovery\ \% = \frac{R_{CT'analyte}}{R_{CT'curve}} \cdot 100 \qquad (17)$$

Finally, the response time is an important parameter to consider for high-speed or high-throughput applications since it can limit the sampling rate used.

It has been demonstrated that the use of SAMs in electrochemical sensors permits to achieve excellent results in terms of the values mentioned above and, moreover, it has the following advantages: *i)* it is an easy and versatile surface functionalization strategy *ii)* large modified surface areas can be achieved, *iii)* it allows device miniaturization and, *iv)* it is a low-cost methodology given that the sample preparation and the electrochemical characterization do not require expensive tools.[7–9]

Going into more detail about the type of molecular interactions between the SAM and the analyte, it has been demonstrated that fast, reversible and repeatable sensors with high selectivity and low LOD can be obtained making use of non-covalent but highly directional supramolecular interactions.[10–12] The governing attractive forces are mainly hydrogen bonds, electrostatic, van der Waals and hydrophobic interactions.[13] The use of supramolecular chemistry in sensing has been inspired by nature, where it plays a vital role (i.e., substrate–enzyme interactions, specific DNA–protein interactions, hydrogen bond guided interactions among nucleobases in DNA and RNA, antigen–antibody interactions, etc.).[14] Furthermore, the discovery by Pedersen of the crown-shaped macrocycle with the ability to selectively capture cationic species initiated the host-guest chemistry field.[15]

In this work, host-guest complexes formation and aromatic π-π interactions have been exploited for sensing applications (see scheme in Figure 3.2).

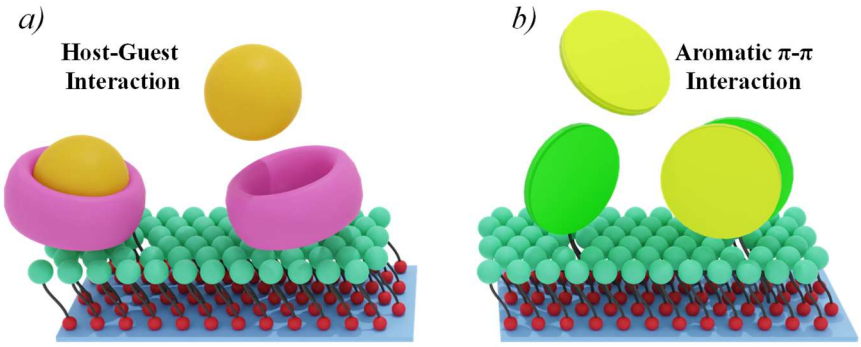

Figure 3.2: Illustration of a SAM interacting with the analyte through a) host-guest and b) π-π interactions.

Host–guest chemistry relies simply on dynamic non-covalent interactions. A widely employed strategy is the use of macrocyclic hosts (in pink in Figure 3.2a) like cyclodextrins (CD), cucurbit[n]urils, calix[n]arens, pillarenes, crown ethers and cyclophenes, among others (Figure 3.3a). They have reasonably rigid hydrophobic cavities with varying dimensions.[16] For the formation of the complexes, guest molecules (in yellow in Figure 3.2a) are partly or entirely encapsulated in the macrocyclic host cavities.[17,18] Although these interactions are weak compared to covalent bonds, the host-guest complex is stabilized by various non-covalent interactions, and can show a remarkable affinity for specific compounds.[19–21]

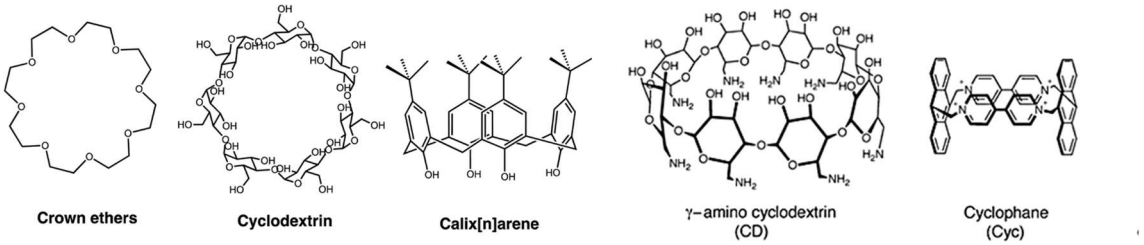

Figure 3.3: Some macrocycles used as supramolecular recognition units for sensing. Adapted from ref.[16,22]

Additionally, the formation of supramolecular assemblies by aromatic π-systems have emerged as an effective approach in sensing. The induced aggregation gives rise to conformational changes and/or different optical and charge transfer properties, which can be measured with a broad range of techniques.[23,24] The π-π interactions between two aromatic species can be classified into three categories: edge-to-face (T-shape), parallel displaced and cofacial parallel, being the latter the most common for substituted and large multiring aromatic compounds.[25]

In this part of the Thesis, we have taken advantage of the above-explained supramolecular interactions to develop two novel electrochemical sensing platforms. Article III presents robust and highly sensitive electrodes modified with SAMs conceived to impedimetrically detect a series of polycyclic aromatic hydrocarbon (PAH) pollutants in water selectively. In Article IV, an electrolyte-gated organic field-effect transistor (EGOFET) that responds to pH is reported based on the pH-dependent host-guest complex formation between β-cyclodextrin and imidazole.

3.1.1. *Article III:* Selective Discrimination of Toxic Polycyclic Aromatic Hydrocarbons in Water by Targeting π-Stacking Interactions

Pollutants in water have become a constant rising problem due to industrial development, population growth, agricultural frontier expansion and the lack of wastewater treatment. Organic pollutants in water are serious environmental and health problems due to their toxicity and hazardous effects.[26] A particular class of organic contaminants that have raised concern are Polycyclic Aromatic Hydrocarbons (PAHs) because they are serious disease promotors, such as cancer and mutagenic illness, among others. PAHs are composed of two or more fused aromatic rings in linear, angular, or cluster arrangements, and they are originated from combustion and industrial processes. The International Agency for Research on Cancer (IARC) and the US Environmental Protection Agency (EPA) have determined that PAHs are the most popular semi-volatile organic contaminants, and their monitoring has become mandatory within the environmental regulations.[23] EPA has proposed to monitor a set of 16 PAHs which are frequently found in environmental samples (Figure 3.4): naphthalene, acenaphthylene, acenaphthene, fluorene, phenanthrene, anthracene, fluoranthene, pyrene, benzo[a]anthracene, chrysene, benzo[b]fluoranthene, benzo[k]fluoranthene, benzo[a]pyrene, benzo(g,h,i)perylene, dibenzo(a,h)anthracene, indene(1,2,3–cd)pyrene.

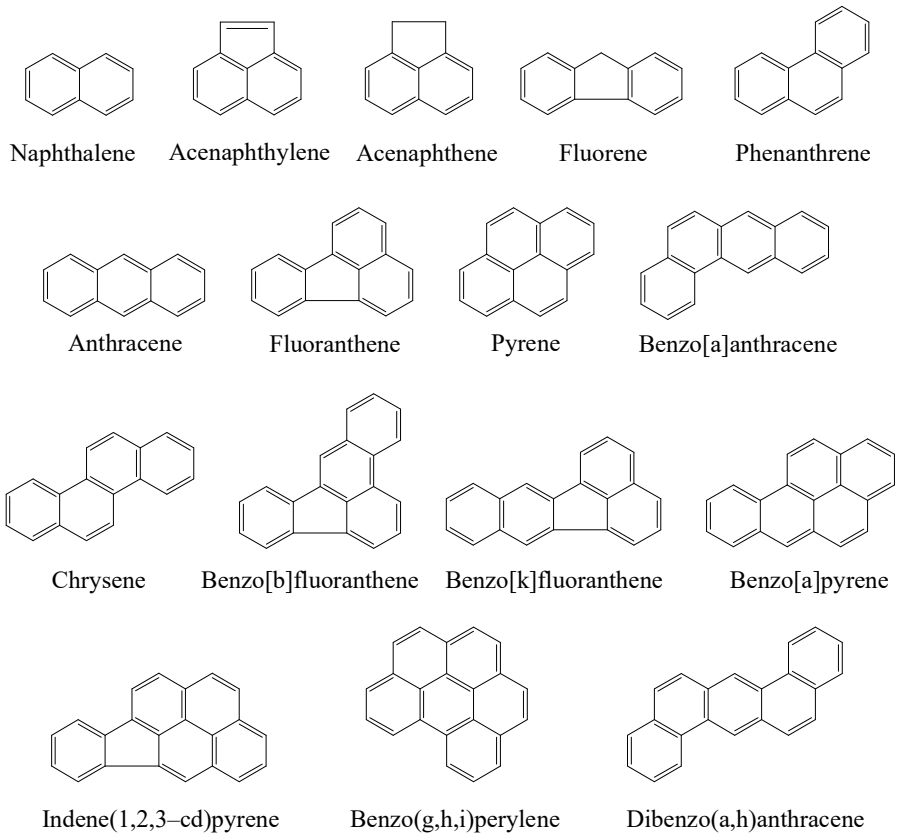

Figure 3.1: Molecular structure of the 16 most critical PAHs present in environmental samples classified by the EPA.

Many techniques have been developed for PAHs determination with great sensitivity and selectivity, such as high-performance liquid chromatography (HPLC) with UV–vis absorbance or fluorescence detection,[27–29] capillary electrophoresis[30,31] and gas-chromatography coupled with mass spectrometry (GC-MS).[32–35] Nevertheless, some limitations can be found, as follows:

- Analyte loss during sample preparation.
- Expensive methodologies.
- High time-consuming.
- Large sample volumes.
- Need of supervision by trained personnel.

Consequently, methodologies that can surmount the mentioned limitations are needed. Electrochemical tools can address these problems through low-cost, multiplexed analysis, ultrasensitive and real-time monitoring.[36] However, due to the low solubility of PAHs in water, these pollutants are found at low concentrations, representing a serious challenge to develop simple voltammetric analysis for their detection. Considering this, surface engineering offers great perspectives since it is a key strategy to fabricate highly sensitive electrochemical platforms that respond to small external stimulus.

In a previous work of the group, a pyrene-based SAM on ITO was exploited to impedimetrically detect pyrene in water through the formation of π–π interactions with a low limit of detection.[37] Remarkably, the sensor did not detect other small PAHs, which was attributed to the most favourable π−stacking interactions formed between identical PAHs. Based on these results, this Thesis aimed to go a step toward customizing the electrodes carrying the desired recognition unit to selectively discriminate between a range of small PAHs.

For the preparation of the electrode surfaces, four different PAHs were covalently grafted on ITO by the reaction between an epoxy-terminated SAM with PAH-amino derivatives. The four model PAH molecules were: naphthalene, anthracene, pyrene, and fluoranthene. Through an electronic tongue approximation and using EIS measurements, we successfully achieved the selective discrimination and quantification of these targeted PAHs in aqueous samples, even at ultra-low concentrations. The formation of π-π sandwich complexes between identical PAHs switched the surface electron transfer capability. A particularity of the investigated system is that counterintuitively upon the binding of the PAHs with the SAM, the measured R_{CT} decreased, i.e., it favored the electron transfer between the redox probe in the electrolyte solution and the electrode. This was explained by a possible reorganization of the SAM after the PAH−PAH

interactions. LODs in the 1-2 ng·mL^{-1} range were achieved for the 4 sensors, which are lower than the values reported for other electrochemical systems used for PAHs sensing.[23] Importantly, the explored PAH-based SAMs also exhibited great sensibility and selectivity, mostly displaying a response signal lower than 10 % for any interference (i.e., for the detection of PAHs differing from the one used in the SAM). Furthermore, the findings were validated by conducting experiments with a certified reference PAH mixture, which further confirmed the accuracy and reliability of the method.

Our novel and generic electrochemical approach provides a promising means to identify and differentiate pollutants based on their unique complementary π-stacking interactions, offering potential applications in environmental monitoring analysis.

3.1.2. *Article IV*: pH Sensor Based on Supramolecular Host-Guest Interactions and an Organic Field-Effect Transistor with a Magnetic Carbon Gate Electrode

Electrolyte-Gated Organic Field-Effect Transistors (EGOFETs) are excellent platforms for the development of sensors because they operate in an aqueous environment at low voltage and can transduce and amplify surface phenomena into electrical signals.[38] EGOFETs are very sensitive to interface changes, and thus, small modifications at the gate/electrolyte or electrolyte/OSC interfaces change the electrical device response. Modifying the gate electrode with a SAM that interacts with a specific analyte is an interesting approximation to progress towards more sensitive and selective (bio)sensors. Gold gate electrodes are usually employed because the surface engineering protocols are well-established, but other electrodes such as carbon-based, can also be used.[39] In particular, carbon composite electrodes (CPE) have been employed for this purpose.

CPEs are prepared from a mixture of a conductor carbon nanoallotrope and an insulator polymer.[40] The CPEs are non-toxic and environmentally friendly and have multiple other benefits such as robustness, convenient electrical conductivity, stable response in water media, high specific surface, facile tunability with a wide range of recognition elements and the active surface of the electrode can be reset by simply polishing it.

In addition, CPEs also offer the possibility to incorporate in them a magnet. In this way, an appealing route that has been followed in electrochemistry has been to functionalize magnetic nanoparticles with recognition groups, incubate them with the target analyte, and collect them on the surface of a CPE.[41] This methodology permits the concentration of the analyte on the electrode surface achieving sensors with higher sensitivity. This approach has been recently applied in our group in EGOFETs, that is, using a magnetic CPE as gate contact for the development of sensors.

Nevertheless, MPNs tend to aggregate being very sensitive to external factors such as ionic strength or pH,[42] which is a drawback for their implementation. In order to prevent irreversible clustering, several strategies have been reported, like the addition of polymers or surfactants forming lipid-like coatings around the magnetic core or nanoparticles that hinder post-nucleation cluster growth, maintaining particle domains against attractive forces.[43,44]

Paper IV describes the development of a low-cost EGOFET pH sensor using a magnetic CPE gate electrode. This electrode is used to collect from the sample solution cobalt iron oxide MNPs decorated with CdS quantum dots (QD) modified with β-cyclodextrin (β-CD) (**β-CD/CdS-QD@MNPs**, Figure 3.5). The latter forms a host-guest complex with imidazole, whose amphoteric character, with a pKa close to 7, makes this material highly suitable for investigating the host-guest interactions at various pH. At pH values above the pKa, imidazole will be mostly deprotonated and complex with β-CD,

whereas at pH values below the pKa, imidazole will be mostly protonated and will not enter into the β-CD hydrophobic cavity (Figure 3.5a). Therefore, here the well-known supramolecular complex formation between β-CD and imidazole ($[C_3H_4N_2]$) was exploited to indirectly sense the pH of the sample.

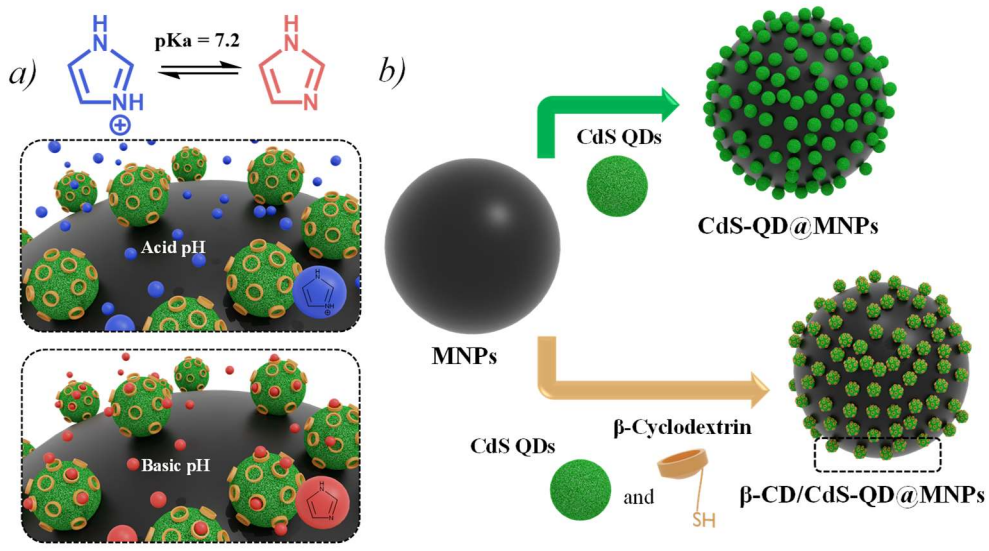

Figure 3.2: a) (top) Equilibrium between the protonated and non-protonated imidazole and (bottom) scheme of the supramolecular β-CD-$[C_3H_4N_2]$ complex formation (at basic pH) and decomplexation (at acid pH). b) Illustration of the MNPs decorated with CdS QDs modified with β-CD (**β-CD/CdS-QD@MNPs**) and without β-CD (**CdS-QD@MNPs**).

As mentioned in the paper, the prepared MNPs tend to aggregate at acid pH. The fluorescence properties of both **CdS-QD@MNPs** and **β-CD/CdS-QD@MNPs** systems were studied at pH = 2.5 to determine the influence of the β-CD on the MNPs colloidal suspension time-stability (Figure 3.6). It was found that the **CdS-QD@MNPs** suspension shows a drastic fluorescence intensity decrease (almost 50 % over 30 min.). On the contrary, the recorded signal for **β-CD/CdS-QD@MNPs** samples was stable during the measured time period. These results highlight the improved colloidal time-stability of the

particles when the QDs are functionalized with the β-CD, which may act as a surfactant stabilizing layer.

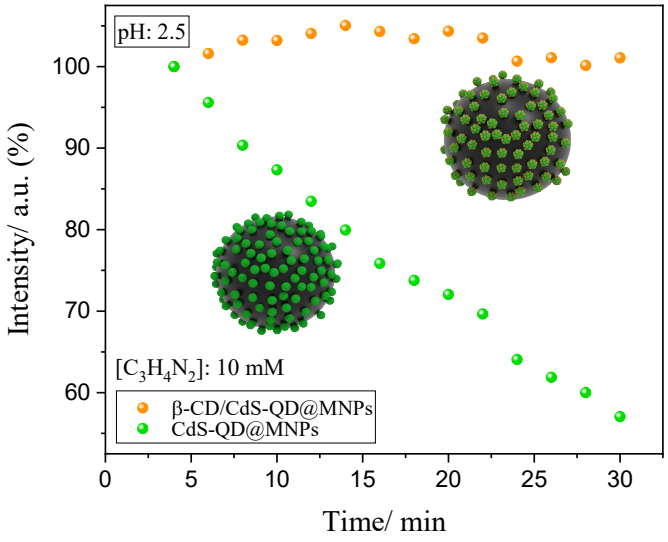

Figure 3.3: Evolution of the maximum of the emission band at 533 nm (λ_{exc} = 390 nm) at pH 2.5 over 30 min. Sample: 1 mg·mL^{-1} **CdS-QD@MNPs** (in green) and **β-CD/CdS-QD@MNPs** (in orange) in a buffer solution containing 0.1 M PBS and 10 mM [$C_3H_4N_2$].

However, the aggregation of the nanoparticles in the suspension hinders the straightforward utilization of fluorescence output for monitoring the complexation process.

Subsequently, the CPE electrodes with collected **β-CD/CdS-QD@MNPs**, after their incubation with [$C_3H_4N_2$] at acid and basic pH, were analyzed by CV and EIS using a redox marker. Using both techniques, an increase in the charge transfer resistance was observed at basic conditions, ascribed to the host-guest complex formation.

Following, the EGOFETs were fabricated and characterized in collaboration with Dr. Adrián Tamayo from our group. For the EGOFET fabrication, an organic semiconductor film based on a blend of 2,8-difluoro-5,11-bis(triethylsilylethynyl)anthradithiophene (diF-TES-ADT) with polystyrene (PS) was

prepared as previously reported.[45,46] The CPE was used as the gate electrode. For the sensor evaluation, **β-CD/CdS-QD@MNPs** were dispersed in a PBS solution containing [$C_3H_4N_2$], and after 10 minutes of incubation, the MNPs were collected at the CGE surface and measured in the EGOFET. This process was performed over a pH range of 1 to 10. It was observed that when using more basic solutions, the transfer curves displayed a notable decrease in current and a shift towards more negative gate voltages. This behaviour was attributed to the deprotonation of imidazole at high pH, allowing it to form the stable complex β-CD-[$C_3H_4N_2$]. To confirm the reversibility of the device, **β-CD/CdS-QD@MNPs** were alternatively incubated in both acid (pH = 3) and basic (pH = 9) solutions containing [$C_3H_4N_2$]. After each measurement, the CGE electrode was polished to remove the collected nanoparticles and re-used. The system exhibited high reversibility and reproducibility.

This study demonstrates the potential of supramolecular interactions for the development of sensors and highlights the broad prospects of employing magnetic gate electrodes in EGOFETs.

3.2 Summary

In summary, we showed that the development of electrochemical sensors based on electrodes functionalized with SAMs bearing recognition groups brings great opportunities to fabricate sensing platforms relevant to environmental and health applications. Remarkably, it has also been demonstrated that supramolecular interactions are an efficient route to achieve high sensitivity and selectivity.

In particular, with the works described in this Chapter, we demonstrated:

1) The successful electrochemical discrimination of hazardous PAH pollutants in aqueous samples by taking advantage of the unique supramolecular π−stacking interactions between identical aromatic small molecules, achieving great sensitivities (in the order of part per million levels, ppt).

2) The fabrication of an EGOFET-based pH sensor using a magnetic CPE gate electrode displaying high sensitivity in a wide pH range from 1 to 10. This has been achieved by exploiting the supramolecular host-guest interactions between β-CD and imidazole which influenced by the pH media. The EGOFET pH sensor exhibited excellent stability, reproducibility and re-usability.

3.3 References

1. He, S. *et al.* A review on the use of impedimetric sensors for the inspection of food quality. *Int. J. Environ. Res. Public Health* **17**, 1–30 (2020).
2. Bahadir, E. B. & Sezgintürk, M. K. A review on impedimetric biosensors. *Artif. Cells, Nanomedicine Biotechnol.* **44**, 248–262 (2016).
3. Paolesse, R., Nardis, S., Monti, D., Stefanelli, M. & Di Natale, C. Porphyrinoids for Chemical Sensor Applications. *Chem. Rev.* **117**, 2517–2583 (2017).
4. Justino, C. I. L., Rocha-Santos, T. A. & Duarte, A. C. Review of analytical figures of merit of sensors and biosensors in clinical applications. *Trends Anal. Chem.* **29**, 1172–1183 (2010).
5. Fraden, J. *Chemical sensors*. *Handbook of Modern Sensors: Physics, Designs, and Applications* (Springer, 2004).
6. Loock, H. & Wentzell, P. D. Chemical Detection limits of chemical sensors: Applications and misapplications. *Sensors Actuators B. Chem.* **173**, 157–163 (2012).
7. Ariga, K. *et al.* Review of advanced sensor devices employing nanoarchitectonics concepts. *Beilstein J. Nanotechnol.* **10**, 2014–2030 (2019).
8. Flink, S., Van Veggel, F. C. J. M. & Reinhoudt, D. N. Sensor functionalities in self-assembled monolayers. *Adv. Mater.* **12**, 1315–1328 (2000).
9. Calhoun, M. F., Sanchez, J., Olaya, D., Gershenson, M. E. & Podzorov, V. Electronic functionalization of the surface of organic semiconductors with self-assembled monolayers. *Nature* **7**, 3–8 (2008).
10. Lim, S., Kuang, Y. & Ardoña, H. A. M. Evolution of Supramolecular Systems Towards Next-Generation Biosensors. *Front. Chem.* **9**, 723111 (2021).
11. Minami, T. Organic transistor-based chemical sensors with self-assembled monolayers. *J. Incl. Phenom. Macrocycl. Chem.* **101**, 1–18 (2021).
12. Crespilho, F. N. *Advances in Bioelectrochemistry*. vol. 1 (Springer, 2022).
13. Minami, T. Design of supramolecular sensors and their applications to optical chips and organic devices. *Bull. Chem. Soc. Jpn.* **94**, 24–33 (2020).
14. Sayed, M. & Pal, H. An overview from simple host–guest systems to progressively complex supramolecular assemblies. *Phys. Chem. Chem. Phys.* **23**, 26085–26107 (2021).
15. Pedersen, C. J. Cyclic Polyethers and Their Complexes with Metal Salts. *J. Am. Chem. Soc.* **157**, 7017–7036 (1967).
16. Ghale, G. & Nau, W. M. Dynamically Analyte-Responsive Macrocyclic Host−Fluorophore Systems. *Acc. Chem. Res.* **47**, 2150–2159 (2014).
17. Shaikh, M., Mohanty, J., Bhasikuttan, A. C. & Pal, H. Tuning dual emission

behavior of p-dialkylaminobenzonitriles by supramolecular interactions with cyclodextrin hosts. *Photochem. Photobiol. Sci.* **7**, 979–985 (2008).

18. Sayed, M. & Pal, H. Supramolecularly assisted modulations in chromophoric properties and their possible applications: an overview. *J. Mater. Chem. C* **4**, 2685–2706 (2016).

19. Dsouza, R. N., Pischel, U. & Nau, W. M. Fluorescent dyes and their supramolecular host/guest complexes with macrocycles in aqueous solution. *Chem. Rev.* **111**, 7941–7980 (2011).

20. Yu, G., Jie, K. & Huang, F. Supramolecular amphiphiles based on host–guest molecular recognition motifs. *Chem. Rev.* **115**, 7240–7303 (2015).

21. Liu, W. & Stoddart, J. F. Emergent behavior in nanoconfined molecular containers. *Chem* **7**, 919–947 (2021).

22. Huang, T., Alyami, M., Kashab, N. M. & Nunes, S. P. Engineering membranes with macrocycles for precise molecular separations. *J. Mater. Chem. A* **9**, 18102–18128 (2021).

23. Comnea-stancu, I. R. Trends in Recent Developments in Electrochemical Sensors for the Determination of Polycyclic Aromatic Hydrocarbons from Water Resources and Catchment Areas. *J. Electrochem. Soc.* **168**, 047504 (2021).

24. Rasheed, T. *et al.* Trends in Analytical Chemistry Conjugated supramolecular architectures as state-of-the-art materials in detection and remedial measures of nitro based compounds : A review. *Trends Anal. Chem.* **129**, 115958 (2020).

25. Thakuria, R., Nath, N. K. & Saha, B. K. The Nature and Applications of π-π Interactions: A Perspective. *Cryst. Growth Des.* **19**, 523–528 (2019).

26. Alulema-pullupaxi, P. *et al.* Chemosphere Fundamentals and applications of photoelectrocatalysis as an efficient process to remove pollutants from water : A review. *Chemosphere* **281**, 130821 (2021).

27. Corps Ricardo, A. I., Guzmán Bernardo, F. J., Zougagh, M., Rodríguez Martín-Doimeadios, R. C. & Ríos, Á. Magnetic nanoparticles—carbon nanotubes hybrid composites for selective solid-phase extraction of polycyclic aromatic hydrocarbons and determination by ultra-high performance liquid chromatography. *Anal. Bioanal. Chem.* **409**, 5125–5132 (2017).

28. Liu, L.-H., Yang, C.-X. & Yan, X.-P. Methacrylate-bonded covalent-organic framework monolithic columns for high performance liquid chromatography. *J. Chromatogr. A* **1479**, 137–144 (2017).

29. Wang, L.-L., Yang, C.-X. & Yan, X.-P. In Situ Growth of Covalent Organic Framework Shells on Silica Microspheres for Application in Liquid Chromatography. *Chempluschem* **82**, 933–938 (2017).

30. Ferey, L. & Delaunay, N. Capillary and microchip electrophoretic analysis of polycyclic aromatic hydrocarbons. *Anal. Bioanal. Chem.* **407**, 2727–2747 (2015).

31. Ferey, L. *et al.* Use of response surface methodology to optimize the simultaneous separation of eight polycyclic aromatic hydrocarbons by capillary zone electrophoresis with laser-induced fluorescence detection. *J. Chromatogr. A* **1302**, 181–190 (2013).

32. Portolés, T., Garlito, B., Nácher-Mestre, J., Berntssen, M. H. G. & Pérez-Sánchez, J. Multi-class determination of undesirables in aquaculture samples by gas chromatography/tandem mass spectrometry with atmospheric pressure chemical ionization: A novel approach for polycyclic aromatic hydrocarbons. *Talanta* **172**, 109–119 (2017).

33. Avino, P., Notardonato, I., Perugini, L. & Russo, M. V. New protocol based on high-volume sampling followed by DLLME-GC-IT/MS for determining PAHs at ultra-trace levels in surface water samples. *Microchem. J.* **133**, 251–257 (2017).

34. Li, Y., Xian, Q. & Li, L. Development of a short path thermal desorption–gas chromatography/mass spectrometry method for the determination of polycyclic aromatic hydrocarbons in indoor air. *J. Chromatogr. A* **1497**, 127–134 (2017).

35. Santos, L. O., dos Anjos, J. P., Ferreira, S. L. C. & de Andrade, J. B. Simultaneous determination of PAHS, nitro-PAHS and quinones in surface and groundwater samples using SDME/GC-MS. *Microchem. J.* **133**, 431–440 (2017).

36. Barhoum, A. *et al.* Modern Designs of Electrochemical Sensor Platforms for Environmental Analyses: Principles, Nanofabrication Opportunities, and Challenges Ahmed. *Trends Environ. Anal. Chem.* **38**, e00199 (2023).

37. Muñoz, J., Crivillers, N. & Mas-Torrent, M. Carbon-Rich Monolayers on ITO as Highly Sensitive Platforms for Detecting Polycyclic Aromatic Hydrocarbons in Water: The Case of Pyrene. *Chem. Eur. J.* **23**, 15289–15293 (2017).

38. Adrahtas, D. Z. *et al.* Electrolyte-gated transistors for enhanced performance bioelectronics. *Nat. Rev. Methods Prim.* **1**, 66 (2021).

39. Tamayo, A., Muñoz, J. & Mas-Torrent, M. Electronic Performance of Polymer Carbon-Paste Nanoallotropes from 0D to 3D as Novel Gate Electrodes in Water-Gated Organic Field-Effect Transistors. *Adv. Electron. Mater.* **6**, 1–8 (2020).

40. Montes, R., Baeza, M. & Muñoz, J. 0D polymer nanocomposite carbon-paste electrodes using carbon nanohorns: Percolating networks, electrochemical achievements and filler comparison. *Compos. Sci. Technol.* **197**, 0–4 (2020).

41. Muñoz, J., Crivillers, N., Ravoo, B. J. & Mas-Torrent, M. Cyclodextrin-based superparamagnetic host vesicles as ultrasensitive nanobiocarriers for electrosensing. *Nanoscale* **12**, 9884–9889 (2020).

42. Guibert, C., Dupuis, V., Peyre, V. & Fresnais, J. Hyperthermia of Magnetic Nanoparticles: Experimental Study of the Role of Aggregation. *J. Phys. Chem. C* **119**, 28148–28154 (2015).

43. Gloag, L., Mehdipour, M., Chen, D., Tilley, R. D. & Gooding, J. J. Advances in the Application of Magnetic Nanoparticles for Sensing. *Adv. Mater.* **31**, 1–26 (2019).

44. Gebre, S. H. Recent developments in the fabrication of magnetic nanoparticles for the synthesis of trisubstituted pyridines and imidazoles: A green approach. *Synth. Commun.* **51**, 1669–1699 (2021).

45. Zhang, Q., Tamayo, A., Leonardi, F. & Mas-Torrent, M. Interplay between Electrolyte-Gated Organic Field-Effect Transistors and Surfactants: A Surface Aggregation Tool and Protecting Semiconducting Layer. *ACS Appl. Mater.*

Interfaces **13**, 30902–30909 (2021).

46. Temiño, I. *et al.* A Rapid, Low-Cost, and Scalable Technique for Printing State-of-the-Art Organic Field-Effect Transistors. *Adv. Mater. Technol.* **1**, 1–7 (2016).

ARTICLE III

Selective Discrimination of Toxic Polycyclic Aromatic Hydrocarbons in Water by Targeting π-Stacking Interactions

AUTHORS: Ángel Campos-Lendinez, † Jose Muñoz, † Núria Crivillers and Marta Mas-Torrent *

PUBLICATION: ACS Appl. Mater. Interfaces 2020, 12, 23, 26688-26693

ACS APPLIED MATERIALS & INTERFACES

www.acsami.org Research Article

Selective Discrimination of Toxic Polycyclic Aromatic Hydrocarbons in Water by Targeting π-Stacking Interactions

Jose Muñoz,[†] Ángel Campos-Lendinez,[†] Núria Crivillers, and Marta Mas-Torrent*

Cite This: ACS Appl. Mater. Interfaces 2020, 12, 26688−26693 Read Online

ACCESS | Metrics & More | Article Recommendations | Supporting Information

ABSTRACT: The development of highly sensitive and selective devices for rapid screening of polycyclic aromatic hydrocarbons (PAHs) in water is nowadays a crucial challenge owing to their alarming abundance in the environment and adverse health effects. Herein, inspired by the unique π−stacking interactions taking place between identical small aromatic molecules, a novel, generic, and straightforward methodology to electrochemically determine and discriminate such pollutants is described. Such a method is focused on covalently anchoring different PAHs on an indium tin oxide electrode surface by means of self-assembled monolayers. The surface-anchored PAHs act as recognition units to selectivity interact with a specific PAH target of the same nature. By tailoring the recognition platform with four different model PAH molecules (naphthalene, anthracene, pyrene, and fluoranthene) and carrying out an electronic tongue approximation, the selective discrimination and quantification of the selected PAHs in aqueous samples at ultralow concentrations were achieved impedimetrically, which were also validated using a certified reference PAH mixture.

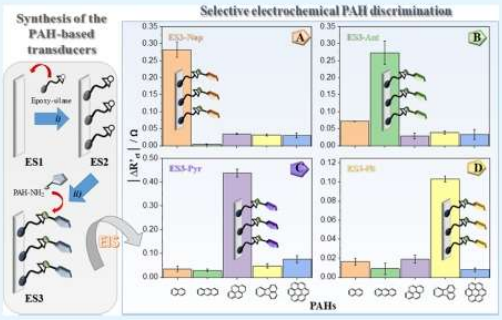

KEYWORDS: *sensors, carbon electrodes, electrochemical impedance spectroscopy, polycyclic aromatic hydrocarbons, supramolecular interactions*

INTRODUCTION

Polycyclic aromatic hydrocarbons (PAHs) are a class of organic pollutants based on fused ring aromatic molecules which possess a potential risk for the environment and human health owing to their carcinogenic and mutagenic properties, as well as high toxicity, persistency, and bioaccumulation.[1−3] More than 100 PAHs are known to be formed naturally, but only 16 of them have been promulgated by different agencies, including the U.S. Environmental Protection Agency (EPA), as priority hazardous compounds.[4,5] Because of their low water solubility, PAHs are present in the aquatic environment in the form of mixtures at trace levels, with 0.2 ppb being the EPA's maximum contaminant level established.

Standard analyses for PAH quantification are based on using bench-top chromatography instrumentation.[6] These methods are quite tedious because they require lengthy preconcentration (enrichment), extraction, and clean-up steps, which makes them not suitable for their integration into at-point-of-use devices. In this sense, electrochemical techniques open up new alternatives to develop facile and easy-to-automate analytical approaches because the transduction method is electronic. However, the electrochemical screening of PAHs is nowadays an important analytical challenge because of their trace concentration in water, which implies that the commonly employed voltammetric tools are not sensitive enough to achieve the demanded agency levels.[7,8]

Surface engineering is a key strategy to achieve highly sensitive electrochemical platforms capable of responding to small external stimuli.[9] The preparation of self-assembled monolayers (SAMs) is a simple bottom-up route employed to form onto solid supports well-defined and organized monolayers from organic molecules containing free anchoring groups for surface immobilization.[10−13] Thus, the preparation of SAMs is highly versatile and has been exploited in a wide range of fields to tune the surface properties,[14−17] including for the development of novel smart electrochemical transducers.[18−20] Very recently, our research group has combined a carbon nanotube-rich SAM surface with impedimetric analysis for determining the sum of PAHs in water via π−stacking interactions, demonstrating promising sensing results.[21] However, the main limitation of this electronic platform is its inability to discriminate between PAH targets,

Received: March 30, 2020
Accepted: May 14, 2020
Published: May 14, 2020

https://dx.doi.org/10.1021/acsami.0c05557
ACS Appl. Mater. Interfaces 2020, 12, 26688−26693

ACS Applied Materials & Interfaces www.acsami.org Research Article

Scheme 1. Schematic Representation of the Four PAH-Based Recognition Platforms Synthesized on ITO Electrodes (ES1); (i) Electrode Activation in an Oxidation Bath and Epoxy-Silane SAM Formation (ES2); (ii) Covalent Grafting of the PAH−NH_2 Recognition Units via Epoxy-Amine Cross-Linking (ES3)

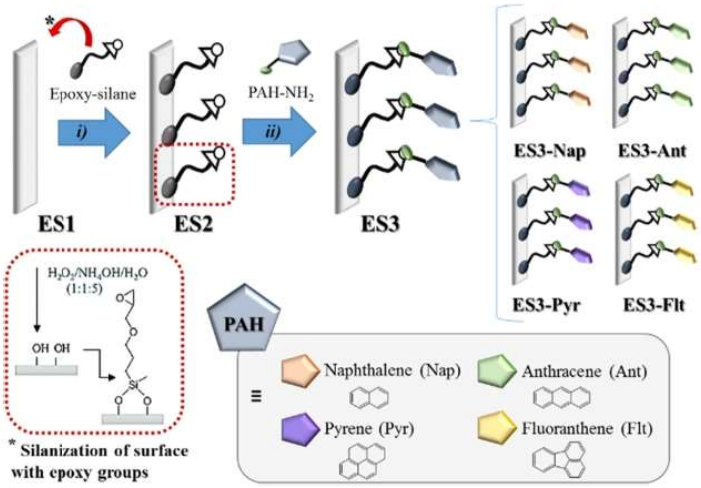

a goal that has been recently achieved utilizing an optical array device.[22]

Herein, inspired by the synergism of the unique supramolecular π−stacking interactions between identical PAH species[23,24] with the enhanced sensitivity provided by the SAM-based impedimetric systems, we report the development of a rapid, straightforward, and highly sensitive sensor focused on customizing the PAH-based recognition unit for the selective discrimination and quantification of PAH pollutants in aqueous samples. For this goal, indium tin oxide (ITO) electrodes have been covalently tuned with four different PAH-based SAMs as model recognition units [naphthalene (Nap), anthracene (Ant), pyrene (Pyr), and fluoranthene (Flt)] to detect PAHs of the same nature. The basis of this work relies on the interesting noninterfering capabilities of an impedimetric device reported previously employing a Pyr molecule as a recognition unit toward additional PAH targets.[25]

■ RESULTS AND DISCUSSION

Scheme 1 summarizes the synthesis of the different PAH-based recognition platforms via two functionalization steps. Briefly, ITO substrates (ES1) were cleaned in a solvent serially with increased polarity (dichloromethane, acetone, and ethanol) for 15 min each to degrease. Subsequently, the surfaces were activated in an oxidizing bath ($NH_4OH/H_2O_2/H_2O$, 1:1:5) for 30 min at 80 °C to promote the formation of hydroxyl groups, rinsed with abundant water, and quickly immersed in a dry toluene solution containing 3-glycidoxypropyltrimethoxysilane [1% (v/v) under inert conditions for 12 h at 60 °C (step i)], obtaining the ES2 platform. Afterward, the selected PAH recognition units bearing an $-NH_2$ group were covalently grafted on the ES2 substrates via epoxy-amine addition. This was realized by immersing them in a 1 mM solution containing either 2-naphthylamine, 2-aminoanthracene, 1-aminopyrene, or 3-aminofluoranthene [PAH−NH_2 in toluene at 80 °C for 24 h (step ii)]. This process resulted in ES3-Nap, ES3-Ant, ES3-Pyr, and ES3-Flt working electrodes. Importantly, steps (ii) and (iii) were carried out under light exclusion and under an inert atmosphere. Substrates were rinsed after each step with plenty of toluene and ethanol in order to remove the unreacted reagents and finally dried with N_2. To optimize the fabrication of the four novel PAH-based systems, the substrates were characterized at each functionalization step by cyclic voltammetry (CV), electrochemical impedance spectroscopy (EIS), and water static contact angle, as is reported in Figures S1−S3 and Table S1.

The feasibility of the different ES3 recognition platforms toward their specific PAH target was studied by EIS (Figure 1). For this aim, the four ES3 substrates were used as working electrodes and dipped into a three-electrode configuration cell filled with a 0.1 M KCl aqueous solution of 10 mM

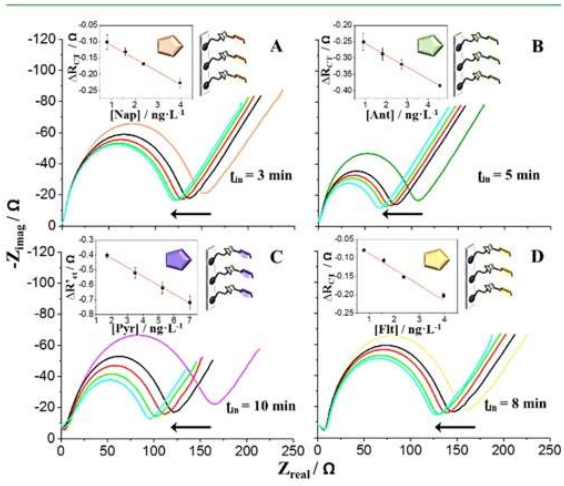

Figure 1. Nyquist plots corresponding to the impedance sensing at the (A) ES3-Nap, (B) ES3-Ant, (C) ES3-Pyr, and (D) ES3-Flt recognition platforms before and after interacting with their corresponding PAH target at different concentrations (t_{in}: incubation time). Inset: calibration plot with their corresponding error bars (n = 9). EIS measurements obtained utilizing a 0.1 M KCl solution containing 10 mM $[Fe(CN)_6]^{3-/4-}$ as the redox marker.

https://dx.doi.org/10.1021/acsami.0c05557
ACS Appl. Mater. Interfaces 2020, 12, 26688−26693

$[Fe(CN)_6]^{3-/4-}$ as the redox marker. The electroanalytical assay is focused on the excellent supramolecular π-stacking interactions between identical small aromatic structures.[25] Therefore, concentrations of Nap, Ant, Pyr, and Flt analytes in the range 0.5−7.0 ng·L^{-1} were impedimetrically monitored at the ES3-Nap, ES3-Ant, ES3-Pyr, and ES3-Flt electrodes, respectively. Aliquots of the different PAHs were directly added into the electrochemical cell and aged for the optimized times of 3, 5, 10, and 8 min, respectively, under soft stirring conditions. The electronic transfer capabilities of each ES3 recognition platform in the frequency domain before and after increasing [PAHs] were determined in terms of charge transfer resistance (R_{CT}). The resulting Nyquist plots (imaginary impedance vs real impedance) were fitted with a typical Randles equivalent circuit.[9]

Figure 1A−D evidences an interesting R_{CT} linear decrease trend with increasing [PAHs]. From an electrochemical point of view, a positive impedimetric change would be expected after supramolecular binding formation because an insulating layer on the electrode surface is generated. However, this reverse behavior can be accounted by a SAM reorganization after PAH−PAH interactions. This fact induces the formation of empty channels exposed on the electrode surface, favoring the penetration of the $[Fe(CN)_6]^{3-/4-}$ redox marker toward the electrode surface and, therefore, facilitating its redox reaction.[25] A blank reference test was run at the bare ES1 electrode using Pyr as a model PAH analyte. As shown in Figure S4, no significant impedimetric changes were observed even after employing concentrations 10^3 times larger, demonstrating the leading role of the PAH-based SAM recognition unit in the supramolecular complex formation.

For the calibration curve construction (see Figure 1, insets), EIS experiments were carried out employing three different electrodes from two different batches in order to explore the reproducibility of the experimental procedure, and each measurement was taken per triplicate in order to determine the repeatability of the analytical signal (n = 9). Importantly, it was tested that the sensing platforms, that is, the electrodes, could be stored and used 2 weeks after their fabrication without altering the performance. The low error bars from the calibration curves in Figure 1 demonstrate that the method is reproducible and repeatable, and the devices are stable along the time. The relative $\Delta R'_{CT}$ signal was calculated as follows:

$$\Delta R_{CT}{}' = \Delta R_{CT}/R_o \quad (1)$$

$$\Delta R_{CT} = R_i - R_o \quad (2)$$

where R corresponds to the electron transfer resistance of the electrodes before (R_o) and after (R_i) incubation with the different PAH concentrations. Importantly, all four ES3 systems exhibited excellent regression curves ($r^2 > 0.99$) with good sensitivities (i.e., slope) as well as extremely low limits of detection (LOD) for their corresponding PAH target in the order of part per trillion (ppt) levels, as summarized in Table 1. Therefore, the synergism of combining the high sensitivity and fast-response EIS technique with a SAM-based active sensing layer permits to simply translate any slight surface modification (as the reported supramolecular π−stacking interactions between small aromatic molecules at trace levels) into a detectable output signal.

Because anti-interference property is a critical factor for sensors, the following step was focused on interrogating the selectivity of the developed ES3 recognition electrodes toward their corresponding PAH target (Figure 2). Accordingly, effects of potential coexisting PAHs were impedimetrically examined for each ES3 system by analyzing separately five different PAH species, such as Nap, Ant, Pyr, Flt, and coronene (Cor), with two, three, four, four, and seven aromatic rings, respectively ($[PAH]_x$ = 2 ppt). As depicted in Figure 2 (dashed line), each ES3 system is much more sensitive and, therefore, selective to the PAH target equal to its recognition group, with interfering signals mostly lower than 10% in the same concentration range. These results reflect preferential supramolecular π−stacking interactions between molecules exhibiting the same aromatic skeleton (see also Figure S5) over other PAH components, which might be present in similar concentrations, driving the superior selectivity of the reported electrodes. Considering the selected PAHs studied, it can be affirmed that such selectivity does not arise only from the number of aromatic rings of the PAHs but instead relies on their molecular structure. This is reflected with the cases of Pyr and Flt; although both systems have the same number of aromatic rings, they are not significantly interfering with each other.

Table 1. Electrode Response Parameters Extracted from the Calibration Curves with Their Corresponding Confident Intervals (n = 9)

ES3	analyte	r^2	sensitivity (Ω·L·ng^{-1})	LOD (ng·L^{-1})
ES3-Nap	Nap	0.993	−0.040 ± 0.002	0.79 ± 0.08
ES3-Ant	Ant	0.999	−0.036 ± 0.004	0.91 ± 0.09
ES3-Pyr	Pyr	0.999	−0.059 ± 0.002	1.70 ± 0.06
ES3-Flt	Flt	0.993	−0.043 ± 0.001	0.79 ± 0.01

Further, an electronic tongue approximation was also carried out in order to evaluate the applicability of the developed method in a complex mixture solution.[26] Figure 3A shows schematically the followed procedure employing the ES3-Nap as a model PAH-based recognition platform, which consists in the following steps: the ES3-Nap substrate was impedimetrically measured in the three-electrode configuration cell (a) before and (b) after adding 2 ppt of Nap (its intrinsic PAH target). Afterward, (c) the three additional PAHs (Ant, Flt, and Pyr for this model system) were added and aged into the electrochemical cell to study the interference signal in terms of R_{CT} changes. Finally, (d) an additional 2 ppt of a Nap aliquot ($[Nap]_T$ = 4 ppt) was spiked for exploring the sensing discrimination in a complex matrix media. The same methodology was carried out for the other three ES3 recognition platforms (ES3-Ant, ES3-Pyr, and ES3-Flt), and the data are presented in Table S2.

Bar charts from Figure 3B represent the relative $|\Delta R'_{CT}|$ signal for a $[PAH]_{target}$ = 2 ppt (i) before and (ii) after adding 2 ppt of each additional interfering PAH, with a final concentration of $[PAH]_T$ = 8 ppt. It can be observed that there is not a significant increase in the impedimetric signal after the three additional PAHs are added into the electrochemical cell, with a $|\Delta R'_{CT}|$ increase of 4.3, 4.4, 7.7, and 7.1% for ES3-Nap, ES3-Ant, ES3-Pyr, and ES3-Flt, respectively. Therefore, this demonstrates that the electroanalytical response of the PAH-based recognition platforms is specific to their PAH target. Additionally, Figure 3C shows the % recovery achieved for a $[PAH]_{target}$ = 4 ppt [after step (d)] and, therefore, in the complex matrix media with $[PAH]_T$ = 10 ppt. The calibration curves from Figure 1 were used for each interpolation. Overall, it is important to point out the excellent

https://dx.doi.org/10.1021/acsami.0c05557
ACS Appl. Mater. Interfaces 2020, 12, 26688−26693

ACS Applied Materials & Interfaces www.acsami.org Research Article

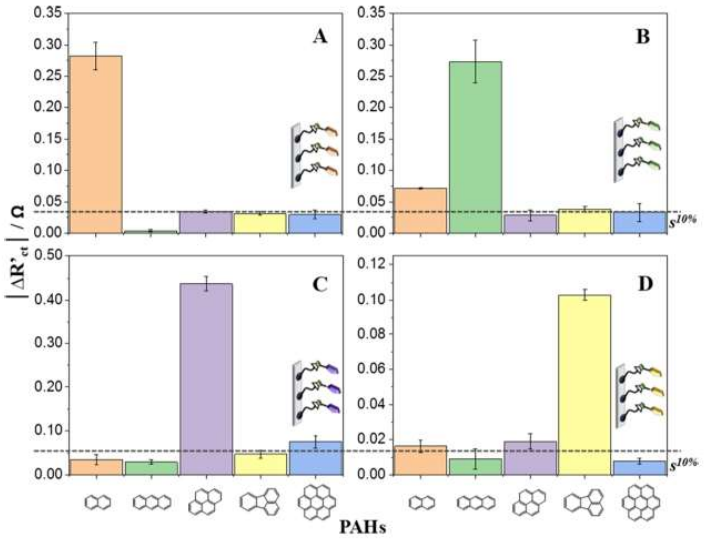

Figure 2. Electrochemical anti-interfering assay at the (A) ES3-Nap, (B) ES3-Ant, (C) ES3-Pyr, and (D) ES3-Flt using five different PAH analytes (Nap, Ant, Pyr, Flt, and Cor) with a 2 ppt concentration (dashed line: 10% of the signal derived from its corresponding PAH target, $s^{10\%}$). Bar charts are represented with their corresponding error bars (n = 9). Redox marker: 10 mM $[Fe(CN)_6]^{3-/4-}$.

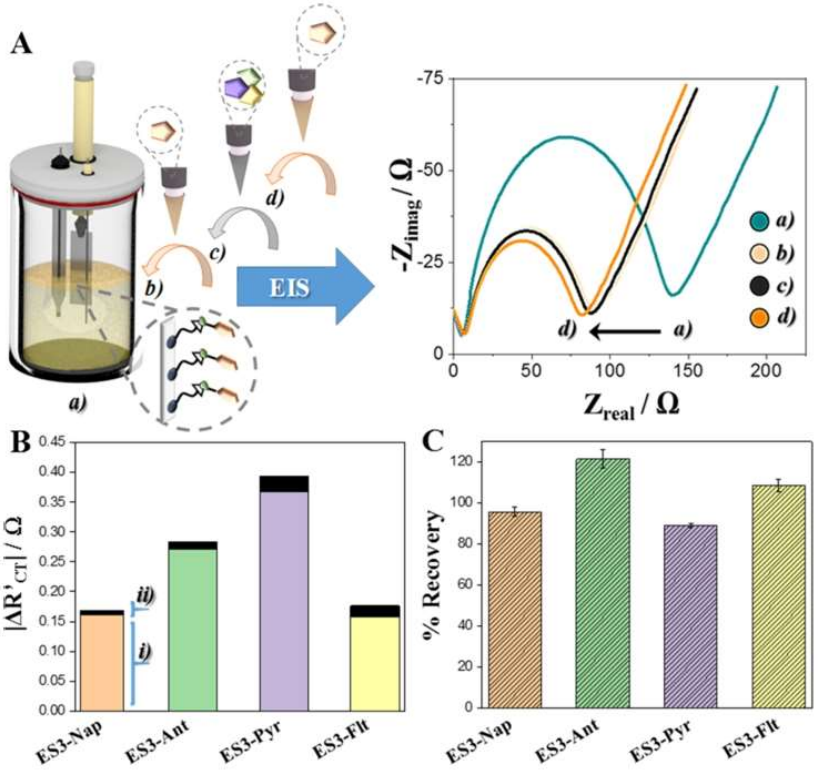

Figure 3. (A) Exemplification of the electronic tongue approximation carried out into the three-electrode configuration cell using the ES3-Nap as the model recognition platform, where the signal was measured: (a) before and (b) after adding a fixed PAH target concentration ([Nap] = 2 ppt; $[PAH]_T$ = 2 ppt), (c) after adding a same fixed concentration of the interferent PAHs ([Ant] = [Pyr] = [Flt] = 2 ppt; $[PAH]_T$ = 8 ppt), and (d) after adding again a fix concentration of the PAH target ([Nap] = 2 ppt; $[Nap]_T$ = 4 ppt and, therefore, $[PAH]_T$ = 10 ppt). (B) Relative $|\Delta R'_{CT}|$ signals derived from a $[PAH]_{target}$ = 2 ppt (i) before and (ii) after adding the three additional PAHs (interfering study). (C) %Recovery yielded for $[PAH]_{target}$ = 4 ppt in the complex matrix. Redox marker: 10 mM $[Fe(CN)_6]^{3-/4-}$.

https://dx.doi.org/10.1021/acsami.0c05557
ACS Appl. Mater. Interfaces 2020, 12, 26688−26693

recovery achieved in complex matrices after interpolating the average impedimetric response on the calibration curves for $[PAH]_{target}$ = 4 ppt (following the data reported in Table S2, 95.7, 118, 89.0, and 108% for ES3-Nap, ES3-Ant, ES3-Pyr, and ES3-Flt, respectively). Thus, these promising results demonstrate again that the interaction between identical PAH species is the most significant among all the PAHs tested in this work even in complex matrices. In this sense, it is possible to tune the sensibility of the developed surfaces toward selected PAHs by tailoring the PAH-based recognition unit.

Finally, a non-interfering method was additionally explored by employing a certified reference material (EPA 525 PAH kit from Sigma-Aldrich), which contains 13 different PAHs, including Ant and Pyr but excluding Nap and Flt, which would act here as the negative blanks (see Figure 4 for schematic illustration) for the validation of the calibration sensing curves. After spiking the electrolyte redox marker solution with the certified standard solution containing 2 ppt of each PAH ($[PAH]_T$ = 26 ppt, with [Ant] = [Pyr] = 2 ppt and [Nap] = [Flt] = 0 ppt), good recoveries were achieved for the ES3-Ant (87%) and ES3-Pyr (101%) after interpolating the average impedimetric response (n = 3) on their corresponding calibration curves (see Figure S6 and Table S3). Remarkably, the ES3-Nap and ES3-Flt electrodes (negative blank experiments) did not present significant responses (13 and 2%, respectively). Hence, it has been elucidated that the here-reported engineered sensing surface is reproducible, robust, and versatile because it can be modified for switching the selectivity of the transducer platform toward the selected EPA PAH pollutant target.

Figure 4. Schematic illustration of the noninterfering assay involving a certified reference material containing 13 different PAHs ($[PAH]_T$ = 26 ppt), which includes Ant and Pyr ([Ant] = [Pyr] = 2 ppt, being impedimetrically recognized by the ES3-Ant and ES3-Pyr, respectively) and excludes Nap and Flt ([Nap] = [Flt] = 0 ppt, negative blanks, and therefore, no impedimetric responses are obtained employing the ES3-Nap and ES3-Flt). Redox marker: 10 mM $[Fe(CN)_6]^{3-/4-}$.

CONCLUSIONS

In summary, the electrochemical discrimination of hazardous PAH pollutants in aqueous samples has been successfully achieved by taking advantage of the unique supramolecular π–stacking interactions that take place between identical aromatic small molecules. The developed method, which could be easily miniaturized because the transduction principle is electronic, paves the way for customizing electrodes with the desired recognition unit for selectively screening a broad range of small aromatic molecules.

MATERIALS AND METHODS

Chemical and Reagents. ITO substrates (single face-coated ITO over unpolished float glass; resistance: 15–25 Ω) were purchased from Delta Technologies. Both SAM-based reagents [glycidoxypropyl-trimethoxysilane (≥98%), 1-aminopyrene (97%), 2-aminoanthracene (96%), 1-naphthylamine (≥99%), and 3-aminofluoranthene (90%)] and PAH targets [Pyr (≥99%)], Ant (99%), Nap (99%), Flt (98%) and coronene (97%)] were purchased from Sigma-Aldrich. Potassium chloride (KCl, 99.5%), potassium ferricyanide/ferrocyanide ($K_3[Fe(CN)_6]/K_4[Fe(CN)_6]$, 99.8%), ammonium hydroxide (NH_4OH, 5 N), and hydrogen peroxide (H_2O_2, 30% wt) were also supplied by Sigma-Aldrich. All the organic solvents (dichloromethane, acetone, ethanol, and toluene) used were of high-performance liquid chromatography grade and acquired by Teknokroma. Aqueous solutions were prepared employing ultrapure water from a Milli-Q system (Millipore).

Apparatus. Electrochemical experiments were carried out employing Novocontrol Alpha-AN impedance and analyzed with a potentiostat POT/GAL 30V/2A electrochemical interface. Both CV and EIS experiments were run in a three-electrode configuration cell filled with a 20 mL of 0.1 M KCl solution containing 0.01 M $K_3[Fe(CN)_6]/K_4[Fe(CN)_6]$. The electrodes employed were: a single-junction Ag/AgCl as the reference electrode, a platinum wire as the counter electrode, and the ITO-based substrates as the working electrodes. The scan rate employed for CV measurements was 50 mV·s^{-1}. EIS measurements were acquired in a frequency range from 100 kHz to 0.1 Hz, using a bias of +150 mV and an AC amplitude of 5 mV. Charge transfer resistance (R_{CT}) parameters were acquired by fitting the impedance spectra to the Randles equivalent circuit with Zview software (Scribner Associates Inc.).

The contact angle (θ) measurements were obtained from a DSA 100 System (KRÜSS) by automatically dispensing 3 μL of Milli-Q water drops. Experiments were obtained per triplicate (n = 3).

Electroanalytical Assay. The electroanalytical assay was impedimetrically monitorized by means of R_{CT} changes. The different ES3 working electrodes were immersed in an aqueous solution containing a desired concentration of the selected PAH for some minutes. Such desired concentrations were achieved by adding aliquots from the stock PAH solutions: Nap 32 ppm, Ant 7.3 ppb, Flt 26 ppb, Pyr 135 ppb, and coronene 14 ppb. Each measurement was token per triplicate in three different electrodes from two different batches (n = 9) in order to evaluate both repeatability and reproducibility. Electrodes were used during two different weeks and exhibited good stability in this time.

ASSOCIATED CONTENT

Supporting Information

The Supporting Information is available free of charge at https://pubs.acs.org/doi/10.1021/acsami.0c05557.

Extended experimental procedures, physical and electrochemical characterizations, blank experiments, and electroanalytical data derived from the certified reference material (PDF)

AUTHOR INFORMATION

Corresponding Author

Marta Mas-Torrent – *Institut de Ciència de Materials de Barcelona (ICMAB-CSIC) and CIBER-BBN, 08193 Bellaterra, Spain;* orcid.org/0000-0002-1586-005X; Email: mmas@icmab.es

Authors

Jose Muñoz – *Institut de Ciència de Materials de Barcelona (ICMAB-CSIC) and CIBER-BBN, 08193 Bellaterra, Spain*

https://dx.doi.org/10.1021/acsami.0c05557
ACS Appl. Mater. Interfaces 2020, 12, 26688–26693

Ángel Campos-Lendinez – *Institut de Ciència de Materials de Barcelona (ICMAB-CSIC) and CIBER-BBN, 08193 Bellaterra, Spain*

Núria Crivillers – *Institut de Ciència de Materials de Barcelona (ICMAB-CSIC) and CIBER-BBN, 08193 Bellaterra, Spain;* orcid.org/0000-0001-6538-2482

Complete contact information is available at: https://pubs.acs.org/10.1021/acsami.0c05557

Author Contributions

†These authors contributed equally.

Notes

The authors declare no competing financial interest.

■ ACKNOWLEDGMENTS

This work was funded by the ERC StG 2012 306826 e-GAMES. The authors also thank the Networking Research Center on Bioengineering, Biomaterials, and Nanomedicine (CIBER-BBN), the DGI (Spain) project FANCY CTQ2016-80030-R, the Generalitat de Catalunya (2017-SGR-918), and the Spanish Ministry of Economy and Competitiveness through the "Severo Ochoa" program for Centers of Excellence in R&D (SEV-2015-0496). J.M. gratefully acknowledges the "Juan de la Cierva" program. A.C.-L. is enrolled in the UAB PhD program and acknowledges a FPI fellowship.

■ REFERENCES

(1) White, A. J.; Bradshaw, P. T.; Herring, A. H.; Teitelbaum, S. L.; Beyea, J.; Stellman, S. D.; Steck, S. E.; Mordukhovich, I.; Eng, S. M.; Engel, L. S.; Conway, K.; Hatch, M.; Neugut, A. I.; Santella, R. M.; Gammon, M. D. Exposure to Multiple Sources of Polycyclic Aromatic Hydrocarbons and Breast Cancer Incidence. *Environ. Int.* **2016**, *89–90*, 185–192.

(2) Shen, H.; Huang, Y.; Wang, R.; Zhu, D.; Li, W.; Shen, G.; Wang, B.; Zhang, Y.; Chen, Y.; Lu, Y.; Chen, H.; Li, T.; Sun, K.; Li, B.; Liu, W.; Liu, J.; Tao, S. Global Atmospheric Emissions of Polycyclic Aromatic Hydrocarbons from 1960 to 2008 and Future Predictions. *Envrion. Sci. Technol.* **2013**, *47*, 6415–6424.

(3) Manoli, E.; Kouras, A.; Karagkiozidou, O.; Argyropoulos, G.; Voutsa, D.; Samara, C. Polycyclic Aromatic Hydrocarbons (PAHs) at Traffic and Urban Background Sites of Northern Greece: Source Apportionment of Ambient PAH Levels and PAH-induced Lung Cancer Risk. *Environ. Sci. Pollut. Res.* **2016**, *23*, 3556–3568.

(4) Bruzzoniti, M. C.; Fungi, M.; Sarzanini, C. Determination of EPA's Priority Pollutant Polycyclic Aromatic Hydrocarbons in Drinking Waters by Solid Phase Extraction-HPLC. *Anal. Methods* **2010**, *2*, 739–745.

(5) Keith, L. H. The Source of US EPA's Sixteen PAH Priority Pollutants. *Polycycl. Aromat. Comp.* **2015**, *35*, 147–160.

(6) Bansal, V.; Kumar, P.; Kwon, E. E.; Kim, K.-H. Review of the Quantification Techniques for Polycyclic Aromatic Hydrocarbons (PAHs) in Food Products. *Crit. Rev. Food Sci. Nutr.* **2017**, *57*, 3297–3312.

(7) Díaz-González, M.; Gutiérrez-Capitán, M.; Niu, P.; Baldi, A.; Jiménez-Jorquera, C.; Fernández-Sánchez, C. Electrochemical Devices for the Detection of Priority Pollutants Listed in the EU Water Framework Directive. *TrAC, Trends Anal. Chem.* **2016**, *77*, 186–202.

(8) Nsibande, S. A.; Montaseri, H.; Forbes, P. B. C. Advances in the Application of Nanomaterial-based Sensors for Detection of Polycyclic Aromatic Hydrocarbons in Aquatic Systems. *TrAC, Trends Anal. Chem.* **2019**, *115*, 52–69.

(9) Muñoz, J.; Montes, R.; Baeza, M. Trends in Electrochemical Impedance Spectroscopy Involving Nanocomposite Transducers: Characterization, Architecture Surface and Bio-Sensing. *TrAC, Trends Anal. Chem.* **2017**, *97*, 201–215.

(10) Marchante, E.; Crivillers, N.; Buhl, M.; Veciana, J.; Mas-Torrent, M. An Electrically Driven and Readable Molecular Monolayer Switch Based on a Solid Electrolyte. *Angew. Chem., Int. Ed.* **2016**, *128*, 376–380.

(11) Mas-Torrent, M.; Rovira, C.; Veciana, J. Surface-Confined Electroactive Molecules for Multistate Charge Storage Information. *Adv. Mater.* **2013**, *25*, 462–468.

(12) Gupta, T.; van der Boom, M. E. Redox-Active Monolayers as a Versatile Platform for Integrating Boolean Logic Gates. *Angew. Chem., Int. Ed.* **2008**, *47*, 5322–5326.

(13) Casalini, S.; Bortolotti, C. A.; Leonardi, F.; Biscarini, F. Self-Assembled Monolayers in Organic Electronics. *Chem. Soc. Rev.* **2017**, *46*, 40–71.

(14) Simão, C.; Mas-Torrent, M.; Veciana, J.; Rovira, C. Multichannel Molecular Switch with a Surface-confined Electroactive Radical Exhibiting Tunable Wetting Properties. *Nano Lett.* **2011**, *11*, 4382–4385.

(15) de Boer, B.; Hadipour, A.; Mandoc, M. M.; van Woudenbergh, T.; Blom, P. W. M. Tuning of Metal Work Functions with Self-Assembled Monolayers. *Adv. Mater.* **2005**, *17*, 621–625.

(16) Angelerou, M. G. F.; Sabri, A.; Creasey, R.; Angelerou, P.; Marlow, M.; Zelzer, M. Surface-directed Modulation of Supramolecular Gel Properties. *Chem. Commun.* **2016**, *52*, 4298–4300.

(17) Galanti, A.; Diez-Cabanes, V.; Santoro, J.; Valášek, M.; Minoia, A.; Mayor, M.; Cornil, J.; Samorì, P. Electronic Decoupling in C3-symmetrical Light-responsive Tris (azobenzene) Scaffolds: Self-Assembly and Multiphotochromism. *J. Am. Chem. Soc.* **2018**, *140*, 16062–16070.

(18) Mandler, D. Chiral Self-Assembled Monolayers in Electrochemistry. *Curr. Opin. Electrochem.* **2018**, *7*, 42–47.

(19) Wong, R. A.; Yokota, Y.; Wakisaka, M.; Inukai, J.; Kim, Y. Discerning the Redox-Dependent Electronic and Interfacial Structures in Electroactive Self-Assembled Monolayers. *J. Am. Chem. Soc.* **2018**, *140*, 13672–13679.

(20) Paul, K. B.; Kumar, S.; Tripathy, S.; Vanjari, S. R. K.; Singh, V.; Singh, S. G. A Highly Sensitive Self-Assembled Monolayer Modified Copper Doped Zinc Oxide Nanofiber Interface for Detection of Plasmodium Falciparum Histidine-rich Protein-2: Targeted Towards Rapid, Early Diagnosis of Malaria. *Biosens. Bioelectron.* **2016**, *80*, 39–46.

(21) Muñoz, J.; Navarro-Senent, C.; Crivillers, N.; Mas-Torrent, M. Study of Carbon Nanotube-rich Impedimetric Recognition Electrode for Ultra-Low Determination of Polycyclic Aromatic Hydrocarbons in Water. *Microchim. Acta* **2018**, *185*, 255.

(22) Tropp, J.; Ihde, M. H.; Williams, A. K.; White, N. J.; Eedugurala, N.; Bell, N. C.; Azoulay, J. D.; Bonizzoni, M. A Sensor Array for the Discrimination of Polycyclic Aromatic Hydrocarbons Using Conjugated Polymers and the Inner Filter Effect. *Chem. Sci.* **2019**, *10*, 10247–10255.

(23) Liu, S.; Wei, M.; Zheng, X.; Xu, S.; Zhou, C. Highly Sensitive and Selective Sensing Platform based on $\pi-\pi$ Interaction between Tricyclic Aromatic Hydrocarbons with Thionine–Graphene Composite. *Anal. Chim. Acta* **2014**, *826*, 21–27.

(24) Shukla, A. D.; Strawser, D.; Lucassen, A. C. B.; Freeman, D.; Cohen, H.; Jose, D. A.; Das, A.; Evmenenko, G.; Dutta, P.; Van Der Boom, M. E. Covalent assembly of stilbene-based monolayers: Factors controlling molecular interactions. *J. Phys. Chem. B* **2004**, *108*, 17505–17511.

(25) Muñoz, J.; Crivillers, N.; Mas-Torrent, M. Carbon-Rich Monolayers on ITO as Highly Sensitive Platforms for Detecting Polycyclic Aromatic Hydrocarbons in Water: The Case of Pyrene. *Chem. Eur J.* **2017**, *23*, 15289–15293.

(26) Podrażka, M.; Bączyńska, E.; Kundys, M.; Jeleń, P. S.; Witkowska Nery, E. Electronic Tongue - A Tool for All Tastes? *Biosensors* **2017**, *8*, 3.

Supporting Information

Selective discrimination of toxic polycyclic aromatic hydrocarbons (PAHs) in water by targeting π-stacking interactions

Jose Muñoz,‡ Ángel Campos-Lendinez,‡ Núria Crivillers, Marta Mas-Torrent*

Institut de Ciència de Materials de Barcelona (ICMAB-CSIC) and CIBER-BBN, Campus UAB, 08193 Bellaterra, Spain

*e-mail: mmas@icmab.es

Table of contents

Supporting Information Figures

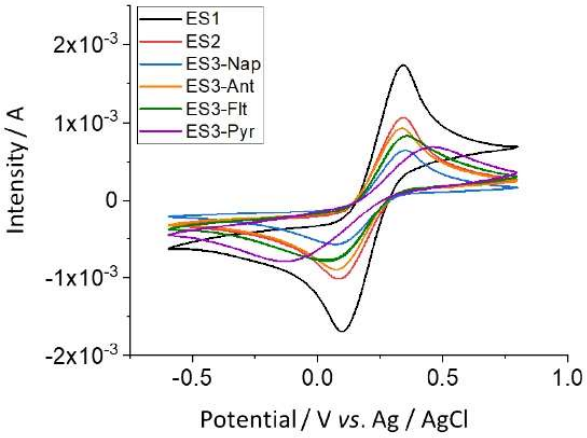

Figure S1: CV characterization of: bare ITO (black, **ES1**), ITO–silane (red, **ES2**) and the four different ITO–silane–PAH (blue, **ES3**-**Nap**; orange, **ES3**-**Ant**; green, **ES3**-**Flt** and purple, **ES3**-**Pyr**) electrodes. Experimental conditions: Redox marker: 0.01 M $[Fe(CN)_6]^{3-/4-}$; scan rate: 50 $mV \cdot s^{-1}$.

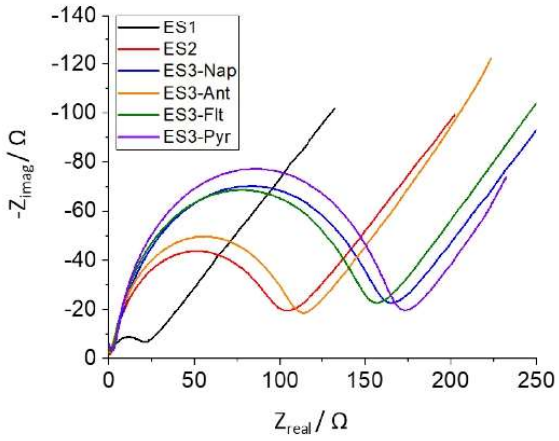

Figure S2: EIS characterization of: bare ITO (black, **ES1**), ITO–silane (red, **ES2**) and the four different ITO–silane–PAH (blue, **ES3**-**Nap**; orange, **ES3**-**Ant**; green, **ES3**-**Flt** and purple, **ES3**-**Pyr**) electrodes. Experimental conditions: Redox marker: 0.01 M $[Fe(CN)_6]^{3-/4-}$; freq.: 100 kHz – 0.1 Hz, bias: +150 mV, AC amplitude: 5 mV.

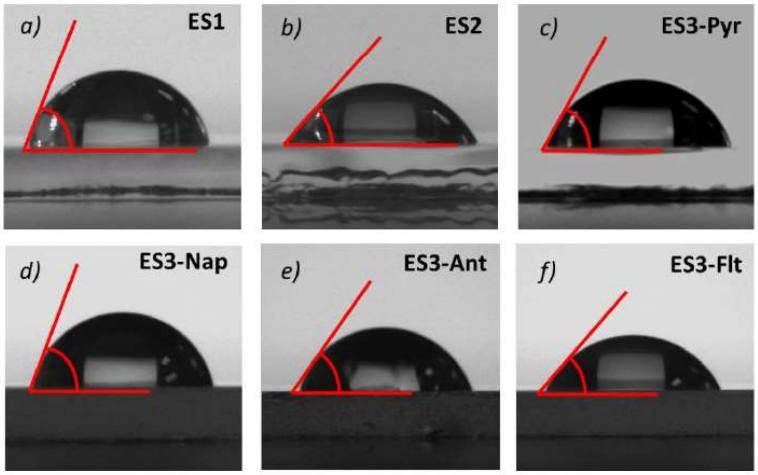

Figure S3: Water contact angle measurements of a) bare ITO (**ES1**), b) ITO–silane (**ES2**) and ITO–silane–PAH made of c) pyrene (**ES3-Pyr**), d) naphthalene (**ES3-Nap**), e) anthracene (**ES3-Ant**) and f) fluoranthene (**ES3-Flt**). Water drops of 3 µL were employed. See **Table S1** for the corresponding values.

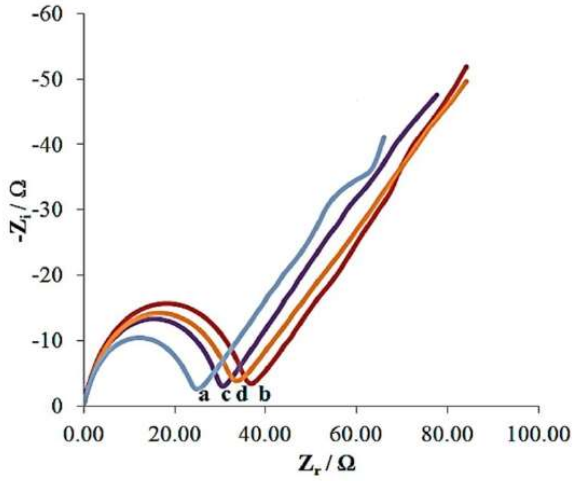

Figure S4: EIS experiments at the bare **S1** electrode in the presence of increasing concentrations of pyrene as a model PAH target. [Pyr] employed: a) 0, b) 1.75, c) 3.50 and d) 7.00 ppb. Note that no significant electrochemical changes or no lineal trend were observed even using concentrations 10^3 times higher than the ones used for the **S3**–based recognition platforms (at ppt levels). Accordingly, this fact verifies the key role of the PAH-based recognition agent in the SAM-based platform for the sensitive supramolecular recognition of the PAH targets.

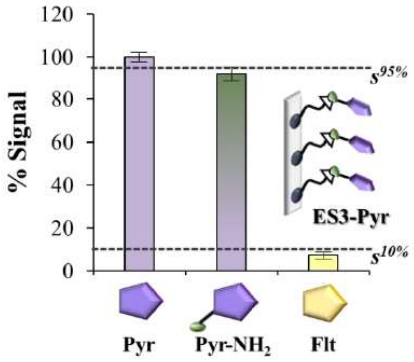

Figure S5. Additional non-interfering experiment using **ES3-Pyr** electrode to detect PAH molecules with the same number of aromatic rings (*n=4*), such as pyrene (Pyr), 1-aminopyrene (Pyr-NH_2) and fluoranthene (Flt). While the **ES3-Pyr** recognition platform is capable to discriminate between PAH molecules of different nature (*i.e.*, Pyr and Flt, note the lower % signal response (< 10%) for Flt) since the structure of fluoranthene differs significantly from the original PAH-based recognition platform, this platform cannot discriminate between PAH molecules exhibiting the same molecular skeleton *(i.e.*, Pyr and Pyr-NH_2, which only differ by a single functionality and therefore, the % signal is ≈ 95%). EIS experiments were run utilizing a fix concentration of PAHs ([PAH] = 7 ppt).

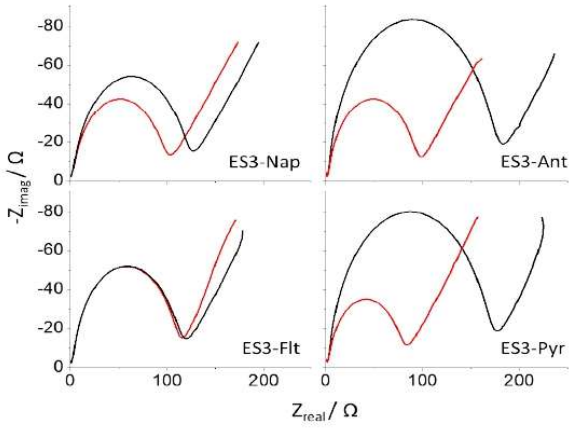

Figure S6: EIS validation experiment at the different **ES3**-based recognition platforms employing a standard EPA 525 PAH complex mixture, which contains 13 different PAHs at 2 ppt each, including Ant and Pyr and excluding Nap and Flt (as the blanks). The non-interfering method shows the EIS signal before (black line) and after incubating the corresponding **ES3** surfaces in the presence of the standard PAH solution (red line).

Supporting Information Tables

Table S1: Summary of the characterization data acquired by [a]CV, [b]EIS and [c]contact angle at each functionalization stage.

Electrodes	[a]ΔE (V)	[a]I_p (μA)	[b]R_{CT} (Ω)	[c]θ (º)
ES1	0.24	1.73	22	82.9 ± 0.1
ES2	0.25	1.05	105	62 ± 4
ES3-Nap	0.27	0.64	208	81 ± 1
ES3-Ant	0.27	0.93	112	76.2 ± 0.2
ES3-Flt	0.32	0.83	156	65.5 ± 0.4
ES3-Pyr	0.59	0.68	175	74 ± 4

Table S2: Data derived from the electronic tongue approximation study (**Figure 3**) at each EIS step employing the four different **ES3** recognition platforms.

Electrode	PAH target	$[PAH]_x$ (ppt)	Step *i)*		Step *ii)*		
			$[PAH]_T$ (ppt)	$\Delta R'_{CT}$ (Ω)	$[PAH]_T$ (ppt)	$\Delta R'_{CT}$ (Ω)	$\lvert\Delta R'_{CT}\rvert_{increase}$ (%)
ES3-Nap	Nap	2	2	0.165	8	0.172	4.3
ES3-Ant	Ant	2	2	0.279	8	0.291	4.4
ES3-Pyr	Pyr	2	2	0.367	8	0.395	7.7
ES3-Flt	Flt	2	2	0.166	8	0.177	7.1

Sensing discrimination study for a $[PAH]_{target}$ = 4 ppt in a complex mixture

Electrode	PAH target	$[PAH]_x$ spiked (ppt)	$[PAH]_{target}$ (ppt)	$[PAH]_T$ (ppt)	$\lvert\Delta R'_{CT}\rvert$ expected (Ω)	$\lvert\Delta R'_{CT}\rvert$ obtained (Ω)	% Recovery
ES3-Nap	Nap	2	4	10	0.232	0.222	95.7
ES3-Ant	Ant	2	4	10	0.364	0.430	118
ES3-Pyr	Pyr	2	4	10	0.540	0.481	89.0
ES3-Flt	Flt	2	4	10	0.218	0.235	108

Table S3: Validation method for the determination of PAHs in water using a standard PAH complex mixture employing the different **ES3**-based recognition platforms. (*) Signal derived from the y-intercept.

Recognition platform	PAH target	$[PAH]_x$ (ppt)	$\|\Delta R_{CT}\|$ expected (Ω)	$\|\Delta R_{CT}\|$ obtained (Ω)	% Recovery
ES3-Nap	Nap	0	0.083*	0.072	87
ES3-Ant	Ant	2	0.336	0.292	87
ES3-Flt	Flt	0	0.045*	0.046	102
ES3-Pyr	Pyr	2	0.414	0.420	101

ARTICLE IV

pH Sensor Based on Supramolecular Host-Guest Interactions and an Organic Field-Effect Transistor with a Magnetic Carbon Gate Electrode

AUTHORS: Ángel Campos-Lendinez, † Adrián Tamayo, † Jose Muñoz Núria Crivillers and Marta Mas-Torrent*

PUBLICATION: *Submitted* (2023)

pH sensor based on supramolecular Host-Guest interactions and an organic field-effect transistor with a magnetic carbon gate electrode

Adrián Tamayo, Ángel Campos-Lendinez, Jose Muñoz, Núria Crivillers and Marta Mas-Torrent

Institut de Ciència de Materials de Barcelona (ICMAB-CSIC), Campus de la UAB, 08193 Bellaterra, Barcelona, Spain. E-mail: mmas@icmab.es

Abstract:

A robust electrolyte-gated organic field-effect transistor (EGOFET) able to respond to pH in the range 1-10 is reported. Novelty, this is realised by exploiting the pH-dependent supramolecular host-guest complexation of imidazol/ β -cyclodextrin (β -CD). The sensing protocol is performed by incubating magnetic nanoparticles functionalised with β-CD with imidazol solutions at different pH and trapping them in a magnetic carbon electrode. Such electrode is then implemented as gate contact in the EGOFET. At higher pH the complexation is more favoured, resulting in a negative shift of the device transfer characteristics. Remarkably, the carbon gate electrode can be polished and re-used and the devices show high stability and reproducibility.

Introduction

The development of chemical sensors is technologically relevant for a wide variety of fields, such as medical diagnostics, security, food safety and environmental monitoring. In particular, there is an increasing demand for low-cost and reliable sensors capable of directly and rapidly detecting analyte molecules without the need of using expensive and time-consuming procedures. Thus, low-cost organic electronic devices have emerged as a promising solution. Electrolyte-Gated Organic Field Effect Transistors (EGOFETs) are particularly well-suited for sensing in aqueous environments due to their high sensitivity to potentiometric and capacitive changes occurring at the electrolyte/device interfaces. [1–14] Further, these devices offer clear advantages like cost-effective production, compatibility with flexible substrates and bio-compatibility.

Most of the reported EGOFET sensors rely on the use of gold gate electrodes chemically modified with bio-receptors that can interact with the target analyte. Typically, antigen-antibody systems are used for this purpose.[8,14–17] The sensing protocol consists in incubating the electrode with the analyte of interest and, subsequently, implementing it as gate contact in the EGOFET device. Recently, we have also reported that: 1) the use of host-guest supramolecular interactions is also a viable route to fabricate EGOFET-based sensors,[18] and 2) low-cost magnetic carbon paste gate electrodes (CGE) able to trap functionalized magnetic nanoparticles (MNPs) on their surface represents a promising sensing platform, being the main advantage that the electrodes can be polished and re-used.[19]

Herein, we developed a pH EGOFET sensor combining the use of supramolecular interactions with magnetic CGE. Low-cost pH sensors are important in various fields, including agriculture, environmental monitoring, and biotechnology. They are critical for measuring the acidity/alkalinity of water and soil and monitoring the pH of fermentation

or cell culture.[20–22] In this work, the sensing is realized by preparing MNPs functionalized with β-cyclodextrin (β-CD) and exploiting the well-known supramolecular complex formation between β-CD and imidazole.[23–30] The amphoteric character of imidazole derivatives, with a pKa with respect to its conjugate acid close to 7, makes this material highly suitable for studying the host-guest interaction at different pH. Our results show that the EGOFET can sense the pH of solutions in a wide window from 1 to 10 with high sensitivity and reproducibility. In addition, thanks to the re-cyclability of the CGE and the fact that the sensing event takes place outside the device, the EGOFETs can be re-used for more than fifty measurements.

Results and Discussion

With the aim of preparing MNPs functionalised with β-CD, we decorated cobalt iron oxide nanoparticles (aprox. 30 nm diameter) with CdS quantum dots (QD), known to form covalent bonds with thiols, such as per-6-thio-β-cyclodextrin.[31,32] The one-pot synthetic protocol followed was adapted from methods from literature (**Figure 1a**).[33] Briefly $Cd(NO_3)_2$ and per-6-thio-β-cyclodextrin were added to an aqueous suspension of $CoFe_2O_4$. Subsequently, the suspension was adjusted at pH 11, $Na_2S{\cdot}9H_2O$ was added, and the mixture was left overnight, giving **β-CD/CdS-QD@MNPs** (see Experimental Section). As reference, also MNPs without β-CD were prepared (**CdS-QD@MNPs**). The nanoparticles exhibited a high propensity to aggregate, which was observed using scanning transmission electron microscopy (STEM) (**Figure S1**). Magnetization data clearly show a reduction in the saturation remanent magnetization after the surface modification of the MNPs owing to a decrease in the relative amount of the magnetic component (**Figure S2**).[34–39] Thermogravimetric Analysis (TGA) shows for **β-CD/CdS-QD@MNPs** a loss of mass (2.5%) at 50-200 ºC due to moisture adsorption,[40] a second

step at 220-320 ºC (10.5 %) ascribed to cleavage of the thiol bonding between the macrocyclic and CdS,[41] and a final mass loss from 320-400 ºC corresponding to CdS degradation (**Figure S3**).[42] X-ray Photoelectron Spectroscopy (XPS) also confirms the modification of the MNPs with CdS and the incorporation of β-CD (**Figure S4**).

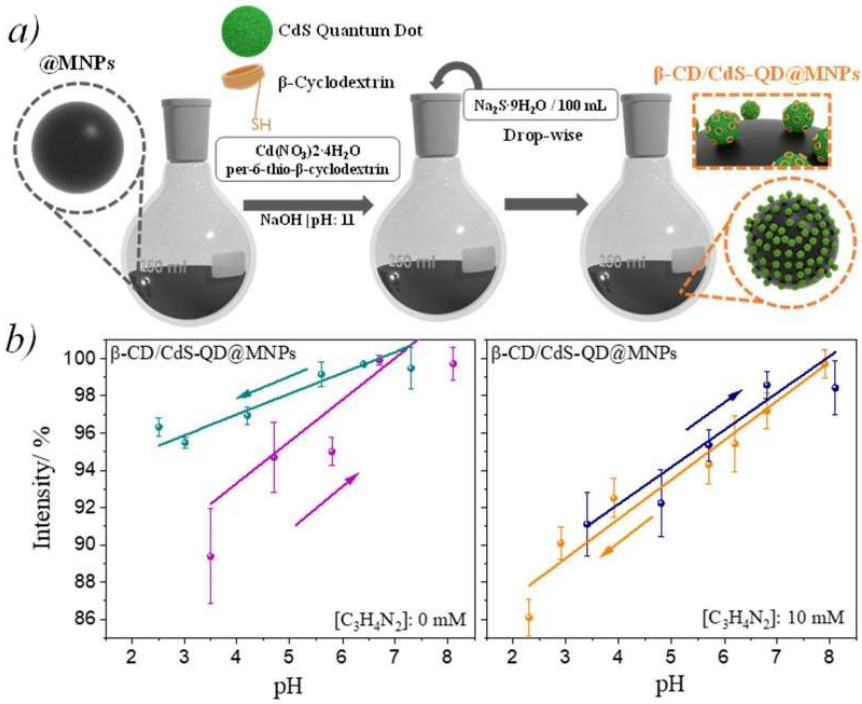

Figure 1. (a) Schematic representation of **β-CD/CdS-QD@MNPs** synthesis. (b) Emission at 533 nm (λ_{ex} = 390 nm) at different pH (from basic to acid media and vice versa) for a suspension of **β-CD/CdS-QD@MNPs** in PBS in the absence (left) and presence (right) of $[C_3H_4N_2]$. The data plotted are the average of 3 different experiments.

As previously mentioned, β-CD and imidazole ($[C_3H_4N_2]$) form a supramolecular complex.[23–25] $[C_3H_4N_2]$ is a weak base with a pKa of around 7, approximately.[43] Hence, at pH values above the pKa, imidazole will be mostly deprotonated and complex with β-

CD, whereas at pH values below the pKa, imidazole will be mostly protonated and will not enter into the β-CD hydrophobic cavity (**Figure 2**).

Taking advantage of the fluorescence properties of the prepared nanoparticles due to the presence of CdS QDs (**Figure S5**), we investigated the influence of the β-CD-[$C_3H_4N_2$] supramolecular complexation at different pHs on the optical properties. The emission properties at 533 nm (λ_{ex} = 390 nm) were investigated in a suspension of **β-CD/CdS-QD@MNPs** (1 mg·ml^{-1}) in a phosphate buffer solution (PBS) solution under stirring conditions with and without the presence of [$C_3H_4N_2$]. The pH was adjusted first from 2.3 to 8.2, and then vice-versa, in two separate experiments. As shown in **Figure 1b,** in the reference sample where imidazole is absent, we observe a quenching of the fluorescence at pH acid caused by the aggregation of the nanoparticles. When the same experiment is performed in the presence of [$C_3H_4N_2$], the same quenching tendency is observed. However, in this latter case, the dependency follows a more reversible and linear behaviour. Thus, the host-guest complexation between β-CD and [$C_3H_4N_2$] seems to stabilise the nanoparticle suspension. DLS data also confirms the aggregation process occurring at acid pH **(Figure S6)**. Hence, although it is clear that the supramolecular complex formation plays a role, due to the aggregation of the nanoparticles in the suspension, the fluorescence output cannot be easily exploited to monitor the complexation process.

Following, we use an EGOFET with a magnetic CGE to electrically read out the state of the supramolecular complex equilibrium. The EGOFETs were fabricated using as OSC film a blend of 2,8-Difluoro-5,11-bis(triethylsilylethynyl)anthradithiophene (diF-TES-ADT) with polystyrene (PS) in a weight ratio 4:1. Thin films were prepared by Bar-Assisted Meniscus Shearing on flexible Kapton substrates with pre-fabricated gold electrodes, as previously reported (see Experimental Section).[44–47] As gate contact, a CGE

was assembled using a carbon paste composite based on reduced graphene oxide and an epoxy resin as conducting filler.[47,48] In the electrode, a magnet was also inserted, as illustrated in **Figure 2**.

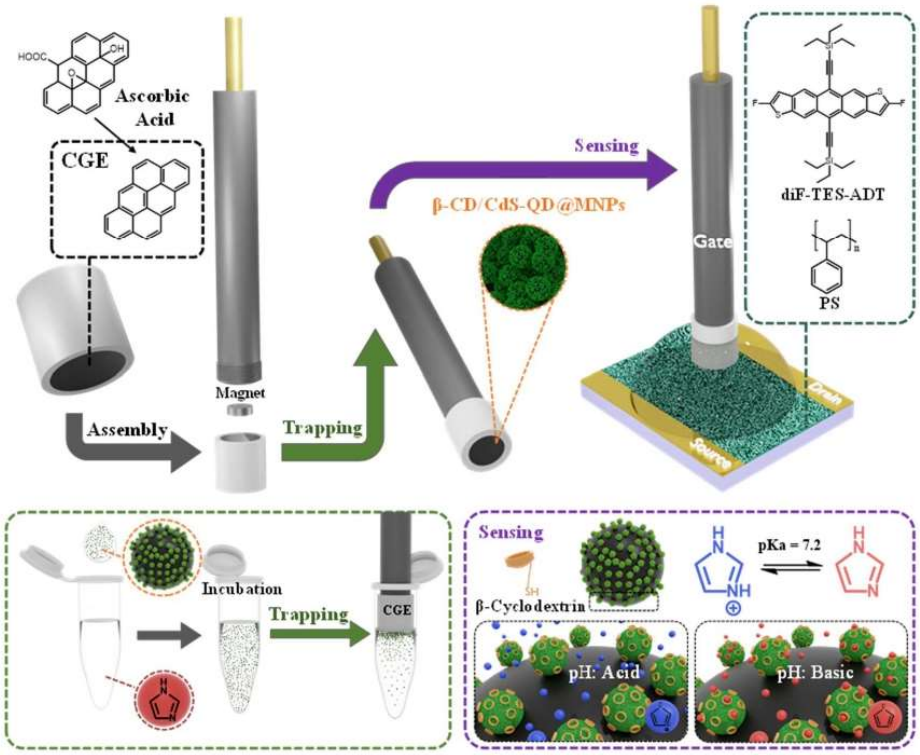

Figure 2. Schematic representation of device fabrication and their implementation as a novel approach to sense supramolecular interactions of imidazole at **β-CD/CdS-QD@MNPs**.

Electrochemical impedance spectroscopy (EIS) and cyclic voltammetry (CV) measurements were used to characterize the CGE electrodes after magnetically collecting **β-CD/CdS-QD@MNPs** (suspension of 0.33 $mg \cdot ml^{-1}$) incubated for 10 min in an imidazole solution (6.7 mM) in PBS at different pH, and rinsing with ultrapure water. The electrolyte solution consisted of a 100 mM PBS solution (pH =7.4) containing 10

mM $[Fe(CN)_6]^{3-/4-}$ as redox marker. After each measurement, the CGE was polished and re-used (see Experimental Section). In the CV, a slight decrease of the anodic and cathodic current intensities is observed with the increasing of the pH (**Figure 3a**). Accordingly, the transfer resistance (R_{CT}) values extracted by EIS show a significant increase in R_{CT} from 137±8 Ω at acid pH to 358±34 Ω at basic pH. This is ascribed to the host-guest complex formation that hinders the charge transfer between the redox probe in the solution and the electrode (**Figure 3b**).

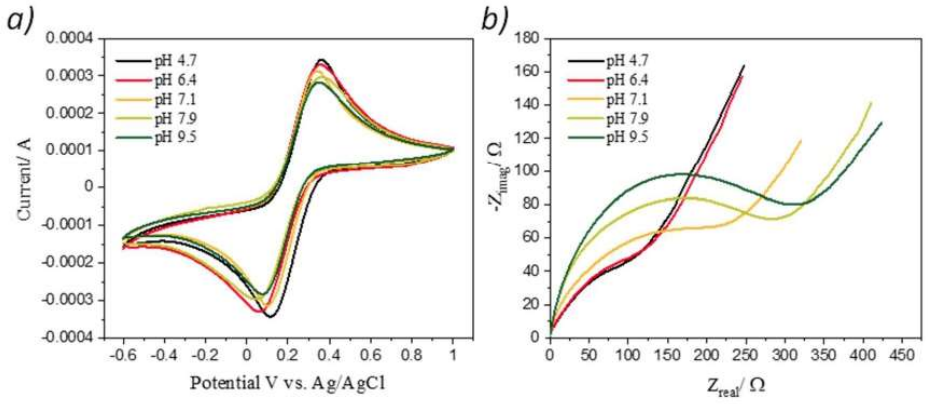

Figure 3. a) Cyclic voltammetry (scan rate: 100 $mV \cdot s^{-1}$) and b) electrochemical impedance spectroscopy characterization (Nyquist plots) recorded in a 100 mM PBS aqueous solution at neutral pH, containing 10 mM of $[Fe(CN)_6]^{3-/4-}$. A three-electrode configuration cell, using a platinum wire as counter, Ag/AgCl as reference, and a CGE coated with **β-CD/CdS-QD@MNPs** as a working electrodes were used. Before each measurement, the **β-CD/CdS-QD@MNPs** suspensions were previously incubated for 10 min in an imidazole solution at different pH. The Nyquist plots were acquired at V_{DC} = 0.2 V and V_{AC} = 5 mV (in a frequency range of 100 kHz to 100 mHz).

The EGOFETs were then characterized using the magnetic CGE electrodes. First, 200 µl of a suspension of **β-CD/CdS-QD@MNPs** (1 mg·ml^{-1}) in PBS were diluted with 400 µl of a [$C_3H_4N_2$] solution in PBS at pH 3 and 9, with increased concentration of [$C_3H_4N_2$] ranging from 10^{-4} to 0.1 M. After 10 min of incubation, the magnetic CGE was immersed in the solutions to trap the **β-CD/CdS-QD@MNPs**, rinsed with ultrapure water and implemented as gate contact in the EGOFET. The transfer characteristics (V_{DS} = -0.4 V) were recorded using Milli-Q water as electrolyte (**Figure 4**). Again, after each transfer measurement, the gate electrode was polished to remove the **β-CD/CdS-QD@MNPs** attached to the electrode surface and re-used.

The measurements performed at pH=3 are not influenced by the [$C_3H_4N_2$] concentration, which is explained by the fact that at this pH, imidazole is protonated and is not forming a complex with β-CD. In contrast, the curves performed at pH=9 show a clear dependence on [$C_3H_4N_2$]. The transfer curves are negatively shifted when increasing [$C_3H_4N_2$]. After correcting the potential offset of the different transfer characteristics recorded at pH=9, a perfect overlap of the curves is observed (**Figure S7**), which indicates that the changes observed are due to a potentiometric effect. **Figure 4c** shows the correlation between the relatve maximum drain-source current (I_{DS}) shift against [$C_3H_4N_2$], and in **Figure S8** the equivalent plot is illustrated using the threshold voltage (V_{TH}). Higher imidazole concentrations displace the complexation equilibrium towards the formation of the complex, which impacts on the device response making it more difficult to switch it on.

8

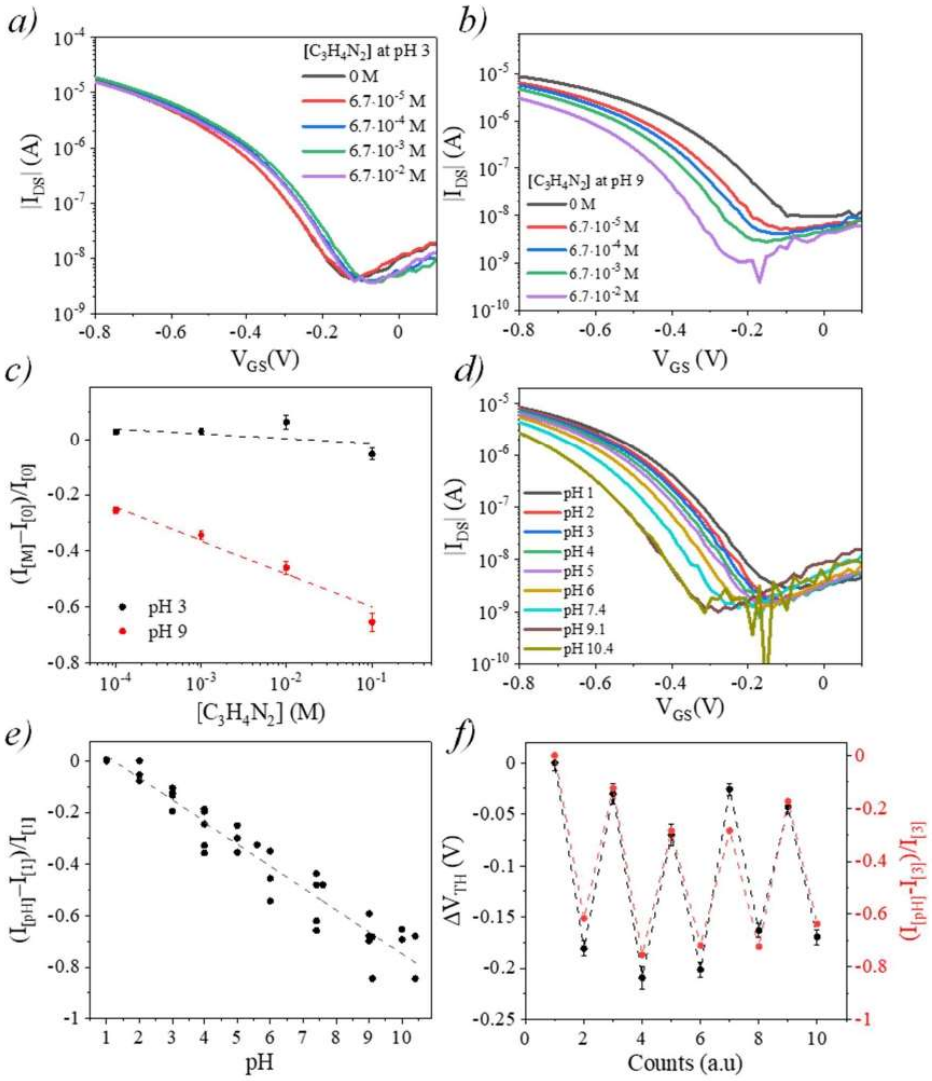

Figure 4. Transfer characteristics of the EGOFET (V_{DS} = -0.4 V) using a CGE with collected **β-CD/CdS-QD@MNPs** that had previously been incubated in a PBS solution with an increasing concentration of [$C_3H_4N_2$] (a) at pH = 3 and (b) pH=9. (c) Relative source-drain current shift (at V_{GS} = - 0.8 mV) against [$C_3H_4N_2$]. (d) Transfer characteristics of the EGOFET (V_{DS} = -0.4 V) using a CGE with collected **β-CD/CdS-QD@MNPs** that had previously been incubated in PBS solutions with [$C_3H_4N_2$] = 6.7 mM at pH ranging from 1 to 10.4. (e) Relative source-drain current (at V_{GS} = - 0.8 mV)

with respect to the current at pH=1, as a function of pH for five different devices. (f) Relative change of the I_{SD} and V_{TH} shift for 10 switching cycles in which the CGE is alternatively collecting **β-CD/CdS-QD@MNPs** incubated in a 6.7 mM imidazole solution at pH = 3 and pH= 9.

Next, the same experiment was performed, fixing the imidazole concentration at 6.7 mM and modifying the pH of the solutions used for the incubation of the nanoparticles from 1 to 10 (**Figure 4d)** and from 10 to 1 (**Figure S9)**. When more basic solutions were employed, the transfer curves exhibited a significant current decrease and a shift towards more negative gate voltages. At high pH, imidazole is not protonated and can form a stable complex with β-CD. This results in a shielding effect on the gate voltage, so then to switch on the EGOFET a higher negative voltage is required. The calibration curves averaged using data from five replicates are plotted in **Figure 4e** and **Figure S10.** Clear linear correlations are found between the relative I_{DS} and the V_{TH} shift with the pH, with a sensitivity of $0.085 \pm 0.004\ pH^{-1}$ and $-25 \pm 1\ mV \cdot pH^{-1}$, respectively. Thus, the EGOFET can be used to electrically read out the pH of a solution in the range 1-10 by exploiting the supramolecular host-guest interaction between imidazole and β-CD. The pH determines the number of empty/filled β-CD cavities, which, in turn, potentiometrically impacts on the device electrical characteristics.

Blank experiments were performed by incubating the **β-CD/CdS-QD@MNPs** in PBS solutions at different pH without [$C_3H_4N_2$]. As observed in **Figure S11**, the acquired transfer curves completely overlapped, demonstrating that there is no effect on the pH. Therefore, employing this methodology in which the magnetic nanoparticles are collected on the electrode surface, the nanoparticle aggregation occurring in the suspension when the pH is modified is not distressing the EGOFET measurements.

In order to verify the reversibility of the system, **β-CD/CdS-QD@MNPs** were incubated in acid (pH= 3) and basic (pH= 9) solutions containing imidazole ([$C_3H_4N_2$]= 6.7 mM). The **β-CD/CdS-QD@MNPs** were alternatively collected on the same CGE surface and used as gate electrode in the EGOFET, polishing the electrode after each measurement. As observed in **Figure 4f** and **Figure S12**, the system shows high reversibility, pointing out also that the polishing of the electrodes is not hampering the device response.

To evaluate the time stability of the host-guest complex, we analyzed the transfer characteristics of the EGOFET with the CGE with collected **β-CD/CdS-QD@MNPs,** previously incubated in a 6.7 mM [$C_3H_4N_2$] solution at pH=9, over a time period of 210 min. As shown in **Figure S13**, there is a shift of the threshold voltage towards positive values with time, which is in agreement with the release of [$C_3H_4N_2$] into the electrolyte solution.

Conclusions

In summary, a pH sensor EGOFET has been developed able to operate in a wide pH range (i.e., from 1 to 10) with high sensitivity. Interestingly, this has been achieved by exploiting the pH-dependence of the supramolecular complex equilibrium between imidazol and β-CD. Magnetic nanoparticles have been decorated with CdS quantum dots and functionalised with thiolated β-CD. A suspension of these **β-CD/CdS-QD@MNPs** were incubated with imidazol at different pH. By analysing the fluorescence emission of the resulting suspensions, we observed that the fluorescence is quenched at pH acid, and hence, the effect of the complexation is mixed with the aggregation of the nanoparticles. Further, the incubated nanoparticles were collected in a magnetic carbon-paste electrode and, subsequently, implemented as gate contact of an EGOFET. The device transfer characteristics clearly showed a dependance on the pH of the solutions. The more basic the pH, the complexation is favoured, which results in a potentiometric effect on the device that requires the application of a higher negative voltage to be switched on. Remarkably, the CGE could be polished and re-used and the devices showed high stability and reproducibility. Hence, this work demonstrates the potential of making use of supramolecular interactions for the development of sensors and also how the use of magnetic gate electrodes in EGOFETs offer wide perspectives in the field.

Experimental Procedures

Chemicals and reagents:

Polystyrene (PS, analytical standard, Mw ≈ 10.000 g mol^{-1}), graphene oxide (GO) powder, 2,3,4,5,6-pentafluorothiophenol (PFBT, 97%), cobalt iron oxide nanopowder (30 nm particle size),), per-6-thio-β-cyclodextrin was acquired from Cyclolab, imidazole

and anhydrous chlorobenzene (CB, ≥99.5%) were purchased from Sigma Aldrich and used as received. 2,8-Difluoro-5,11-bis(triethylsily-lethynyl)anthradithiophene (diF-TES-ADT) was purchased from Lumtec and used as received. The Epotek H77 polymeric matrix was obtained from Epoxy Technology (Billerica, MA, USA). Kapton substrates (Kapton HN, 75 μm thick) for transistor fabrication were delivered by DuPont (Wilmington, DE, USA). Polydimethylsiloxane (PDMS) was purchased from Dow Corning Corporation (Barry, UK) and prepared according to the standard protocol. All organic solvents were of HPLC grade. Deionized water (18.2 MΩ·cm) was obtained from a Milli-Q system (Millipore, Billerica, MA, USA). All the rest of the reagents were of at least analytical grade and used as received.

Nanoparticles Synthesis

β-CD/CdS@MNPs: 75 mg of MNPs were suspended in a 250 mL round-bottomed flask containing 50 mL of Milli-Q water (1.5 $mg \cdot mL^{-1}$) and ultrasonicated for 1 h. Next, *i)* 50 mL of an aqueous solution containing 5.0 mM $Cd(NO_3)_2 \cdot 4H_2O$ (the Cd^{2+} precursor) and *ii)* 1.0 mM of per-6-thio-β-cyclodextrin (thiolated β–CD), were added. The solution was adjusted at pH 11 with a 1.0 M NaOH solution and sonicated 30 min more. In this step, the driving force is focused on the electrostatic interactions between the hydroxyl groups present on the MNPs surface and the Cd^{2+} metal ion precursor. Afterwards, *iii)* 100 mL of a 2.5 mM solution of $Na_2S \cdot 9H_2O$ (the S^{2-} precursor) was added dropwise. The molar ratio of Cd^{2+} /S^{2-} was fixed at 2:1. Then, the solution was aged overnight at 65 ºC under sonication, inducing the in situ nucleation of CdS–QDs in the proximity of the MNPs. The resulting **β-CD/CdS–QD@MNPs** were magnetically removed, washed several times with Milli-Q water and ethanol, and dried overnight at 80 ºC.

CdS@MNPs: Magnetic nanoparticles containing CdS quantum dots were synthesized following the same protocol as described above but without adding the thiolated β–CD.

Electronic Device Fabrication

Interdigitated source-drain electrodes were patterned on Kapton substrates by photolithography (MicroWriter ML Laser Lithography System) and subsequent thermal evaporation of 5/45 nm of a Cr/Au (Evaporation System Auto 306 from BOC Edwards). The channel width (W) and length (L) was 10000 μm and 50 μm, respectively. Prior to the organic thin-film layer deposition, substrates were cleaned in an ultrasonic bath containing acetone and then isopropanol for 15 min. Afterwards, the substrates were exposed to an ultraviolet ozone cleaner for 25 min and then immersed in a 15×10^{-3} M PFBT solution in isopropanol for 15 min to functionalise the source-drain electrodes and rinsed with ethanol. Finally, solutions of diF-TES-ADT and PS in chorobenzene (2 wt%) were mixed in a 4:1 volume ratio and deposited in ambient conditions using the bar-assisted meniscus shearing (BAMS) technique (coating speed: 10 mm s^{-1}, substrate temperature: 105°C), as previously reported.[8,44–47]

Magnetic carbon pasted electrode fabrication

Reduced graphene oxide (rGO) was synthesized from graphene oxide (GO) via ascorbic acid reduction.[47–49] Carbon-paste electrodes were hand-made fabricated by manually mixing the rGO and the insulating epoxy resin in a 13:87 ratio (w/w) for 30 min.[47,48] Then, the paste was confined in a PVC tube (6 mm of internal diameter and 20 mm of length), with a cooper disk (5 mm of diameter and 1 mm thick) which was soldered to a connector. A neodymium magnet (3 mm diameter) was placed in the center of the

matrix electrode.[34] The electrodes were then cured at 80 °C for 24 h and finally polished with sandpapers of decreasing grain size (800 and 1200).

Apparatus and Characterization Procedures

Fluorescence Assays were recorded using a Cary Eclipse Fluorimeter. The excitation wavelength was 390 nm, and the acquisition wavelength was from 500 to 550 nm. The experiments were performed using a quartz fluorescence cuvette under stirring conditions (400 rpm).

Dynamic Light Scattering (DLS) measurements were carried out by a Zetasizer Nano ZS using a plastic micro cuvette from Malvern Panalytical. All reported results are averaged over three consecutive measurements of the same samples.

Cyclic voltammetry (CV) and electrochemical impedance spectroscopy (EIS) were recorded using an AutoLab Metrohm PGSTAT128N potentiostat/galvanostat equipped with NOVA 2.1.4 software. CV and EIS experiments were performed in a three-electrode configuration cell filled with 15 mL of 0.1 M PBS aqueous solution containing 10 mM $[Fe(CN)_6]^{3-/4-}$ as redox marker. A single junction reference electrode Ag/AgCl (3 M) and a platinum wire were used as a reference and auxiliary electrodes, respectively. The developed carbon paste electrodes were employed as working electrodes.

For the EIS measurements, a frequency range between 100 kHz to 100 mHz was employed at redox equilibrium potential (+200 mV). The signal amplitude to perturb the system was 5 mV, and the equilibrium time was 10 s. Impedimetric values were determined by plotting the Nyquist plots (Z_{real} vs Z_{imag}).

Electrical transistor characteristics were measured using an Agilent 5100A connected to the samples with a SÜSS probe station. The transfer and output characteristics were performed at ambient and dark conditions by confining 300 µL of

Milli-Q water on the interdigitated electrodes area with a PDMS pool, where the CGE was immersed. The transfer characteristics were recorded at V_{DS}= −0.4 V.

Sensing procedure

The CGE was cleaned by first polishing the surface and then rinsing it with ultrapure water to remove any polishing residues.

The [$C_3H_4N_2$] solutions were prepared in PBS 1x pH 7.2 with a concentration from 10^{-4} to 0.1 M. The pH was adjusted by adding NaOH or HCl 0.1 M to reach the desired pH (from 1 to 10.4).

The incubation protocol for the **β-CD/CdS-QD@MNPs** consisted of the following steps:

(i) 0.2 mL of a of 1 mg·mL^{-1} suspension of **β-CD/CdS-QD@MNPs** in PBS were introduced in an Eppendorf tube and filled with 0.4 mL of the [$C_3H_4N_2$] solution in PBS. The mixture was incubated for 10 minutes at room temperature under gentle stirring (Heidolph Inkubator 1000).

(ii) The **β-CD/CdS-QD@MNPs** were magnetically collected on the CGE surface by immersing the CGE in the solution.

(iii) The CGE was rinsed with ultrapure water.

(iv) The CGE with the collected nanoparticles was implemented as gate electrode in the EGOFET.

(v) After the electrical measurement, the CGE was polished and re-used.

Acknowledegements

This work was funded by the Spanish Government within the research project GENESIS PID2019-111682RB-I00 and the "Severo Ochoa" Programme for Centers of Excellence in R&D (FUNFUTURE CEX2019-000917-S). Funding was also provided by the Generalitat de Catalunya (2021 SGR 00443). Á.C.-L. is enrolled in the UAB Materials Science PhD program.

References

(1) Kergoat, L.; Herlogsson, L.; Braga, D.; Piro, B.; Pham, M. C.; Crispin, X.; Berggren, M.; Horowitz, G. A Water-Gate Organic Field-Effect Transistor. *Adv. Mater.* **2010**, *22* (23), 2565–2569.

(2) Kergoat, L.; Piro, B.; Berggren, M.; Pham, M. C.; Yassar, A.; Horowitz, G. DNA Detection with a Water-Gated Organic Field-Effect Transistor. *Org. Electron.* **2012**, *13* (1), 1–6.

(3) Kyndiah, A.; Checa, M.; Leonardi, F.; Millan-Solsona, R.; Di Muzio, M.; Tanwar, S.; Fumagalli, L.; Mas-Torrent, M.; Gomila, G. Nanoscale Mapping of the Conductivity and Interfacial Capacitance of an Electrolyte-Gated Organic Field-Effect Transistor under Operation. *Adv. Funct. Mater.* **2020**, *31* (5), 2008032.

(4) Magliulo, M.; Mallardi, A.; Mulla, M. Y.; Cotrone, S.; Pistillo, B. R.; Favia, P.; Vikholm-Lundin, I.; Palazzo, G.; Torsi, L. Electrolyte-Gated Organic Field-Effect Transistor Sensors Based on Supported Biotinylated Phospholipid Bilayer. *Adv. Mater.* **2013**, *25* (14), 2090–2094.

(5) Wang, D.; Noël, V.; Piro, B. Electrolytic Gated Organic Field-Effect Transistors for Application in Biosensors—A Review. *Electronics* **2016**, *5* (1), 9.

(6) Leonardi, F.; Tamayo, A.; Casalini, S.; Mas-Torrent, M. Modification of the Gate Electrode by Self-Assembled Monolayers in Flexible Electrolyte-Gated Organic Field Effect Transistors: Work Function: Vs. Capacitance Effects. *RSC Adv.* **2018**, *8* (48), 27509–27515.

(7) Casalini, S.; Leonardi, F.; Cramer, T.; Biscarini, F. Organic Field-Effect

Transistor for Label-Free Dopamine Sensing. *Org. Electron.* **2013**, *14* (1), 156–163.

(8) Ricci, S.; Casalini, S.; Parkula, V.; Selvaraj, M.; Saygin, G. D.; Greco, P.; Biscarini, F.; Mas-Torrent, M. Label-Free Immunodetection of α-Synuclein by Using a Microfluidics Coplanar Electrolyte-Gated Organic Field-Effect Transistor. *Biosens. Bioelectron.* **2020**, *167*, 112433.

(9) Macchia, E.; Manoli, K.; Holzer, B.; Di Franco, C.; Ghittorelli, M.; Torricelli, F.; Alberga, D.; Mangiatordi, G. F.; Palazzo, G.; Scamarcio, G.; Torsi, L. Single-Molecule Detection with a Millimetre-Sized Transistor. *Nat. Commun.* **2018**, *9* (1), 3223.

(10) Torsi, L.; Magliulo, M.; Manoli, K.; Palazzo, G. Organic Field-Effect Transistor Sensors: A Tutorial Review. *Chem. Soc. Rev.* **2013**, *42* (22), 8612–8628.

(11) Seshadri, P.; Manoli, K.; Schneiderhan-Marra, N.; Anthes, U.; Wierzchowiec, P.; Bonrad, K.; Di Franco, C.; Torsi, L. Low-Picomolar, Label-Free Procalcitonin Analytical Detection with an Electrolyte-Gated Organic Field-Effect Transistor Based Electronic Immunosensor. *Biosens. Bioelectron.* **2018**, *104* (October 2017), 113–119.

(12) Selvaraj, M.; Greco, P.; Sensi, M.; Saygin, G. D.; Bellassai, N.; D'Agata, R.; Spoto, G.; Biscarini, F. Label Free Detection of MiRNA-21 with Electrolyte Gated Organic Field Effect Transistors (EGOFETs). *Biosens. Bioelectron.* **2021**, *182* (February), 113144.

(13) Berto, M.; Diacci, C.; D'Agata, R.; Pinti, M.; Bianchini, E.; Lauro, M. Di; Casalini, S.; Cossarizza, A.; Berggren, M.; Simon, D.; Spoto, G.; Biscarini, F.; Bortolotti, C. A. EGOFET Peptide Aptasensor for Label-Free Detection of

Inflammatory Cytokines in Complex Fluids. *Adv. Biosyst.* **2018**, *2* (2), 1700072.

(14) Sailapu, S. K.; Macchia, E.; Merino-Jimenez, I.; Esquivel, J. P.; Sarcina, L.; Scamarcio, G.; Minteer, S. D.; Torsi, L.; Sabaté, N. Standalone Operation of an EGOFET for Ultra-Sensitive Detection of HIV. *Biosens. Bioelectron.* **2020**, *156*, 112103.

(15) Berto, M.; Di Lauro, M.; Biscarini, F.; Bortolotti, C. A.; Diacci, C.; Theuer, L.; Simon, D. T.; Berggren, M.; Beni, V. Label Free Urea Biosensor Based on Organic Electrochemical Transistors. *Flex. Print. Electron.* **2018**, *3* (2), 024001.

(16) Berto, M.; Casalini, S.; Di Lauro, M.; Marasso, S. L.; Cocuzza, M.; Perrone, D.; Pinti, M.; Cossarizza, A.; Pirri, C. F.; Simon, D. T.; Berggren, M.; Zerbetto, F.; Bortolotti, C. A.; Biscarini, F. Biorecognition in Organic Field Effect Transistors Biosensors: The Role of the Density of States of the Organic Semiconductor. *Anal. Chem.* **2016**, *88* (24), 12330–12338.

(17) Diacci, C.; Berto, M.; Di Lauro, M.; Bianchini, E.; Pinti, M.; Simon, D. T.; Biscarini, F.; Bortolotti, C. A. Label-Free Detection of Interleukin-6 Using Electrolyte Gated Organic Field Effect Transistors. *Biointerphases* **2017**, *12* (5), 05F401.

(18) Muñoz, J.; Leonardi, F.; Özmen, T.; Riba-Moliner, M.; González-Campo, A.; Baeza, M.; Mas-Torrent, M. Carbon-Paste Nanocomposites as Unconventional Gate Electrodes for Electrolyte-Gated Organic Field-Effect Transistors: Electrical Modulation and Bio-Sensing. *J. Mater. Chem. C* **2019**, *7* (47), 14993–14998.

(19) Tamayo, A.; Muñoz, J.; Martínez-Domingo, C.; Mas-Torrent, M. Magnetic Carbon Gate Electrodes for the Development of Electrolyte-Gated Organic Field Effect Transistor Bio-Sensing Platforms. *submitted.*

(20) Bi, X.; Hartono, D.; Yang, K.-L. Real-Time Liquid Crystal PH Sensor for Monitoring Enzymatic Activities of Penicillinase. *Adv. Funct. Mater.* **2009**, *19*, 3760–3765.

(21) Qin, M.; Guo, H.; Dai, Z.; Yan, X.; Ning, X. Advances in Flexible and Wearable PH Sensors for Wound Healing Monitoring. *J. Semicond.* **2019**, *40* (11), 111607.

(22) Manjakkal, L.; Szwagierczak, D.; Dahiya, R. Metal Oxides Based Electrochemical PH Sensors: Current Progress and Future Perspectives. *Prog. Mater. Sci.* **2020**, *109* (February 2019), 100635.

(23) Saha, S.; Ray, T.; Basak, S.; Roy, M. N. NMR, Surface Tension and Conductivity Studies to Determine the Inclusion Mechanism: Thermodynamics of Host-Guest Inclusion Complexes of Natural Amino Acids in Aqueous Cyclodextrins. *New J. Chem.* **2016**, *40* (1), 651–661.

(24) Wickstrom, L.; He, P.; Gallicchio, E.; Levy, R. M. Large Scale Affinity Calculations of Cyclodextrin Host-Guest Complexes: Understanding the Role of Reorganization in the Molecular Recognition Process. *J. Chem. Theory Comput.* **2013**, *9* (7), 3136–3150.

(25) Xu, W.; Nan, Y.; Jin, Y.; Chen, X.; Xie, M.; Chen, C.; Zhao, C. Synergy of Host-Guest and Cation-IIInteractions for an Ultrastretchable, PH-Tunable, Surface-Adaptive, and Salt-Resistant Hydrogel Adhesive. *Chem. Mater.* **2022**, *34* (19), 8740–8748.

(26) Chowdhury, P.; Panja, S.; Chakravorti, S. Photophysical Behaviour of 4-(Imidazole-1-Yl) Phenol and Its Complexation with β-Cyclodextrin in Ground and Excited States. *Spectrochim. Acta - Part A Mol. Biomol. Spectrosc.* **2004**, *60* (10), 2295–2303.

(27) Suresh, P.; Pitchumani, K. Per-6-Amino-β-Cyclodextrin as an Efficient Supramolecular Ligand and Host for Cu(I)-Catalyzed N-Arylation of Imidazole with Aryl Bromides. *J. Org. Chem.* **2008**, *73* (22), 9121–9124.

(28) Niehues, M.; Engel, S.; Ravoo, B. J. Photo-Responsive Self-Assembly of Plasmonic Magnetic Janus Nanoparticles. *Langmuir* **2021**, *37* (37), 11123–11130.

(29) Samanta, A.; Bart Jan, R. Magnetic Separation of Proteins by a Self-Assembled Supramolecular Ternary Complex. *Angew. Chemie Int. Ed.* **2014**, *53* (47), 12946–12950.

(30) Engel, S.; Möller, N.; Stricker, L.; Peterlechner, M.; Ravoo, B. J. A Modular System for the Design of Stimuli-Responsive Multifunctional Nanoparticle Aggregates by Use of Host–Guest Chemistry. *Small* **2018**, *14* (16), 1704287.

(31) Tavasoli, E.; Guo, Y.; Kunal, P.; Grajeda, J.; Gerber, A.; Vela, J. Surface Doping Quantum Dots with Chemically Active Native Ligands: Controlling Valence without Ligand Exchange. *Chem. Mater.* **2012**, *24* (21), 4231–4241.

(32) Chang, C. M.; Orchard, K. L.; Martindale, B. C. M.; Reisner, E. Ligand Removal from CdS Quantum Dots for Enhanced Photocatalytic H2 Generation in PH Neutral Water. *J. Mater. Chem. A* **2016**, *4* (8), 2856–2862.

(33) Mahapatra, N.; Panja, S.; Mandal, A.; Halder, M. A Single Source-Precursor Route for the One-Pot Synthesis of Highly Luminescent CdS Quantum Dots as Ultra-Sensitive and Selective Photoluminescence Sensor for Co2+ and Ni2+ Ions. *J. Mater. Chem. C* **2014**, *2* (35), 7373–7384.

(34) Muñoz, J.; González-Campo, A.; Riba-Moliner, M.; Baeza, M.; Mas-Torrent, M.

Chiral Magnetic-Nanobiofluids for Rapid Electrochemical Screening of Enantiomers at a Magneto Nanocomposite Graphene-Paste Electrode. *Biosens. Bioelectron.* **2018**, *105* (October 2017), 95–102.

(35) Goya, G. F.; Berquó, T. S.; Fonseca, F. C.; Morales, M. P. Static and Dynamic Magnetic Properties of Spherical Magnetite Nanoparticles. *J. Appl. Phys.* **2003**, *94* (5), 3520–3528.

(36) Gutiérrez, L.; De La Cueva, L.; Moros, M.; Mazarío, E.; De Bernardo, S.; De La Fuente, J. M.; Morales, M. P.; Salas, G. Aggregation Effects on the Magnetic Properties of Iron Oxide Colloids. *Nanotechnology* **2019**, *30* (11), 112001.

(37) Mohammadzadeh Kakhki, R. Application of Magnetic Nanoparticles Modified with Cyclodextrins as Efficient Adsorbents in Separation Systems. *J. Incl. Phenom. Macrocycl. Chem.* **2015**, *82* (3), 301–310.

(38) Hadadian, Y.; Masoomi, H.; Dinari, A.; Ryu, C.; Hwang, S.; Kim, S.; Cho, B. K.; Lee, J. Y.; Yoon, J. From Low to High Saturation Magnetization in Magnetite Nanoparticles: The Crucial Role of the Molar Ratios between the Chemicals. *ACS Omega* **2022**, *7*, 15996–16012.

(39) Yuan, Y.; Rende, D.; Altan, C. L.; Bucak, S.; Ozisik, R.; Borca-Tasciuc, D. A. Effect of Surface Modification on Magnetization of Iron Oxide Nanoparticle Colloids. *Langmuir* **2012**, *28* (36), 13051–13059.

(40) Ansari, M.; Habibi-Rezaei, M.; Salahshour-Kordestani, S.; Ferdousi, M.; Movehedi, A. A. M. An Investigation on the Effect of β-CD Modified Fe3O4 Magnetic Nanoparticles on Aggregation of Amyloid b Peptide (25-35). *Mater. Technol.* **2016**, *31* (6), 315–321.

(41) Liu, J.; Chen, G.; Guo, M.; Jiang, M. Dual Stimuli-Responsive Supramolecular Hydrogel Based on Hybrid Inclusion Complex (HIC). *Macromolecules* **2010**, *43* (19), 8086–8093.

(42) Sahiner, N.; Sel, K.; Meral, K.; Onganer, Y.; Butun, S.; Zay, O.; Silan, C. Hydrogel Templated CdS Quantum Dots Synthesis and Their Characterization. *Colloids Surfaces A* **2011**, *389*, 6–11.

(43) Gašparac, R.; Martin, C. R.; Stupnišek-Lisac, E. In Situ Studies of Imidazole and Its Derivatives as Copper Corrosion Inhibitors. I. Activation Energies and Thermodynamics of Adsorption. *J. Electrochem. Soc.* **2000**, *147*, 548.

(44) Zhang, Q.; Tamayo, A.; Leonardi, F.; Mas-Torrent, M. Interplay between Electrolyte-Gated Organic Field-Effect Transistors and Surfactants : A Surface Aggregation Tool and Protecting Semiconducting Layer. *ACS Appl. Mater. Interfaces* **2021**, *13* (26), 30902–30909.

(45) Zhang, Q.; Leonardi, F.; Casalini, S.; Temiño, I.; Mas-Torrent, M. High Performing Solution-Coated Electrolyte-Gated Organic Field-Effect Transistors for Aqueous Media Operation. *Sci. Rep.* **2016**, *6*, 39623.

(46) Zhang, Q.; Leonardi, F.; Casalini, S.; Mas-Torrent, M. Mercury-Mediated Organic Semiconductor Surface Doping Monitored by Electrolyte-Gated Field-Effect Transistors. *Adv. Funct. Mater.* **2017**, *27* (46), 1703899.

(47) Tamayo, A.; Muñoz, J.; Mas-Torrent, M. Electronic Performance of Polymer Carbon-Paste Nanoallotropes from 0D to 3D as Novel Gate Electrodes in Water-Gated Organic Field-Effect Transistors. *Adv. Electron. Mater.* **2020**, *6* (7), 2000431.

(48) Muñoz, J.; Brennan, L. J.; Céspedes, F.; Gun'ko, Y. K.; Baeza, M. Characterization Protocol to Improve the Electroanalytical Response of Graphene-Polymer Nanocomposite Sensors. *Compos. Sci. Technol.* **2016**, *125*, 71–79.

(49) Fernández-Merino, M. J.; Guardia, L.; Paredes, J. I.; Villar-Rodil, S.; Solís-Fernández, P.; Martínez-Alonso, A.; Tascón, J. M. D. Vitamin C Is an Ideal Substitute for Hydrazine in the Reduction of Graphene Oxide Suspensions. *J. Phys. Chem. C* **2010**, *114* (14), 6426–6432.

Supplementary Information

pH sensor based on supramolecular Host-Guest interactions and an organic field-effect transistor with a magnetic carbon gate electrode

Adrián Tamayo, Ángel Campos-Lendinez, Jose Muñoz, Núria Crivillers and Marta Mas-Torrent

Institut de Ciència de Materials de Barcelona (ICMAB-CSIC), Campus de la UAB, 08193 Bellaterra, Barcelona, Spain. E-mail: mmas@icmab.es

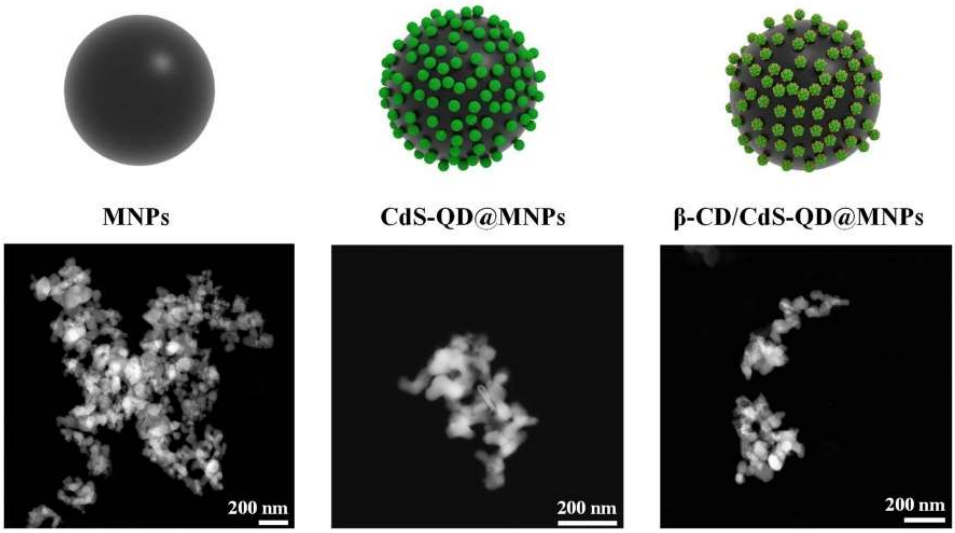

Figure S1: STEM of **MNPs**, **CdS-QD@MNPs** and **β-CD/CdS-QD@MNPs** samples.

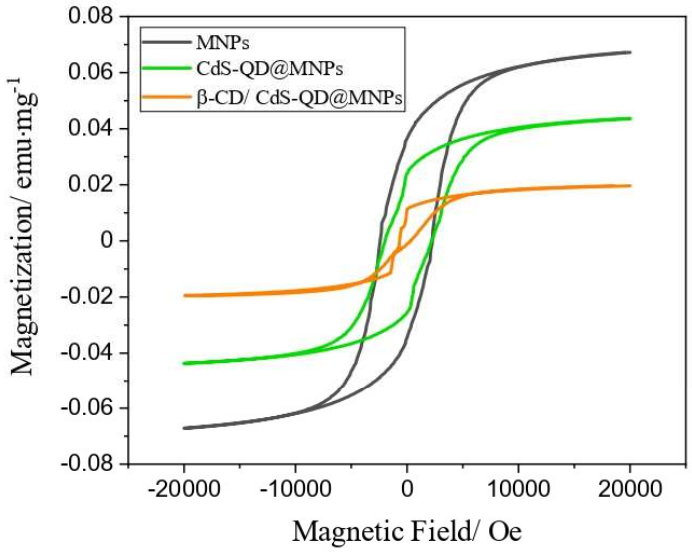

Figure S2. Field dependent magnetization curves for **MNPs** (black), **CdS-QD@MNPs** (green) and **β-CD/CdS-QD@MNPs** (orange) samples measured at room temperature between -20.000 and 20.000 Oe.

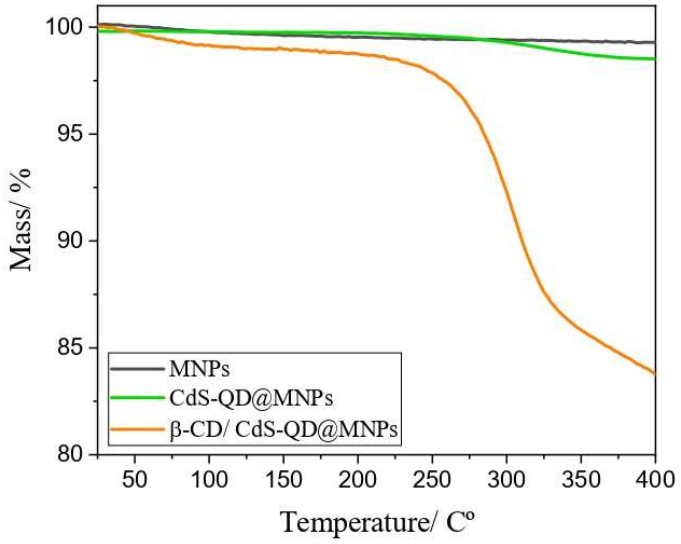

Figure S3. TGA measurements for MNPs (black), CdS-QD@MNPs (green) and β-CD/CdS-QD@MNPs (orange). The final weight loss at 400 ºC was estimated to be 0.7 %, 1.5 % and 17.3 % for **MNPs**, **CdS-QD@MNPs** and **β-CD/CdS-QD@MNPs**, respectively.

S3

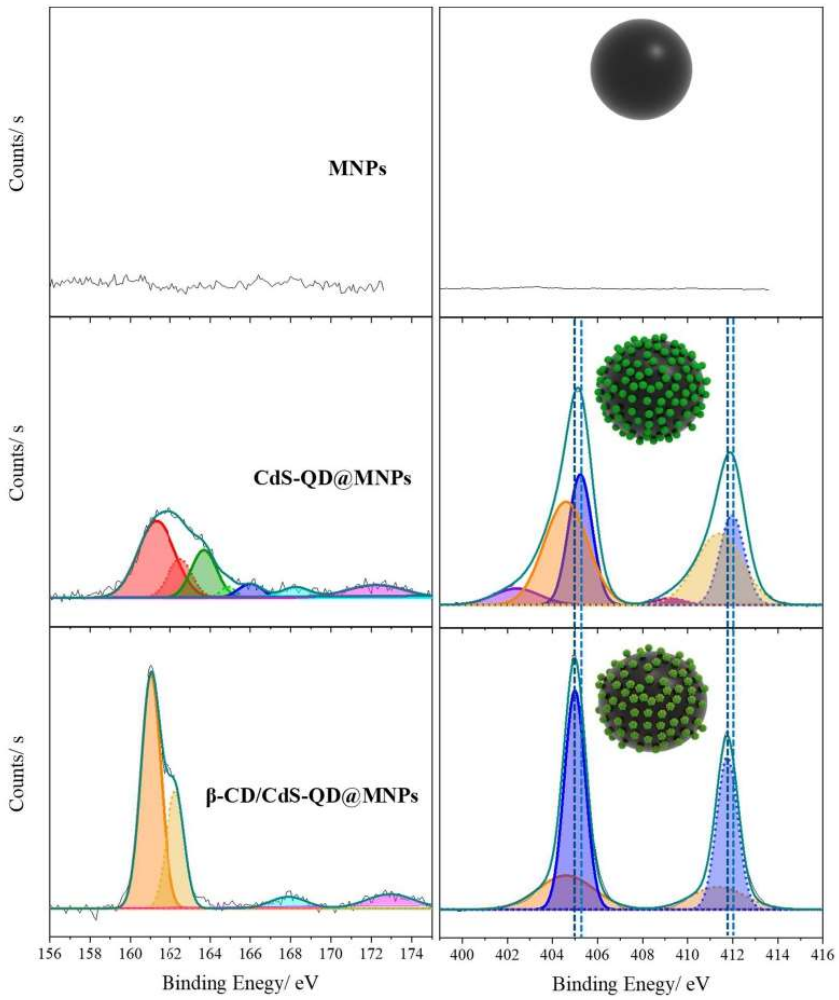

Figure S4. High resolution S2p and Cd3d XPS spectra for **MNPs**, **CdS-QD@MNPs** and **β-CD/CdS-QD@MNPs**.

High resolution XPS spectra in the region of S2p and Cd3d binding energies (BE) were acquired for **MNPs**, **CdS-QD@MNPs** and **β-CD/CdS-QD@MNPs** samples (Figure S4). The peaks assignment was done based on previous reports. For the raw magnetic nanoparticles, as expected no peaks assigned to the presence of S2p were found,

owing to the lack of sulphur atoms on the surface. Contrary, two doublets at 161.4 eV - 162.5 eV and 163.7 - 164.9 eV (for $S2p_{1/2}$ and $S2p_{3/2}$, respectively) were clearly observed in the **CdS-QD@MNPs** attributed to Cd-S and most probably to disulfides, respectively**.** In the **β-CD/CdS-QD@MNPs** sample the doublet was found at 161.0 eV ($S2p_{1/2}$) and 162.2 eV ($S2p_{3/2}$), ascribed to Cd-S-R bond.[1] Next, a peak at 166.0 eV was ascribed to a satellite emission in **CdS-QD@MNPs**.[2,3] Finally, the peaks at 168.2 eV and 172.2 eV for **CdS-QD@MNPs,** and 167.9 eV and 172.9 eV for **β-CD/CdS-QD@MNPs** are attributed to other oxidation states.[2,4]

For Cd3d spectra, as expected, no peaks were found for the **MNPs**. Contrary, several peaks (as doublets, for $Cd3d_{5/2}$ and $Cd3d_{3/2}$) with the typical 6.74 eV splitting[5] are observed in the case of capped magnetic nanoparticles (**CdS-QD@MNPs** and **β-CD/CdS-QD@MNPs***)*. For **CdS-QD@MNPs** a doublet ascribed to Cd-S is found at 405.2 eV and 412.0 eV[6] and, a second doublet at 402.4 eV and 409.2 eV is assigned to CdO.[7] In the case of the **β-CD/CdS-QD@MNPs** the peaks at 405.0 and 411.7 are attributed to the Cd-S ($Cd3d_{5/2}$ and $Cd3d_{3/2,}$ respectively). Finally, the doublet at 404.6 eV and 411.4 eV, present in both samples, is attributed to the presence of $Cd(OH)_2$.[8] The small shift observed in the peak position[9,10] of Cd-S upon the incorporation of the β-CD, is ascribed to the grafting of the β-CD onto the QD surface.

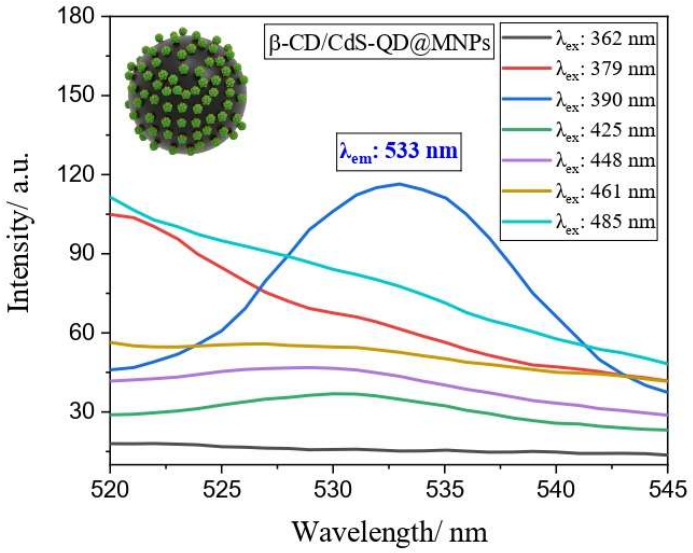

Figure S5. Emission spectra for **β-CD/CdS-QD@MNPs** measured at different excitation wavelengths.

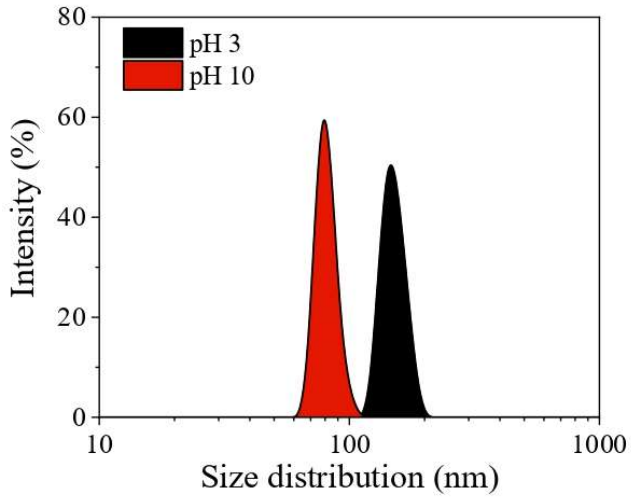

Figure S6: DLS measurements for 0.03 mg·mL^{-1} **β-CD/CdS-QD@MNPs** suspensions in Mili-Q water containing 0.67 mM of [$C_3H_4N_2$] at pH 3 and 10.

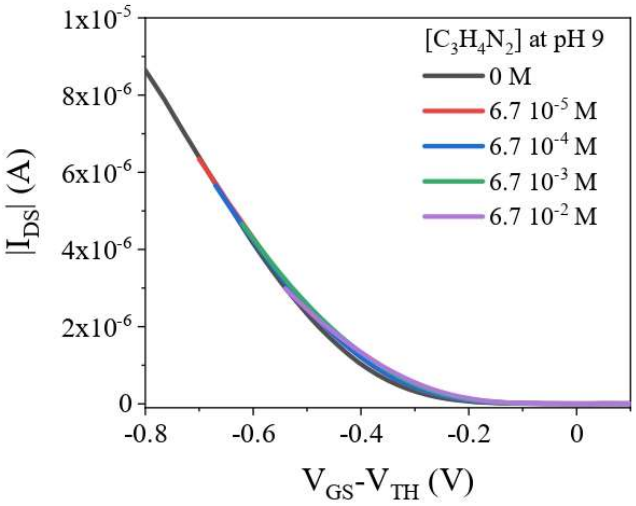

Figure S7. Transfer characteristics shown in Figure 4b as a function of the effective gate voltage (V_{GS} - V_{TH}).

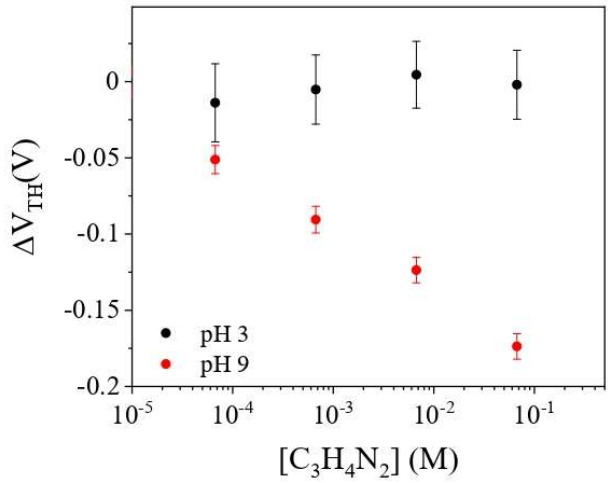

Figure S8. Threshold voltage shift change vs. imidazole concentration extracted from the transfer characteristics of EGOFETs (V_{DS} = -0.4 V) with a CGE with collected **β-CD/CdS-QD@MNPs** that had previously been incubated in a PBS solution with an increasing concentration of $[C_3H_4N_2]$ at pH = 3 and pH=9. The error bar is relative to two different devices.

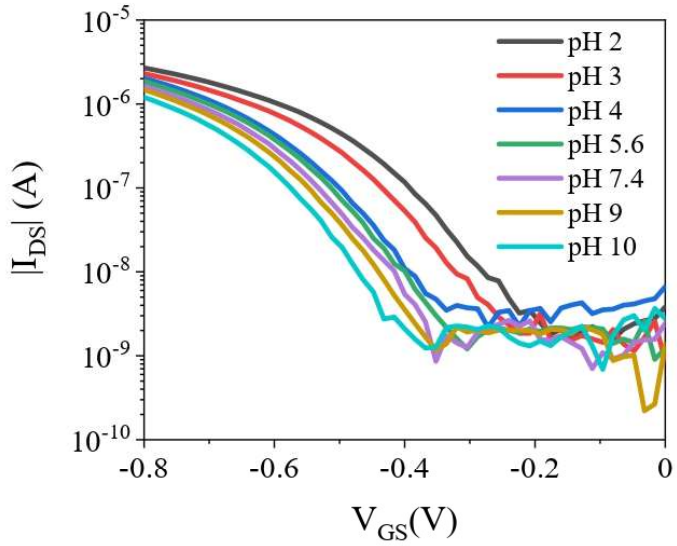

Figure S9. Transfer characteristics (V_{DS} = -0.4 V) of an EGOFET employing as gate electrode a CGE with collected **β-CD/CdS-QD@MNPs** previously incubated in a PBS solution with 6.7 mM of imidazole at pH ranging from 10 to 2.

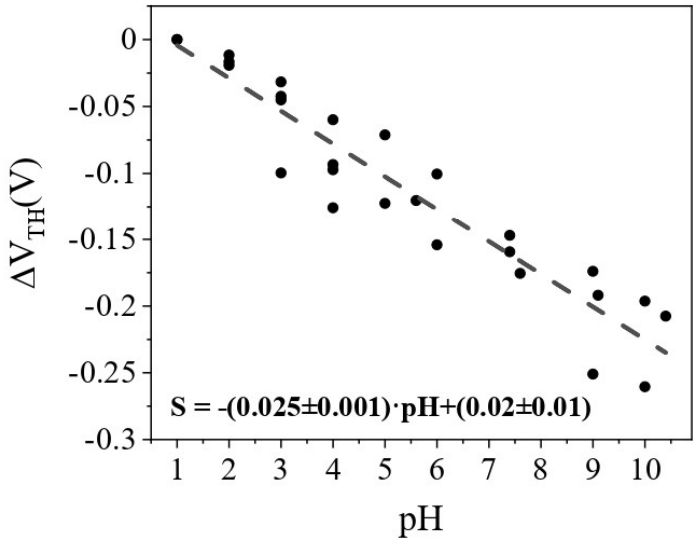

Figure S10. V_{TH} shift as a function of the pH for the five different devices shown in Figure 4e.

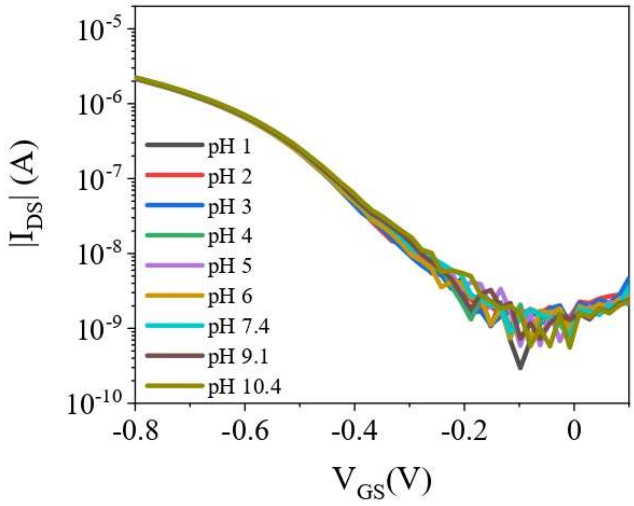

Figure S11. Transfer characteristic (V_{DS} = -0.4 V) of an EGOFET with a CGE gate electrode with collected **β-CD/CdS-QD@MNPs** incubated at different pH without imidazole.

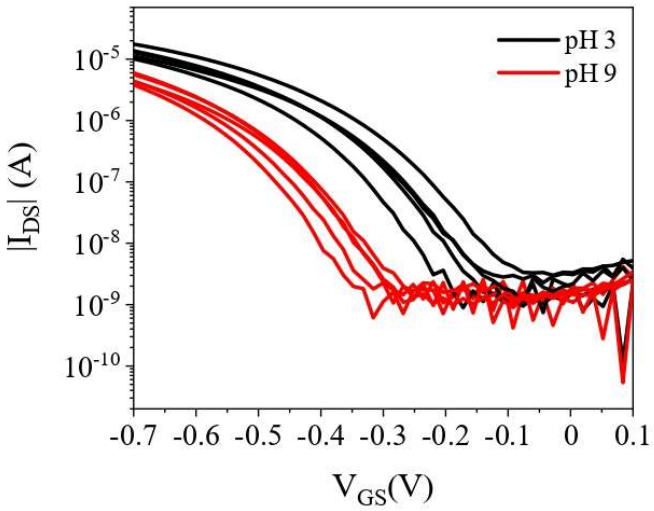

Figure S12. Transfer characteristic (V_{DS} = -0.4 V) of an EGOFET with a CGE gate electrode with collected **β-CD/CdS-QD@MNPs** incubated in a PBS solution with 6.7 mM of imidazole at pH 3 and 9.

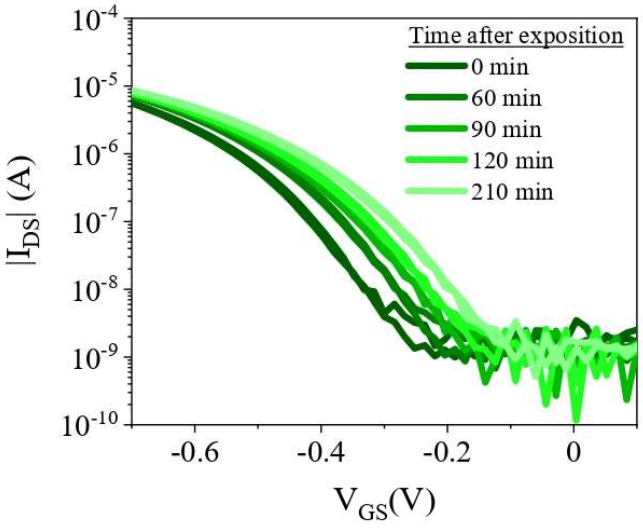

Figure S13. Transfer characteristic (V_{DS} = -0.4 V) measured over time of an EGOFET with a CGE gate electrode with collected **β-CD/CdS-QD@MNPs** incubated in a PBS solution with 6.7 mM of imidazole at pH 9.

References

(1) Zhu, Y.; Li, Z.; Chen, M.; Cooper, H. M.; (Max) Lu, G. Q.; Xu, Z. P. One-Pot Preparation of Highly Fluorescent Cadmium Telluride/Cadmium Sulfide Quantum Dots under Neutral-PH Condition for Biological Applications. *J. Colloid Interface Sci.* **2013**, *390* (1), 3–10.

(2) Sun, C.; Zhang, Y.; Wang, P.; Yang, Y.; Wang, Y.; Xu, J.; Wang, Y.; Yu, W. W. Synthesis of Nitrogen and Sulfur Co-Doped Carbon Dots from Garlic for Selective Detection of Fe3+. *Nanoscale Res. Lett.* **2016**, *11* (1), 110.

(3) Ghazzal, M. N.; Wojcieszak, R.; Raj, G.; Gaigneaux, E. M. Study of Mesoporous Cds-Quantum-Dot-Sensitized TiO2 Films by Using x-Ray Photoelectron Spectroscopy and Afm. *Beilstein J. Nanotechnol.* **2014**, *5* (1), 68–76.

(4) K. Algethami, F.; Saidi, I.; Ben Jannet, H.; Khairy, M.; Abdulkhair, B. Y.; Al-Ghamdi, Y. O.; Abdelhamid, H. N. Chitosan-CdS Quantum Dots Biohybrid for Highly Selective Interaction with Copper(II) Ions. *ACS Omega* **2022**, *7* (24), 21014–21024.

(5) Moulder, J. F.; Stickle, W. F.; Sobol, P. E.; Bomben, K. D.; Chastian, J. *X-Ray Photoelectron Spectroscopy*; 1992.

(6) Jiang, X.; Li, H.; Shang, Y.; Wang, F.; Chen, H.; Xu, K.; Yin, M.; Liu, H.; Zhou, W.; Ning, Z. Bi-Inorganic-Ligand Coordinated Colloidal Quantum Dot Ink. *Chem. Commun.* **2019**, *55* (64), 9483–9486.

(7) Subila, K. B.; Kishore Kumar, G.; Shivaprasad, S. M.; George Thomas, K. Luminescence Properties of CdSe Quantum Dots: Role of Crystal Structure and Surface Composition. *J. Phys. Chem. Lett.* **2013**, *4* (16), 2774–2779.

(8) Yang, T.; He, R.; Nie, G.; Wang, W.; Zhang, G.; Hu, Y.; Wu, L. Creation of Hollow Calcite Single Crystals with CQDs: Synthesis, Characterization, and Fast and Efficient Decontamination of Cd(II). *Sci. Rep.* **2018**, *8*, 17603.

(9) Ye, Y.; Xu, Y.; Huang, L.; Fan, D.; Feng, Z.; Wang, X.; Li, C. Roles of Adsorption Sites in Electron Transfer from CdS Quantum Dots to Molecular Catalyst Cobaloxime Studied by Time-Resolved Spectroscopy. *Phys. Chem. Chem. Phys.* **2016**, *18* (26), 17389–17397.

(10) Choi, J.; Choi, W.; Jeon, D. Y. Ligand-Exchange-Ready CuInS2/ZnS Quantum Dots via Surface-Ligand Composition Control for Film-Type Display Devices. *ACS Appl. Nano Mater.* **2019**, *2* (9), 5504–5511.

Conclusions

In this Thesis we studied the fabrication of new molecular hybrid materials based on functional self-assembled monolayers (SAMs) grafted on inorganic electrodes for electrochemical sensing and switching applications.

In particular, the research conducted led to the following conclusions:

i. The preparation of functional SAMs is a versatile, easy and low-cost methodology for tailoring surfaces with specific properties. In addition, anchoring specific molecules or nanoparticles on surface can increase their stability by avoiding nanoparticle aggregation or specific intermolecular reactions. Hence, the surface grafting of materials can be an appealing route to boost their potential in practical applications.
ii. Magnetically and redox-active SAMs have been prepared using urazole radical derivatives, a particular class of nitrogen-centred stable organic radicals. The optimization of the protocol to achieve a high surface coverage has been carried out. It was elucidated that the generation of the radical by oxidizing the SAM of the urazole precursor is preferable compared to the direct formation of the SAM using the previously formed radical in solution. Remarkably, although urazole radicals cannot be

isolated in solid state and might show limited stability in solution, here it was demonstrated that urazole radicals can be successfully stabilised in a SAM.

iii. SAMs on ITO based on CdSe/ZnS quantum dots (QDs) functionalized with a monolayer of redox-active ferrocenes (Fc) have been prepared. The QDs were covalently anchored to the ITO through an on-surface ligand reaction with a thiol-terminated SAM and were then further modified with ferrocenyl alkane thiol derivatives in the last step. This novel methodology has permitted to prepare a stable electrochemically triggered switch using the QD fluorescence properties as output. It has been demonstrated that different parameters, such as the spacer length between the QD and the Fc or the ratio of oxidized/reduced Fc units at the particle surface, allow tuning the quenching efficiency and, thus, the switching response. This approach can be expanded to include other relevant functional molecules that may interact or contribute differently to the optical response of QDs, opening a broad range of possibilities to explore in sensing and information storage.

iv. The use of SAMs that can interact with certain analytes by supramolecular interactions has been demonstrated to be a successful strategy for developing sensing platforms with excellent limits of detection (LODs), sensibility and selectivity.

v. Impedimetric sensors based on SAMs bearing polycyclic aromatic hydrocarbons (PAHs) have been developed for the successful electrochemical differentiation of hazardous PAH pollutants in aqueous samples. This approach benefits from the supramolecular π-stacking interactions present among identical aromatic molecules. This achievement demonstrates the feasibility of achieving selective discrimination of a wide range of small aromatic molecules.

vi. The supramolecular complex formation/desorption between imidazole and β-cyclodextrin (β-CD) at different pHs was exploited to develop a pH indicator. Magnetic

nanoparticles (MNPs) decorated with CdS quantum dots (QD) functionalized with thiolated β-CD were synthesized. The **β-CD/CdS-QD@MNPs** were incubated with imidazole at different pHs and collected on a magnetic carbon-paste electrode, which was used as gate contact in an Electrolyte-Gated Organic Field-Effect Transistor (EGOFET). The device showed high sensitivity and reversibility in a wide pH range from 1 to 10 as well as excellent re-usability.

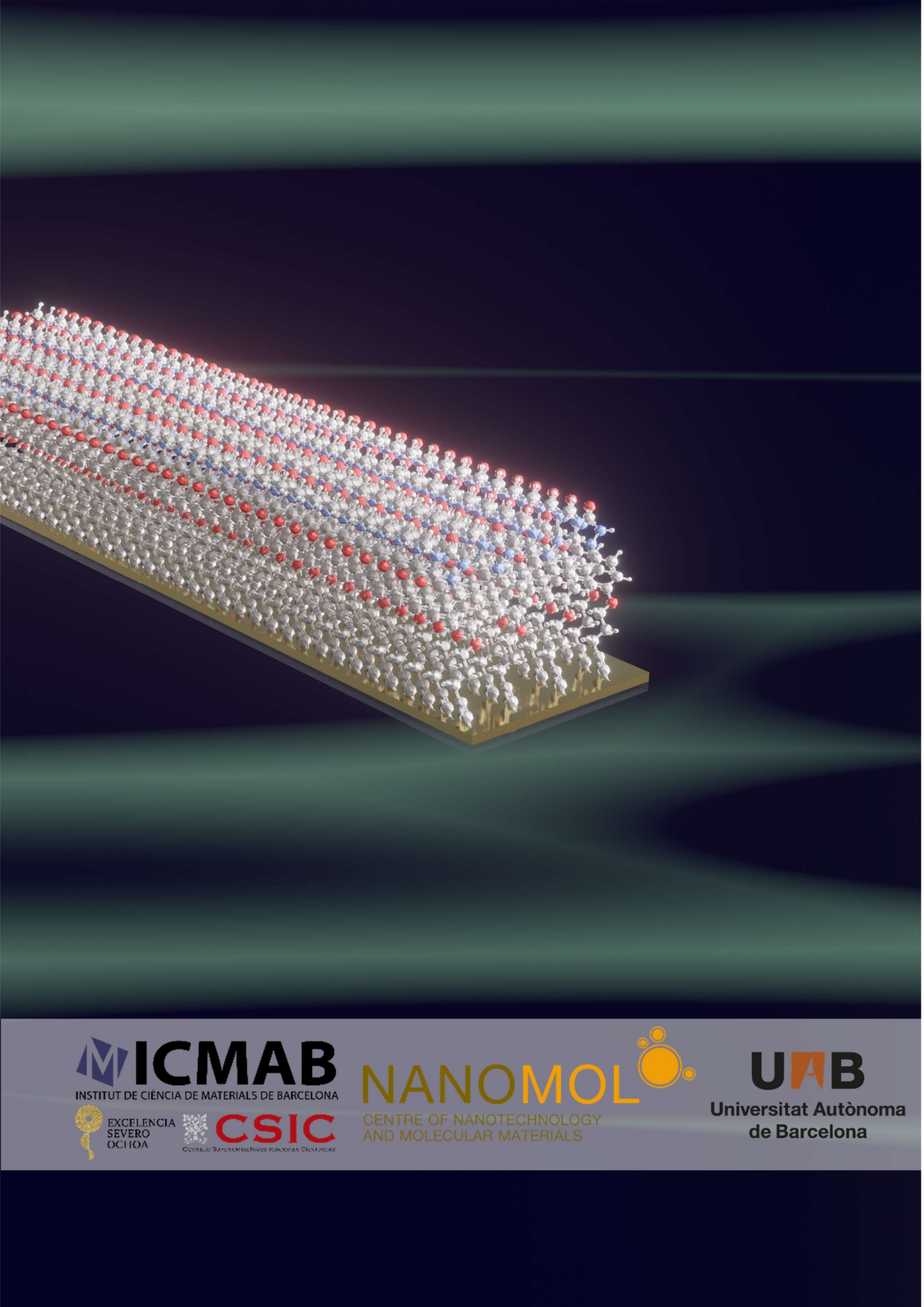

ICMAB
INSTITUT DE CIÈNCIA DE MATERIALS DE BARCELONA
EXCELENCIA SEVERO OCHOA
CSIC
NANOMOL
CENTRE OF NANOTECHNOLOGY AND MOLECULAR MATERIALS
UAB
Universitat Autònoma de Barcelona